

AD-A253 788 ON PAGE

Form Approved
OMB No. 0704-0188Public release
collection
Date May

1 hour per response, including the time for reviewing instructions, searching existing data sources, gathering of information. Send comments regarding this burden estimate or any other aspect of this collection of information, including suggestions for reducing the burden, to Washington Headquarters Services, Directorate for Information Operations and Reports, 1215 Jefferson Avenue, Washington, DC 20540.

1. AGENCY USE ONLY (Leave blank)

2. REPORT DATE
June 1992

3. REPORT TYPE AND DATES COVERED

Final Technical Report (1 Nov 88 - 30 Apr 92)

4. TITLE AND SUBTITLE

Probing Cosmic Infrared Sources: a Computer Modeling Approach
(Final Technical Report)

5. FUNDING NUMBERS

61102F

(2)

Grant AFOSR-89-0104

2311

A1

6. AUTHOR(S)

Chun Ming Leung (Principal Investigator)

7. PERFORMING ORGANIZATION NAME(S) AND ADDRESS(ES)

Rensselaer Polytechnic Institute
110 Eighth Street
Troy, New York 12180-35908. PERFORMING ORGANIZATION
REPORT NUMBER

AFOSR-TR-92-0759

9. SPONSORING/MONITORING AGENCY NAME(S) AND ADDRESS(ES)

Air Force Office of Scientific Research
AFOSR/NP, Building 410
Bolling Air Force Base, D.C. 2-332-6448
Dr Radoski10. SPONSORING/MONITORING
AGENCY REPORT NUMBERDTIC
ELECTE
AUG 5 1992
S A D

11. SUPPLEMENTARY NOTES

12a. DISTRIBUTION/AVAILABILITY STATEMENT

Approved for public release;
distribution unlimited.

92-21209



13. ABSTRACT (Maximum 200 words)

Phenomenological computer models were constructed to interpret observations of cosmic infrared sources and to make predictions which would stimulate further studies. The research was divided into four areas:

- (1) Detailed radiation transport models, incorporating both the equilibrium heating of large dust grains and the transient heating of very small grains, were constructed for interstellar dust clouds and circumstellar dust shells of evolved stars to parameterize the observed radiation characteristics in terms of their physical source properties.
- (2) Existing methods of analysis (e.g., semi-analytical methods for determining the dust mass, dust temperature, and grain emissivity laws) in infrared astronomy were critically evaluated to determine the conditions under which these approaches were valid and reliable. Semi-empirical relationships were then developed to facilitate the rapid interpretation of infrared observations.
- (3) Theoretical models were developed to study various physical phenomena involving dust grains, e.g., molecule formation on grains, grain formation in expanding circumstellar envelopes.
- (4) Several computational techniques were investigated which could automate and improve the efficiency of existing radiation transport codes for modeling infrared sources.

14. SUBJECT TERMS

Astronomy
Astrophysics
Cosmic DustCircumstellar Grains
Interstellar Grains
Radiation Transport

15. NUMBER OF PAGES

278

16. PRICE CODE

17. SECURITY CLASSIFICATION
OF REPORT

Unclassified

18. SECURITY CLASSIFICATION
OF THIS PAGE

Unclassified

19. SECURITY CLASSIFICATION
OF ABSTRACT

Unclassified

20. LIMITATION OF ABSTRACT

UL

TABLE OF CONTENTS.

	Page
COVER PAGE	1
TABLE OF CONTENTS	3
1.0 INTRODUCTION AND OVERVIEW	5
2.0 DETAILED MODELING OF INFRARED SOURCES	6
2.1 Infrared Sources with Transiently Heated Dust Grains	8
2.1.1 Radiation Transport for Transiently Heated Grains	8
2.1.2 Model for the Barnard 5 Dense Cloud	9
2.1.3 Model for the Chamaeleon Diffuse Cloud	10
2.2 Dust Envelopes Around Evolved Stars	10
2.2.1 Interpreting IRAS Observations of Evolved Stars	10
2.2.2 Nature of 100 μ m Emission of Carbon Stars	12
2.2.3 Models for C R Borealis and W Hydrae	13
2.3 Modeling Ice Features in Circumstellar Shells	13
2.4 Radiation Transport in Sources with Disk Geometry	15
3.0 EVALUATION OF METHODS OF ANALYSIS IN INFRARED ASTRONOMY	16
4.0 THEORETICAL STUDIES INVOLVING DUST GRAINS	16
4.1 Theory of Molecule Formation on Dust Grains	17
4.2 Modeling Grain Formation in Stellar Outflows	18
4.3 Infrared Emission from Fractal Grains	19
4.4 Photochemistry in Circumstellar Envelopes	19
5.0 OTHER RELATED RESEARCH PROJECTS	20
5.1 Chemical Effects of MHD Waves in Dusty Plasmas	20
5.2 Probing [C]/[O] Ratios in Dense Interstellar Clouds	21
5.3 Improvements to Radiation Transport Codes	22
5.3.1 Adaptive Grid Technique	22
5.3.2 Finite Element Method	23
5.3.3 Automation of Modeling Process	24
6.0 REFERENCES	25

Approved for public release
distribution unlimited.

Approved for public release
distribution unlimited.

Approved for public release
distribution unlimited.

TABLE OF CONTENTS (continued)

Page

APPENDICES

A1.	Professional Personnel Associated with Research Effort	27
A2.	List of Publications, Contributed Papers/Talks, and Invited Talks Resulted from Research Effort	28
A3.	Reprints of Papers Published	
A3.1	"Infrared Emission from Isolated Dust Clouds in the Presence of Very Small Dust Grains."	
A3.2	"Size and Density Distribution of Very Small Dust Grains in the Barnard 5 Cloud."	
A3.3	"On the Nature of the Excess 100 μm Flux Associated with Carbon Stars."	
A3.4	"Radiation Transport in Dust in Disk Geometry: I. Application to Externally Heated Interstellar Clouds."	
A4.	Preprints of Papers Submitted	
A4.1	"Probing Infrared Sources by Computer Modeling."	
A4.2	"Models of Highly Extended Dust Shells Around R C Borealis and W Hydrae."	
A4.3	"A Critical Evaluation of Semi-Analytic Methods in the Study of Unresolved, Centrally Heated Infrared Sources."	
A4.4	"Modeling Grain Formation in Stellar Outflows: A Master Equation Approach."	
A5.	Selected Poster Papers Presented	
A5.1	"Modeling the 3 μm Ice Feature in the Infrared Spectra of Circumstellar Envelopes."	
A5.2	"Modeling the 3 μm Water Ice Band of Evolved Stars: Temperature Effects?"	
A5.3	"A Chemical Kinetic Model of Radical Reactions in Molecular Mantles."	
A5.4	"Modeling the Infrared Spectra of Fractal Grains."	
A5.5	"Effects of Radiative Transfer on the Photochemistry of Evolved Circumstellar Envelopes."	
A5.6	"Probing the Carbon-to-Oxygen Ratio in Dense Interstellar Clouds."	

1.0 INTRODUCTION AND OVERVIEW

Infrared radiation is the primary tracer of the dust component in the universe because cool dust grains radiate most of their energy at infrared wavelengths. Dust grains, although a minor constituent, play a very important role in the thermodynamics and evolution of many astronomical objects. The association of this dust with stars, nebulae, interstellar molecular clouds, and nuclei of some galaxies is well established from observations in the infrared. Infrared astronomy has played a unique role in our exploration of the cosmos. For example, the Air Force Sky Survey, the first infrared all-sky survey carried out at wavelengths beyond $2.2 \mu\text{m}$, made a substantial contribution to infrared astronomy and produced two important catalogs of infrared sources: *The AFCRL Infrared Sky Survey* (Walker and Price 1975) and *The AFGL Four Color Infrared Sky Survey* (Price and Walker 1976). This survey has shown that the appearance of the sky changes dramatically in the mid-infrared, and studies of isolated objects discovered by the survey have revealed extreme examples of evolved, dust-enshrouded stars and dense interstellar dust clouds that may be in very early stages of stellar evolution. In the last decade, NASA has launched a number of space-based observatories: the Infrared Astronomical Satellite (IRAS), the Hubble Space Telescope (HST), and the Cosmic Background Explorer (COBE). In particular, the IRAS, launched in 1983, carried out a comprehensive infrared survey of the sky and a wide variety of astronomical objects were detected in the infrared. Thus we have discovered infrared cirrus, detected protoplanetary disks, gained access to dust-enshrouded regions of star formation, found galaxies far brighter in the infrared than in all other wavelength bands combined, probed the properties of interstellar dust, and gained insight into the cooling mechanisms for interstellar medium. The IRAS has stimulated advances in most branches of astrophysics and the IRAS database remains a vital tool for current research in infrared astronomy.

In recognition of the importance and impact of infrared astronomy, the astronomical community has recently identified the 1990's to be the decade of infrared astronomy. Several new infrared observational facilities have been proposed which will bring about a manifold increase in sensitivity as well as spatial and spectral resolutions over existing instruments. Thus in this decade we should see a dramatic growth in the quality and variety of infrared astronomical data which, however, would require increasingly sophisticated analytical techniques for interpretation. To meet the scientific challenges presented by existing and the next generation of infrared observations from ground-based, airborne, and space facilities, it is imperative that complementary theoretical studies with increasing degree of sophistication be undertaken to analyse these high-quality observations.

We have initiated a comprehensive research program to study and model the phenomenology of cosmic infrared sources. The main objectives of the research program are:

- (A) To construct detailed models for a variety of cosmic infrared sources and parameterize the observed radiation characteristics in terms of their physical source properties.
- (B) To critically evaluate existing methods of analysis in infrared astronomy and investigate the conditions under which these approaches are valid and reliable; to identify more sophisticated diagnostic tools for probing the characteristics of infrared sources and develop reliable semi-empirical relationships to facilitate the rapid interpretation of observations.
- (C) To develop further physical concepts to understand and theoretical tools to model physical phenomena involving dust grains, e.g., molecule formation on grain dust grains, grain formation in expanding shells around cool stars; the primary emphasis is on studying the detailed effects of radiation transport and opacity and their observational consequences.

The modeling strategy is to take a phenomenological approach by comparing observations with results from detailed computer modeling, the choice of model parameters being guided by observational evidence. Emphasis is on making predictions which can be checked against

future observations.

During the tenure of this grant, much progress has been made in the development of detailed models for cosmic infrared sources. Models with increasing degree of physical realism have been constructed. In particular, several major advances have been made in the computer modeling of cosmic infrared sources: radiation transport including transient heating of very small grains, radiation transport in 2-D disk geometry, realistic modeling of grain nucleation and growth. In Figure 1 we summarize schematically the recent advances made. The left-hand column indicates past assumptions, in contrast with present capabilities shown in the right-hand column. Clearly models of infrared sources have become increasingly sophisticated (see Appendix A4.1 for an overview). Future research will incorporate other important physical processes so that self-consistent physical models can ultimately be constructed: a) transfer of polarized radiation, b) radiation hydrodynamics, c) radiation transport in 3-D geometries, d) grain nucleation and growth, and e) gas-phase and grain-surface chemistry. In addition, improvements in computational techniques will be made: a) better algorithms and iteration procedures, and b) automation of model fitting.

From a scientific standpoint, these phenomenological studies have contributed greatly to our general understanding of the physics of various infrared sources and stimulated further observations. From a utilitarian standpoint, the completed research should be relevant to some important programs of the United States Air Force such as the Celestial Backgrounds Scene Descriptor project whose goal is to develop an accurate description of the location, extent, variability, and nature of various cosmic infrared sources for target discrimination and tracking against this natural radiation background.

In the following narrative of this report we only highlight the major results of the research accomplished. Detailed discussions can be found in the papers which have been published/submitted/presented. Copies of these are included in the appendices. The research results can be divided into following four general areas:

- a) detailed modeling of infrared sources,
- b) evaluation of methods of analysis in infrared astronomy,
- c) theoretical studies involving dust grains, and
- d) other related research projects.

2.0 DETAILED MODELING OF INFRARED SOURCES

A good strategy for a systematic analysis and interpretation of spaced-based infrared observations (e.g., IRAS data) includes the following steps: a) perform statistical analyses and correlation studies, and develop classification schemes, e.g., histograms, two-color diagrams, correlation plots, classification of spectral feature profiles; b) construct *phenomenological* models for each class of objects to parameterize the observed radiation characteristics in terms of their physical source properties; c) from the phenomenological models, develop self-consistent *physical* models which can explain coherently present and future observations. The phenomenological modeling of infrared sources invariably requires solving in detail the problem of scattering, absorption, and emission of photons by dust grains, i.e., radiation transport in a dusty medium.

To model the observed characteristics of an infrared source, we solve the equation of radiation transport in a dusty medium, subject to the constraint of radiative equilibrium. In the model the input parameters are: a) luminosity and spectral energy distribution of the central heat source, b) source geometry and dimensions, c) size, composition, and optical properties of each grain species (e.g., extinction coefficient, albedo, and scattering asymmetry parameter), d) dust density distribution, and e) other local heating mechanisms, e.g., viscosity, collision with

MODELING INFRARED SOURCES: PAST & PRESENT

MODELING APPROACH

- | | |
|-----------------|-----------------------------------|
| • analytical | • numerical |
| • single source | • single source, class of sources |

GRAIN PROPERTIES

- | | |
|---------------------|------------------------|
| • grey opacity | • non-grey opacity |
| • single grain type | • multiple grain types |
| • single size grain | • size distribution |
| • spherical shape | • arbitrary shapes |

PHYSICAL PROCESSES

- | | |
|-------------------------------|-----------------------------------|
| • isotropic radiation | • anisotropic radiation |
| • single or no scattering | • anisotropic multiple scattering |
| • equilibrium heating | • equilibrium + transient heating |
| • temp.-independent opacity | • temp.-dependent opacity |
| • classical nucleation theory | • master equation approach |

SOURCE GEOMETRY

- | | |
|------------------------|----------------------------|
| • 1 - D slab or sphere | • 1 - D sphere, 2 - D disk |
|------------------------|----------------------------|

Figure 1: Comparison of past (left column) and present (right column) capabilities in models of infrared sources

gas particles. The model output consists of the following: a) temperature distribution of each grain species, b) combined energy spectrum of central heat source and dust cloud, and c) intensity variation across the source at each wavelength, and d) properties of internal radiation field. The choice of model parameters is guided by observations. The most important observational constraints are: a) spectral energy distribution, b) surface brightness or apparent source size as a function of wavelength, c) strength and shape of emission and absorption features, and d) color temperatures in different parts of spectrum. The interplay between observational constraints and model parameters has been considered (cf. Leung 1976b, Jones, et al. 1977), e.g., the source luminosity can be estimated from a), the dust density distribution and geometrical source size from b), the grain composition and optical depth information from c), and the dust temperature distribution from d).

2.1 Infrared Sources with Transiently Heated Dust Grains

2.1.1 Radiation Transport for Transiently Heated Grains

Among the unexpected results from IRAS was the discovery of excess mid-infrared emission detected in a number of infrared sources, e.g., in diffuse clouds, in dark globules, in visual reflection nebulae, and high-latitude dust clouds or infrared cirrus. It is now believed that the emission at short wavelengths ($< 30 \mu\text{m}$) comes from transient heating of very small grains (Draine and Anderson 1985) and large polycyclic aromatic hydrocarbons or PAHs (Boulanger et al. 1985; Puget et al. 1985). Temperature fluctuations in small grains occur whenever the energy input from photons or energetic particles is considerably larger than the average energy content of the grain. This non-equilibrium grain heating can significantly change the energy distribution of the radiation field in infrared sources. To properly interpret the IRAS observations, one needs a radiation transport model which takes into account self-consistently the effects of temperature fluctuations due to transient heating of small grains and PAHs. By formulating the radiation transport problem involving transient heating in a fashion similar to a non-LTE line transfer problem involving many transitions and energy levels, we have developed a computer code which, *for the first time*, treats self-consistently the thermal coupling between the transient heating of small grains and the equilibrium heating of conventional large grains.

In this code, we used the method proposed by Guhathakurta and Draine (1989) to calculate the probability distribution of grain temperatures for transient heating. In this method the allowed enthalpy range is divided into a number of discrete bins (cf. energy levels in an atom) and the rate matrix with transition rates between different bins is set up. The rate matrix includes cooling (treated as a continuous process) and discrete heating induced by photons and gas particles with energy corresponding to the energy difference between any two enthalpy bins under consideration. The enthalpy space is closed by assuming that all transitions to above the highest bin end up in the highest bin and by treating the heating by photons with wavelengths longer than an arbitrarily chosen cut-off (typically $0.1 \mu\text{m}$, corresponding to an energy much smaller than the total enthalpy of the smallest dust grains) as a *continuous* process which modifies slightly the cooling rate. The enthalpy of the first bin is chosen such that the *net* cooling rate out of the first bin is equal to zero, so the grain cannot attain temperatures lower than that of the first bin. The equations describing the transition rates (assumed known) form a system of linear equations which can be solved for the temperature probability density function (i.e., the bin populations). Due to the discreteness of the enthalpy grid, the method of Guhathakurta and Draine (1989) is subject to an error which becomes substantial under certain circumstances. Let us assume, for simplicity, that the enthalpy grid is uniform and all bins have equal widths. The longest wavelength of the radiation field included in the discrete heating part is that corresponding to the energy difference between the two neighboring bins. The radiation energy density between this wavelength and the continuous heating cut-off wavelength is simply missing in the

calculations. For some classes of sources (internally heated clouds with low central source temperature) this may be a significant fraction of the total energy and results in underestimating the grain temperature. While the problem may be corrected by using larger number of bins, this becomes impractical as the computing time would be prohibitive for large grids. We overcome this problem by redefining the cut-off wavelength of the continuous heating rate to correspond to the energy difference between the two neighboring bins. This way we ensure that no energy is missing from the rate equations. Similarly we renormalized the discrete heating rates so that the sum of all rates out of any given bin is equal to the value given by the integral over all wavelengths shorter than the cut-off wavelength. Our modified method of calculating the temperature probability distribution has been tested for a broad range of radiation fields. Accurate results were obtained for a reasonable number of bins (between 200 and 300).

To incorporate the transient heating of small grains into the existing radiation transport code of Egan, Leung and Spagna (1988), we utilized the concept of a *mean* dust temperature introduced in the original code to reduce the computation time in the multiple grain case. The mean temperature has been redefined to include the small grain temperature summed over all bins and weighted by the bin population. From the initial guess for the mean temperature distribution we first calculate the radiation field intensity. Knowing the intensity we then calculate the equilibrium temperature for large grains (by solving the local energy balance equation) and temperature distribution function for small grains (by solving the rate equations as described above) and update the source function. From the source function we recalculate a new radiation field intensity. The iteration procedure is continued until convergence is achieved. The number of iterations required for convergence is typically 5 - 10 for externally heated sources and about 20 - 30 for internally heated sources with a reasonable initial guess for the mean temperature distribution. With 200 enthalpy bins the computing time required for a model of an externally heated cloud to converge ranges from 4 to 30 hours of the CPU time on a Silicon Graphics Personal IRIS workstation (rated at 0.9 Mflop). For comparison, a model without small grains took only 10 minutes of CPU time. To ensure that the results of the code are physical we made a local energy conservation test for the small grains at each shell, which, contrary to the case of large grains, is not directly incorporated into the equations. Even in the worst cases energy is conserved locally to within a few percent which is comparable to the global flux conservation for internally heated models.

Infrared limb brightening at the four IRAS wavelength bands (12, 25, 60, and 100 μm) has been observed in clouds heated externally by the interstellar radiation field, e.g., in diffuse clouds and in dark globules. Using the computer code, we have constructed a series of models to study the effects of temperature fluctuations due to transient heating of small grains on the infrared spectrum and surface brightness of externally heated interstellar dust clouds.

Further details on the results of this research can be found in Appendix A3.1.

2.1.2 Model for the Barnard 5 Dense Cloud

Infrared limb brightening at the four IRAS wavelength bands (12, 25, 60, and 100 μm) has been observed in the dense interstellar cloud Barnard 5 (Beichman et al. 1988). The infrared limb brightening at short wavelengths (10-30 μm) is probably due to small grains, as indicated by the much higher color temperature (a few hundred degrees) derived from the 12 and 25 μm emission. The color temperature derived from the 60 and 100 μm emission is an order of magnitude lower. Using the computer code and realistic grain opacities, we have constructed models to interpret the IRAS observations of the Barnard 5 cloud. We find that the 25 μm emission is most likely produced by small grains with a $\sim 6 - 10 \text{ \AA}$ radius. These grains also contribute up to 50% of the observed 12 μm emission. The missing 12 μm flux may be produced by PAHs. The emission at 60 and 100 μm is most likely due to large grains

(with radius $\approx 0.1 \mu\text{m}$) heated under equilibrium conditions. Our model results indicate that the small grains responsible for the short-wavelength emission account for 1 - 2% of the total opacity in the visible, and 10 - 20% of the total dust mass of the cloud. Furthermore, to produce the observed limb-brightening at various infrared wavelengths, their spatial distribution must be more extended than that of the large grains. However, we cannot exclude the possibility that small grains are also present in the cloud core. Small grains in the cloud interior would produce only weak emission in the short-wavelength IRAS bands due to the strong attenuation of UV photons responsible for heating the grains to high temperatures.

Further details on the results of this research can be found in Appendix A3.2.

2.1.3 Model for the Chamaeleon Diffuse Cloud

Chlewicki et al. (1987) studied the infrared emission from a diffuse cloud in Chamaeleon. They presented surface brightness profiles as a function of the distance from the cloud center at the four IRAS bands. The cloud is isolated and highly regular and the data thus appear ideal for testing spherically symmetric cloud models. We have also constructed models to interpret the IRAS observations of this diffuse cloud in Chamaeleon (Chlewicki et al. 1987). We have modified the computer code to effectively model the presence and size distribution of different grains. In particular, our code can presently handle up to five types of conventional large grains (either graphite or silicate), as well as eight types of small grains (graphite, silicate, or PAHs). For the silicate and graphite grains of different sizes we use the cross-sections tabulated by Draine (1987). The cross-sections for PAHs are taken from Desert, Boulanger, & Puget (1990). We assume power law size distributions for each grain components and typically use 5 large grain sizes, 5 small grain sizes, and 3 PAH sizes to model the grain size distributions. The power law exponents and relative abundances between different grain types are free parameters varied in the models.

For the relative contributions of different grain components to the emission of the Chamaeleon cloud model, we find that longward of $100 \mu\text{m}$, the emission is dominated by conventional large grains; between $30\text{-}100 \mu\text{m}$, the emission is produced mainly by very small grains; shortward of $30 \mu\text{m}$, both PAHs and small grains are responsible for the emission. When the model results are compared with observations for the surface brightness at the four IRAS bands, we find that the agreement between the model results and observations is very good. The model also indicates that very small grains account for $\approx 15\%$ of the total opacity in the visible, and $\approx 5\%$ of the total dust mass of the cloud. On the other hand, PAHs account for $\approx 10\%$ of the cloud opacity and $\approx 20\%$ of the dust mass. Furthermore, to produce the observed infrared limb brightening at short wavelengths, the spatial distribution of small grains and PAHs must be more extended than that of large grains. Further research of this work is in progress.

2.2 Dust Envelopes Around Evolved Stars

2.2.1 Interpreting IRAS Observations of Evolved Stars

IRAS observations of cool stars (either oxygen-rich or carbon-rich) provide low resolution spectra in the mid-infrared ($7.8 - 22 \mu\text{m}$) and also give fluxes at four wavelength bands ($12, 25, 60,$ and $100 \mu\text{m}$) from which color-color diagrams are constructed. A major factor in determining the position of either C-rich ($[\text{C}]/[\text{O}] > 1$) and O-rich ($[\text{C}]/[\text{O}] < 1$) stars on the $12\text{-}25\text{-}60 \mu\text{m}$ color-color diagram is the presence of spectral features in the mid-infrared. O-rich stars show a $9.8 \mu\text{m}$ silicate feature, while C-rich stars have a SiC feature at $11.2 \mu\text{m}$. IRAS observations indicate that the SiC feature is quite narrow and uniform in shape showing little variation from star to star. On the other hand, the silicate feature is much wider and its shape varies widely among the O-rich stars (Little-Marenin 1986). Furthermore,

the regions occupied by the O-rich and C-rich stars on the 12-25-60 μm color-color diagram are quite distinct (Zuckerman and Dyck 1986). Willems (1987) has proposed that some O-rich stars evolve into carbon stars. As the photosphere of the O-rich star becomes C-rich (due to dredge up of C-rich material from the stellar interior), the formation of O-rich dust stops and the existing O-rich dust shell becomes detached and moves away. After the O-rich dust shell becomes optically thin and before the formation of C-rich dust begins, the underlying star may be identified as a visual carbon star. Eventually mass loss from the star begins again, forming a new, and this time C-rich dust shell. Subsequently stars with a substantial C-rich dust shell are identified as infrared or radio carbon stars. In the 60-25-12 μm color-color diagram the infrared and radio carbon stars lie along a line defined by the color of a blackbody. Chan and Kwok (1988) have shown that the visual carbon stars occupy a region on this diagram consistent with the predictions of Willems' model of detached shells. On the 100-60-25 μm color-color diagram, however, the infrared and radio carbon stars do not lie on the blackbody line, but show excess flux at 60 and 100 μm . This could be due to the presence of cool dust in the intervening interstellar medium or to a remnant O-rich dust shell far beyond the C-rich shell.

Since the characteristics of circumstellar dust shells should manifest themselves both in the flux spectrum and in the details of the spectral features, there should be a correlation between the characteristics of the spectral features observed in these cool stars and their corresponding positions on the color-color diagram. In this study we seek to provide a coherent interpretation for these IRAS observations. We have constructed radiation transport models of dust shells around O-rich and C-rich stars using realistic grain opacities which include spectral features of varying intrinsic widths. We have studied the observable characteristics of the following model parameters: shell opacity, dust shell distance from star, dust density distribution, and stellar luminosity. Each affects the dust temperature distribution which in turn is manifested in the shape of spectral features and the energy spectrum. We find that the difference in variations of the shape of SiC and silicate features is due to the smaller intrinsic width of the SiC feature in the presence of varying dust temperature distributions. Spectral features with greater intrinsic width are more sensitive to changing physical conditions in the dust shell. Furthermore, the observed differences in the width of the silicate feature in O-rich stars can be explained by the variations in the dust shell distance from the star. Variations in shell optical depth, dust density distribution, or grain composition cannot easily account for the range of shifts observed in the silicate feature. This interpretation is consistent with the theory of Willems, and we decided to pursue some more detailed modeling of the detached shell models.

Willems' scenario predicts two distinct mass loss phases for O-rich stars. In the first phase, the mass loss rate increases implying an increasing opacity through the dust shell, with the inner radius remaining roughly constant at the dust condensation radius. The second phase begins when the O-rich material is exhausted and dust formation ends. The dust shell becomes detached and the opacity decreases as the shell expands and moves away. We have modeled the photometric and spectroscopic evolution of these sources. Our model results indicate that one can distinguish between the two phases on the basis of the shape of the 9.8 μm silicate feature and by tracks on the 60-25-12 μm color-color diagram. We find that when the opacity increases, the wavelength centroid of the silicate feature remains constant while the width of the feature increases. These models define a nearly linear progression toward the region of the color-color diagram occupied by cooler objects. On the other hand, for models in which the dust shell has become detached and moves away, the dust cools and the shell becomes more transparent, revealing the underlying star. This results in a shift in the centroid of the 9.8 μm feature toward longer wavelengths. On the color-color diagram the detached shell models trace a loop toward the position occupied by cool stars without circumstellar dust shells. Hence a correlation between the shifts of the silicate features observed in O-rich stars and their corresponding positions on the color-color diagram would provide strong support for the

hypothesis that O-rich stars evolve to form carbon stars. Our study indicates that if the detached shell model of Willems is correct, several effects which can be checked with the IRAS observations should be seen. First, sources with dust shells at various stages of detachment should be seen at certain places on the color-color diagram. Correlated with this should be the equivalent width of the feature and its wavelength centroid. Those sources which are thought to have detached shells should exhibit greater feature shifts. Our models also indicate that these results should hold even across variations in stellar parameters. The IRAS class On objects (sources with no discernable emission or absorption at $10\text{ }\mu\text{m}$) appear to be very good candidates for detached shell objects. A large fraction of these sources lie in the region of the 60-25-12 μm color-color diagram shown by the models to be occupied by sources with detached dust shells at tens to hundreds of stellar radii.

2.2.2 Nature of the 100 μm Emission of Carbon Stars

The IRAS survey has made available a large and uniform sample of high-quality data from both photometric and spectroscopic observations of asymptotic giant branch (AGB) stars. In particular, IRAS data indicates that many carbon stars, especially those with optically thin dust shells, have large fluxes at 60 and 100 μm . It has been suggested that a remnant dust shell from an earlier mass-loss episode can explain the excess fluxes. Two hypotheses have been proposed to explain the origin of the remnant dust shell. First, that O-rich AGB stars may undergo a transformation to C-rich by carbon dredge-up, resulting in the formation of an inner C-rich dust shell and a remnant O-rich dust shell (Willems 1987). In the second scenario, a C-rich remnant dust shell is formed when helium shell-flashes stop the mass-loss process which resumes later (Oloffsson et al. 1990).

To produce an excess of flux at long wavelengths requires cool dust. We have identified three possible sources of cool dust around carbon stars. (1) In the outer parts of a single extended dust shell. (2) In a detached remnant dust shell from an earlier episode of mass loss. (3) In the interstellar medium surrounding the star. To test these hypotheses, radiation transport models of dust around carbon stars have been constructed: models with either a single C-rich dust shell or double shells. Figure 6 shows the color-color diagrams for selected carbon stars in the IRAS-LRS catalog. The thick solid line is the blackbody line. The gray-shaded areas indicate the limits on the colors for carbon stars of various ages imposed by the models. Clearly single-shell models cannot explain the observed color distribution, while two-shell models with either a C-rich or an O-rich remnant shell can.

Our modeling program for dust shells around carbon stars lead to the following conclusions:

1. A single dust shell model cannot account for the 60 and 100 μm flux necessary to explain the observed IRAS colors of visual carbon stars.
2. Interstellar reddening cannot account for the discrepancies between single shell models and the observations.
3. Two shell models can explain the colors of all carbon stars on both color-color diagrams. The timescale between the two mass loss episodes must be about 10^4 years, with a remnant shell geometrical thickness of about 1 pc.
4. Although the color-color diagrams alone do not allow us to determine the composition of the remnant shell, determination of the mass loss rate with respect to the 100/60 μm flux ratio indicates that no carbon stars with single dust shells are observed. This constitutes evidence in favor of Willems' evolutionary hypothesis.

Thus by constructing models for a class of infrared sources and comparing the results with observations, one can identify trends and determine more reliably the physical source parameters, thereby maximizing the scientific returns of the IRAS observations.

Further details on the results of this research can be found in Appendix A3.3.

2.2.3 Models for C R Borealis and W Hydrae

We have constructed radiation transport models for the dust shells around the hydrogen-deficient supergiant star R Coronae Borealis (R CrB) and the oxygen-rich red giant W Hydrae. IRAS observations of R CrB (Gillet et al. 1986) have been used as constraints in selecting the model parameters. Based on suggestions from earlier work a *double shell model* is employed as a standard scenario for R CrB. The first shell is a hot dust inner shell of radius 6" surrounding the central star. The second shell is the cooler remnant dust shell, which is highly extended with a radius 10' at a source distance of 1.6 kpc from earth. The two shells can be spatially well *separated* from each other and can have completely different mechanisms of heating of their dust grains. A comparison of *analytic models* and self-consistent *radiative transfer models* is made to delineate their usefulness in interpreting the IRAS observations. A detailed parametric study of the system has been undertaken.

The extended shell of W Hya has a radius of 20' at a source distance of 130 pc from earth. The IRAS data (Hawkins 1990) are used to constrain the model parameters of W Hya. The models are based on the scenario of *single* large circumstellar dust shell, much like the familiar dust shells around late type giants. We find that somewhat higher density of hot dust is required in the hot core of the shell, compared to extended part of the shell (which is not separated) starting very near this core, in order to fit the near infrared ($< 25 \mu\text{m}$) flux densities. A comparison of analytic approach and radiative transfer approach is also made. A parametric study of this system is presented along the same lines as for R CrB, although these two systems are very different in nature. The models of R CrB clearly point to the configuration of a large, well-separated, cool shell surrounding a tiny hot dust shell, thus supporting the current view that this extended shell is a *fossil shell*. However, the distance to which such an extended shell has moved as a whole, leaving a cavity in between the two shells, cannot be fixed from the radiative transfer analysis. Thus it can be treated as an unknown parameter of the system for modelling purposes. The ISRF incident on outer boundary plays a considerable role in modeling the IRAS 60 μm and 100 μm surface brightness data of R CrB. The observed isothermal temperature of R CrB fossil shell poses serious problems. We favor models in which the density varies as r^{-p} ($p \approx 1.0 - 1.5$) over inverse square law ($p = 2$) models. The source of dust heating in such models is an even combination of central star radiation and ISRF. Our models of W Hya indicate, on the other hand, that its enormous cool shell is heated predominantly by the central star radiation (in agreement with earlier suggestions). No excess ISRF is required to model the IRAS 60 μm and 100 μm surface brightness profiles of W Hya. The density distribution in W Hya shell is possibly of the form r^{-p} ($p \approx 0.5 - 1.0$). It is not clear from our models if this shell is a remnant shell. The amorphous carbon in the case of R CrB and amorphous silicate in the case of W Hya give better fits to the IRAS data, than crystalline dust grains.

Further details on the results of this research can be found in Appendix A4.2.

2.3 Modeling Ice Features in Circumstellar Shells

In the cool, thick circumstellar envelopes of O-rich evolved stars, water molecules will condense onto previously-formed silicate grains to form ice mantles which exhibit an infrared absorption feature at 3.1 μm . Circumstellar ice mantles thus form in a different manner to those observed in the dense interstellar medium where the accretion of O and H atoms, followed by hydrogenation reactions on the grain surface, leads to water ice formation. Due to the low gas and dust temperatures in molecular clouds, the ices formed there are observed to be amorphous and to contain other molecules besides H_2O . Observational studies of the 3 μm region in the circumstellar shells of several late-type stars (e.g. OH231.8+4.2 and IRAS

09371+1212) show that it is narrower than the interstellar one and, furthermore, that the absence of any significant additional absorption is consistent with the ices being very pure (Geballe et al. 1988). The narrowness of the feature is interpreted as being due to crystalline ice mantles which are formed in the hotter regions of the circumstellar envelope ($\approx 112\text{K}$), although an amorphous ice component may also be present (Smith et al. 1988). Recent observations of the 40-70 μm ice bands in some shells clearly confirm the presence of crystalline ice (Omont et al. 1990).

Information concerning the physical conditions in the shell and on the state of the ice mantles is normally obtained by fitting models to the observed feature. Conclusions from such studies depend upon two factors in the analysis of the observational data: a) the accuracy of the continuum fitted to the observed spectrum to estimate the optical depth in the ice feature, and b) the validity of a simple Mie theory analysis which assumes that the total extinction is due entirely to absorption, and which ignores radiative transfer effects such as dust emission and self-absorption when calculating a flux spectrum for comparison with observation. It is not clear that such a simple treatment of the radiative transfer problem in these dust shells is justified. We have thus computed theoretical fluxes from a full solution of the radiation transport problem, and have compared these with those fluxes obtained using the simple Mie theory treatment.

We modeled the shell as comprising of two dust components. At radii where the dust temperature is greater than the condensation temperature of crystalline ice the grains are amorphous silicates of radius 0.5 μm , whereas in the cooler outer regions of the shell they also possess crystalline ice mantles of thickness 0.1 or 0.6 μm . We have modeled a spherically symmetric dust shell with parameters characteristic of late-type stars. The method of analysis is as follows: we compute a theoretical flux spectrum using the radiative transfer code and regard this as an 'observation'; we then fit a continuum from three Planck functions to the 3 μm feature to estimate the optical depth in ice, and finally attempt to reproduce the theoretical flux using a simple Mie theory analysis. We have examined the applicability of this approach in light of the radiative transfer effects.

We find that the ice optical depths obtained from this fitting are typically underestimated by up to a factor of 10. The simple Mie theory treatment cannot reproduce the shape of the 'observed' flux profile obtained from the transfer code. Also, the fit at longer wavelengths from the Mie treatment worsens as the ice optical depth increases. The variation of the shape of the theoretical 3 μm feature with total optical depth can be understood as being due to radiative transfer effects arising from the presence of differing amounts of hot dust in the shell. At the higher optical depth, photon trapping occurs deep in the shell and this leads to saturation of the short wavelength wing of the 3 μm feature, and to an increase in the dust temperature there. A simple analysis based on Mie theory fails to reproduce the shape of the theoretical ('observed') 3 μm feature. Our calculations emphasize that radiative transfer effects must be considered when modeling the observed ice spectra of circumstellar shells, and that caution should be exercised in drawing conclusions from analyses which neglect to do so. Currently, we are looking at other spectral features of water ice for a more pronounced effect than that seen here.

The theoretical work described here should prove to be a valuable tool in the interpretation and modelling of the observed spectra to obtain diagnostic information concerning the physical conditions in these shells, e.g., about the presence of other molecules, the relative amounts of hot dust and ice, the density and temperature distributions, and the location of dust condensation.

Further details on the results of this research can be found in Appendices A5.1 and A5.2.

2.4 Radiation Transport in Sources with Disk Geometry

Although there is growing observational and theoretical evidence for a large number of disk-shaped or toroidal objects of astrophysical interest (e.g., circumstellar disks, protoplanetary disks, protostellar accretion disks, bipolar molecular flows, and disk galaxies), the majority of radiation transport models currently in use invoke the assumption of spherical geometry. This assumption is made because spherically symmetric geometry is the only 1-D geometry which accounts for the finite dimensions of a system in all directions. Establishing the source geometry can provide severe constraints on the origin, dynamics, and properties of infrared sources. Hence it is crucial to solve the problem of radiation transport in a dusty medium with 2-D disk geometry and apply the results to infrared observations.

A few attempts have been made to model infrared sources with nonspherical geometry. Lefevre et al. (1983) have performed Monte Carlo simulations of ellipsoidal dust shells around cool stars, while Ghosh & Tandon (1985) calculated dust temperature distributions in cylindrical clouds with embedded stars. The latter work has been extended by Dent (1988) to calculate the temperature distribution and energy spectrum of circumstellar disks around young stars.

We have extended the "quasi-diffusion method" developed by Leung (1975, 1976a) for spherical geometry to the problem of scattering, absorption, and re-emission by dust grains in a coordinate system appropriate for describing disk-shaped clouds (Spagna, 1986; Spagna & Leung, 1987). We have modified this 2-D code to incorporate the technique of "short characteristics" (Olson & Kunasz, 1988; Kunasz and Auer, 1988) into the solution of the ray equations. This improvement enhances the numerical stability of the solution. A previous version of this code was shown to be highly sensitive to grid spacing and variations in assumed grain opacities. This yielded results which were self-consistent but not physically meaningful at all wavelengths. These modifications have yielded a much more robust computational tool. Using this computer code, we have considered radiation transport in disk-shaped interstellar clouds which are heated externally by the ambient interstellar radiation field (ISRF). We have explored the model results which might suggest an observational "signature" for determining the geometry, aspect ratio, and orientation relative to the line of sight. An important result was that the ratio of the observed flux at peak emission and maximum absorption ($200\ \mu\text{m}$ for emission, $1.2\ \mu\text{m}$ for absorptions; hereafter {200:1.2}) in the infrared may be used as an indicator of disk geometry for unresolved clouds. The result at those specific wavelengths is clearly dependent on the assumed ISRF and grain properties, but is suggestive that similar infrared colors could be used with more realistic parameters. Subsequent analysis of these model results shows that an indicator of disk geometry persists in the infrared flux ratios whether or not the fluxes are corrected for the background radiation field. Other physical and geometrical effects of 2-D radiative transfer in various disk configurations have been studied.

Further details on the results of this research can be found in Appendix A3.4.

The ubiquity of disk-shaped structures in dynamical simulations of star formation suggests that at least some of these disks should be observable prior to any substantial internal heating due to the formation of a protostar. The result for {100:12} is expected to be useful because these wavelengths fall within two of the IRAS bands, so that a search of the IRAS data base could be used to test the models. The criterion used for the preliminary search was to find sources in the Faint Source Survey Catalog (FSS) for which {100:60} lies in the range 3.5 - 10 as indicated by the total flux calculated in the models. This criterion effectively selects only those sources which are cool, typically with dust temperatures $\sim 15\ \text{K}$. The search revealed approximately 1200 sources which meet the {100:60} criterion stated above. Considering the model dependent nature of the calculated fluxes, we had hoped only for some

evidence of clustering in the other infrared flux ratios about values other than their means. In particular, no adjustment has been made for convolution of the signal with other sources or for beam dilution. This sample has not been edited to remove identified stellar or galactic sources. Without further modeling it is not possible at this time to do more than identify those sources as interesting - but based on the preliminary models, further study is certainly warranted to determine if these are in fact protostellar disks.

A program of further study has begun to more thoroughly search the existing data base, analyze the infrared spectra of the identified sources, and refine the models to aid in the interpretation of those sources. In particular, additional modeling will be required to account for variation in the interstellar radiation field, and for specific optical properties of dust grains. Extension of the numerical models to include pre-main sequence central heat sources will be used to direct a further search of the IRAS data set to identify and analyze those objects as well. It is expected that this search will confirm the broader conclusion that an observational signature for disk geometry is available in the infrared colors of unresolved sources. More specific conclusions are expected to depend on the assumed ISRF and grain properties. Accordingly, we expect the analysis of observational data to serve as an invaluable tool in refinement of the model assumptions. Adams *et al.* (1987) have suggested an evolutionary sequence which permits the classification of young stellar objects from protostars to pre-main-sequence objects. Our models may allow the identification of objects at an even earlier phase.

3.0 EVALUATION OF METHODS OF ANALYSIS IN INFRARED ASTRONOMY

We have critically evaluated existing methods of analysis in infrared astronomy and investigated the conditions under which these approaches are reliable. Specifically, the usual assumptions of homogeneities in dust density and temperature, and neglect of opacity effects are examined. To accomplish this, a series of self-consistent, realistic models for various infrared sources have been constructed. The results from these models are then treated as observed quantities and analysed using simple semi-analytical approaches to derive the source characteristics. A comparison of the derived parameters with those used in constructing the models will then give a measure of the inherent errors in the analysis procedure and assumptions. Applying this approach to centrally heated, unresolved infrared sources (e.g., circumstellar dust shells), we have studied in detail the following diagnostic problems: a) estimation of dust temperatures from their infrared spectra by fitting a diluted blackbody, b) determination of dust mass for unresolved sources from their far infrared fluxes and luminosity, c) determination of empirical grain emissivity law (for both continuum and spectral features) in the mid- and far infrared, and d) determination of source opacity.

The major conclusions of this research can be summarized as follows:

1. Estimates of dust mass obtained from fitting the energy spectra with dilute blackbodies are more reliable than those derived directly from the luminosities. The error introduced by neglecting opacity effects is less than that due to the assumption of uniform temperature. Although the ratio of dust masses between similar sources can be determined fairly well, the absolute dust mass is much more difficult to determine due to gross uncertainties in dust and source parameters.
2. The dust temperature distribution is well approximated by a power law. However, the power law index deviates significantly from the optically thin value once $\tau > 0.5$. We have found a way to determine the index using the color temperature, accurate to much larger optical depths.
3. The continuum opacity function index can be accurately determined from the infrared excess flux, for wavelengths greater than about $300 \mu\text{m}$. Better determinations are possible by actually fitting the flux spectrum. Although large errors are introduced by assuming an isothermal source, these can be reduced by employing a realistic

temperature distribution.

4. Opacity functions derived from spectral features tend to be too small in comparison to their actual values. The "inversion" methods tends to yield better results than actually fitting the feature, as the latter artificially widens the derived feature.
5. Optical depths derived from absorption features yield results which are too small, and the derived value approaches a constant even though the actual optical depth continues to increase. The effect cannot be easily corrected due to its dependence on source parameters.

Further research in this topic is required and the following topics are suggested:

1. Find a more reliable method to determine the optical depth from absorption features.
2. Extend the study to resolved sources (e.g., interstellar dust clouds, infrared galaxies). As new observations become available, the added information from spatial resolution could drastically alter the method of analysis.
3. Extend the study to line as well as continuum radiation.

Further details on the results of this work can be found in Appendix A4.3.

4.0 THEORETICAL STUDIES INVOLVING DUST GRAINS

4.1 Theory of Molecule Formation on Dust Grains

Infrared observations of the 2-15 μm spectral range indicate that a significant amount of the molecular material in dense interstellar clouds is frozen onto the surfaces of cold grains. Absorption features at 3.1, 4.62 and 2.97 microns, in many lines of sight, are identified as being due to the presence of solid water, carbon monoxide and ammonia. Other molecules such as methanol, methane, formaldehyde, hydrogen sulphide, and possibly carbon dioxide, have also been observed (Tielens & Allamandola 1987; d'Hendecourt & de Muizon 1990). IR observations of different objects may provide information as to the composition of the molecular mantles, the physical conditions under which the mantles were laid down, and also the amount of chemical processing that has occurred in them (e.g. Charnley, Whittet & Williams 1990).

We have developed a time-dependent chemical model to study the formation of complex molecules on the surfaces of dust grains in dense molecular clouds. In this model simple gas phase atomic and molecular species accrete and subsequently undergo activationless reactions on the grain surface, forming an icy mantle. Due to their low mass, hydrogen atoms can quantum tunnel through surface potential barriers and interact with heavier species at a rate which is many orders of magnitude faster than that at which reactions between heavy species can proceed. Reactions between heavy radicals are controlled by their thermal diffusion in the mantle and occur at negligible rates at a dust temperature of 10K. At higher temperatures the radicals may diffuse and react amongst themselves. Since an energetic cosmic ray impact can raise the temperature of an entire 0.1 μm grain such that mantle heating, due to exothermic radical-radical reactions, dominates cooling by radiation and evaporation of volatile CO molecules (L'eger et al. 1985), we have also modelled the thermal balance of the mantle following cosmic ray heating.

In agreement with previous work (Brown & Charnley 1990), due to fast hydrogenation reactions, the composition of the grain mantle is mostly H_2O , NH_3 , CH_4 , H_2O_2 , N_2 and CO. We have simulated the photodestruction of mantle molecules by a weak flux of UV photons from the Prasad-Tarafdar mechanism (Prasad & Tarafdar 1983). We find that for times of the order of a few million years, and prior to total hydrogenation of the mantle, a small population of radicals can persist in the mantle, mainly CH_3 , NH_2 , OH, HO_2 and some atoms. These

radicals are present even in the absence of UV photons.

In an independent treatment of the basic mantle heating model, we find that the physics of this process is controlled by three model parameters: for given concentrations of radicals and CO molecules in the mantle, there exists a critical temperature which, if attained following by cosmic ray impact, will lead to mantle heating. A thermal runaway can eventually occur when most of the CO molecules have been desorbed and the cooling due to this process never dominates the heating by chemical reactions. This is reminiscent of the explosions which are seen to occur when UV-radiated laboratory analogues of interstellar ices are rapidly heated (d'Hendecourt et al. 1982).

Using information experience gained from the behaviour of the simple heating model we are studying in detail the chemistry and physics of complex molecule formation following a cosmic ray heating event. We are including desorption rates for mantle species obtained from laboratory measurements. We shall eventually be able to investigate how the molecular composition of an ice mantle is altered by cosmic ray impacts during the lifetime of an interstellar cloud. In particular, to elucidate which complex molecules are likely to form in mantles with a given composition of simple ones.

Further details on the results of this work can be found in Appendix A5.3.

4.2 Modeling Grain Formation in Stellar Outflows

Knowledge of the physical properties of dust grains formed in circumstellar shells is of major importance in infrared astronomy. To this end, a few studies of grain formation in circumstellar environments have been made. The process of grain formation is usually divided into two parts: nucleation and growth. The alternative, solving the kinetic equations (master equations) is impractical due to the large number of monomers per grain. Consequently, previous studies have relied on classical nucleation theory to predict the rate at which nuclei form in a supersaturated vapor, generally under the assumption of local thermodynamic equilibrium. The growth of the nuclei can then be determined by the solution of a system of differential equations involving moments of the grain size distribution function. The moment equations, however, are strongly dependent on the nucleation rate of particles in the gas. We have developed a method in which a truncated set of master equations (which govern grain nucleation) is coupled to the moment equations (which govern the grain growth). This allows a self-consistent treatment of grain nucleation and growth. This method can also handle the coagulation of larger clusters in a straight forward way. In addition, we have included the effect of radiation pressure on the grain formation process. We have obtained results showing the difference between a classical nucleation plus growth approach versus the self-consistent method.

We find that the classical nucleation theory predicts the onset of grain formation at a supersaturation ratio which is too low (by a factor of 2-3), resulting in a large number of small grains. The master equation approach predicts fewer but larger grains. We also find that the inclusion of radiation pressure on grains results in a drift motion of the grains relative to the gas. This drift motion enhances the nucleation and growth rate, thereby increasing the rate of grain formation. Furthermore, since the force due to radiation pressure increases with grain size, there will be a differential drift velocity between grains of different sizes. The net effect is to produce a grain size distribution which depends on position within the circumstellar shell. We have used the master equation method to model the effect of streaming velocities of grains due to radiation pressure on the coagulation of grains. Inclusion of these velocities results in a large degree of cluster coagulation, resulting in a much lower grain number density than is computed if radiation pressure effects are ignored. Correspondingly, the grains are much larger.

Further details on the results of this research can be found in Appendix A4.4.

4.3 Infrared Emission from Fractal Grains

In modeling the energy spectrum of dust emission from infrared sources, spherical dust grains are often assumed and the dust opacity is calculated from Mie theory using optical constants of bulk material. The assumption of a spherical shape is questionable when faced with explaining polarization measurements of infrared radiation. In astrophysical environments dust grains most likely have irregular shapes formed by fractal growth processes, e.g., particle-by-particle aggregation or cluster-by-cluster aggregation. For fractal grains, the use of bulk optical constants in calculating the dust opacity may not be appropriate. A computational technique now exists for calculating the dust opacity for fractal grains of irregular geometries (Draine 1988; Bazell and Dwek 1990). The method is based on the so-called "discrete dipole approximation" in which a fractal grain is approximated by a collection of dipoles. Using these dust opacities for fractal grains, we have studied the effects of fractal dust grains on the energy spectrum of infrared sources by considering non-spherical dust grains produced by the two fractal processes. We have constructed radiation transport models for circumstellar dust shells and interstellar dust clouds. Compared to models with spherical grains of the same composition and volume, models with fractal grains show a shift in the peak flux toward longer wavelengths, implying that fractal dust grains are cooler than spherical grains. These differences can be attributed to a higher ratio (p) of geometric cross section to volume for the less compact fractal grains. Spherical grains attain a higher temperature due to a smaller p . For fractal grains with the same p but different shape (e.g., a rod vs. a square donut), they show almost no difference in the absorption cross sections and energy spectrum. This implies that, for the same p , the overall grain shape plays only a minor role.

We also find that in the case of Mie scattering theory, the use of bulk optical constants underestimates the absorption cross section at shorter wavelengths and overestimates it at longer wavelengths. This creates a situation in the dust shell where the use of bulk optical constants in the standard Mie scattering theory yields grains which are cooler than those calculated using the amorphous cluster optical constants. The use of these amorphous cluster optical constants in calculating the absorption cross sections of a fractal grain differ very little from the cross sections of the same grain shape using bulk optical constants. These results indicate that the grain temperatures could be inaccurately calculated depending on whether one chooses to use bulk versus amorphous cluster optical constants and whether one chooses Mie scattering theory versus a non-spherical geometry to obtain the absorption cross sections. In either case, the dominant factor being the shape of the grain over the choice of optical constants.

Further details on the results of this research can be found in Appendix A5.4.

4.4 Photochemistry in Circumstellar Envelopes

Evolved stars and their circumstellar envelopes (CSEs) play an important role in replenishing the interstellar medium (ISM) with dust, and various molecular and atomic species. CSEs are also rich chemical environments with many different molecular species observed. To explain the observed species and their abundances, many models of these sources have been constructed by other authors. In these cases, the transfer of continuum radiation is usually approximated by: $I = I_0 \exp(-a\tau^b)$, while ignoring scattering by dust.

To understand the coupling between the radiation field and the chemistry, we have constructed a comprehensive model including detailed ion-molecule chemistry, self-shielding of CO and H₂, and solve self-consistently for the continuum radiation field. We have

concentrated on studying the photodissociation of CO ($\text{CO} + h\nu \rightarrow \text{C} + \text{O}$; $\text{C} + h\nu \rightarrow \text{C}^+ + \text{e}^-$) and the relatively fast ion-molecule chemistry that ensues.

We find that the errors introduced by the analytic approximation for the continuum transfer are appreciable. By neglecting the effect of scattering by dust, one underestimates the radiation field deep into the CSE. In particular, for $r > 10^{17}$ cm, CO abundance differs by two orders of magnitude between the analytic and self-consistent solutions. These differences are reduced (but are still appreciable) once CO and H_2 shielding are included. This suggests that although the line shielding is dominant, the shielding by dust is also important.

As a tracer of the effect of enhanced radiation field, we also explore the ion-molecule chemistry in the CSE. For models with physical parameters similar to the source IRC 10+216, we find that the difference in CO and C^+ abundance have a pronounced effect on the chemical abundances of more complicated species. In general, we find that differences of 2-3 orders of magnitudes are fairly common, especially among the hydrocarbons. We conclude that detailed reaction networks and the self-consistent determination of the radiation field are necessary to accurately model the ion-molecule chemistry in evolved CSEs.

Further details on the results of this research can be found in Appendix A5.5.

5.0 OTHER RELATED RESEARCH PROJECTS

5.1 Chemical Effects of MHD Waves in Dusty Plasmas

Hydromagnetic waves are possibly a major source of line broadening in molecular clouds, and are also important in transporting angular momentum during gravitational collapse. Ambipolar diffusion between ions and neutrals determines the loss of magnetic flux from magnetically supported clumps of gas and thus plays a critical role in the initial stages of low-mass star formation. However, no *direct* evidence for the existence of hydromagnetic waves or the presence of ambipolar diffusion has been obtained to date. We have employed results from a model of the physics of these wave packets to study molecular chemistry which may follow from the ion-neutral streaming which can occur in them.

Appreciable ion-neutral drift speeds can be attained in a propagating isothermal wave and these motions may drive some endothermic chemical reactions at enhanced rates, in a manner analogous to that which occurs in the magnetic presursors of C-type MHD shock waves (e.g. Shull and Draine 1987). However, as the typical drift speeds of a few times 0.1 km s^{-1} are lower than those occurring in C-shocks ($\approx 5\text{-}10 \text{ km s}^{-1}$), only the rate coefficients of reactions which have small temperature barriers will be significantly affected. Four potentially important reactions are :



The (exothermic) reverse reactions of (1)-(3) are ultimately responsible for the large degree of deuterium fractionation observed in cold, molecular material ($\approx 10\text{K}$). At elevated gas temperatures the amount of fractionation is reduced. Reaction (4) has a barrier of about 85K and, if efficient, leads to the formation of ammonia.

The theoretical model of MHD disturbances, which are hypothesised to perturb the chemical evolution of dense gas, considers a Gaussian packet of planar, shear Alfvén waves

propagating parallel to a uniform magnetic field (Roberge & Hanany 1990). The hydrodynamical structure and evolution of the wave packet are governed by Maxwell's equations, plus dynamical equations for the coupled fluids of neutral particles, ions, electrons, and dust grains. The plasma is treated as a system of interacting fluids, consisting of ions and electrons, plus spherical dust grains, plus neutral particles. The grains are coupled to the neutrals by gas-grain collisions and also, being charged, to the magnetic field. The charged and neutral particles are coupled by elastic ion-neutral scattering (e.g. Mouschovias 1987).

In cold gas each of the deuterated ions in reactions (1)-(3) lead to the formation of particular deuterated molecules (Millar, Bennett and Herbst 1989). For example, H_2D^+ leads to N_2D^+ , DCO^+ and NH_2D ; CH_2D^+ leads to HDCO and DCN ; C_2HD^+ to C_3D and C_3HD . We have estimated how the rate coefficient of each of the reactions (1)-(4) may vary within a wave packet. We used the rate coefficients listed in the compilation of Millar et al. for the rate coefficients of reactions (2), (3), and (4) respectively, and have followed Herbst (1982) to calculate the temperature dependence of (1). We employed an effective temperature (e.g. Draine 1986) to compute the rate coefficient of each endothermic ion-neutral reaction.

The timescale over which a parcel of gas is affected by such a wave is greater than the chemical timescales of these reactions, and consequently the molecular chemistry is altered by its presence. Due to the strong time-dependence of the D fractionation of several species, a detailed kinetic treatment is necessary to study the chemical evolution in a wave packet. This has been done, and preliminary computations indicate that indeed destruction of H_2D^+ and N_2D^+ is efficient in such a wave, leading to reduced fractionation in N_2H^+ , HCO^+ and ammonia. High fractionation however persists in, for example, H_2CO and HCN which only vary slightly in the wave. The enhanced formation rate of NH^+ also increases the NH_3 abundance. This implies that one chemical diagnostic of the presence of hydromagnetic waves in dusty material could be low deuterium fractionation of NH_3 in gas for which fractionation of H_2CO is high, and which is ostensibly cold (~ 10 K).

We are currently studying the detailed chemistry in a parcel of gas and dust which is continuously perturbed by MHD waves. The aim of this work is to construct innovative models with which to determine the effect of interstellar turbulence on molecular abundances, and to compare the results with those from static, cold cloud, models in which, for example, reactions (1)-(4) proceed at negligible rates.

5.2 Probing the [C]/[O] Ratios in Dense Interstellar Clouds

The two dense interstellar clouds TMC-1 and L134N (also known as L183) have similar physical conditions (e.g. gas temperature and density) but display remarkable differences in chemical composition. In particular, whereas TMC-1 exhibits relatively large abundances of many complex, unsaturated carbon-rich species (e.g. cyanopolyynes and complex hydrocarbons), L134N has larger abundances of some oxygen-rich species as well as simple saturated molecules (e.g. NH_3 , H_2S , SO_2).

The focus of our research is to determine if this discrepancy is due to a difference in the initial gas phase carbon-to-oxygen ratio. To delineate the effects of different initial composition versus cloud evolutionary status, the pseudo-time-dependent models of Herbst and Leung (1989) are used to study the chemical evolution of these clouds. The original reaction network has been expanded to include 3517 reactions involving 385 chemical species. The model results are then compared to observations of 45 species. Our models assume that the physical conditions (gas temperature and clouds density) remain constant during the calculation. In effect, the interplay between dynamical and chemical timescales is ignored. Gas-grain interactions are not taken into account except for the formation of H_2 and the charge neutralization of certain ions. Since molecular evolution occurs mostly after a cloud becomes

opaque to interstellar ultraviolet radiation, photodissociation reactions are ignored. The initial chemical composition in the models pertains to a diffuse cloud with a significant amount of H_2 . The initial species are H_2 , He, N, O, Cl, e^- , C^+ , Si^+ , S^+ , Fe^+ , Na^+ , Mg^+ , P^+ , and neutral grains. The chemistry is then allowed to evolve for 10^8 years in the calculation.

Three main models have been constructed: Model 1 employs a "standard" value of the C/O ratio (γ) of 0.4; for Model 2, $\gamma = 0.8$ via oxygen depletion; for Model 3, $\gamma = 0.8$ via carbon enrichment. The effect of the C/O ratio can be summarized as follows. All the C and O is channeled into CO and the equilibrium CO abundance (attained after 10^6 years) reflects the initial abundance of C or O, whichever is lower. After the CO formation, an excess of carbon (in an O-depleted medium) will lead to an overproduction of hydrocarbons, while an excess of oxygen (in an O-enriched medium) will result in an overabundance of O-bearing molecules. For complex molecules, significant production occurs only when the abundance of C is high and when the C/CO ratio is of order 1.

One can use the abundance ratio of certain molecules to distinguish between the effects of C-enrichment and O-depletion. NO is an example of a molecule which shows significant sensitivity to the actual abundance of C and O. SO and SO_2 are extremely dependent on the C/O ratio but not on their actual abundances. The observed value for NH_3 in L134N is higher than predicted by any of our models. This may be due to grain surface chemistry which is not considered by our models. On the other hand, TMC's observed abundance is not higher than predicted, perhaps implying that grain surface chemistry does not play as important a role in this cloud. TMC shows very high abundances of the cyanopolyynes (HC_nN) relative to L134N which may imply L134N is in a later stage of evolution than TMC-1, since all of these molecules undergo a steep drop in abundance after 10^5 years. Like NH_3 , OH and H_2S are observed at higher abundances than our models predict. This is consistent with the fact that OH and H_2S are thought to play a role in the mantle chemistry. The abundance ratio of certain molecules, such as SO/CH and $HCOOH/H_2CCO$ can be used to probe the C/O ratio. For a given value of γ , these ratios are insensitive to the actual abundance of O or C, (i.e., they are insensitive to γ). In contrast, the ratios NO/CO and N_2H^+/CO are sensitive to γ and hence can be used to delineate models with C-enrichment and O-depletion. Despite uncertainties in the chemical reactions and their rate coefficients, the overall agreement between the calculated abundances and those observed in TMC-1 and L134N is good. Using these observations, our models imply that either TMC-1 has a higher gas phase C-to-O ratio than L134N, or TMC-1 is at a slightly earlier stage of evolution. Preliminary results of models with extreme C/O ratios ($\gamma = 0.2, 1.2$) indicate that the behavior of certain families of molecules is not a simple function of gamma. A closer look at these results may yield more clues to explain the chemical differences between TMC-1 and L134N.

Further details on the results of this research can be found in Appendix A5.6.

5.3 Improvements to Radiation Transport Codes

5.3.1 Adaptive Grid Technique

Computer modeling of infrared sources generally involves solutions of the radiation transport problem in different geometries and for different physical conditions, depending on the type of objects to be modeled. Since the number of input parameters is large, construction of a large grid of models to cover the parameter space is inevitable, requiring large amounts of computing time. Minimizing the CPU time for the construction of a single model is crucial in making the computer modeling economical. The CPU time required for a given model depends on the rate of convergence of the iteration. We have been modifying the 1-D radiation transport code for modeling infrared sources to enhance its robustness and efficiency. Several numerical and computational improvements are being considered: high order

discretization scheme, better starting solution and acceleration technique for iteration, adaptive grid technique, reorganization and iterative solution of the grand matrix. The most important of these is the use of adaptive grid technique which will allow the computer modeling process to be more automated and efficient. The rate of convergence and accuracy of the solution depend sensitively on the relative distribution of grid points. Currently the problem is solved on a predetermined grid which must be provided by the user. For a given problem, an optimal grid is obtained only by a trial-and-error procedure and considerable amount of computer time can be wasted through this process. In many cases the grid finally chosen may not necessarily be the optimal one for the problem.

In the adaptive grid technique, the grid selection process is made fully automatic by using a grid equation which is solved simultaneously with the physical equations. The grid equation contains the criteria for distribution of grid points (e.g., more grid points should be placed in regions where the solution changes rapidly). For our problems, the most important physical variables are the mean intensity of the radiation field and the dust temperature of the medium. They are called primary variables. Other less significant variables which also affect the solution include the density and opacity of the medium. They are called secondary variables and also participate in the grid equation. The adaptive grid technique was originally developed for time dependent problems such as those encountered in radiation hydrodynamics (Winkler, Mihalas, and Norman 1985). The grid equation is used to track the evolving structure in the fluid flows. To apply the adaptive grid technique to our time-independent problems, we use the fact that in an iterative solution, an approximate initial solution evolves or relaxes to the final converged solution through a series of iteration steps. We can then view this relaxation process as a time evolution if the successive iterations are treated as solutions at some imaginary time steps which are equally spaced. We have mathematically formulated a grid equation using this approach. The grid equation takes into account the spatial variation of quantities such as temperature, density, opacity, and radiation intensity. It is nonlinear and must be linearized and solved along with other equations (radiation transport and energy balance). The success of the method depends crucially on a judicious choice of weight factors which determine the relative magnitudes of different terms in the grid equation (e.g., terms for grid definition, grid stabilization, maximum and minimum cutoff, etc). These weight factors may depend on the physics of the problem. The next step is to incorporate the grid equation into the radiation transport code and test it using various sample problems. This will involve restructuring the grand matrix equation.

5.3.2 Finite Element Method

We have been investigating the use of finite element methods (FEM) in solving the radiation transport problem in dusty media with 1-D spherical and 2-D disk geometries. For 2-D disk geometry, an intrinsic property of the finite difference method (FDM) is the use of a rectangular (or orthogonal) grid which has many regions with highly uneven grid spacings, when one demands small grid spacings at both the inner and outer boundaries (required for internally heated disk models). This results in numerical instability when the grid size is not large enough, producing negative intensities for the radiation field. FEM can overcome this numerical problem since it uses non-rectangular shaped elements (e.g., triangles or polygons). The FEM has the other usual advantages over the FDM in terms of being locally higher order and also being global in nature. The global nature comes because we can transform the entire system of differential equations, jump conditions and boundary conditions into a single equation in which all features of the solution are intrinsically present. Such an ability is provided by the piecewise continuous nature of the basis functions used in the FEM and more importantly, the variational approach providing the mathematical basis.

We have performed some preliminary calculations to test the advantages of using FEM over the FDM for solving second order differential equation as a two point boundary value

problem. We found that the two methods are comparable in computing speed to obtain a solution. However, FEM can be made highly accurate by using quadratic or cubic shape functions in the evaluation of matrix elements, without incurring much expense on CPU. We have also started to develop a program for solving the 1-D radiation transport problem using FEM. In this case the stiffness matrix (similar to grand matrix of FDM) is organised in the Feautrier form. Written in this manner, the stiffness matrix takes a characteristic structure, namely all the nodes on which FEM element matrices are calculated are connected nodes (superposition of finite elements) except the first and the last. The FEM recursive equations for the nodes take different forms depending on the shape function used. We have shown that the final algebraic equations for the FDM are just a special case of FEM which inherently has higher order terms built in even for a linear shape function (the simplest and lowest order FEM). We hope to be able to continue our FEM approach, after incorporating the adaptive grid equation into the existing code for solving transfer problems in spherical geometry.

5.3.3 Automation of Modeling Process

Constructing computer models for specific infrared sources (model fitting) is a labor-intensive task, since one needs to adjust many model parameters and run many models. It is not unusual to require several hundreds of models before one finds a few models which can fit the observations. To expedite the analysis of space-based infrared observations, a critical task is to *automate* the modeling process so that researchers can model infrared sources on workstations in real time. When computer modeling becomes as easy as performing least-square fits to observational data, it will become a routine part of data analysis. With automation researchers can perform computer experiments to test various hypotheses and determine the physical parameters for infrared sources. With such a research tool, predictions on certain observational consequences can be made which will stimulate further observations and theoretical studies, efforts which are essential to the scientific missions of the Infrared Space Observatory and the Space Infrared Telescope Facility. Recently we have started to develop a procedure which will automate the modeling-fitting process, using the 1-D radiation transport modeling code as an test case. The method chosen is the so-called simplex method (Nedler and Mead 1965). Traditional optimization algorithms require finding partial derivatives, often a difficult task. No derivatives are needed in this technique. We find that typically it takes several hundred iterations (equivalent to running several hundred models) to obtain a convergence (fitted model). A drawback of the simplex method is that it often converges to a local minimum. We are exploring other modifications of the simplex method to overcome this problem.

6.0 REFERENCES

- Adams, F. C., Lada, C. J. & Shu, F. H., 1987, *ApJ*, 312, 788.
 Bazell D. & Dwek, E. 1990, *ApJ*, 360, 142.
 Beichman, C. A., Wilson, R. W., Langer, W. D. & Goldsmith, P. F. 1988, *ApJ*, 332, L81.
 Boulanger, F., Baud, B. & van Albada, T. 1985, *A&A*, 144, L9.
 Brown, P.D. & Charnley, S.B. 1990, *MNRAS*, 244, 432.
 Chan, S. J. & Kwok, S. 1988, *ApJ*, 334, 362.
 Charnley, S.B., Whittet, D.C.B. & Williams, D.A. 1990, *MNRAS*, 245, 161.
 Chlewicki, G., Laureijs, R. J., Clark, F. O. & Wesselius, P. R. 1987, in *Star Formation in Galaxies*, ed. C. J. Lonsdale Persson (NASA CP-2466), p. 113.
 d'Hendecourt, L.B., Allamandola, L.J., Baas, F. & Greenberg, J.M. 1982, *A&A*, 109, L12.
 d'Hendecourt, L.B. & de Muizon, M. 1990, *A&A*, 223, L5.
 Dent, W. R. F. 1988, *ApJ*, 325, 252.
 Desert, F. X., Boulanger, F. & Puget, J. L. 1990, *A&A*, 237, 215.
 Draine, B.T. 1986, *ApJ*, 220, 133.
 ———. 1987, *Princeton Observatory Reprint*, 213.
 ———. 1988, *ApJ*, 333, 848.
 Draine, B. T. & Anderson, A. 1985, *ApJ*, 292, 494.
 Egan, M. P., Leung, C. M. & Spagna, G. F., Jr. 1988, *Comput. Phys. Comm.*, 48, 271.
 Geballe et al. 1988, *ApJ*, 326, L65.
 Ghosh, S. K. & Tandon, S. N. 1985, *MNRAS*, 215, 315.
 Gillett, F. C., Backman, D. E., Beichman, C. & Neugebauer, G., 1986, *ApJ*, 310, 842.
 Guhathakurta, P. & Draine, B. T. 1989, *ApJ*, 345, 230.
 Hawkins, G. W. 1990, *A&A*, 229, L5.
 Herbst, E. 1982, *ApJ*, 111, 76.
 Herbst, E., & Leung, C. M. 1989, *ApJS*, 69, 271.
 Jones, T. W., Leung, C. M., Gould, R. J. & Stein, W. A. 1977, *ApJ*, 212, 52.
 Kunasz, P. B. & Auer, L. H., 1988, *JQSRT*, 39, 67.
 Lefevre, J., Daniel, J.-Y. & Bergeat, J. 1983, *A&A*, 121, 51.
 Leger, A., Jura, M. & Omont, A. 1985, *A&A*, 144, 147.
 Leung, C. M. 1975, *ApJ*, 199, 340.
 ———. 1976a, *JQSRT*, 16, 559.
 ———. 1976b, *ApJ*, 209, 75.
 Little-Marenin, I. 1986, *ApJ*, 307, L15.
 Millar, T.J., Bennett, A. & Herbst, E. 1989, *A&A*, 340, 906.
 Mouschovias, T. Ch. 1987, in *Physical Processes in Interstellar Clouds*, eds. G.E. Morfill & M. Scholer, Reidel, p.491.
 Nelder, J. A. & Mead, R. 1965, *Comput. J.*, 7, 308.
 Olofsson, H., Carlstrom, U., Eriksson, K., Gustafsson, B. & Willson, L.A. 1990, *A&A*, 230, L13.
 Olson, G. L. & Kunasz, P. B., 1988, *JQSRT*, 38, 325.
 Omont, A. et al. 1990, *A&A*, 355, L27.
 Prasad, S.S. & Tarafdar, S.P. 1983, *ApJ*, 267, 603.
 Price, S. D. & Walker, R. G. 1976, *The AFGL Four Color Infrared Sky Survey*, AFGL-TR-76-0208, Hanscom AFB, MA: Air Force Geophysics Laboratory.
 Puget, J. L., Leger, A. & Boulanger, F. 1985, *A&A*, 142, L19.
 Roberge, W.G. & Hanany, S., 1990, *BAAS*, 22, 862.
 Shull, J.M. & Draine, B.T. 1987, in *Interstellar Processes*, eds. D.J. Hollenbach & H.A. Thronson Jr., Reidel, p.283.

- Spagna, G. F. Jr. 1986, PhD thesis, Rensselaer Polytechnic Institute.
 Spagna, G. F., Jr. and Leung, C. M., 1987, JQSRT, 37, 565.
 Tielens, A.G.G.M. & Allamandola, L.J. 1987. in *Physical Processes in Interstellar Clouds*,
 eds. G.E. Morfill and M. Scholer., Kluwer, p.333.
 Walker, R. G. & Price, S. D. 1975, *AFGL Infrared Sky Survey, Vol. 1*, AFGL-TR-75-0373,
 Hanscom AFB, MA: Air Force Geophysics Laboratory.
 Willems, F. J. 1987, Ph. D. thesis, Universiteit van Amsterdam.
 Winkler, K.-H., Mihalas, D. & Norman, M. L. 1985, Comput. Phys. Comm., 36, 121.
 Zuckerman, B. & Dyck 1986, ApJ, 311, 345.

Acronyms for Journals Cited

ApJ	Astrophysical Journal
ApJS	Astrophysical Journal Supplement
A&A	Astronomy and Astrophysics
BAAS	Bulletin of the American Astronomical Society
JQSRT	Journal of Quantitative Spectroscopy and Radiative Transfer
MNRAS	Monthly Notices of the Royal Astronomical Society

APPENDIX 1: PROFESSIONAL PERSONNEL ASSOCIATED WITH RESEARCH EFFORT

A. Principal Investigator

Dr. Chun Ming LEUNG

B. Postdoctoral Fellows

Dr. K. N. NAGENDRA (April 1989 - March 1991; now at Indian Institute of Astrophysics)

Dr. Steven B. CHARNLEY (October 1989 - October 1990; now at NASA Ames Research Center)

C. Consultants

Dr. Sun KWOK (University of Calgary, Canada)

Dr. George F. SPAGNA, Jr. (Randolph Macon College, Virginia)

Dr. Dariusz C. LIS (California Institute of Technology)

D. Graduate (Doctoral) Students

Michael P. EGAN -- just completed his fifth year graduate study; recently selected as a Palace Knight by the U. S. Air Force; will be working in the Celestial Backgrounds Branch at the Air Force Geophysics Laboratory of the Hanscom Air Force Base.

Steven D. DOTY -- just completed his third year graduate study; last year was awarded a 3-year National Defense Science and Engineering Graduate Fellowship

Michael E. FOGEL -- just completed his first-year graduate study

Monika E. KRESS -- just completed her first-year graduate study; recipient of a Department of Education graduate fellowship

Curt W. POTTERVELD -- just completed his first-year graduate study

APPENDIX 2: LIST OF PUBLICATIONS, CONTRIBUTED PAPERS/TALKS, AND INVITED TALKS RESULTED FROM RESEARCH EFFORT

A. Papers Published (in Appendices A3.1 - A3.4)

1. Lis, D. C. and Leung, C. M., "Infrared Emission from Isolated Dust Clouds in the Presence of Very Small Dust Grains.", *Icarus*, 91, 7 (1991).
2. Lis, D. C. and Leung, C. M., "Size and Density Distribution of Very Small Dust Grains in the Barnard 5 Cloud.", *Astrophysical Journal (Letters)*, 372, L107 (1991).
3. Spagna, G. F., Jr., Leung, C. M., and Egan, M. P., "Radiation Transport in Dust in Disk Geometry: I. Application to Externally Heated Interstellar Clouds.", *Astrophysical Journal*, 379, 233 (1991).
4. Egan, M. P. and Leung, C. M., "On the Nature of the Excess 100 μ m Flux Associated with Carbon Stars.", *Astrophysical Journal*, 383, 314 (1991).

B. Papers Submitted (in Appendices A4.1 - A4.4)

1. Leung, C. M., "Probing Infrared Sources by Computer Modeling.", invited review paper to appear in the conference proceeding "Astronomy in New York State" (ed. A. G. D. Philip).
2. Doty, S. D. and Leung, C. M., "A Critical Evaluation of Semi-Analytic Methods in the Study of Unresolved, Centrally Heated, Infrared Sources.", submitted to the *Astrophysical Journal*.
3. Nagendra, K. N. and Leung, C. M., "Models of Highly Extended Dust Shells Around R C Borealis and W Hydrae.", submitted to the *Astrophysical Journal*.
4. Egan, M. P. and Leung, C. M., "Modeling Grain Formation in Stellar Outflows: A Master Equation Approach.", submitted to the *Astrophysical Journal*.

C. Papers in Preparation

1. Lis, D. C., Leung, C. M., and Doty, S. D. "Continuum Radiative Transfer in the Presence of Transiently Heated Dust Grains.", to be submitted to the *Astrophysical Journal*.
2. Leung, C. M. and Egan, M. P., "Using IRAS Observations to Probe Dust Shells Around Cool Stars: Some Theoretical Considerations.", to be submitted to the *Astrophysical Journal*.
3. Fogel, M. E. and Leung, C. M., "Modeling Infrared Emission from Fractal Dust Grains.", to be submitted to the *Astrophysical Journal*.

D. Contributed Papers/Talks Presented in AAS Meetings/Other Conferences

1. Egan, M. P. and Leung, C. M., "Modeling Dust Shells Around Cool Stars: Interpreting IRAS Observations.", contributed poster paper given at the 173rd AAS Meeting (Boston, Massachusetts) in January 1989. Abstract appeared in *Bull. Amer. Astron. Soc.*, 21, 713 (1989).
2. Doty, S. D. and Leung, C. M., "Some Diagnostic Problems in the Study of Infrared Sources: a Critical Evaluation.", contributed poster paper given at the 173rd AAS Meeting (Boston, Massachusetts) in January 1989. Abstract appeared in *Bull. Amer. Astron. Soc.*, 21, 721 (1989).
3. Egan, M. P. and Leung, C. M., "Modeling Dust Shells Around Cool Stars: Interpreting IRAS Observations.", contributed talk given at the ASNY (Astronomical Society of New York) meeting in October 1989.
4. Doty, S. D. and Leung, C. M., "Some Diagnostic Problems in the Study of Infrared

- Sources: a Critical Evaluation.", contributed talk given at the ASNY (Astronomical Society of New York) meeting in October 1989.
5. Egan, M. P. and Leung, C. M., "On the Origin of the 100 μm Excess Flux Associated with Carbon Stars.", contributed poster paper presented at the 175th AAS Meeting (Washington, DC) in January 1990. Abstract appeared in *Bull. Amer. Astron. Soc.*, 21, 1123 (1989).
 6. Nagendra, K. N. and Leung, C. M., "A Model for the Extended Dust Shell around the Supergiant R Coronae Borealis.", contributed poster paper presented at the 175th AAS Meeting (Washington, DC) in January 1990. Abstract appeared in *Bull. Amer. Astron. Soc.*, 22, 749 (1990).
 7. Lis, D. C. and Leung, C. M., "Radiation Transport in the Presence of Very Small Dust Grains.", contributed poster paper presented at the *Protostars and Planets III* Conference (Tucson, Arizona) in March 1990.
 8. Charnley S. B. and Leung, C. M., "Modeling the 3 μm Feature in the Infrared Spectra of Circumstellar Envelopes.", contributed poster paper presented at the 176th AAS Meeting (Albuquerque, NM) in June 1990. Abstract appeared in *Bull. Amer. Astron. Soc.*, 22, 1151 (1990).
 9. Doty, S. D. and Leung, C. M., "Determination of Dust Parameters for Centrally Heated IR Sources.", contributed talk given at the ASNY (Astronomical Society of New York) meeting in November 1990.
 10. Egan, M. P. and Leung, C. M., "Evidence for Remnant Dust Shells around IRAS Carbon Stars.", contributed talk given at the ASNY (Astronomical Society of New York) meeting in November 1990.
 11. Nagendra, K. N. and Leung, C. M., "Models of Highly Extended Dust Shell around the Supergiants R Coronae Borealis.", contributed talk given at the ASNY (Astronomical Society of New York) meeting in November 1990.
 12. Kress, M. E., Charnley S. B., and Leung, C. M., "A Chemical Kinetic Model of Radical Reactions in Molecular Mantles.", contributed talk given at the ASNY (Astronomical Society of New York) meeting in November 1990.
 13. Doty, S. D. and Leung, C. M., "Determination of Dust Parameters for Centrally Heated IR Sources.", contributed poster paper presented at the 177th AAS Meeting (Philadelphia, PA) in January 1991. Abstract appeared in *Bull. Amer. Astron. Soc.*, 22, 1245 (1990).
 14. Egan, M. P. and Leung, C. M., "Evidence for Remnant Dust Shells around IRAS Carbon Stars.", contributed poster paper presented at the 177th AAS Meeting (Philadelphia, PA) in January 1991. Abstract appeared in *Bull. Amer. Astron. Soc.*, 22, 1207 (1990).
 15. Leung, C. M. and Lis, D. C., "Radiation Transport in Interstellar Dust Clouds with Very Small Grains: Interpreting the IRAS Observations of B5.", contributed talk given at the 177th AAS Meeting (Philadelphia, PA) in January 1991. Abstract appeared in *Bull. Amer. Astron. Soc.*, 22, 1230 (1990).
 16. Nagendra, K. N. and Leung, C. M., "Models of Highly Extended Dust Shell around the Supergiants R Coronae Borealis and W Hydrae.", contributed poster paper presented at the 177th AAS Meeting (Philadelphia, PA) in January 1991. Abstract appeared in *Bull. Amer. Astron. Soc.*, 22, 1248 (1990).
 17. Charnley S. B., Kress, M. E., and Leung, C. M., "A Chemical Kinetic Model of Radical Reactions in Molecular Mantles.", contributed poster paper presented at the 177th AAS Meeting (Philadelphia, PA) in January 1991. Abstract appeared in *Bull. Amer. Astron. Soc.*, 22, 1230 (1990).
 18. Egan, M. P. and Leung, C. M., "Grain Formation in Stellar Outflows: How Valid is Classical Nucleation Theory?", contributed talk given at the ASNY (Astronomical Society of New York) meeting in November 1991.
 19. Fogel, M. E. and Leung, C. M., "Observational Effects of Fractal Dust Grains on the Infrared Spectrum.", contributed talk given at the ASNY (Astronomical Society of New York) meeting in November 1991.

20. Kress, M. E., Leung, C. M., and Irvine, W. M., "Probing the Carbon-to-Oxygen Ratio in Dense Interstellar Clouds.", contributed poster paper presented at the 179th AAS Meeting (Atlanta, GA) in January 1992. Abstract appeared in *Bull. Amer. Astron. Soc.*, 23, 1370 (1991).
21. Egan, M. P. and Leung, C. M., "Grain Formation in Stellar Outflows: How Valid is Classical Nucleation Theory?", contributed poster paper presented at the 179th AAS Meeting (Atlanta, GA) in January 1992. Abstract appeared in *Bull. Amer. Astron. Soc.*, 23, 1410 (1991).
22. Fogel, M. E. and Leung, C. M., "Observational Effects of Fractal Dust Grains on the Infrared Spectrum.", contributed poster paper presented at the 179th AAS Meeting (Atlanta, GA) in January 1992. Abstract appeared in *Bull. Amer. Astron. Soc.*, 23, 1368 (1991).
23. Doty, S. D. and Leung, C. M., "Modeling the Effect of Radiative Transfer on the Photochemistry of Evolved Circumstellar Envelopes.", contributed poster paper presented at the 25th Anniversary Meeting of the Astronomical Society of New York in April 1992.
24. Egan, M. P. and Leung, C. M., "Grain Formation in Stellar Outflows: Coagulation Effects.", contributed poster paper presented at the 25th Anniversary Meeting of the Astronomical Society of New York in April 1992.
25. Fogel, M. E. and Leung, C. M., "Modeling the Infrared Spectra of Fractal Dust Grains.", contributed poster paper presented at the 25th Anniversary Meeting of the Astronomical Society of New York in April 1992.
26. Kress, M. E. and Leung, C. M., "Probing the Carbon-to-Oxygen Ratio in Dense Interstellar Clouds.", contributed poster paper presented at the 25th Anniversary Meeting of the Astronomical Society of New York in April 1992.
27. Potterveld, C. and Leung, C. M., "Modeling the 3 μ m Water Ice Band of Evolved Stars: Temperature Effects?", contributed poster paper presented at the 25th Anniversary Meeting of the Astronomical Society of New York in April 1992.

E. Invited Lectures and Colloquia (given by PI)

1. "Probing Infrared Sources in Molecular Clouds.", Department of Physics, McMaster University, Canada (November 1988).
2. "Probing Infrared Sources by Bits and Bytes.", Canadian Institute for Theoretical Astrophysics, University of Toronto, Canada (November 1988).
3. "Probing the Late Stages of Stellar Evolution: a New Diagnostic Tool.", Department of Physics and Astronomy, University of Massachusetts (February 1989).
4. "Probing the Late Stages of Stellar Evolution: a New Diagnostic Tool.", Department of Physics, Rensselaer Polytechnic Institute (February 1989).
5. "Probing the Late Stages of Stellar Evolution: a New Diagnostic Tool.", National Radio Astronomy Observatory, Charlottesville (March 1989).
6. "Using IRAS Observations to Probe the Late Stages of Stellar Evolution.", Department of Astronomy, University of Texas (July 1989).
7. "Probing the Late Stages of Stellar Evolution: a New Diagnostic Tool.", Theoretical Division, Los Alamos National Laboratory, (January 1990).
8. "Probing the Late Stages of Stellar Evolution: a New Diagnostic Tool.", Department of Physics and Astronomy, University of New Mexico (January 1990).
9. "Using IRAS Observations to Probe the Late Stages of Stellar Evolution.", Department of Physics, California Institute of Technology (May 1990).
10. "Probing Infrared Sources by Bits and Bytes.", NASA Goddard Space Flight Center, Green Belt, Maryland (May 1990).
11. "Probing Infrared Sources by Computer Modeling.", review talk given at the 25th Anniversary Meeting of the Astronomical Society of New York (April 1992).

12. "Recent Advances in the Phenomenological Modeling of Infrared Sources.", review talk given at the Astronomical Infrared Spectroscopy Conference, University of Calgary (June 1992).

F. Thesis/Dissertation Completed

1. Doty, S. D., "Some Diagnostic Problems in the Study of Infrared Sources: a Critical Evaluation.", unpublished Undergraduate Senior Thesis, May 1989. This thesis won the Class 1902 Research Prize (given to a senior of Rensselaer who presents the best thesis involving research in any branch of engineering or science).

APPENDIX 3: REPRINTS OF PAPERS PUBLISHED

- A3.1 Lis, D. C. and Leung, C. M., "Infrared Emission from Isolated Dust Clouds in the Presence of Very Small Dust Grains.", *Icarus*, 91, 7 (1991).
- A3.2 Lis, D. C. and Leung, C. M., "Size and Density Distribution of Very Small Dust Grains in the Barnard 5 Cloud.", *Astrophysical Journal (Letters)*, 372, L107 (1991).
- A3.3 Egan, M. P. and Leung, C. M., "On the Nature of the Excess 100 μm Flux Associated with Carbon Stars.", *Astrophysical Journal*, 383, 314 (1991).
- A3.4 Spagna, G. F., Jr., Leung, C. M., and Egan, M. P., "Radiation Transport in Dust in Disk Geometry: I. Application to Externally Heated Interstellar Clouds.", *Astrophysical Journal*, 379, 233 (1991).

Infrared Emission from Isolated Dust Clouds in the Presence of Very Small Dust Grains

DARIUSZ C. LIS*† AND CHUN MING LEUNG†

*California Institute of Technology, 320-47, Pasadena, California 91125 and; †Department of Physics, Rensselaer Polytechnic Institute, Troy, New York 12180

Received May 7, 1990; revised August 15, 1990

We have developed a continuum radiation transport code which incorporates the transient heating of small dust grains. Using this computer code, we have constructed models to study the effects of the temperature fluctuations due to small grains on the infrared spectrum and surface brightness of externally heated interstellar dust clouds. From comparison of the model results with *IRAS* observations, we conclude that the observed emission in the 12- and 25- μm bands is most likely produced by small grains with radius of $\sim 10 \text{ \AA}$, while the 60- and 100- μm emission comes primarily from large grains heated under the equilibrium conditions. Our models, based on the assumption of a constant fractional abundance of large and small grains throughout a cloud, predict infrared limb brightening only for models with a visual optical depth ≥ 20 . The fact that relatively strong limb brightening has been observed for more diffused globules indicates that the small grain abundance is likely to be increased in outer parts of these objects. © 1991 Academic Press, Inc.

I. INTRODUCTION

Among unexpected results from *IRAS* was the discovery of excess midinfrared emission detected in a number of infrared sources, including diffuse clouds, dark globules, visual reflection nebulae, and high-latitude dust clouds or infrared cirrus. The emission at short wavelengths (10–30 μm) is now thought to be due to small grains ($a \leq 50 \text{ \AA}$) which are transiently heated, while the emission at long wavelengths ($\lambda \geq 50 \mu\text{m}$) is due to large grains heated under the equilibrium conditions. Infrared limb brightening at the four *IRAS* wavelength bands (12, 25, 60, and 100 μm) is observed in diffuse clouds heated externally by the interstellar radiation field (Chlewicki *et al.* 1987) and in the globule B5 (Beichman *et al.* 1988). The infrared limb brightening at short wavelengths is probably due to small grains, as indicated by the high color temperature (a few hundred degrees) derived from the 12- and 25- μm emission. The color temperature derived from the 60- and 100- μm emission is an order of magnitude lower.

Small dust grains exposed to the interstellar radiation field can attain temperatures much higher than those predicted assuming the equilibrium conditions (Draine and Anderson 1985, Désert *et al.* 1986, Dwek 1986). This occurs whenever there is a discrete heating event in which the energy input (from photons or gas particles) is considerably larger than the energy content of a grain. This nonequilibrium grain heating can significantly change the energy distribution of the radiation field and has important significance for understanding the observed *IRAS* emission from interstellar dust clouds. Recently Guhathakurta and Draine (1989) presented a very efficient method of calculating the probability distribution of grain temperatures for transient heating, making it computationally feasible to include the physics of small grain heating into radiation transport modeling of infrared sources. Accordingly, we incorporated the transient heating of small dust grains into the radiation transport code of Egan, Leung, and Spagna (1988). In the present paper we discuss the effect of the transient heating of small dust grains on the observed spectrum and surface brightness of isolated interstellar dust clouds without internal heating sources. Details of the model calculations will be presented in a separate paper.

II. MODEL RESULTS FOR EXTERNALLY HEATED GLOBULES

In order to study the importance of the transient heating of small dust grains we computed a number of models of externally heated clouds with different small grain sizes, optical depths, and density distributions. The absorption efficiencies for graphite and astronomical silicates were taken from Draine (1987) and the interstellar radiation field intensity was taken from Mathis, Mezger, and Panagia (1983). The models include a mixture of large graphite and silicate grains (0.1 μm in radius) with equal abundances by number, and one type of small graphite grains with

radius varying between 10 and 30 Å for different models. Models with one type of small grains clearly oversimplify the true structure of interstellar dust clouds, where a continuous grain size distribution exists. Including a mixture of transiently heated small grains with different sizes or compositions in the models, however, is not feasible from the computational viewpoint at the present time. For all the models we assumed equal optical depths of small and large grains in the visual (5500 Å). The total visual optical depth from the center of the cloud varied from 5 to 1000. Since the optical depths due to small and large grains are equal for each model, and the absorption cross section of small grains is proportional to their radius, the optical depth ratios remain the same for all models. A 5500-Å optical depth of 100 corresponds to the optical depths of 1.4, 1.0, 0.32, and 0.12 at 12, 25, 60, and 100 μm, respectively. Our model cloud has a 1-pc radius and a power law density distribution with radial exponents of -1 and 0. Only radiative processes were considered in the calculations and any possible interactions with high energy particles that will affect the transient heating of small grains were neglected. The emergent intensities were convolved with a 0.25-pc FWHM Gaussian beam.

In Section III (a)–(c) we discuss the temperature distribution function for small grains, the emergent spectrum, and surface brightness predicted by our models. In Section III (d) we compare our results with the observational data.

(a) Temperature Distribution for Small Grains

The temperature distribution function for small grains of different sizes is shown in Fig. 1. The value plotted is the logarithm of the probability density function in the logarithmic variable ($dP/d \ln T$). The upper panel corresponds to the cloud surface, and the lower panel to the center of a cloud with a visual optical depth of 300 from the center to the edge. The highest temperature that a grain can attain increases with decreasing grain radius (from ~125 K for a 30 Å grain to ~400 K for a 10 Å grain, at the cloud surface). As expected, this maximum temperature decreases with distance from the cloud surface as the high energy photons responsible for the transient heating are attenuated by the dust in the outer layers of the cloud. The sharp cut-off in the temperature distribution function corresponds to the wavelength of the Lyman continuum. Although smaller grains can attain higher temperatures, they are on the average colder than larger grains because the cross section for interaction with a photon varies as a^3 , a being the grain radius (for small grain radii the absorption efficiency $Q \propto a$). The mean time between discrete heating events increases with decreasing radius and smaller grains can cool down to lower temperatures than those of larger grains which interact more frequently.

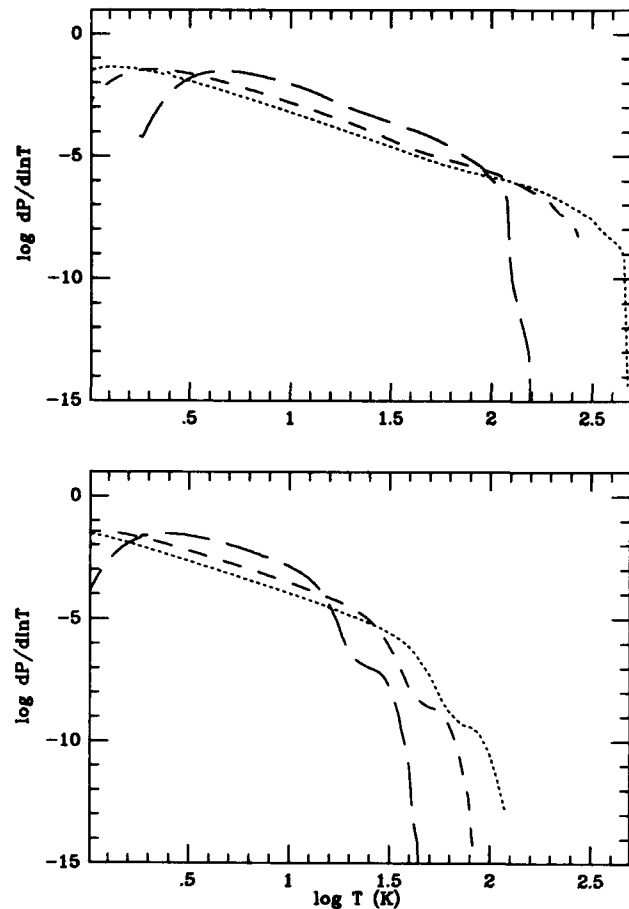


FIG. 1. The temperature distribution function for small grains at the cloud surface (upper panel) and at the center of a cloud with a visual optical depth of 300 from the center to the surface (lower panel). The results correspond to a model with a mixture of large graphite and silicate grains with 0.1 μm radius and equal abundances by number, and small graphite grains with 30 Å (long-dashed line), 15 Å (short-dashed line), and 10 Å (dotted line) radii. All models have equal optical depths of large and small grains at 5500 Å. The quantity plotted is a logarithm of the probability density function in a logarithmic variable ($dP/d \ln T$). The equilibrium temperature of the large grains varies from 6 K at the center to 18 K at the surface for graphite grains, and from 6 K to 14 K for silicate grains.

(b) Emergent Spectrum

The effect of the small grain size on the emergent spectrum is shown in Fig. 2, for cloud models with a visual optical depth of 300 from the center to the edge, and an r^{-1} density distribution. The small grain sizes are 10, 15, and 30 Å (dotted, short-dashed, and long-dashed lines, respectively). The upper panel shows spectra toward the center of a cloud and the lower panel at an offset of 0.9 pc from the center (cloud radius is 1 pc). The solid line in each panel corresponds to a model without small grains and with the same large grain density as in the models with small grains (and therefore a visual optical depth of

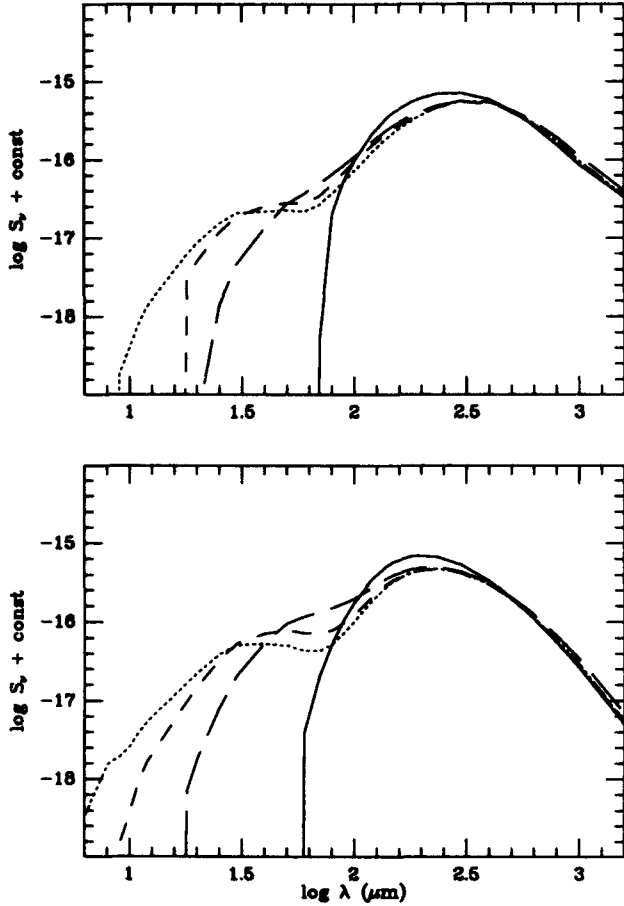


FIG. 2. The observed spectrum of the continuum emission from a model cloud with a visual optical depth of 300 from the center to the edge, a mixture of large graphite and silicate grains with $0.1 \mu\text{m}$ radius and equal abundances by number, and small graphite grains with 30 \AA (long-dashed line), 15 \AA (short dashed line), and 10 \AA (dotted line) radii. The emergent intensity was convolved with a 0.25-pc FWHM Gaussian beam. The upper panel shows spectra toward the center of the cloud and the lower panel at an 0.9-pc offset from the center. The models have an r^{-1} density distribution. The off-center spectrum extends more toward the shorter wavelengths. This is indicative of the limb brightening effect. The solid line corresponds to a model without small grains and a visual optical depth of 150 (the same large grain abundances as in the models including small grains).

150 from the center to the edge). Results for a cloud with a uniform density distribution are shown in Fig. 3. The shortest wavelength at which the emission is still observable, λ_{sh} , decreases with decreasing small grain size. This results from the fact that smaller grains can be heated to higher temperatures. The cut-off wavelengths at the center of our model cloud are ~ 10 , 18 , and $22 \mu\text{m}$ for 10 , 15 , and 30 \AA small grain radii, respectively. The short wavelength cut-off for the large grain model is $\sim 70 \mu\text{m}$. The calculated spectrum close to the edge of the cloud extends more toward the short wavelengths, compared to the cloud center. This is an indication of the limb

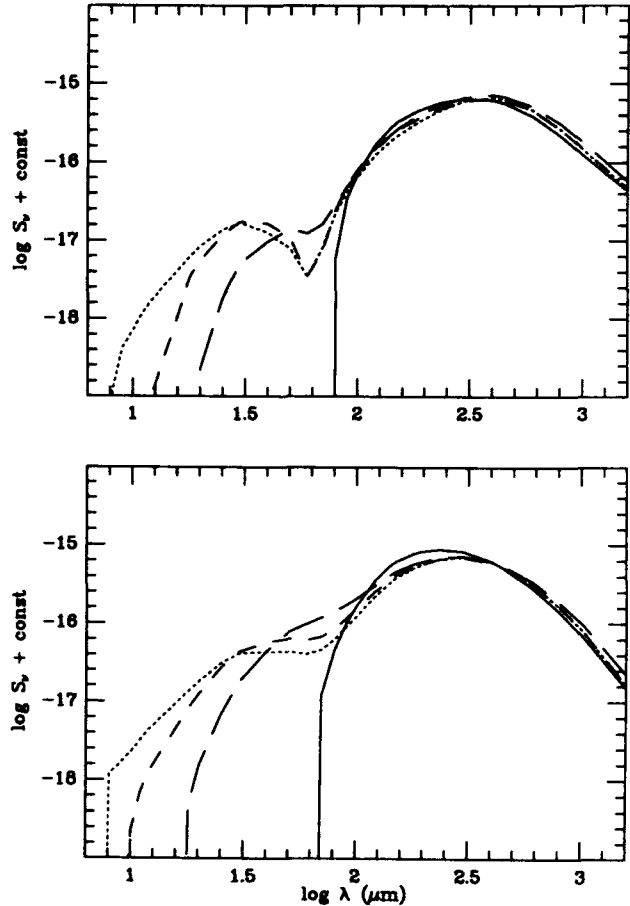


FIG. 3. Same as Fig. 2, but for models with a uniform density distribution.

brightening effect which is further discussed in Section III (c).

The effect of the total optical depth on the emergent spectrum is shown in Figs. 4 and 5 for models with r^{-1} and uniform density distributions, respectively. The visual optical depths from the center to the edge of the cloud are 30 (solid line), 100 (dotted line), 300 (short-dashed line), 550 (long-dashed line, r^{-1} density law only), and 1000 (dashed-dotted line). The upper panel shows spectra toward the center of a cloud and the lower panel at a 0.9-pc offset from the center. The long wavelength flux increases with τ . This is simply a result of the increasing dust column density through the cloud. The short-wavelength flux decreases with τ due to increasing attenuation of the UV photons responsible for the transient heating of small grains. The effect is strongest at the center of the cloud. For very high optical depths, the part of the spectrum between ~ 50 and $80 \mu\text{m}$ goes from emission to absorption (see Figs. 4 and 5). The quantity plotted in Figs. 4 and 5 is the excess flux above the background, and the energy of the background radiation heating the cloud

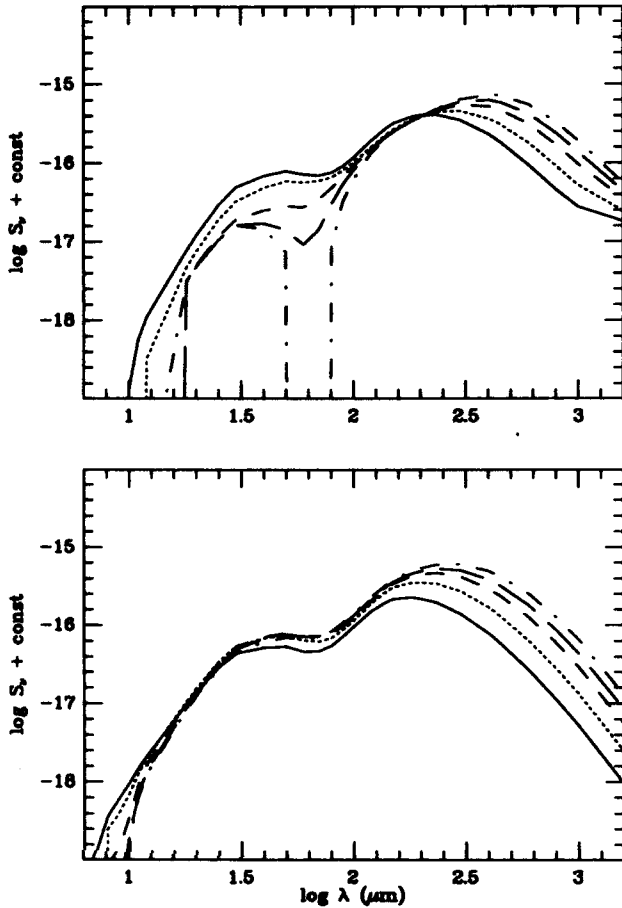


FIG. 4. The effect of the optical depth on the emergent spectrum from a cloud with an r^{-1} density distribution. The cloud is made of a mixture of large graphite and silicate grains with $0.1\text{-}\mu\text{m}$ radius having equal abundances by number, and small graphite grains with a $15\text{-}\text{\AA}$ radius. The visual optical depths are: 30 (solid line), 100 (dotted line), 300 (short dashed line), 550 (long-dashed line), and 1000 (dashed-dotted line). The upper panel shows spectra toward the center of the cloud, and the lower panel at an 0.9-pc offset from the center.

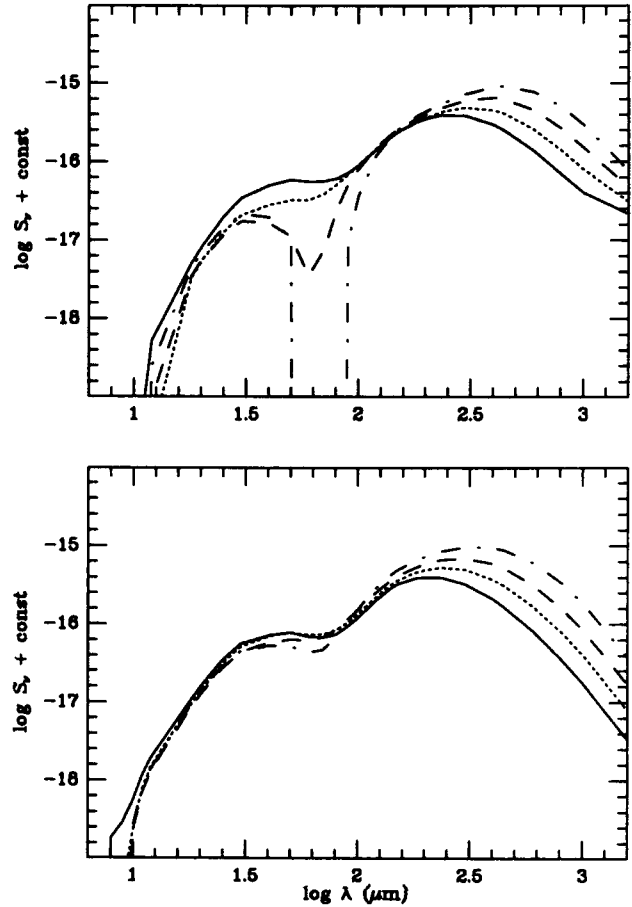


FIG. 5. Same as Fig. 4, but for a cloud with uniform density distribution.

$$L_{\lambda} = \max \left[\frac{I_{\lambda}(p)}{I_{\lambda}(0)} \right], \quad (1)$$

is redistributed in wavelength. The absence of an excess flux in the $\sim 50\text{--}80\text{ }\mu\text{m}$ wavelength range reflects the fact that the large grains emit primarily at $\lambda \gtrsim 70\text{ }\mu\text{m}$, while $15\text{ }\text{\AA}$ small grains emit at $\lambda \sim 30\text{ }\mu\text{m}$. The lack of an excess emission between 50 and $80\text{ }\mu\text{m}$ is accompanied by increased submillimeter emission, so the total energy radiated by the cloud is conserved. The outer part of the cloud in the $50\text{--}80\text{ }\mu\text{m}$ range is still observed in emission, so the cloud looks like a bright rim with a dark core.

(c) Limb Brightening Effect

The infrared limb brightening effect can be seen in Fig. 6 which shows the surface brightness as a function of the offset from the center of a cloud at the four *IRAS* bands for a series of cloud models. For each model we have calculated the limb brightening ratio L_{λ} defined as

where p is the offset from the center of the cloud. This quantity is well defined only for clouds seen in emission at all offsets from the center (the center is most likely to be seen in absorption against the background radiation for the lowest value of τ). The results are shown in Table I. Several trends at 100 and $60\text{ }\mu\text{m}$ can be clearly seen: (1) the limb brightening ratio increases with τ ; (2) the limb brightening ratio is always higher for models with a uniform density distribution, compared to models with an r^{-1} density distribution; (3) the limb brightening ratio is stronger at $60\text{ }\mu\text{m}$ than it is at $100\text{ }\mu\text{m}$. These trends agree with the results of Leung, O'Brien, and Dubisch (1989) for large-grain models, suggesting that the 100- and $60\text{-}\mu\text{m}$ emission is dominated by the equilibrium processes. The first trend is caused by the higher optical depth resulting in a steeper temperature distribution of large grains as a function of the distance from the cloud surface. In particu-

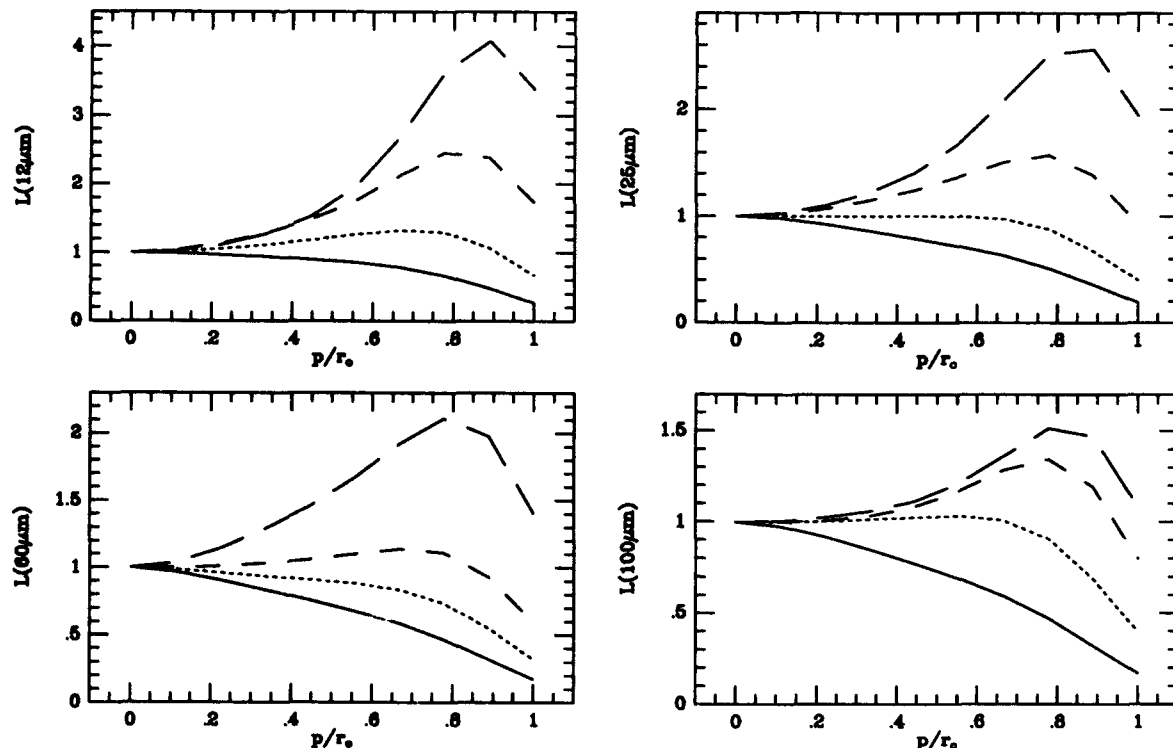


FIG. 6. The normalized intensity as a function of the projected offset from the cloud center for a series of models with 10-Å graphite grains and an r^{-1} density distribution. The visual optical depths from the center to the edge of the cloud are 5 (solid line), 20 (dotted line), 80 (short-dashed line), and 100 (long-dashed line).

lar, the relatively uniform temperature distribution inside clouds with low optical depths results in almost no limb brightening ratio, $L_\lambda \approx 1$, at all wavelengths, including 12 and 25 μm . The second trend is due to the higher dust density in the outer part of a cloud with a uniform density distribution, resulting in a steeper temperature distribution of large grains compared to models with an r^{-1} density distribution. The third trend results from the fact that the 60- μm emission is a more sensitive function of the dust temperature than the 100- μm emission.

At 12 and 25 μm the situation is much more complicated. Models with $\tau \geq 300$ and a uniform density distribution are characterized by lower values of L than the corresponding models with an r^{-1} density distribution. This is due to the fact that for high optical depths one observes only the outer part of the cloud characterized by a relatively uniform radiation field intensity. The 12- and 25- μm bands are different in this respect from the 60- and 100- μm bands where the optical depth is significantly lower and one sees much deeper into the cloud, into the region with significant radiation field intensity and temperature gradients. This effect is most clearly seen at 25 μm for a series of models with 15-Å grains, where the limb brightening as a function of τ starts decreasing after reaching a maximum for $\tau \sim 100$ –500, depending on the density

distribution. The surface brightness of very dense dust clouds depends critically on the small grain size. As an example one can take models with $\tau = 300$, and an r^{-1} density distribution. For a small grain radius of 10 Å the model cloud shows limb brightening and is seen in emission, for a 15-Å small grain radius the center of the cloud is seen in absorption while the edge is still seen in emission, and finally for a 30-Å small grain radius the whole cloud is seen at this wavelength in absorption against the background radiation.

Similar to the 60- and 100- μm limb brightening ratio, the limb brightening ratio at 12 and 25 μm also approaches unity for low optical depths, due to deeper penetration of the external radiation field into the cloud for low values of τ . The limb brightening at shorter wavelengths is observed for lower values of τ compared to longer wavelengths, as the short wavelength emission comes from hottest grains, heated by hardest photons which are most strongly attenuated with the depth into the cloud.

(d) Comparison with IRAS Observations

An important result of our model calculations is an upper size limit for small grains responsible for the observed infrared emission at the 12- and 25- μm IRAS wave-

TABLE I
Limb Brightening in Model Clouds at *IRAS* Wavelengths

a (Å)	n	τ	$L_{100\mu\text{m}}$	$L_{60\mu\text{m}}$	$L_{25\mu\text{m}}$	$L_{12\mu\text{m}}$
10	-1	20	1.0	1.0	1.0	1.3
		80	1.3	1.1	1.6	2.5
		300	1.5	2.1	2.6	4.1
	0	300	1.9	5.1	2.3	2.7
15	-1	30	1.1	1.0	1.3	2.1
		100	1.3	1.4	2.0	8.1
		300	1.5	2.6	2.9	+ ^a
		550	1.8	5.2	3.0	+
	0	1000	2.4	23	2.7	+
30	-1	30	1.4	1.4	1.8	4.2
		100	1.6	2.2	2.5	+
	0	300	2.0	6.3	2.4	39
		1000	3.8	98	2.0	7
LG ^c	-1	300	1.9	3.2	5.9	- ^b
	0	300	2.8	6.3	3.9	-
LG ^c	-1	150	1.9	+	-	-
	0	150	2.3	+	-	-

Note. The entries in the table are: small grain radius (Å), density law exponent, optical depth from the center to the edge of the cloud at 5500 Å, and the predicted limb brightening ratios at the four *IRAS* bands as a function of a , n , and τ . The emergent fluxes used in calculating the limb brightening ratio were convolved with the corresponding *IRAS* filter functions.

^a The center of the cloud is observed in absorption but the edge is still observed in emission.

^b The whole cloud is observed in absorption against the background radiation.

^c Large grains only.

lengths. Figure 2 shows that 30-Å graphite grains produce very little flux at wavelengths $\leq 20 \mu\text{m}$. The 12- μm *IRAS* emission is most likely produced by grains with a radius of $\sim 10 \text{ Å}$. These grains also dominate the 25- μm emission, although larger grains (15–30 Å) will also contribute to the flux density at this wavelength. The results of course depend on the composition of small grains. Guhathakurta and Draine (1989) showed that the highest temperature that can be attained by a silicate grain is lower than the corresponding temperature of a graphite grain of the same size. Accordingly λ_{sh} is shorter for graphite grains than it is for silicate grains.

Infrared limb brightening is observed by Beichman *et al.* (1988) toward the Barnard 5 cloud. This cloud is characterized by 5–10 magnitudes of the visual extinction. For this optical depth range our models do not predict any limb brightening. In our calculations, however, we used

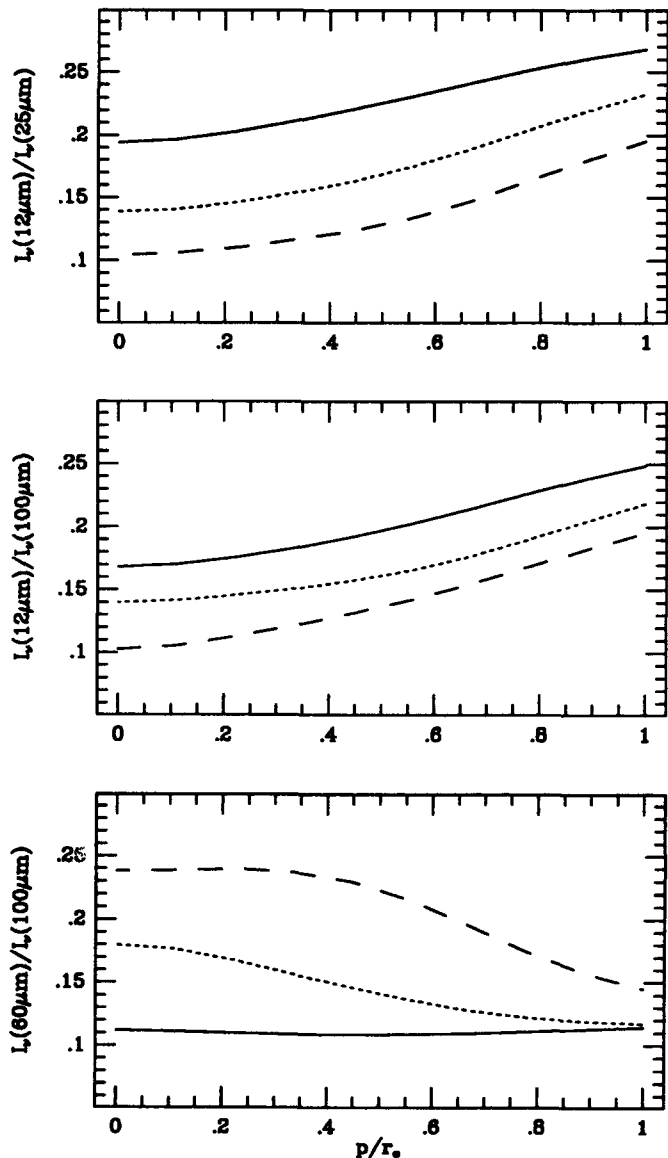


FIG. 7. The predicted intensity ratios between different *IRAS* bands for the models with 10-Å grains as a function of the projected offset from the center of the cloud. The visual optical depths from the center to the edge of the cloud are: 5 (solid line), 20 (dotted line), and 80 (dashed line). The predicted 12- to 25- μm ratio is a factor of ~ 5 lower than the value observed in B5 (~ 1), the 12- to 25- μm ratio is close to the observed ratio, and the 60 to 100 μm ratio is a factor of ~ 2 higher than the ratio observed in B5.

a constant relative abundance of small and large grains inside the cloud. The data of Beichman *et al.* (1988) show that the 12- μm emission is much more extended than the 100- μm emission, suggesting that the abundance of small grains may be enhanced relative to large grains in the outer part of the cloud. Detailed models of the *IRAS* emission from the B5 cloud will be presented in a subsequent paper (Lis and Leung 1991). These new models

show that increased small grain abundance in the outer part of the cloud is sufficient for producing a limb brightening at short wavelengths even for low values of the visual extinction. The small grains responsible for the short wavelength *IRAS* emission from B5 contribute only ~ 1 – 2% of the total optical depth at the visual wavelengths, and ~ 10 – 20% of the total mass of this cloud.

Our present models with $10\text{-}\text{\AA}$ small grains predict a 12- to $25\text{-}\mu\text{m}$ flux ratio ≤ 0.15 (Fig. 7), compared to a typical observed value of ~ 1 . The 12- to $25\text{-}\mu\text{m}$ ratio can be increased by increasing the small grain abundance in the outer part of a cloud, especially if smaller ($\sim 5\text{ }\text{\AA}$) transiently heated grains are used (see Lis and Leung 1991 for details). Even in the best model for B5, however, the predicted 12- to $25\text{-}\mu\text{m}$ ratio is only ≤ 0.50 , still a factor of 2 smaller than the observed ratio. Although the calibration errors of the extended *IRAS* emission will clearly affect the observed flux ratio, the difference between the predicted and observed 12- to $25\text{-}\mu\text{m}$ ratios seems significant. The 12- to $100\text{-}\mu\text{m}$ ratio predicted by the present models with $10\text{-}\text{\AA}$ small grains (~ 0.05) is close to the ratio observed in B5 (Beichman *et al.* 1988), and the predicted 60- to $100\text{-}\mu\text{m}$ ratio (~ 0.4) is a factor of 2 higher than the observed ratio.

The spectra from the model clouds presented in Figs. 2–4 show the far-infrared emission peaking at a wavelength of $\sim 200\text{ }\mu\text{m}$. This prediction is consistent with the observed far-infrared spectra of globules (Keene 1981, Keene *et al.* 1983).

IV. CONCLUSION

We developed a continuum radiation transport code which incorporates the transient heating of small dust grains. We constructed a series of models to study the effect of the temperature fluctuations in small ($\leq 30\text{ }\text{\AA}$) graphite grains on the spectrum and surface brightness of externally heated interstellar dust clouds. From comparison with *IRAS* observations we conclude that the $12\text{-}\mu\text{m}$ *IRAS* emission is most likely produced by grains with radius $a \sim 10\text{ }\text{\AA}$. These grains also dominate the $25\text{-}\mu\text{m}$ flux, although larger grains (15 – $30\text{ }\text{\AA}$) also contribute to the observed flux density in the $25\text{-}\mu\text{m}$ band. The $100\text{-}\mu\text{m}$ emission is dominated by large grains heated under the equilibrium conditions.

Infrared limb brightening is predicted by our models only for visual optical depths from the center to the edge ≥ 20 . Our models, based on the assumption of a constant fractional abundance ratio between the small and large grains throughout the cloud *do not* predict the limb bright-

ening for more diffuse clouds (visual optical depth ≤ 5 – 10). The fact that the limb brightening is observed in these objects suggests that the small grain abundance is likely to be increased in their outer parts.

ACKNOWLEDGMENTS

We thank B. Draine for providing us with the absorption and emission efficiencies for graphite and astronomical silicates, as well as for useful discussions concerning the original method of calculating the grain temperature distribution function; and J. Carlstrom for proofreading this manuscript. This research has been partially supported by the U.S. Air Force under Grant AFOSR 89-0104, by NASA under Grant NAG 5-1182 to Rensselaer Polytechnic Institute, and by NSF under Grant AST 88-14405 to Caltech Submillimeter Observatory.

REFERENCES

- BEICHMAN, C. A., R. W. WILSON, W. D. LANGER, AND P. F. GOLD-SMITH 1988. Infrared limb brightening in the Barnard 5 cloud. *Astrophys. J.* **332**, L81–L85.
- CHEWICKI, G., R. J. LAUREIS, F. O. CLARK, AND P. R. WESSELIUS 1987. Infrared properties of dust grains derived from *IRAS* observations. In *Star Formation in Galaxies* (C. J. Lonsdale Persson, Ed.), pp. 113–116. NASA CP-2466.
- DÉSERT, F. X., F. BOULANGER, AND S. N. SHORE 1986. Grain temperature fluctuations a key to infrared spectra. *Astron. Astrophys.* **160**, 295–300.
- DRAINE, B. T., AND N. ANDERSON 1985. Temperature fluctuations and infrared emission from interstellar grains. *Astrophys. J.* **292**, 494–499.
- DRAINE, B. T. 1987. *Tabulated Optical Properties of Graphite and Silicate Grains*. Princeton Observatory Preprint 213.
- DWEK, E. 1986. Temperature fluctuations and infrared emission from dust particles in a hot gas. *Astrophys. J.* **302**, 363–370.
- EGAN, M. P., C. M. LEUNG, AND G. F. SPAGNA 1988. Csdust3: A radiation transport code for a dusty medium with 1-d planar, spherical and cylindrical geometry. *Comput. Phys. Commun.* **48**, pp. 271–292.
- GUHATHAKURTA, P., B. T., AND DRAINE 1989. Temperature fluctuations in interstellar grains: I. Computational methods and sublimation of small grains. *Astrophys. J.* **345**, 230–244.
- KEENE, J. 1981. Far-infrared observations of globules. *Astrophys. J.* **245**, 115–123.
- KEENE, J., J. A. DAVIDSON, D. A. HARPER, R. H. HILDEBRAND, D. T. JAFFE, R. F. LOEWENSTEIN, F. J. LOW, AND R. PERNIC 1983. Far-infrared detection of low-luminosity star formation in the Bok globule B335. *Astrophys. J.* **274**, L43–L47.
- LEUNG, C. M., E. V. O'BRIEN, AND R. DUBISCH 1989. Using far-infrared limb brightening to probe isolated dark globules. *Astrophys. J.* **337**, 293–305.
- LIS, D. C., AND C. M. LEUNG 1991. Size and density distribution of very small dust grains in the Barnard 5 cloud. *Astrophys. J.* submitted for publication.
- MATHIS, J. S., P. G. MEZGER, AND N. PANAGIA, 1983. Interstellar radiation field and dust temperatures in the diffuse interstellar matter and in giant molecular cloud. *Astron. Astrophys.* **128**, 212–229.

SIZE AND DENSITY DISTRIBUTION OF VERY SMALL DUST GRAINS IN THE BARNARD 5 CLOUD

DARIUSZ C. LIS¹

Downs Laboratory of Physics 320-47, California Institute of Technology, Pasadena, CA 91125

AND

CHUN MING LEUNG

Department of Physics, Rensselaer Polytechnic Institute, Troy, NY 12180

Received 1990 December 3; accepted 1991 February 27

ABSTRACT

We have developed a radiation transport code which treats self-consistently the thermal coupling between the transient heating of very small dust grains and the equilibrium heating of conventional large grains. Using this computer code and realistic grain opacities, we have constructed a series of models to study the effects of the temperature fluctuations in small graphite grains on the energy spectrum and infrared surface brightness of an isolated dust cloud heated externally by the interstellar radiation field. By comparing the model results with the *IRAS* observations of the Barnard 5 cloud, we have found that the 25 μm emission is most likely produced by small grains with a 6–10 \AA radius. These grains also contribute $\sim 50\%$ or less of the observed 12 μm emission. The remaining 12 μm flux may be produced by the polycyclic aromatic hydrocarbons. The 60 and 100 μm emission is primarily due to large grains ($\sim 0.1 \mu\text{m}$ radius) heated under equilibrium conditions. Our models indicate that small grains responsible for the short-wavelength *IRAS* emission account for $\sim 1\%$ – 2% of the total opacity in the visible, and $\sim 10\%$ – 20% of the total dust mass of the cloud. Furthermore, to produce the observed infrared limb brightening, the spatial distribution of small grains must be more extended than that of large grains. Because of the strong attenuation of UV photons responsible for the transient heating, small grains in the cloud interior would produce only weak emission in the short-wavelength *IRAS* bands. We therefore cannot rule out the possibility that small grains are present also in the cloud core.

Subject headings: infrared: spectra — interstellar: grains — nebulae: general — radiative transfer

1. INTRODUCTION

An unexpected result from the *Infrared Astronomical Satellite* (*IRAS*) was the detection of excess mid-infrared emission in a variety of infrared sources, e.g., diffuse clouds (Chlewicki et al. 1987, 1988), dark globules (Beichman et al. 1988), visual reflection nebulae (Castelaz, Sellgren, & Werner 1987), and high-latitude dust clouds or infrared cirrus (Low et al. 1984). This excess emission is always accompanied by relatively high color temperatures derived from the 12 to 25 μm flux ratio, typically an order of magnitude higher than color temperatures derived from the 60 to 100 μm flux ratio.

Small dust grains exposed to the interstellar radiation field (ISRF) can attain temperatures much higher than those predicted assuming equilibrium conditions (Draine & Anderson 1985; Desert, Boulanger, & Shore 1986; Dwek 1986; Puget & Léger 1989). This occurs whenever there is a discrete heating event in which the energy input from photons (or high-energy particles) is considerably larger than the grain energy content. This nonequilibrium or transient grain heating can change considerably the energy distribution of the radiation field. It is now believed that while the emission at long wavelengths ($\lambda \gtrsim 50 \mu\text{m}$) is due to conventional large grains heated under equilibrium conditions, the emission at short wavelengths (10–30 μm) is due to very small grains ($a \lesssim 50 \text{\AA}$) which are transiently heated. Guhathakurta & Draine (1989) presented an efficient method of calculating the probability distribution of grain temperatures for the transient heating, making it computa-

tionally feasible to include the physics of the small-grain heating in radiation transport modeling of infrared sources. Accordingly, we incorporated the transient heating of very small dust grains into the radiation transport code of Egan, Leung, & Spagna (1988). Using this computer code and realistic grain opacities, we constructed a series of models to study the effects of the temperature fluctuations in small graphite grains on the energy spectrum and surface brightness of an externally heated dust cloud.

Theoretical calculations (Spencer & Leung 1978; Lee & Rogers 1987; Leung, O'Brien, & Dubisch 1989) predicted that isolated dark globules heated externally by the ISRF may exhibit limb brightening in the far-infrared ($\lambda \gtrsim 60 \mu\text{m}$) and that there should be no emission in the mid-infrared, if only conventional dust grains heated under equilibrium conditions are considered. However, infrared limb brightening at all four *IRAS* bands has been observed in diffuse clouds (Chlewicki et al. 1987, 1988) and in the Barnard 5 cloud (Beichman et al. 1988; Langer et al. 1989). Recent modeling of externally heated dust clouds which included the transient heating of small grains (Lis & Leung 1991) *did not* predict any infrared limb brightening in the *IRAS* bands for models with visual optical depths of ~ 20 or less. Those models, however, assumed a constant abundance ratio of large and small grains throughout the cloud. The fact that infrared limb brightening has been observed in diffuse clouds suggests that the small-grain abundance is likely to be nonuniform. In this *Letter*, we study the infrared limb brightening in clouds with moderate visual optical depths ($\lesssim 10$). In particular, we discuss constraints on the size and density distribution of small grains that are

¹ Also Department of Physics, Rensselaer Polytechnic Institute, Troy, NY 12180.

imposed by the *IRAS* observations of B5, which has a visual extinction of 5–10 mag. Although we try to reproduce the observed mean characteristics of the emission from B5 with radiation transport models, our objective is to study the general nature of models which are consistent with various observational constraints, i.e., emphasis is on general physical understanding rather than detailed model fitting.

2. *IRAS* OBSERVATIONS AND MODEL PARAMETERS

2.1. *IRAS* Observations of Barnard 5

We define the limb-brightening ratio $L_\lambda \equiv \max I_\lambda(p)/I_\lambda(p=0)$, where p is the impact parameter. Thus $L_\lambda > 1$ indicates limb brightening, while $L_\lambda = 1$ implies limb darkening. This quantity depends on both the wavelength and the telescope beam size. The *IRAS* observations of B5 presented by Beichman et al. (1988) and Langer et al. (1989) show considerable deviations of the intensity distribution from spherical symmetry. Mean flux densities at the cloud center and limb-brightening ratios (see Table 1) can still be compared, however, with results of spherically symmetric models. The 100 μm emission is confined to a region of ~ 0.8 pc from the cloud center (assuming a distance of 350 pc; Langer et al. 1989). The 25 and 12 μm emission is more extended and peaks at a position of ~ 1.2 pc from the center (see Fig. 1). Although B5 contains a number of infrared sources (Beichman et al. 1988; Myers et al. 1987) and high-velocity flows (Goldsmith, Langer, & Wilson 1986) thought to be associated with protostellar objects, the luminosities of these objects are so low that their influence on the overall energetics of the cloud is negligible.

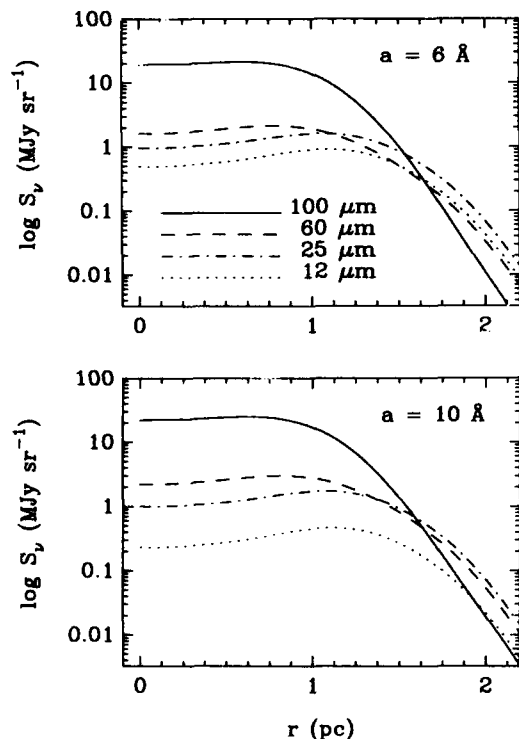


FIG. 1.—Spatial distribution of the emission in the four *IRAS* bands as a function of the offset from the cloud center for models L (bottom panel: 10 Å grain radius) and N (top panel: 6 Å grain radius). The emission at each *IRAS* band has been convolved with a 5' FWHM Gaussian beam and the corresponding spectral filter function. The emission at 12 μm is most sensitive to the small-grain size.

2.2. Assumptions and Model Parameters

We considered a static, spherically symmetric dust cloud with both large and small grains. For transiently heated small grains the temperature distribution function was calculated at each cloud radius. For large grains heated under equilibrium conditions, a single equilibrium temperature was computed. The radiative interaction between these two heating modes was treated self-consistently. We took into account the anisotropy of the internal radiation field and first-order anisotropic scattering. In determining the dust temperature distribution, the thermal coupling between gas and dust through collisions was ignored, since it was found to be insignificant at the typical gas and dust densities of dark globules (Leung 1975). We also neglected any possible heating by high-energy particles such as cosmic rays.

Our model cloud had a radius of 2.5 pc. It was heated externally by the ISRF and did not contain any internal heat source. The ISRF intensity in the solar neighborhood was taken from the model of Mathis, Mezger, & Panagia (1983). We allowed for an enhancement (described by a scaling factor f) in the UV and visible component ($\lambda \leq 1 \mu\text{m}$) of the ISRF. In our models we included a mixture of large graphite and silicate grains each having a 0.1 μm radius, as well as small graphite grains with a radius varying between 4 and 15 Å. For most models the large-grain composition (by number density) was 50% graphite, 50% silicate. Grain opacities were taken from the compilation of Draine (1987). Large grains were assumed to be uniformly distributed inside a 0.8 pc radius, smoothly merging with a Gaussian density distribution $\exp[-100(r-0.8)^2]$ outside 0.8 pc (discontinuities in the density distribution would affect stability of the numerical solution). Since models with a constant abundance ratio of large and small grains (Lis & Leung 1991) predict similar sizes of the emitting region at 100 μm and 12–25 μm , while the *IRAS* observations of B5 show the 12–25 μm emission to be more extended, we chose a small-grain density distribution in the form of a spherical shell surrounding the core of large grains with density peaking at a distance of 1.2 pc from the cloud center. We assumed the following form of the density distribution of small grains: $\exp[-\alpha_{1,2}(r-1.2)^2]$, where r is the distance from the cloud center in parsecs, and $\alpha_{1,2}$ correspond to $r < 1.2$ pc and $r \geq 1.2$ pc, respectively. For most models we took $\alpha_1 = \alpha_2 = 50$.

We used a radial grid with 50 points and a frequency grid with 59 points which spanned in wavelength from 0.091 to 5000 μm . For models with a small-grain radius less than 10 Å we used 250 enthalpy bins, and for models with larger grain size we used 150 enthalpy bins. To compare our model results with observations, we first subtracted the ISRF from the emergent intensities. The subtracted intensities were then convolved with a Gaussian antenna beam. A FWHM beam width of 5' was used, corresponding to a value of 0.1 for the ratio of the beam size to the cloud size. To stimulate the emission observed at each *IRAS* band, the monochromatic intensities were convolved with the corresponding *IRAS* filter functions.

3. DISCUSSION OF MODEL RESULTS

The input parameters that were varied in the models are the small-grain density distribution parameter (α_1), the total optical depth at the visual wavelength from the center to the edge of the cloud (τ), the small-grain radius (a), the UV scaling factor (f), and the contribution of small grains to the total visual optical depth (β). The model results are presented in

TABLE 1
IRAS OBSERVATIONS AND MODEL RESULTS FOR BARNARD 5

Model	a	τ	f	β	γ	S_{100}	S_{60}	S_{25}	S_{12}	L_{100}	L_{60}	L_{25}	L_{12}
IRAS ^a	22	3	1.1	1.1	1.1	1.3	1.6	1.6
A	10	7.5	1.0	1.0	8	18	1.5	0.7	0.16	1.1	1.4	1.8	2.1
B	15	7.5	1.0	1.0	8	18	2.1	0.7	0.06	1.1	1.4	1.8	2.5
C	6	7.5	1.0	1.0	8	18	1.1	0.4	0.19	1.1	1.4	1.8	2.0
D	10	7.5	2.0	1.0	8	34	3.9	1.5	0.38	1.2	1.3	1.8	2.1
E	10	7.5	5.0	1.0	8	94	15	3.2	0.90	1.2	1.3	1.7	1.9
F	10	5.0	2.0	1.0	8	40	4.5	1.0	0.28	1.1	1.2	1.7	1.9
G	10	2.5	1.0	1.0	8	21	2.0	0.4	0.10	1.0	1.0	1.6	1.8
H	10	1.0	1.0	1.0	8	14	1.6	0.2	0.05	1.0	1.0	1.6	1.7
I ^b	10	7.5	1.0	1.0	5	15	1.3	0.6	0.12	1.1	1.4	1.9	2.8
J ^b	10	7.5	1.0	1.0	13	19	1.6	0.7	0.19	1.1	1.4	1.7	1.8
K ^c	10	7.5	1.3	1.2	8	23	2.1	0.8	0.19	1.2	1.4	1.6	1.9
L	10	7.5	1.3	1.2	10	22	2.2	1.0	0.23	1.2	1.4	1.6	1.9
M	8	7.5	1.3	1.9	15	20	2.0	1.2	0.41	1.1	1.4	1.7	1.9
N	6	7.5	1.3	2.5	19	19	1.6	1.0	0.50	1.1	1.3	1.7	1.9
O	4	7.5	1.5	4.3	29	20	1.4	0.7	0.51	1.1	1.3	1.7	1.8
P ^b	6	7.5	1.3	2.0	26	22	1.8	0.8	0.48	1.1	1.3	1.6	1.6

NOTE.—Entries in the table are as follows: model; small-grain size in \AA (a); optical depth from the center to the edge of the cloud at 5500 \AA (τ); UV scaling factor (f); contribution of small grains to the visual optical depth in percent (β); fractional abundance of small grains by mass in percent (γ); flux densities (S_λ) in MJy sr^{-1} ; and limb-brightening ratios (L_λ) at the wavelengths of 100, 60, 25, and $12 \mu\text{m}$. Flux densities from the models have been convolved with the corresponding IRAS spectral filter functions and a $5'$ FWHM Gaussian telescope beam.

^a Average values based on the data of Beichman et al. 1988 and Langer et al. 1989.

^b The large-grain composition (by number density) is 20% graphite, 80% silicates for model I; 80% graphite, 20% silicates for model J; 95% graphite, 5% silicates for model P. For all the remaining models we have a mixture of 50% graphite and 50% silicate large grains.

^c Model K has a small-grain density distribution more extended inward ($\alpha_1 = 10$ and $\alpha_2 = 50$, compared with all remaining models, for which $\alpha_1 = \alpha_2 = 50$).

Table 1. Below we discuss the effects of different parameters on the model results.

3.1. Size of Small Grains

We first consider model A, which gives a correct $100 \mu\text{m}$ to $25 \mu\text{m}$ flux ratio, although the two fluxes at the cloud center are $\sim 30\%$ lower than the observed values. Considering the calibration errors in the IRAS data, these may be considered as roughly consistent with observations. The model flux at $60 \mu\text{m}$ is too low by $\sim 50\%$. The limb-brightening ratios at 100, 60, and $25 \mu\text{m}$ are all consistent with observations. The calculated $12 \mu\text{m}$ flux, however, is a factor of 6 lower than the observed value, while the limb-brightening ratio is slightly too high. The effect of the small-grain size on the model results is best seen in models A, B, and C. The $12 \mu\text{m}$ flux is a sensitive function of the grain size. The $100 \mu\text{m}$ flux, on the other hand, is hardly affected, suggesting that the $100 \mu\text{m}$ emission is dominated by large grains heated under equilibrium conditions. The flux density at 60 and $25 \mu\text{m}$ is approximately a linear function of the grain size, while the $12 \mu\text{m}$ flux exhibits a more complicated behavior. In general, the limb-brightening ratios at the four IRAS bands are not sensitive to the small-grain size.

3.2. Interstellar UV Radiation Field

Models A, D, and E show the effect of the UV radiation field enhancement. Because of the low optical depth through the small-grain envelope, the UV photons penetrate relatively deep inside the cloud. Consequently, the total flux at all IRAS bands increases approximately linearly with the UV scaling factor, and the flux ratios between different IRAS bands are hardly affected. The limb-brightening ratios are also not sensitive functions of f .

3.3. Cloud Opacity

The effect of the cloud opacity is best seen in models D and F, as well as in models H, G, and A. The flux density depends on both the grain temperature and the dust column density. The temperature distribution function of the small grains in the optically thin envelope is hardly affected by the change in the cloud opacity. Since the column density of small grains scales linearly with the cloud opacity, the 12 and $25 \mu\text{m}$ flux densities are also approximately linear functions of τ . The emission at 60 and $100 \mu\text{m}$ dominated by large grains is somewhat more complicated. When the cloud opacity is small (see models G and H), the temperature distribution of large grains in the cloud core is fairly uniform, since the cloud is not yet opaque to UV and visual photons. The flux densities at 60 and $100 \mu\text{m}$ increase with cloud opacity because of increasing dust column density, similar to the 12 and $25 \mu\text{m}$ emission. When the cloud opacity becomes significant (see model A), increasing cloud opacity results in decreasing the large-grain temperature in the cloud interior. The flux densities at 60 and $100 \mu\text{m}$ thus decrease in spite of the increasing dust column density. In general, a lower cloud opacity leads to a lower limb-brightening ratio at all wavelengths.

3.4. Composition of Large Grains

Models A, I, and J illustrate the effect of the large-grain composition. In general, the emission at all wavelengths increases with the relative abundance of graphite grains because graphite grains, having a lower albedo compared with silicate grains, can attain higher temperatures. Except at $100 \mu\text{m}$, the limb-brightening ratios decrease with increasing graphite content in the cloud, with L_{12} being the most sensitive to changes in the large-grain composition.

3.5. Spatial Distribution of Small Grains

Models K and L show the effect of the spatial distribution of small grains. Except for the distribution of small grains, both models have the same parameters. The density distribution of small grains in model K, however, is more extended inward. This has an effect of slightly reducing the limb-brightening ratios. The most important difference, however, is that the 25 and 12 μm flux densities in model K are significantly decreased. This results from a strong attenuation in the cloud core of the UV photons responsible for the transient heating of small grains. Although total column densities of small grains are the same in both models, small grains in model K are on average colder and the short-wavelength flux density is decreased compared with model L. This further supports our conclusion that small grains responsible for the 12 and 25 μm emission have a different spatial distribution compared with that of large grains, forming an extended halo around the cloud core made of large grains. However, this does not necessarily mean that small grains are completely excluded from the cloud interior. Because of the strong attenuation of UV photons, small grains that may be present in the core will not contribute significantly to the 12 and 25 μm emission. Based on the data available, we can only conclude that the short-wavelength *IRAS* emission is produced by small grains in an envelope surrounding the cloud core made of large grains and characterized by a low visual optical depth.

4. COMPARISON WITH *IRAS* OBSERVATIONS

By adjusting model parameters, we constructed several models which provide reasonable fits to most of the *IRAS* observations of B5 (see models M–P). The most discrepant result is the 12 μm flux density, the observed value being approximately a factor of 2 higher than the model predictions. This may be related to possible calibration errors in the *IRAS* data. In the following discussion we assume, however, that the observed 12 μm flux density is correct. The 12 μm flux density in our models could be increased by increasing the contribution of small grains to the optical depth. This would not, however, change the 25 to 12 μm flux ratio and would have important consequences for the dynamical structure of the cloud. Because small grains are distributed in the outer part of the cloud, they contribute significantly to the total mass, even for a relatively small contribution to the optical depth. A 1% contribution from small grains to the optical depth corresponds to about an 8% contribution to the mass. Because the total mass of the cloud has to be dominated by the core traced by the 100 μm emission, a small-grain contribution to the optical depth of $\sim 2\%$ or more is unlikely.

The 25 to 12 μm flux ratio predicted by our models is a sensitive function of the small-grain size. This is most easily seen in models L–P. Input parameters of these models were chosen to give a 100 μm flux density of $\sim 20 \text{ MJy sr}^{-1}$. The 25 to 12 μm flux ratio changes from ~ 4 for 15 \AA grains to ~ 1.3 for 4 \AA grains. This indicates that the smallest grains provide the best fit to the data. However, Guhathakurta & Draine (1989) showed that graphite grains smaller than $\sim 3.8 \text{\AA}$ will be destroyed by the interstellar radiation field on a time scale of 10^{13} s. The size of smallest grains we adopted approaches this

limit, especially considering the enhanced UV radiation field. Also, the contribution of small grains to the total cloud mass becomes significant for models with smallest grain sizes. Small grains contribute $\sim 29\%$ of the total mass in model O and yet, although the 25 to 12 μm flux ratio is close to the observed value, the predicted flux densities at the two wavelengths are too low. In order to obtain the required 25 μm flux density, one would have to increase the small-grain contribution to the optical depth to $\sim 7\%$ – 8% , resulting in a small-grain contribution to the total cloud mass of roughly 40% or higher, which seems very unlikely. It is possible that the 12 μm flux is partially produced by the polycyclic aromatic hydrocarbons (PAHs), which have not been included in our calculations. From our calculations we derive a lower limit of $\sim 50\%$ for the contribution of PAHs to the 12 μm flux density in B5 (model N). Transiently heated silicate grains might be expected to produce a lower 25 to 12 μm flux ratio than the graphite grains of the same size, due to the presence of the 10 μm emission feature. However, because of the high albedo, these grains attain lower temperatures than graphite grains, and are therefore expected to produce a weaker emission in the two wavelength bands.

5. CONCLUSION

We developed a radiation transport code incorporating the transient heating of small dust grains. We constructed a series of models to study the effects of the temperature fluctuations in small graphite grains on the spectrum and surface brightness of an interstellar dust cloud heated externally by the ISRF. From comparison with the *IRAS* observations of B5 we conclude that the 25 μm emission is most likely produced by grains with a 6–10 \AA radius. These grains also contribute up to 50% of the observed 12 μm emission, which is a critical observational constraint for our models. The remaining 12 μm flux could be produced by the PAHs. The 60 and 100 μm radiation is dominated by emission from large grains heated under equilibrium conditions. Small grains responsible for the 12–25 μm emission are distributed in the outer part of the cloud and contribute $\sim 1\%$ – 2% of the total optical depth at the visual wavelength, and $\sim 10\%$ – 20% of the total mass of the cloud. Our calculations do not exclude the possibility that the small grains may also be present in the core of the cloud. A more extended spatial distribution of small grains compared with the large-grain distribution, however, seems a necessary condition for explaining the observed distribution of the short-wavelength emission in B5. This conclusion is somewhat similar to that of Beichman et al. (1988), although the small-grain contribution to the total visual optical depth in our models is considerably lower than their estimate of $\sim 50\%$.

We thank B. Draine for useful discussions concerning the original method of calculating the grain temperature distribution function. This research has been partially supported by the Air Force under grant AFOSR 89-104 and by NASA under grant NAG 5-1182 (both to Rensselaer Polytechnic Institute), and by NSF under grant AST 88-14405 (to Caltech Submillimeter Observatory).

REFERENCES

- Beichman, C. A., Wilson, R. W., Langer, W. D., & Goldsmith, P. F. 1988, *ApJ*, 332, L81
- Castelaz, M. W., Sellgren, K., & Werner, M. W. 1987, *ApJ*, 313, 853
- Chlewicki, G., Laureijs, R. J., Clark, F. O., & Wesselius, P. R. 1987, in *Star Formation in Galaxies*, ed. C. J. Lonsdale Persson (NASA CP-2466), 113
- . 1988, in *Experiments on Cosmic Dust Analogues*, ed. E. Bussoletti, C. Fusco, & G. Longo (Dordrecht: Kluwer), 313
- Desert, F. X., Boulanger, F., & Shore, S. N. 1986, *A&A*, 160, 295
- Draine, B. T. 1987, Princeton Obs. Preprint 213
- Draine, B. T., & Anderson, A. 1985, *ApJ*, 292, 494
- Dwek, E. 1986, *ApJ*, 302, 363
- Egan, M. P., Leung, C. M., & Spagna, G. F. 1988, *Computer Phys. Comm.*, 48, 271
- Goldsmith, P. F., Langer, W. D., & Wilson, R. W. 1986, *ApJ*, 303, L11
- Guhathakurta, P., & Draine, B. T. 1989, *ApJ*, 345, 230
- Langer, W. D., Wilson, R. W., Goldsmith, P. F., & Beichman, C. A. 1989, *ApJ*, 337, 355
- Lee, M. H., & Rogers, C. 1987, *ApJ*, 317, 197
- Leung, C. M. 1975, *ApJ*, 199, 340
- Leung, C. M., O'Brien, E. V., & Dubish, R. 1989, *ApJ*, 337, 293
- Lis, D. C., & Leung, C. M. 1991, *Icarus*, 89, in press
- Low, F. J., et al. 1984, *ApJ*, 278, L19
- Mathis, J. S., Mezger, P. G., & Panagia, N. 1983, *A&A*, 128, 212
- Myers, P. C., Fuller, G. A., Mathieu, R. D., Beichman, C. A., Benson, P. J., Schild, R. E., & Emerson, J. P. 1987, *ApJ*, 319, 340
- Puget, J. L., & Léger, A. 1989, *ARA&A*, 27, 161
- Spencer, R. G., & Leung, C. M. 1978, *ApJ*, 222, 140

ON THE NATURE OF THE EXCESS 100 MICRON FLUX ASSOCIATED WITH CARBON STARS

MICHAEL P. EGAN AND CHUN MING LEUNG

Department of Physics, Rensselaer Polytechnic Institute, Troy, NY 12180-3590

Received 1991 March 18; accepted 1991 June 18

ABSTRACT

Infrared Astronomical Satellite (IRAS) data indicates that many carbon stars, especially those with optically thin dust shells, have large fluxes at 60 and 100 μm . It has been suggested that a remnant dust shell from an earlier mass-loss episode can explain the excess fluxes. Two hypotheses have been proposed to explain the origin of the remnant dust shell. First, that O-rich asymptotic giant branch stars may undergo a transformation to C-rich by carbon dredge-up, resulting in the formation of an inner C-rich dust shell in 10^4 yr and a remnant O-rich dust shell. In the second scenario, a C-rich remnant dust shell is formed when helium shell flashes stop the mass-loss process which resumes in 10^4 yr. We have constructed radiation transport models of dust around carbon stars: models with either a single C-rich dust shell or double shells. We find that single-shell models cannot explain the observed color distribution, while two-shell models with either a C-rich or an O-rich remnant shell can. Typically the remnant shell must be about 1 pc thick and lie at a distance of 0.1 pc from the inner dust shell. To differentiate between the above two scenarios, we examined the relation between mass-loss rate and the flux ratio at long wavelengths (60/25 and 100/60 μm flux ratios). We compared the model results with observations using the relation between mass-loss rate and the strength of the SiC feature at 11.2 μm . We find that models with a single dust shell do not reproduce the observed relationship between mass-loss rate and flux ratio (i.e., objects with a low-mass loss rate have a larger flux ratio at long wavelengths), but the two-shell models do. The time scales required by the models and the necessity of a prior O-rich phase are consistent with the hypothesis that some O-rich stars evolve to form carbon stars. While we cannot rule out the existence of C-rich remnant shells, we conclude that they can only be formed after a phase of O-rich mass loss has occurred.

Subject headings: infrared: sources — stars: carbon — stars: circumstellar shells — stars: mass loss

1. INTRODUCTION

Several authors (Thronson et al. 1987; Willems 1988; Chan & Kwok 1988, 1990) have noted that optically identified (visual) carbon stars show excess flux at 60 and 100 μm . To explain the excess flux at 60 μm , Willems & de Jong (1988) and Chan & Kwok (1988, 1990) have invoked the detached shell model of Willems (1987). Originally proposed to explain observations of carbon stars with 10 μm silicate emission (Little-Marein 1986; Willems & de Jong 1986), Willems's model hypothesized that carbon stars evolved from oxygen-rich (O-rich) stars: as the photosphere of an O-rich star becomes carbon-rich (C-rich) due to dredge-up, the formation of O-rich dust stops; the existing O-rich dust shell becomes detached and moves away, revealing the underlying star which is identified as a visual carbon star; after the formation of C-rich dust begins, those with a substantial C-rich dust shell are identified as infrared (IR) carbon stars. On the 12-25-60 μm color-color diagram constructed from the *IRAS* photometric data, Chan & Kwok (1988) have shown that visual carbon stars occupy a region consistent with Willems's model of detached shells. On this diagram the IR carbon stars lie along a line defined by the color of a blackbody. On the 25-60-100 μm color-color diagram, however, most carbon stars show an excess of 100 μm flux. In particular, the IR carbon stars do not lie on the blackbody line. The nature of this excess flux and the behavior of the 25-60-100 μm colors for carbon stars have not been investigated by these authors. To test the detached shell model, Zuckerman & Maddalena (1989) looked for SiO and OH maser emission from several carbon stars, assuming that an O-rich detached shell would produce O-rich maser emission. This search was unsuccessful, but de Jong (1989) claims that the

small sample of stars observed makes the negative result statistically insignificant. Recently Olofsson et al. (1990) proposed that the excess 60 μm emission could be due to C-rich dust shells which have become detached due to helium shell flashes.

To determine the origin of the excess flux in the far-IR and to test the detached shell hypotheses of Willems (1987) and Olofsson et al. (1990), we have modeled the emission from carbon stars of circumstellar dust shells of different structure, composition, opacities, and ages. We identify three possible sources for the excess flux: (1) cool dust in a single extended shell, (2) emission from dust in the intervening interstellar medium (ISM), or (3) emission from a two-shell system, the additional shell being a remnant from an earlier mass-loss episode. We find that neither the single-shell model nor the emission from the ISM can account for the observed 100 μm flux excess seen in carbon stars with dust shells of a given opacity. On the other hand, the 60 and 100 μm flux excesses can be explained by the two-shell model with a remnant shell which is at least 1 pc thick. Unfortunately, we cannot conclusively determine whether the remnant shell is O- or C-rich, as both grain types produce similar flux excesses in the far-infrared. We do show, however, that the time scales for production of the detached shells and of the carbon star lifetime are consistent with the evolutionary scenario proposed by Willems.

2. IRAS OBSERVATIONS

Our sample of 125 carbon stars is taken from the *IRAS* Low Resolution Spectrometer (LRS) catalog. They all have good photometric fluxes at 12, 25, 60, and 100 μm . Under the LRS classification, 104 of these sources are 4n objects (classified as

having SiC emission at $11.3 \mu\text{m}$), 10 are $1n$ objects (classified as having featureless spectra), 7 are $2n$ objects (with features around $10 \mu\text{m}$), and 4 are class $0n$ objects (with low-quality spectra). Of the $0n$ objects, 3 are class 04 (indicating SiC emission) and 1 is class 01 (indicating a blue spectrum with low signal-to-noise). All of the $0n$, $1n$, and $2n$ objects and 47 of the $4n$ objects have been identified as visible carbon stars in the General Catalogue of Cool Carbon Stars (Stephenson 1973, hereafter GCCCS). Of the remaining $4n$ objects, an additional 10 (denoted by crosses in Fig. 1) are probably also visual carbon stars, while 47 are IR carbon stars. The properties of the carbon stars in our sample are listed in Table 1, where LRSC is the LRS classification, $S(\text{SiC})$ is the strength of the SiC feature above the continuum as computed in the *IRAS* Explanatory Supplement (Beichman et al. 1985), and d is the distance to the source.

Figure 1 shows the color-color diagrams of the carbon stars in our sample. The color derived from the fluxes at two wavelengths λ_j and λ_i is given by

$$\log [\lambda_j F_\lambda(\lambda_j \mu\text{m}) / \lambda_i F_\lambda(\lambda_i \mu\text{m})] \\ = \log [\lambda_i F_\lambda(\lambda_j \mu\text{m}) / \lambda_j F_\lambda(\lambda_i \mu\text{m})] . \quad (1)$$

We have used the second form since the *IRAS* fluxes are given as $F_\lambda(\lambda)$. The color-corrected fluxes listed in Table 1 are of the form $F_\lambda(\lambda)$ and have units of janskys.

To facilitate our discussion, we have identified five regions on the color-color diagrams as defined in the figure caption. On the $12\text{-}25\text{-}60 \mu\text{m}$ color-color diagram, the 78 visual carbon stars (68 from the GCCCS and 10 probable candidates) lie almost exclusively in region I, while the IR carbon stars occupy regions II and III. On the $25\text{-}60\text{-}100 \mu\text{m}$ color-color diagram, about 70% (55 out of 78) of the visual carbon stars lie in region V, while most (26 out of 30) IR carbon stars in region III of the $12\text{-}25\text{-}60 \mu\text{m}$ diagram lie in region IV. On the other hand, the

17 stars in region II of the $12\text{-}25\text{-}60 \mu\text{m}$ diagram divide almost equally between regions IV (10 stars) and V (7 stars) of the $25\text{-}60\text{-}100 \mu\text{m}$ diagram.

3. MODELS

To interpret these *IRAS* observations we constructed computer models for dust shells around carbon stars. We used the quasi-diffusion method developed by Leung (1975) to solve the problem of radiation transport, accounting for the scattering, absorption, and reemission of photons by dust grains. The details of the computational procedure have been given elsewhere (Leung 1976), and the computer code has been documented by Egan, Leung, & Spagna (1988). We considered expanding circumstellar dust shells with steady-state outflows (or constant mass-loss rate) and assumed spherically symmetric geometry. We took into account both the anisotropy of the internal radiation field and first-order anisotropic scattering. In determining the dust temperature distribution, the thermal coupling between gas and dust through collisions was ignored since it was found to be insignificant. For a medium with multiple grain types, the temperature distribution for each grain component was computed self-consistently. We used a radial grid with 100 points and a frequency grid with 130 points which spanned in wavelength from 0.091 to $1000 \mu\text{m}$. A typical model required about eight iterations and took slightly less than 8 minutes of CPU time on our Silicon Graphics (Personal Iris) workstation which has a speed rated at 10 MIPS. For models involving the ISM, we used a radial grid with 229 points.

We have constructed three classes of models: (1) single dust shell, (2) single shell with intervening ISM, and (3) two-shell system with a remnant shell. The flux from the models was convolved with the *IRAS* spectral response functions (Beichman et al. 1985). From the flux ratios, color-color diagrams were constructed and compared with observations.

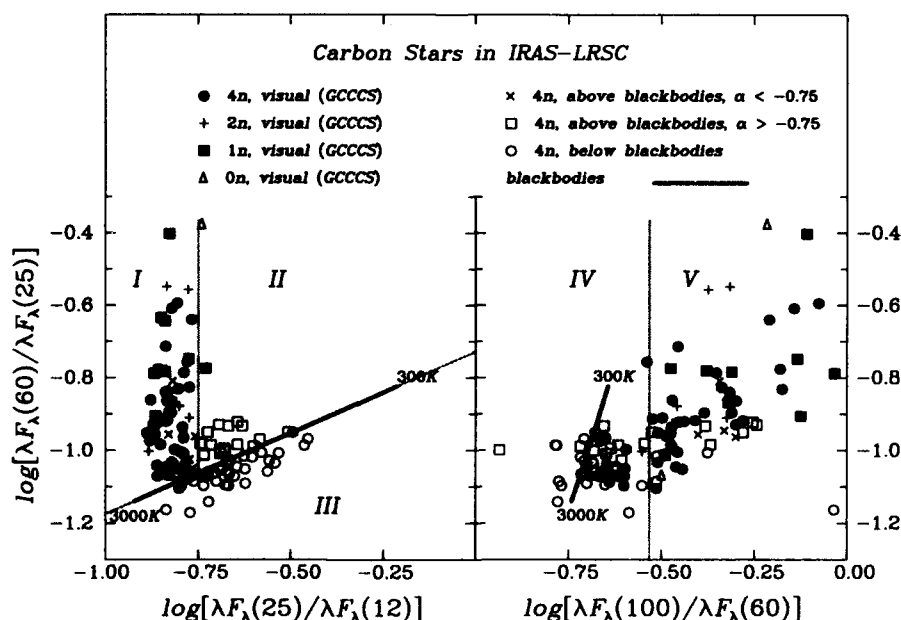


FIG. 1.—Color-color diagrams for selected carbon stars in the *IRAS*-LRSC catalog. The thick solid line is the blackbody line. Five regions are defined in the diagrams as follows: (I) above blackbody line, $\alpha \equiv \log [\lambda F_\lambda(25)/\lambda F_\lambda(12)] < -0.75$; (II) above blackbody line, $\alpha > -0.75$; (III) below blackbody line; (IV) $\zeta \equiv \log [\lambda F_\lambda(100)/\lambda F_\lambda(60)] < -0.53$; (V) $\zeta > -0.53$.

Note that most visual carbon stars (filled symbols and crosses) occupy regions I and V, while the infrared carbon stars (open symbols) spread out in all regions except region I. Note that three GCCCS stars have values of ζ slightly greater than 0.0 and are not plotted since they lie outside the diagram.

TABLE 1
PROPERTIES OF IRAS CARBON STARS

IRAS NAME	LRSC	<i>d</i> (pc)	<i>S</i> (SiC)	COLOR - CORRECTED IRAS FLUXES (Jy)				NOTES
				<i>F_V</i> (12)	<i>F_V</i> (25)	<i>F_V</i> (60)	<i>F_V</i> (100)	
00172+4425	24			4.069E+01	1.188E+01	3.383E+00	1.914E+00	
00247+6922	43		2.390E+00	2.769E+02	1.149E+02	2.265E+01	6.330E+00	
00248+3518	43	8.700E+02	1.650E+00	1.972E+01	6.197E+00	3.663E+00	4.394E+00	1,3
01133+2530	22	6.000E+02		2.684E+01	8.838E+00	2.808E+00	1.630E+00	1
01324+4907	44		2.460E+00	2.865E+01	8.691E+00	1.432E+00	2.200E+00	3
02152+2822	43		2.110E+00	1.295E+02	9.293E+01	2.303E+01	6.294E+00	3
02270-2619	43	7.700E+02	3.010E+00	1.968E+02	5.640E+01	1.229E+01	4.642E+00	1,3
02293+5748	42		1.380E+00	1.851E+02	1.327E+02	3.282E+01	9.046E+00	3
03112-5730	43		1.880E+00	7.865E+01	2.755E+01	5.593E+00	2.153E+00	3
03186+7016	42	1.600E+03	2.070E+00	1.408E+02	7.360E+01	1.809E+01	5.771E+00	2,3
03229+4721	44	1.000E+03	3.380E+00	4.420E+02	1.499E+02	3.056E+01	1.092E+01	1,3
03374+6229	45	4.800E+02	4.280E+00	9.742E+01	3.366E+01	1.414E+01	6.811E+00	1,3
03448+4432	42	1.150E+03	1.380E+00	1.305E+02	7.525E+01	1.691E+01	5.532E+00	1,3
03557+4404	43		1.670E+00	3.795E+01	2.459E+01	6.625E+00	3.292E+00	3
04262+3945	45	8.300E+02	3.910E+00	3.606E+01	1.129E+01	3.438E+00	2.363E+00	1,3
04307+6210	45	1.000E+03	4.070E+00	2.070E+02	6.853E+01	1.345E+01	5.137E+00	2,3
04365+6349	45		1.920E+00	2.119E+01	8.318E+00	2.237E+00	1.955E+00	3
04459+6804	42	5.000E+02	1.720E+00	7.169E+01	2.010E+01	5.681E+00	4.749E+00	1,3
04483+2826	22	6.400E+02		2.628E+01	9.142E+00	6.088E+00	4.291E+00	1
04530+4427	42		2.020E+00	1.036E+02	6.338E+01	1.495E+01	5.624E+00	3
05028+0106	44	3.500E+02	3.200E+00	1.395E+02	4.005E+01	1.172E+01	5.850E+00	1,3
05104+2055	42		1.740E+00	7.335E+01	2.480E+01	6.749E+00	5.250E+00	3
05405+3240	42		1.480E+00	1.904E+02	1.035E+02	2.664E+01	9.633E+00	3
05418-4628	41	6.200E+02	8.200E-01	4.372E+01	1.322E+01	4.587E+00	3.689E+00	1,3
05418-3224	43		2.470E+00	5.308E+01	1.868E+01	3.023E+00	1.303E+00	3
05426+2040	45	4.900E+02	4.490E+00	1.170E+02	3.955E+01	1.026E+01	3.826E+00	1,3
05585+2927	01			5.230E+00	1.981E+00	1.998E+00	2.026E+00	
06149+0832	45	1.110E+03	1.460E+00	1.250E+01	3.821E+00	1.334E+00	2.280E+00	1,3
06192+4657	42		1.260E+00	4.068E+01	2.321E+01	4.872E+00	1.679E+00	3
06192+0722	46	1.230E+03	3.560E+00	2.133E+01	7.224E+00	2.835E+00	2.100E+00	1,3
06216-2702	44	1.260E+03	1.680E+00	1.602E+01	4.887E+00	1.604E+00	1.345E+00	1,3
06225+1445	16	5.700E+02		3.504E+01	1.096E+01	3.563E+00	2.840E+00	1
06226-0905	43	1.380E+03	3.180E+00	9.874E+01	3.042E+01	8.067E+00	5.341E+00	1,3
06238+0904	43		2.390E+00	3.426E+01	1.532E+01	4.287E+00	2.968E+00	3
06268+0849	42		1.350E+00	4.869E+01	2.305E+01	5.737E+00	4.102E+00	3
06291+4319	43		2.830E+00	9.567E+01	3.782E+01	6.553E+00	1.817E+00	3
06331+3829	43	3.000E+02	2.680E+00	1.816E+02	5.501E+01	1.585E+01	9.621E+00	1,3
06342+0328	43		2.480E+00	2.390E+02	9.857E+01	2.049E+01	8.431E+00	3
06487+0551	43		2.700E+00	5.762E+01	2.213E+01	5.150E+00	2.777E+00	3
06528-4218	42	8.000E+02	5.400E-01	2.922E+01	1.023E+01	3.659E+00	2.800E+00	1,3
06529+0626	44	9.400E+02	3.320E+00	8.295E+01	2.274E+01	5.799E+00	2.101E+00	1,3
07065-7256	45		3.850E+00	1.673E+02	5.570E+01	1.067E+01	4.459E+00	3
07149-0046	43		2.010E+00	2.343E+01	1.142E+01	3.196E+00	1.179E+00	3
07161-0111	42		1.010E+00	3.981E+01	1.495E+01	3.743E+00	1.776E+00	3
07217-1246	42		1.770E+00	8.760E+01	3.137E+01	6.720E+00	2.239E+00	3
07373-4021	45		3.840E+00	1.509E+02	4.962E+01	9.357E+00	4.783E+00	3
07411-4404	16			8.947E+00	2.696E+00	1.469E+00	2.701E+00	
07454-7112	43		2.440E+00	5.595E+02	2.384E+02	5.047E+01	1.991E+01	3
07487-0229	42	1.510E+03	1.110E+00	3.512E+01	1.073E+01	2.319E+00	1.339E+00	1,3
07582-1933	44		2.510E+00	7.694E+01	3.440E+01	6.595E+00	1.872E+00	3
08045-1524	44		2.690E+00	4.078E+01	1.470E+01	2.899E+00	1.483E+00	3
08305-3314	41		9.600E-01	4.412E+01	3.235E+01	8.349E+00	2.725E+00	3
08340-3357	42		1.920E+00	1.121E+02	4.292E+01	8.239E+00	3.850E+00	3
08416-2525	44	1.250E+03	3.650E+00	6.293E+01	2.237E+01	4.563E+00	1.911E+00	1,3
08470-5710	43		1.970E+00	2.469E+01	1.040E+01	2.934E+00	2.797E+00	3
08525+1725	42	4.500E+02	1.510E+00	6.850E+01	1.976E+01	5.822E+00	3.086E+00	1,3
08538+2002	23	7.800E+02		4.535E+01	1.234E+01	2.943E+00	1.375E+00	1

TABLE 1—Continued

IRAS NAME	LRSC	<i>d</i> (pc)	<i>S</i> (SiC)	COLOR - CORRECTED IRAS FLUXES (Jy)				NOTES
				$F_{\nu}(12)$	$F_{\nu}(25)$	$F_{\nu}(60)$	$F_{\nu}(100)$	
09112-2311	45	1.280E+03	3.160E+00	2.666E+01	7.528E+00	2.006E+00	1.120E+00	1,3
09116-2439	42		1.800E+00	6.900E+02	3.100E+02	6.401E+01	2.055E+01	3
09452+1330	43	2.900E+02	1.360E+00	4.286E+04	1.820E+04	4.376E+03	8.459E+02	1,3
09513-5324	42		2.040E+00	1.505E+02	7.465E+01	1.591E+01	5.963E+00	3
09521-7508	43		2.610E+00	3.208E+02	1.407E+02	2.714E+01	1.009E+01	3
09533-4120	44		3.140E+00	6.716E+01	1.890E+01	4.970E+00	2.694E+00	3
10131+3049	04	7.100E+02		2.733E+03	9.309E+02	2.111E+02	7.899E+01	1
10154-4950	45		3.520E+00	4.116E+01	1.272E+01	3.884E+00	3.166E+00	3
10249-2517	46	1.500E+03	3.790E+00	4.338E+01	1.476E+01	3.143E+00	1.889E+00	1,3
10329-3918	21			1.236E+02	3.764E+01	2.555E+01	2.058E+01	
10416+6740	42	5.400E+02	1.570E+00	3.840E+01	1.107E+01	4.451E+00	4.903E+00	1,3
11145-6534	43		2.480E+00	1.730E+02	8.520E+01	1.971E+01	1.009E+01	3
11186-5528	44		3.620E+00	1.384E+02	4.893E+01	1.019E+01	3.807E+00	3
11308-1020	44		2.630E+00	4.778E+01	1.675E+01	3.791E+00	1.275E+00	3
11318-7256	44		3.640E+00	2.726E+02	8.565E+01	1.904E+01	9.809E+00	3
12118-5115	16			2.015E+01	7.837E+00	3.160E+00	1.765E+00	
12203-7513	17			1.435E+01	4.069E+00	1.213E+00	1.518E+00	
12226+0102	04	5.900E+02		7.207E+01	2.142E+01	4.411E+00	1.624E+00	1
12394-4338	43		2.460E+00	1.391E+02	5.394E+01	1.095E+01	4.468E+00	3
12427+4542	42	2.900E+02	1.560E+00	1.963E+02	5.284E+01	1.416E+01	7.314E+00	1,3
12447+0425	44	1.020E+03	3.760E+00	1.791E+02	5.147E+01	1.049E+01	3.550E+00	1,3
12540-6845	42		1.880E+00	2.418E+02	1.059E+02	2.532E+01	8.780E+00	3
12544+6615	41	4.700E+02	9.700E-01	8.269E+01	2.388E+01	6.845E+00	4.008E+00	1,3
13136-4426	43		1.800E+00	4.537E+01	1.546E+01	3.163E+00	1.211E+00	3
13173-7410	42		8.800E-01	1.770E+01	5.406E+00	1.567E+00	1.369E+00	3
13549-5606	42	8.000E+02	1.230E+00	2.527E+01	8.977E+00	4.938E+00	5.080E+00	1,3
14107-5341	18			3.867E+01	1.089E+01	4.253E+00	6.570E+00	
15082-4808	42		1.940E+00	7.393E+02	3.327E+02	7.423E+01	2.550E+01	3
15094-6953	42	3.200E+02	1.880E+00	1.532E+02	4.389E+01	1.272E+01	8.261E+00	1,3
15148-4940	42		2.130E+00	1.540E+02	5.124E+01	1.216E+01	7.091E+00	3
17049-2440	42		1.640E+00	7.656E+02	3.970E+02	9.121E+01	2.917E+01	3
17079-6554	43		2.420E+00	1.366E+02	4.747E+01	9.808E+00	3.725E+00	3
17389-5742	45		3.670E+00	9.331E+01	3.133E+01	8.700E+00	4.879E+00	3
17446-7809	43		2.950E+00	3.715E+02	1.465E+02	3.070E+01	1.128E+01	3
17556+5813	45	6.900E+02	3.840E+00	1.583E+02	5.067E+01	1.222E+01	5.183E+00	1,3
18194-2708	43		2.400E+00	5.725E+02	2.081E+02	5.454E+01	1.972E+01	3
18240+2326	42	1.330E+03	1.800E+00	7.027E+02	3.492E+02	6.796E+01	2.257E+01	2,3
18276-4717	44		3.630E+00	2.016E+02	6.375E+01	1.310E+01	4.706E+00	3
18306+3657	04	5.100E+02		7.432E+01	2.306E+01	4.721E+00	2.489E+00	1
18333+0533	42	2.000E+03	1.320E+00	3.279E+02	2.609E+02	5.920E+01	1.972E+01	2,3
18410+3654	42	9.000E+02	1.450E+00	1.776E+01	5.448E+00	1.814E+00	1.455E+00	1,3
18475+0926	42		1.670E+00	2.090E+02	9.706E+01	1.978E+01	7.037E+00	3
19017-0545	42	3.800E+02	1.980E+00	1.065E+02	2.933E+01	9.676E+00	5.450E+00	1,3
19162-1600	18	1.320E+03		2.179E+01	6.405E+00	3.565E+00	6.338E+00	!
19175-0807	43	9.200E+02	3.100E+00	3.506E+02	1.528E+02	3.713E+01	1.431E+01	1,3
19233+7627	23	4.400E+02		5.120E+01	1.480E+01	4.241E+00	3.739E+00	1
19272+4556	17	1.000E+03		1.724E+01	5.198E+00	2.052E+00	1.674E+00	1
19314-1629	43	5.600E+02	2.100E+00	4.532E+01	1.482E+01	5.243E+00	5.849E+00	1,3
19321+2757	43	1.450E+03	2.300E+00	3.008E+02	1.334E+02	3.008E+01	1.239E+01	1,3
19390+3229	17	9.700E+02		1.156E+01	3.584E+00	3.404E+00	4.420E+00	1
19594+4047	42		1.690E+00	3.490E+02	2.088E+02	4.621E+01	1.596E+01	3
20028+2030	17	9.700E+02		1.361E+01	4.754E+00	2.038E+00	2.497E+00	1
20072+3116	43		2.780E+00	1.619E+02	7.656E+01	2.198E+01	2.045E+01	3
20396+4757	44	5.800E+02	3.750E+00	5.400E+02	1.766E+02	3.777E+01	1.587E+01	1,3
20472+3302	46	1.250E+03	2.670E+00	1.347E+01	4.378E+00	2.674E+00	3.735E+00	1,3

TABLE 1—Continued

IRAS NAME	LRSC	<i>d</i> (pc)	<i>S</i> (SiC)	COLOR - CORRECTED IRAS FLUXES (Jy)				NOTES
				<i>F_V</i> (12)	<i>F_V</i> (25)	<i>F_V</i> (60)	<i>F_V</i> (100)	
20570+2714	42		2.090E+00	2.606E+02	1.158E+02	2.435E+01	8.523E+00	3
21003+4801	44		2.990E+00	9.336E+01	5.129E+01	1.213E+01	8.511E+00	3
21032-0024	45	8.100E+02	4.110E+00	2.555E+02	8.703E+01	1.736E+01	6.606E+00	1,3
21168-4514	17			3.569E+01	1.054E+01	4.189E+00	2.921E+00	
21197-6956	22			5.973E+01	2.092E+01	6.170E+00	4.877E+00	
21262+7000	45	1.180E+03	3.960E+00	5.125E+01	1.730E+01	4.518E+00	3.774E+00	1,3
21320+3850	44	1.030E+03	3.720E+00	2.114E+02	7.148E+01	1.676E+01	9.024E+00	1,3
21373+4540	43	1.610E+03	2.100E+00	1.079E+02	5.087E+01	1.101E+01	4.376E+00	1,3
21399+3516	42	4.800E+02	1.640E+00	5.753E+01	1.740E+01	8.068E+00	4.712E+00	1,3
21440+7324	44	6.700E+02	2.830E+00	1.076E+02	3.154E+01	7.844E+00	4.394E+00	1,3
21489+5301	42		1.480E+00	1.167E+02	7.796E+01	2.096E+01	7.330E+00	3
22424+7431	45		4.390E+00	4.673E+01	1.475E+01	5.491E+00	4.148E+00	3
23320+4316	42	1.180E+03	1.890E+00	8.671E+02	3.683E+02	8.661E+01	3.248E+01	1,3

NOTES.—(1) Distance from Claussen et al. 1987; (2) Distance from Skinner & Whitmore 1988; (3) *S*(SiC) from Chan 1988.

Typical model parameters used were stellar temperature $T_* = 2500$ K, luminosity $L_* = 10^4 L_\odot$, and mass outflow velocity $v = 10$ km s⁻¹. The composition of the dust in single-shell models and in the inner shell of double-shell systems was taken to be amorphous carbon (93% by mass; optical constants from Mathis & Whiffen 1989) and silicon carbide (7% by mass; optical constants from Pegourie 1988) grains with radius 0.1 μ m. The composition of the dust in the remnant shell of double-shell systems was taken to be either amorphous silicate grains (grain radius of 0.1 μ m; optical constants from Day 1979, 1981) or amorphous carbon grains. For the interstellar grains, opacities of the composite grains (silicate, graphite, and amorphous carbon conglomerates) proposed by Mathis & Whiffen (1989) were used. Figure 2 shows the extinction cross sections and albedos (calculated from the Mie theory) for the various grain types used in our models. To match the LRS SiC features, models with shell opacities in the visible (at 0.5 μ m) ranging from 0.3 to 100 were run.

Standard carbon star models have a single C-rich circumstellar dust shell. For steady-state outflow, the opacity of the dust shell is determined by the mass-loss rate (\dot{M}). For a constant outflow velocity, the dust density distribution has an inverse power-law form [$n(r) = n_0(r_0/r)^2$], and the opacity through the shell is given by

$$\tau(\lambda) = \int_{r_0}^R \langle Q(\lambda)\pi a^2 \rangle n_0 r_0^2 r^{-2} dr \\ = \langle Q(\lambda)\pi a^2 \rangle n_0 r_0^2 [(r_0)^{-1} - (R)^{-1}], \quad (2)$$

where $\langle Q(\lambda)\pi a^2 \rangle$ is the extinction cross section of a dust grain of radius a , r_0 is the inner radius of the dust shell, and R is the outer radius. The geometric thickness of the shell, $(R - r_0)$, is determined by the duration of the mass-loss phase, which has an upper limit of about 10^6 yr (Iben & Renzini 1983; Jura 1987) corresponding to a maximum shell thickness of about 10 pc. We modeled carbon stars with mass loss occurring on time scales from 10^2 to 10^6 yr. If $R \gg r_0$, the opacity may be written as

$$\tau(\lambda) \approx \langle Q(\lambda)\pi a^2 \rangle n_0 r_0. \quad (3)$$

Assuming a gas-to-dust ratio (by mass) of β , a dust grain of mass m_d , and a constant outflow velocity of v , we can express the total mass-loss rate as

$$\dot{M} = (\beta + 1)\dot{M}_d \approx \beta \dot{M}_d = \beta 4\pi r^2 (dr/dt) (m_d n_0 r_0^2 r^{-2}) \\ = \beta 4\pi v m_d n_0 r_0^2. \quad (4)$$

Expressing $n_0 r_0$ in terms of \dot{M} and substituting into (3) for $\tau(\lambda)$ yields

$$\tau(\lambda) = \langle Q(\lambda)\pi a^2 \rangle \dot{M} (4\pi \beta m_d r_0 v)^{-1} = C_\lambda \dot{M} (r_0 v)^{-1}, \quad (5)$$

where $C_\lambda = \langle Q(\lambda)\pi a^2 \rangle (4\pi \beta m_d)^{-1}$. Using the above expression one can relate models with different shell opacities to stars with different mass-loss rates by an appropriate choice of β , v , and m_d . Note that our model results (e.g., energy spectrum) depend only on the form of the grain opacity and not on any assumptions for β , v , or m_d .

Most of the carbon stars in the LRS catalog lie within a couple of kpc of Earth (Claussen et al. 1987; Chan & Kwok 1988; Jura & Kleinmann 1989, 1990). To determine the importance of emission from intervening interstellar dust as a component of the 100 μ m flux, we modeled carbon stars of various opacities surrounded by 1 kpc of dust, assuming an extinction of one visual magnitude per kpc. The interstellar material was modeled as constant density dust beyond the C-rich dust shell. This approach neglects the patchy nature of the infrared cirrus, but the effect of cirrus should be negligible as shown in § 4. To simulate the flux measured by IRAS, the emergent intensity was convolved with a flat beam pattern having a beam size equal in area to that of the IRAS detectors.

To reproduce the 60 μ m flux of visual carbon stars, Willems has shown that two mass-loss episodes separated by 10^4 yr are needed. In general we expect the 12 and 25 μ m emission to be produced mainly by dust at temperatures greater than 100 K, such as those found in the inner dust shell, while the bulk of the 60 and 100 μ m flux will be produced by dust in the outer regions, at temperatures of 40 and 20 K, respectively. Consequently the 100/60 μ m flux ratio depends on the geometric thickness of the remnant shell since this will determine the

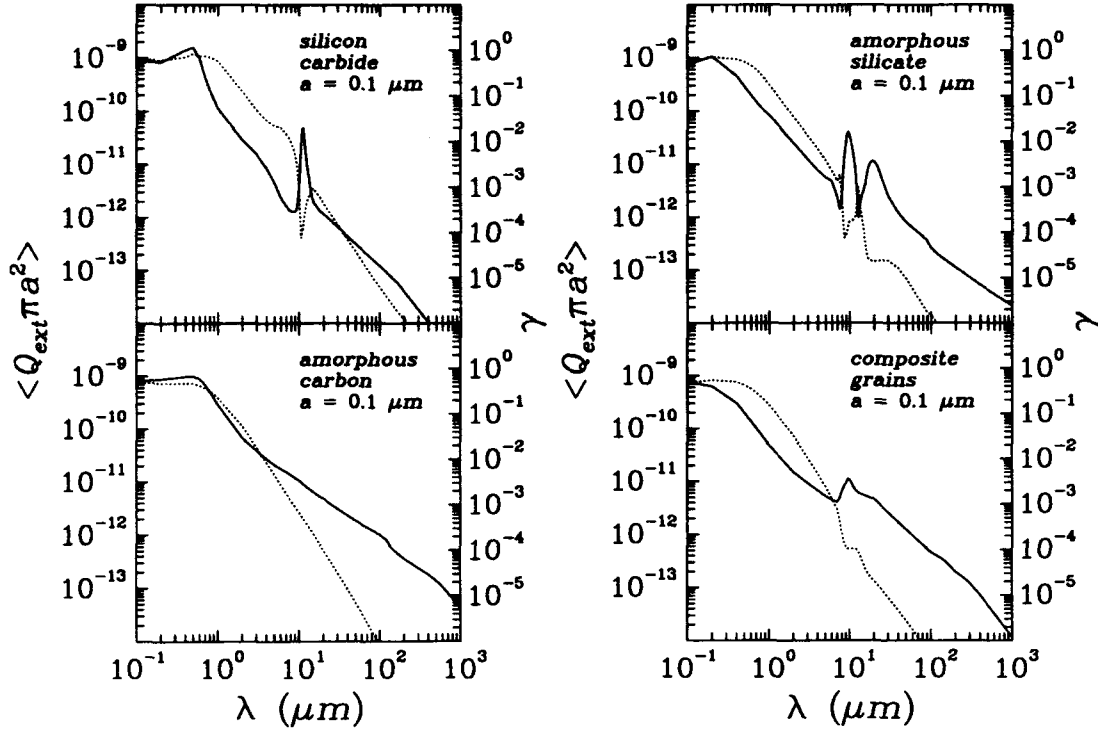


FIG. 2.—Extinction cross section ($\langle Q_{\text{ext}} \rangle \pi a^2$, solid line) and albedo (γ , dotted line) plotted as a function of wavelength for the various grain types used in the models: (a) silicon carbide (SiC) grains, (b) amorphous carbon grains, (c) amorphous silicate grains, and (d) composite grains (silicate, graphite, and amorphous carbon conglomerates).

relative amounts of dust at 20 K to that at 40 K. To determine this thickness and hence the lifetime of the first mass-loss episode, we have modeled two-shell systems in which the remnant shells have thicknesses of 0.1, 1, and 10 pc, corresponding to mass-loss durations of 10^4 , 10^5 , and 10^6 yr. In all three cases we have assumed that the remnant shell had an optical depth of 26 (corresponding to $\dot{M} \approx 10^{-6} M_{\odot} \text{ yr}^{-1}$) at the cessation of mass loss. Expansion of the remnant shell dilutes the dust density and hence the opacity of the shell. For example, if a dust shell with an inner radius of r_0 becomes detached and expands for t_{exp} yr, and then expands for another t_c yr during a C-rich phase of mass loss, the inner radius of the remnant shell will be

$$r'_0 = r_0 + v(t_{\text{exp}} + t_c). \quad (6)$$

Likewise, if the initial phase of mass loss had lasted t_r yr, resulting in a shell of geometrical thickness $(R - r_0)$, the outer radius of the remnant shell will be

$$R' = r_0 + v(t_r + t_{\text{exp}} + t_c). \quad (7)$$

Since the dust density distribution is still following an inverse square law (assuming a constant outflow), mass conservation in the dust shell implies that $n'_0(r'_0)^2 = n_0 r_0^2$ and the opacity of the remnant shell becomes (from eq. [2])

$$\tau'(\lambda) = \langle Q(\lambda) \pi a^2 \rangle n_0 r_0^2 [(r'_0)^{-1} - (R')^{-1}]. \quad (8)$$

Equations (2) and (8) lead to

$$\frac{\tau'(\lambda)}{\tau(\lambda)} = \frac{[(r'_0)^{-1} - (R')^{-1}]}{[(r_0)^{-1} - (R)^{-1}]} \quad (9)$$

Using this result we find that after $t_{\text{exp}} = 10^4$ yr and $t_c = 10^3$ yr the optical depth for remnant shells of 0.1, 1.0, and 10 pc in

thickness becomes 7×10^{-3} , 1.4×10^{-2} , and 1.5×10^{-2} , respectively. For these two-shell models the inner C-rich dust shell had a geometrical thickness of 0.01 pc and the same grain opacities as in the single-shell models described above. Because the scenario proposed by Willems allows for carbon star lifetimes (i.e., t_c in our models) of up to 3×10^4 yr (de Jong 1989), we also modeled shells for which $t_c = 100$ and $t_c = 10^4$ yr. To see if it is possible to determine the composition of the remnant shell we have constructed models with amorphous silicate grains or amorphous carbon grains in the remnant shell. To construct the two-shell models emergent intensities and flux results from the output of the single-dust shell models were used as boundary conditions for the inner edge of the second dust shell.

4. RESULTS AND DISCUSSION

4.1. Analysis of Color-Color Diagrams

As shown in Figure 3, the single-shell models of visual carbon stars do not extend very far into region I on the 12-25-60 μm color-color diagram. This can be understood by noting that for all t_c , the temperature at the inner radius of the dust shell is about 1200 K corresponding to the condensation temperature of the dust. However, the temperature at the outer radius, $T(R)$, of the dust shell depends on R and hence on t_c . For $t_c = 10^2$, 10^3 , and 10^4 yr, $T(R) \approx 280$, 100, and 50 K, respectively. If $t_c \geq 10^5$ yr, $T(R) \approx 20$ K. The increase of 60/25 μm flux ratio with shell thickness is due to the presence of more cool dust in the geometrically thicker dust shells. Extending t_c beyond 10^4 yr adds only a very small amount of cool dust ($T < 40$ K) to the shell and little additional 60 μm flux is produced in these extended dust shells, while the 100 μm flux is somewhat enhanced. Thus the 60/25 μm flux ratio approaches a limiting value as shown in Figure 3.

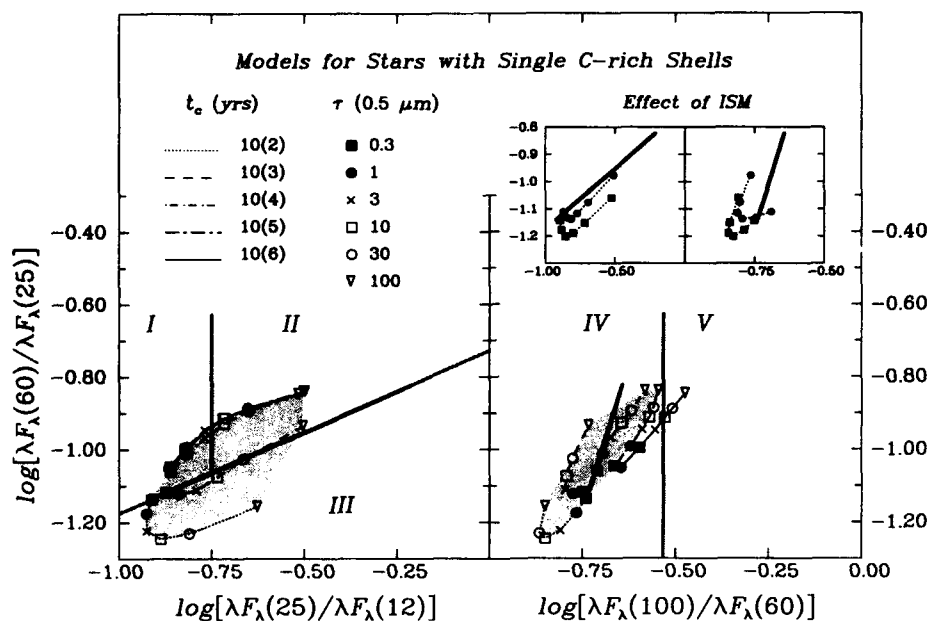


FIG. 3.—Color-color diagrams for model carbon stars with a single dust shell. Thick solid line is the blackbody line. Symbols signify the opacity of the dust shell at $0.5 \mu\text{m}$. For each series of models with increasing opacity (or mass-loss rate) the parameter t_c represents the time since the onset of C-rich mass loss. Models with $t_c \geq 10^4$ yr have very similar tracks on the 12-25-60 μm color-color diagram. The gray-shaded area is for models with blue spectra, corresponding to those single-shell models with spectral energy distributions consistent with the sample stars. Note that regions I and V are practically unoccupied, in disagreement with observations. Inset portion of the figure shows the effect of dust emission from the intervening interstellar medium (assuming a distance of 1 kpc) on models with $t_c = 10^3$ yr. Filled circles represent models with the ISM taken into account; filled squares are those without ISM. Colors are slightly different from those in the main figure due to beam convolution effects.

Further disagreement with observation can be seen in the 25-60-100 μm color-color diagram. Here the least extended shells do not correspond to any observation, and models with thicker dust shells match the observed 100 μm flux of less than 30% of visual carbon stars. It must also be pointed out that between 7 and 25 μm the flux spectra from those models corresponding to $t_c \geq 10^5$ yr would be classified as *red* under the classifications in the *IRAS* Explanatory Supplement and thus do not correspond to any of the observed data shown in Figure

1. In Figure 3 we have shaded the area occupied by models with blue spectra, corresponding to those single-shell models with spectral energy distributions consistent with the sample stars. This result supports the scenario, proposed by Willems, in which the lifetime of the carbon star phase is 3×10^4 yr (de Jong 1989). It is important to note that the single-shell models have 60/25 μm and 100/60 μm flux ratios which increase with shell opacity, while the observations indicate that carbon stars with the lowest shell opacity should have the highest flux ratios.

The inset in Figure 3 shows that the excess 100 μm flux cannot be explained by emission from interstellar grains. At a distance of 1 kpc, even models with the lowest shell opacity show only minor enhancement in 100 μm flux. Increasing the distance to 5 kpc increases the 100 μm flux by only a few percent and cannot extend the model colors into region V. We conclude that emission from the intervening ISM cannot account for the large excess flux observed at 100 μm . The effect of the infrared cirrus on the 100 μm flux from carbon stars has also been examined. Figure 4 shows a plot of 100-60 μm color versus the *IRAS* cirrus flags, CIRR1 and CIRR2. CIRR1 denotes the number of 100 μm only sources (cirrus) within an $\frac{1}{2}^\circ$ by $\frac{1}{2}^\circ$ box centered on the source, while CIRR2 compares the "cirrus flux" (the spatially filtered sky brightness) to the source flux at 100 μm (Beichman et al. 1985). For CIRR1 > 3, or CIRR2 > 5, there may be contamination of the 100 μm data by cirrus. However, as shown in Figure 4, the amount of cirrus contamination does not seem to affect the 100-60 μm color of the sources. Examination of individual sources shows as wide a range of colors for sources with CIRR1 ≤ 3 as for CIRR ≥ 4 , and likewise for CIRR2 ≤ 5 and CIRR2 ≥ 6 . Fitting a line to the mean of the colors for each cirrus bin, we find that the slope (m) is virtually flat [$m(\text{CIRR1}) = 0.0021 \pm 0.021$; $m(\text{CIRR2}) = 0.021 \pm 0.023$], indicating that the presence of

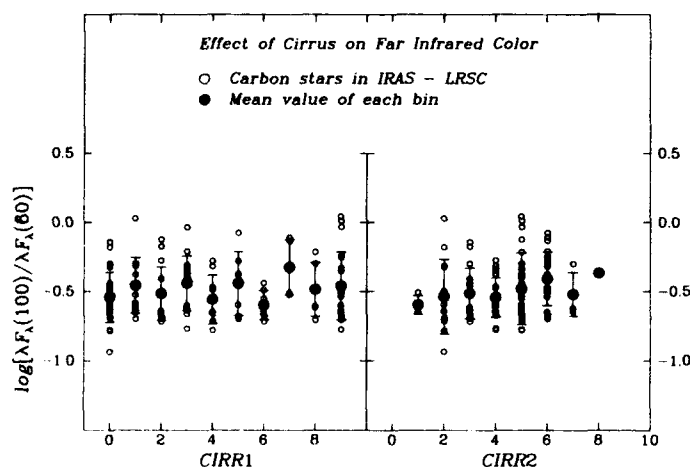


FIG. 4.—Plot of 100-60 μm color vs. *IRAS* cirrus flags, CIRR1 (left panel) and CIRR2 (right panel), for the sample carbon stars. Probable contamination of the 100 μm flux by infrared cirrus occurs when CIRR1 ≥ 4 or CIRR2 ≥ 6 . In each plot the sources are binned by cirrus flag value, and the mean of each bin is also shown (large filled dot). Error bars for the mean are 1 standard deviation from the mean. Note that there is essentially no increase in 100 μm flux with the amount of cirrus near the source.

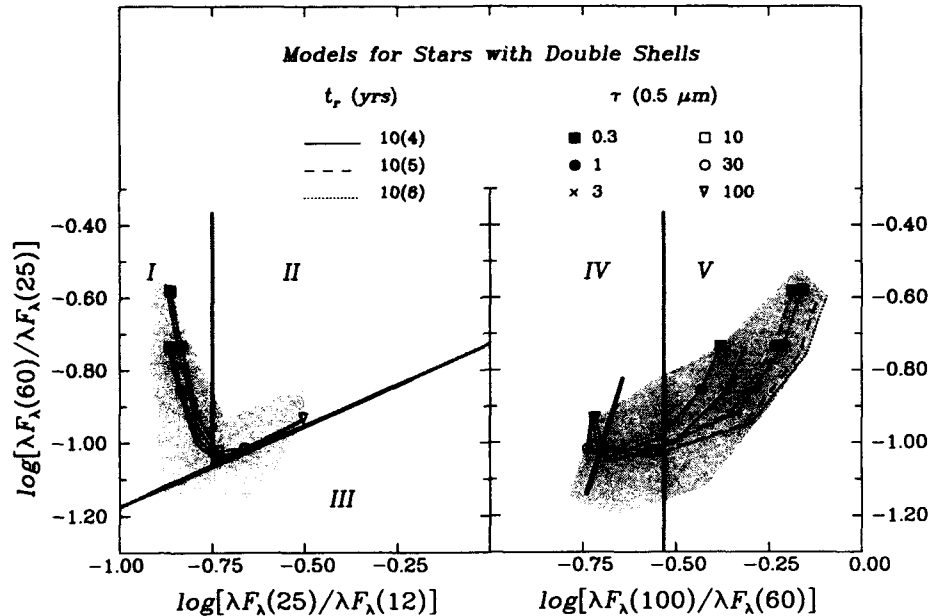


FIG. 5.—Color-color diagrams for model carbon stars with double shells. The thick solid line is the blackbody line. The symbols signify the opacity at $0.5 \mu\text{m}$ of the inner C-rich shell. For each series of models with increasing opacity (or mass-loss rate) the parameter t_r represents the duration of the mass-loss phase which formed the remnant shell. Tracks with symbols are for models with O-rich remnant shells, those without symbols correspond to C-rich shells. All remnant shells are 0.1 pc from the inner shell. The geometric thickness of the remnant shells scales linearly with t_r (e.g., $t_r = 10^4 \text{ yr}$ corresponds to 0.1 pc). The gray-shaded area indicates the limits on the colors for carbon stars of various ages imposed by these models. Note that the two-shell models place the visual carbon stars in regions I and V of the figure, in agreement with observations as shown in Fig. 1.

infrared cirrus is not a major factor in determining the 100-60 μm color of carbon stars.

To explain the colors of most visual and IR carbon stars, a two-shell model with a geometric thickness of at least 1 pc for the remnant shell is required. As seen in Figure 5, models with remnant shells thinner than this have too much flux at 25 and $60 \mu\text{m}$, and not enough $100 \mu\text{m}$ flux. A thicker remnant shell (cf. models with a 10 pc thick remnant shells) increases the $100 \mu\text{m}$ flux slightly, with almost no change in the 12, 25, or $60 \mu\text{m}$ fluxes. The dust temperatures in the remnant shell with $t_{\text{gap}} = 10^4 \text{ yr}$ range from about 45 K at the inner radius to 20 K at the outer radius. This results in a much greater total flux at 60 and $100 \mu\text{m}$ as compared to single-shell models because the much larger dust mass in the remnant shell emits mainly at wavelengths longer than $60 \mu\text{m}$. Varying the geometric extent of the inner dust shell will change somewhat the 60/25 μm flux ratio of the two-shell models because the inner dust shell may also contribute some $60 \mu\text{m}$ flux as discussed above. In terms of the late stages of stellar evolution, these models suggest that at least two distinct mass-loss episodes are required to explain the colors of most carbon stars, with the first episode lasting about 10^3 yr .

The dependence of dust temperature on its location in the dust shell can also be used to explain the anomalous 100-60 μm color of the carbon star IRC +10216 (IRAS 09452+1330) which has a 100-60 μm color of -0.93 , much smaller than the rest of the stars in the sample. This star is quite nearby, at a distance between 130 pc (Jura & Kleinmann 1989) and 290 pc (Claussen et al. 1987). According to our two-shell models, the diameter of the source should be greater than two parsecs, corresponding to an angular diameter on the sky of over $34''$, if a distance to the source of 200 pc is assumed. The IRAS $100 \mu\text{m}$ detectors are only $3' \times 5'$, and thus will miss most of the dust mass emitting in the far-infrared. On the other hand, since most of the emission shortward of $60 \mu\text{m}$ comes from within

0.1 pc in radius of the central star, one can get a fairly accurate measurement of these fluxes using detectors with similar beam sizes. Models in which the source has been placed within 300 pc and then convolved with an IRAS equivalent beam also show that the $100 \mu\text{m}$ flux is underreported in such sources. Thus the unusual far-infrared color of IRC +10216 can be readily explained.

On the basis of the far-infrared color alone, we cannot conclusively determine the grain composition in the remnant shell since the colors of both O-rich and C-rich remnant shells are quite similar. This is probably due to the fact that dust grains in both the O-rich and C-rich remnant shells are assumed to be amorphous, so that both have opacity proportional to λ^{-1} in the far-infrared. The C-rich remnant does show slightly more $100 \mu\text{m}$ flux than the O-rich remnant and is in better agreement with the observations. A mechanism for producing a C-rich remnant shell by helium flashing of carbon stars has been proposed (Olofsson et al. 1990). By allowing the C-rich remnant shell to dissipate, this temporary termination of mass loss would also alleviate the problems of the red spectrum and lifetime as noted above. In principle it should be possible to determine the dust composition in the remnant shells by exploiting the probable difference in emissivity at long wavelengths of C-rich and O-rich dust. However, the lack of laboratory-measured optical constants in the very far-IR for silicates and amorphous carbon makes this difficult at the present time.

4.2. Distances and Mass-Loss Rates

Of the 104 carbon stars with SiC emission in our sample, we have estimates of the distance to 48 (Claussen et al. 1987; Skinner & Whitmore 1988). Using this data it is possible to perform various checks on the results presented above.

First, we can use the distance to the source and the 100-60 μm color to determine if the flux excesses at long wavelengths

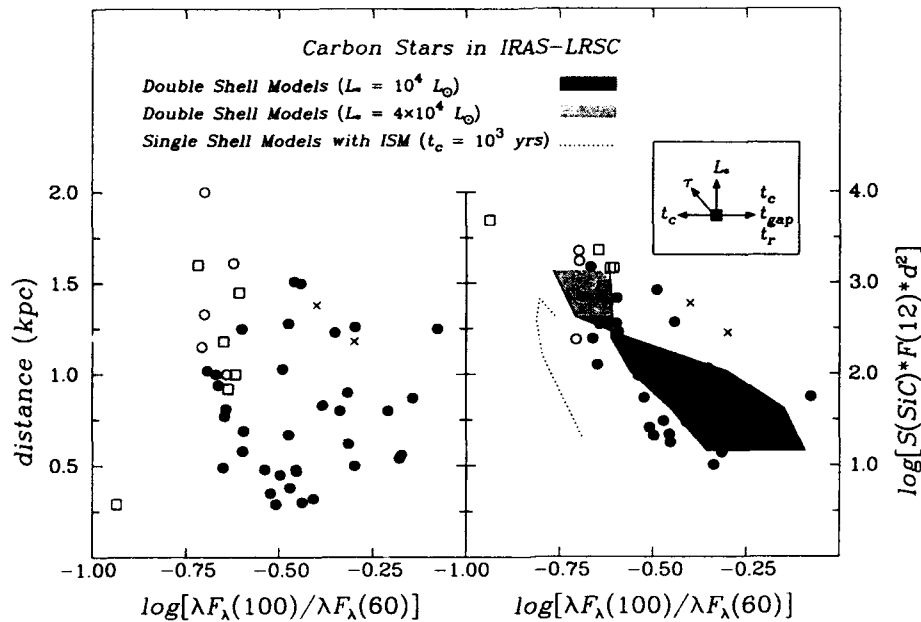


FIG. 6.—Plots of distance (left panel) and $S(\text{SiC})F(12 \mu\text{m})d^2$ (Jy kpc²) (right panel) vs. 100-60 μm color. Symbols are the same as those in Fig. 1. Left panel shows that there is no correlation between source distance and the 100/60 μm flux ratio. In the right panel the dotted line shows results of single-shell models with $t_c = 10^3$ yr, $L_* = 10^4 L_\odot$. Shaded area is the region bounded by two-shell models with $t_c = 10^3$ yr, $t_{\text{gap}} = 10^4$ yr, $t_r = 10^6$ yr and $t_c = 10^4$ yr, $t_{\text{gap}} = 10^3$ yr, $t_r = 10^4$ yr. Here t_{gap} is time scale on which mass loss does not occur. Note that to correctly model high mass-loss rates the models in which $\tau(0.5 \mu\text{m}) = 100$ have luminosities of $L_* = 4 \times 10^4 L_\odot$. Note also that the two-shell models agree with the observed measures of mass loss and long-wavelength color, while the single-shell models do not. Inset indicates the direction a model point would move as the value of a given parameter is increased.

are solely due to the intervening ISM or infrared cirrus. If this were the case, the 100/60 μm flux ratio would increase with distance to the source (amount of intervening material). An examination of Figure 6a, which is a plot of source distance and flux ratio, shows that this is clearly not the case.

Second, we can have an independent check on the two-shell hypothesis. From the two-shell models we know that both the 60/25 and 100/60 μm flux ratios decrease as the opacity of the inner shell (and hence the "current" mass-loss rate) is increased. For models in which the inner shell has a higher opacity, the dust in the remnant shell constitutes a much smaller fraction of the total circumstellar dust, and the far-infrared colors of these sources will be similar to those of single shell sources. On the color-color plots this effect appears to reduce the 60/25 and 100/60 μm flux ratios. The opacities of the IRAS sources are roughly known, that is, fairly small if it is in the GCCCS or in region I, larger if it lies in regions II or III. While the models are apparently consistent with the observations under this classification, a better test of the two-shell model could be made if the actual opacities of the sources were known. Skinner & Whitmore (1988) have shown that the quantity $S(\text{SiC})F(12 \mu\text{m})d^2$ is proportional to the total mass-loss rate of the star. Here $S(\text{SiC})$ is the strength of the SiC feature above the continuum as computed in the IRAS Explanatory Supplement, $F_\lambda(12 \mu\text{m})$ is the IRAS flux at 12 μm , and d is the distance to the source. Plotting this quantity versus the 100/60 μm flux ratio (Fig. 6b), we find that the observations agree with the prediction of the models in that this flux ratio decreases as the mass-loss rate (opacity) increases. Furthermore, from the model flux spectrum we can calculate the quantity $S(\text{SiC})F(12 \mu\text{m})d^2$ for each model and compare the results directly with the IRAS observations. One should note that, consistent with theories of mass loss, higher luminosities are required to produce higher values of $SF d^2$ [by raising the value of $F_\lambda(12$

$\mu\text{m})$]. From our models, we find that at a given opacity and within the luminosity values used, the luminosity is not a major factor in determining the infrared color of the source.

The inset of Figure 6b shows qualitatively how increasing a given model parameter changes the model's position on the plot. Enhancing the luminosity simply raises the value of $SF d^2$. An inner shell with a higher opacity has more hot dust, which increases $SF d^2$ and reduces the 100/60 μm flux ratio. The parameters t_{gap} and t_r determine the ratio of 100 μm to 60 μm emission from the remnant shell. As either t_{gap} or t_r increases, so does the proportion of very cool (20 K) dust in the remnant shell. Thus the 100-60 μm color increases with these two parameters. The value of $SF d^2$ is unchanged because the remnant shell has no hot dust so there is little emission at wavelengths shortward of 60 μm . The geometric thickness of the inner shell, parameterized by t_c , plays a more complicated role. Like t_{gap} and t_r , it does not affect the value of $SF d^2$. However, depending on the opacity of the inner shell, it will either increase or decrease the 100-60 μm color. As noted above, two-shell models with inner shells of very high opacity have colors similar to their single-shell counterparts. Single-shell models with $t_c = 10^4$ yr have more cool dust (and hence higher 100/60 μm flux ratios) and those with $t_c = 10^3$ yr. Therefore the 100-60 μm color will increase with t_c for models with high opacities. For optically thin sources, the remnant shell is the dominant source of 100 μm flux. Since increasing t_c produces more cool dust in the inner shell (and hence more 60 μm flux) the 100/60 μm flux ratio is decreased. This dual effect of t_c produces the crossover of the tracks from the two sets of models in the figure.

Figure 6b indicates that some stars with fairly high mass-loss rates are included in the GCCCS (probably observed in the near-IR rather than the visible). This fact explains the location of the 14 GCCCS stars in region IV of Figure 1, making it

possible to reconcile them with the two-shell model. Of the GCCCS stars for which we have $SF d^2$ data, eight are listed as having high mass-loss rates by Jura & Kleinmann (1989, 1990). These eight (02270–2619, 03229+4721, 08416–2525, 10249–2517, 12447+0425, 20396+4757, 21032–0024, and 21320+3850) have values of $SF d^2 > 2.5$, indicating they have high mass-loss rates. Figure 6b shows that, over a reasonable range of model parameters, single-shell models have too little 100 μm flux and cannot reproduce the observations whereas two-shell models can. This rules out any scenario in which AGB stars undergo a transition from type M to S to C with continuous dusty mass loss. The time scale for which the models require no dust formation (10^3 – 10^4 yr) is consistent with the hypotheses of both Willems and Olofsson. However, our model results indicate that at least 10^4 yr of O-rich mass loss must precede the carbon star phase (to avoid the formation of single-shell carbon stars), and that the O-rich dust shell must become detached about 10^4 yr before the onset of C-rich mass loss. These requirements are consistent with the predictions of Willems's model. We also note that the remnant shell modeled here may actually be made up of several detached shells, due to several thermal pulse events.

5. CONCLUSIONS

By comparing our radiation transport models of dust shells around carbon stars with *IRAS* observations, we arrive at the following conclusions:

1. Carbon stars with a single continuous dust shell are incompatible with observations for the following reasons:

(a) Models with a single dust shell cannot reproduce the 60 and 100 μm fluxes observed for visual carbon stars in our sample, even after extending the dust shells to the maximum extent allowed by the carbon star lifetime.

(b) Those single-shell models with long-wavelength colors compatible with some *IRAS* carbon stars have long wavelength color increasing in the wrong sense with shell opacity.

(c) Analysis of mass-loss rates together with the long wavelength colors also indicate that carbon stars with a continuous single dust shell are not present.

(d) Theories on the evolution of carbon stars, which predict a single continuous dust shell, require lifetimes for

carbon stars of about 10^6 yr. However, a carbon star lifetime of $\geq 10^5$ yr produces a dust shell which would have a red *IRAS*-LRS spectrum. Such sources are not found in this sample.

2. Emission from dust in the intervening interstellar medium cannot account for the large discrepancy between single-shell models and the observations. It is also apparent that the infrared cirrus is not a major contributor to the 100 μm flux of carbon stars.

3. Two-shell models can adequately account for the distribution of carbon stars in all five regions of the 12–25–60 μm and 25–60–100 μm color-color diagrams.

4. The mass-loss episode forming the remnant shell must have ended about 10^4 yr before the onset of the next episode. To produce the observed 100 μm flux, the geometric thickness of the remnant shell should be about 1 pc and at a distance of 0.1 pc from the inner dust shell.

5. On the basis of the color-color diagrams alone, we cannot distinguish between Willems's theory (on the evolution of O-rich stars to form carbon stars) and the scenario proposed by Olofsson et al. (1990), since either C-rich or O-rich dust in the remnant shell will produce the observed colors. It is possible that the remnant shell is composed of multiple remnants of both C-rich and O-rich material.

6. Mass-loss calculations, together with *IRAS* flux ratios, indicate that a remnant dust shell is required to produce the observed relationship between mass-loss and the flux ratio. The time scale for the gap between mass-loss episodes, plus the fact that previous episodes of mass loss must have been O-rich (by all evolutionary models and to avoid having a single-shell object), both argue in favor of Willems's model.

We would like to thank Sun Kwok of the University of Calgary for his hospitality during our stay in Calgary while C. M. L. was on sabbatical leave from Rensselaer in 1988, and for allowing us to access the *IRAS*-LRS database at Calgary. This research has been partially supported by NASA under grant NAGW-1103 and by the Air Force under grant AFOSR 89-104. We also thank the referee for a thorough review and for making numerous suggestions to improve the presentation.

REFERENCES

- Chan, S. J. 1988, M.S. thesis, Univ. Calgary
 Chan, S. J., & Kwok, S. 1988, *ApJ*, 334, 362
 ———. 1990, *A&A*, 237, 354
 Clausen, M. J., Kleinmann, S. G., Joyce, R. R., & Jura, M. 1987, *ApJS*, 65, 385
 Day, K. L. 1979, *ApJ*, 234, 158
 ———. 1981, *ApJ*, 246, 110
 de Jong, T. 1989, *A&A*, 223, L23
 Egan, M. P., Leung, C. M., & Spagna, G. F. 1988, *Comput. Phys. Comm.*, 48, 271
 Iben, I., & Renzini, A. 1983, *ARA&A*, 21, 271
IRAS Catalogs and Atlases: Explanatory Supplement. 1985, ed. C. A. Beichman, G. Neugebauer, H. J. Habing, P. E. Clegg, & T. J. Chester (Washington: GPO)
 Jura, M. 1987, *ApJ*, 313, 743
 Jura, M., & Kleinmann, S. G. 1989, *ApJ*, 341, 359
 ———. 1990, *ApJ*, 364, 663
 Leung, C. M. 1975, 199, 340
 ———. 1976, *J. Quant. Spectrosc. Rad. Transf.*, 16, 559
 Little-Marenin, I. R. 1986, *ApJ*, 307, L15
 Mathis, J., & Whiffen, G. 1989, *ApJ*, 341, 808
 Olofsson, H., Carlstrom, U., Eriksson, K., Gustafsson, B., & Willson, L. A. 1990, *A&A*, 230, L13
 Pegourie, B. 1988, *A&A*, 194, 335
 Skinner, C. J., & Whitmore, B. 1988, *MNRAS*, 234, 79P
 Stephenson, C. B. 1973, *A General Catalogue of Cool Carbon Stars*, Publ. Warner & Swasey Obs., 1, No. 4 (GCCCS)
 Thronson, H. A., Latter, W. B., Black, J. H., Bally, J., & Hacking, P. 1987, *ApJ*, 322, 770
 Willems, F. J. 1987, Ph.D. thesis, Universiteit van Amsterdam
 ———. 1988, *A&A*, 203, 51
 Willems, F. J., & de Jong, T. 1986, *ApJ*, 309, L39
 ———. 1988, *A&A*, 196, 173
 Zuckerman, B., & Maddalena, R. J. 1989, *A&A*, 223, L20

RADIATION TRANSPORT IN DUST IN DISK GEOMETRY. I. APPLICATION TO EXTERNALLY HEATED INTERSTELLAR CLOUDS

GEORGE F. SPAGNA, JR.,^{1,2} CHUN MING LEUNG,^{1,3,4} AND MICHAEL P. EGAN^{1,3,4}

Received 1989 November 28; accepted 1991 April 2

ABSTRACT

The problem of radiation transport is solved numerically for both one-dimensional spherical and two-dimensional disk geometries, to determine self-consistently the dust temperature distribution and the infrared energy spectrum of disk-shaped interstellar dust clouds which are heated externally by the ambient interstellar radiation field. The effects of source geometry (disk versus sphere, varying degree of disk flattening) and cloud opacity on the dust temperature distribution, radiation field anisotropy, and infrared energy spectrum are studied. It is found that the equilibrium grain temperature is *not* extremely sensitive to the cloud geometry or degree of disk flattening. Compared to a spherical model of the same opacity, a similar disk model (of the same radius R and half-thickness Z) shows a nearly identical temperature distribution and emergent flux spectrum. However, we find that the internal radiation in the far-infrared is more anisotropic in disk models and is predominantly radially streaming. The emergent infrared flux for unresolved disks is not a sensitive function of the viewing angle, since radiation anisotropy and geometric projection effect essentially cancel each other. Estimates of dust mass based on observed flux may be uncertain by as much as a factor of 2 or 3, if spherical geometry is incorrectly assumed. The ratio of observed flux at 200 and 1.2 μm may be used as an indicator of disk geometry for unresolved clouds.

Subject headings: infrared: spectra — interstellar: grains — nebulae: general — radiative transfer

1. INTRODUCTION

Both the thermodynamics and evolution of many astronomical objects are affected by the presence of dust grains. The presence of dust in circumstellar shells around evolved stars, in interstellar molecular clouds, and in nuclei of some galaxies is well established from observations in the infrared. Since thermal emission by dust is believed to be the dominant mechanism for producing the infrared radiation, any interpretation of infrared observations based on modeling of the sources will invariably involve studies of radiation transport through dust. Although there is growing observational and theoretical evidence for a large number of disk-shaped or toroidal objects of astrophysical interest (e.g., circumstellar disks, protoplanetary disks, protostellar accretion disks, bipolar molecular flows, and disk galaxies), the majority of radiative transfer models currently in use invoke the assumption of spherical geometry. This assumption is made because spherically symmetric geometry is the only one-dimensional geometry which accounts for the finite dimensions of a system in all directions. A key theoretical problem not addressed by existing models of radiation transport in dust is the geometry of the infrared source. Establishing the source geometry can provide severe constraints on the origin, dynamics, and properties of the infrared sources. Hence it is crucial to solve the problem of radiation transport in a dusty medium with two-dimensional disk geometry and apply the results to interpreting infrared observations.

Progress toward the solution of multidimensional transport problems has been largely concerned with two-dimensional planar geometry. Literature on multidimensional transfer cal-

culations has been reviewed by Jones & Skumanich (1980). A few attempts have been made to solve the problem of scattering, absorption, and emission by dust grains in a medium with nonspherical geometry. Lefevre, Daniel, & Bergeat (1983) have performed Monte Carlo simulations of ellipsoidal dust shells around cool stars, while Ghosh & Tandon (1985) calculated dust temperature distributions in cylindrical clouds with embedded stars. The latter work has been extended by Dent (1988) to calculate the temperature distribution and energy spectrum of circumstellar disks around young stars. In this paper we consider radiation transport in disk-shaped interstellar clouds which are heated externally by the ambient interstellar radiation field (ISRF), for example, isolated dark globules (Leung 1985).

Recently we generalized the "quasi-diffusion" method developed by Leung (1975, 1976) for spherical geometry to solve the problem of scattering, absorption, and reemission by dust grains in a medium of disk geometry (Spagna 1986; Spagna & Leung 1987). Using this technique and realistic grain opacities we construct theoretical models to determine self-consistently the dust temperature distribution and infrared emission from disk-shaped, quiescent dark globules heated externally by the ISRF. We address three key questions here: (1) Given the ubiquitous nature of disk-shaped objects resulting from the collapse of cool, dusty molecular clouds, what is the effect of the underlying disk geometry on the observable properties of the dust cloud? (2) How does cloud geometry affect the dust temperature distribution? (3) How does the energy spectrum depend on the degree of flattening of the disk, and on the angle at which the disk is observed?

The outline of this paper is as follows. In § 2 the method of solving the radiation transport problem in two-dimensional disk geometry is described, and the model parameters are given. Section 3 contains a discussion of the numerical results regarding the effects of cloud geometry (e.g., disk versus sphere and varying degree of disk flattening) on the dust temperature

¹ Department of Physics, Rensselaer Polytechnic Institute, Troy, NY 12180-3590.

² Department of Physics, Randolph-Macon College, Ashland, VA 23005.

³ Also Department of Physics, University of Calgary.

⁴ Also Canadian Institute for Theoretical Astrophysics.

distribution, the angular distribution of the internal radiation field, and the infrared energy spectrum. The observational implications are considered in § 4. Finally, in § 5 we summarize the main conclusions of the paper and plan for future work. The relevant equations used in solving the radiation transport problem for disk geometry are given in Appendix A, while Appendix B contains analytic expressions for the opacity and mass of clouds with a Gaussian density distribution, for both spherical and disk geometries. These equations and expressions are used in discussions throughout the paper.

2. METHOD OF SOLUTION AND MODEL PARAMETERS

2.1. Basic Equations and Method of Solution

To construct cloud models with disk geometry, we used the quasi-diffusion method (QDM) developed by Spagna & Leung (1987) to solve the radiation transport problem for a dusty medium with two-dimensional geometry. In this method the zeroth and first moment equations of radiation transport are combined and cast into quasi-diffusion form by introducing a set of auxiliary functions. The first set of functions, called anisotropy factors, forms the elements of the anisotropy tensor (also called the Eddington tensor in the literature of stellar atmospheres) and measures the anisotropy of the radiation field. The second is the configuration function which depends on an integral involving the anisotropy factors. By first assuming the radiation field to be isotropic (diffusion approximation), we initially fix the anisotropy factors and the configuration function. We then linearize and solve the coupled nonlinear system of moment and energy balance equations using the Newton-Raphson iteration method to estimate the mean intensity and the dust temperature distribution, that is, the source function. From the source function, we solve for the angular distribution of the radiation field by a ray-tracing technique and use the solution to update the anisotropy factors and the configuration function. This iteration procedure is repeated until the solution converges. Physically the success of the QDM rests upon the fact that the dust temperature distribution depends strongly on the radiation energy density and only weakly on the radiation field anisotropy, thus allowing the problem to be separated into two distinct steps: solution of the moment and energy-balance equations for a given radiation field anisotropy, followed by solution of the ray equations to determine the angular distribution of the radiation field for a given source function.

To describe the two-dimensional disk geometry, we use cylindrical coordinates (r, z, θ, ϕ) to define an element ds at some point (r, z) along a photon trajectory in the disk. The polar angle made with the figure (symmetry) axis is θ , while the azimuthal angle to the outward radial direction is ϕ , as shown in Figure 1. Since the equations of the QDM for disk geometry have been derived and the numerical method discussed elsewhere (Spagna & Leung 1987), here we shall only summarize in Appendix A the basic equations and boundary conditions relevant for externally heated cloud models. To construct models with one-dimensional spherical geometry, we used the radiative-transfer code developed by Leung (1975, 1976) and documented by Spagna & Leung (1983), and recently updated by Egan, Leung, & Spagna (1988) to include other one-dimensional geometries (plane-parallel and cylindrical).

2.2. Assumptions and Model Parameters

The basic assumptions are much the same as those of Leung (1975), and Spencer & Leung (1978). We consider static clouds

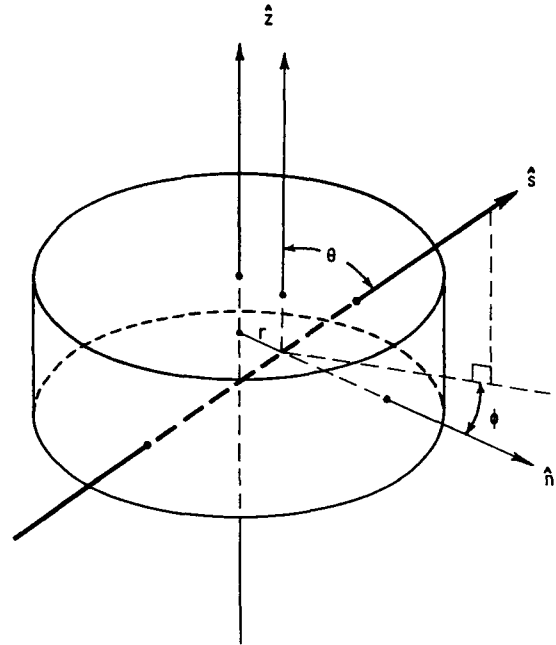


FIG. 1.—Direction of photon propagation, denoted by s , and its relation to the spatial (r, z) and angular (θ, ϕ) variables in disk geometry.

with spherical or disk geometry and without internal heat source. We take into account the anisotropy of the internal radiation field and assume isotropic scattering. In determining the dust temperature distribution, the thermal coupling between gas and dust through collisions is ignored since it is found to be insignificant at the typical gas and dust densities of dark globules (Leung 1975).

For models with disk geometry, since most (over 99%) of the computing effort is taken up by the solution of the ray equations to determine the radiation field anisotropy, we have assumed the diffusion approximation in calculating the dust temperature distribution. This is a reasonable assumption for externally heated models (Leung 1975) since the temperature does not depend strongly on the angular distribution of the radiation field and the ambient radiation field is assumed to be isotropic. From the converged solution of the dust temperature distribution we then solve the ray equations at selected wavelengths to determine the emergent intensities and infrared flux spectrum. Comparison with a fully self-consistent solution indicates that, for externally heated clouds, the dust temperature distribution is affected only slightly (typically by a few percent), with a somewhat greater effect on the flux spectrum. To be consistent, this approach is used in constructing models for both spherical and disk geometries.

2.2.1. Interstellar Radiation Field (ISRF)

Values for the ISRF in the solar neighborhood (most globules that have been studied are within 500 pc from the Sun) are taken from the model of Mathis, Mezger, & Panagia (1983), which takes into account recent surveys of Galactic emission. In their model four components comprise the stellar contribution to the ISRF, to which we have added the cosmic microwave background at a temperature of 2.9 K. The spectral region in our computations extends from the Lyman edge at 912 Å in the UV to 5000 μm in the microwave region. The incident ISRF is assumed to be isotropic.

2.2.2. Dust Density Distribution

Observations based on star-counting techniques (Tomita, Saito, & Ohtani 1979) indicate that the dust in dark globules is centrally condensed. For our models we assumed a Gaussian dust density distribution,

$$n(x) = n_c \exp[-\ln(n_c/n_s)x^2], \quad (1)$$

where n_c is the dust density at the cloud center [$n_c \equiv n(0)$], n_s is the density at the surface [$n_s \equiv n(1)$], $x \equiv r/R$ for spherical models, and $x^2 \equiv (r^2 + z^2)/R^2$ for disk models. In our study, the ratio ($\rho_{cs} \equiv n_c/n_s$) varies from 1 to 500. For all the models reported here a value of 100 was adopted. The disk models all have the same radius as the spherical models, taken to be 1 pc. For both spherical and disk models we define τ_o to be the total optical depth to the cloud center at the visible wavelength of $0.55 \mu\text{m}$. For disk models, τ_o is measured in the midplane. In the models described here τ_o ranges from 5 to 500. The disk models are further characterized by an aspect ratio (ratio of disk radius to half-thickness, $R:Z$) which ranges from 1:1 to 10:1.

2.2.3. Grain Opacities

The actual composition of dust grains in dark globules is not known, although it might be similar to that in the interstellar medium. Mathis, Rumpl, & Nordsieck (1977) modeled the interstellar dust with a mixture of graphite and silicate grains, each with a power-law distribution of sizes. Recently this model has been superseded by one in which the proposed interstellar grains are collections of very small individual particles of silicates, amorphous carbon, and graphite, bonded together into a loose aggregate (Mathis & Whiffen 1989). The model grains include a substantial proportion of vacuum along with solid particles. These composite grains are assumed to have a power-law distribution of sizes. Although this latest model reproduced reasonably well the observed features of the interstellar extinction curve (especially at short wavelengths), it failed poorly when used as a grain model for dark globules, in that for any reasonable cloud opacity (e.g., $\tau_o = 5-100$) the calculated far-infrared spectrum is too broad and peaks at a wavelength ($\geq 340 \mu\text{m}$) too long compared to the observed value of $200 \mu\text{m}$ (Keene 1981). Since the composition of dust grains in dark globules is uncertain and the purpose of this study is to examine the physics of radiation transport in disk geometry (rather than the effects of grain composition), we have adopted the following model for grain opacities. The extinction coefficients are assumed to have a wavelength dependence obeying an inverse power law ($\propto \lambda^{-\beta}$). The constants of proportionality are determined by matching the opacities with those of graphite grains (of radius $0.05 \mu\text{m}$) at $\lambda = 200 \mu\text{m}$ for the absorption component and $\lambda = 2.2 \mu\text{m}$ for the scattering component. A different choice of constants will only produce a different scaling of the cloud opacities. The exponent β is chosen to be 1.5 so that for models with $\tau_o = 5-100$, the overall shape of the calculated spectrum in the far-infrared agrees reasonably well with observations of dark globules (e.g., the emission peak occurs at around $200 \mu\text{m}$).

In our models we have ignored the possible presence of small grains since their temperatures are determined by nonequilibrium processes (Draine & Anderson 1985), rather than by thermal equilibrium as in the case of the larger grains. More importantly, the nonequilibrium emission of these grains, which are thought to be polycyclic aromatic hydrocarbons (PAHs) (Puget, Leger, & Boulanger 1985), occurs mostly at

short wavelengths ($10-30 \mu\text{m}$) and hence is not expected to contribute significantly to the far-infrared emission of globules. In any event, we are mostly interested in the effects of source geometry on the transport of radiation rather than on the details of grain emission and absorption.

3. DISCUSSION OF NUMERICAL RESULTS

To study the effects of radiation transport in two-dimensional disk geometry and how source geometry affects the observables, we have calculated two sets of models: one-dimensional models with spherical geometry and two-dimensional disk models with varying aspect ratios of 1:1, 3:1, and 10:1. In both sets of models, we used $n_c/n_s = 100$ and assumed the same radius of 1 pc. In our discussion below, we will first compare a 1:1 disk model with one of spherical geometry. One expects the 1:1 disk model to most closely mimic the spherical case, especially when the dust density distribution is centrally condensed. Then we will study the effects of disk flattening by considering disk models of larger aspect ratios.

3.1. Grain Temperature Distributions

The physics of grain heating and dust temperature distribution in externally heated dark globules has been explored in detail by Leung (1975). Here we briefly summarize the major results. The regions of the dark cloud where different heating mechanisms dominate may be characterized by the parameters τ_1 and τ_2 . The first of these represents the optical depth of penetration by UV and optical photons from the ISRF; the second the limit of penetration by all but the extreme infrared. Due to the increased shielding from UV and optical photons, the dust temperature falls monotonically as the cloud optical depth is increased. For optically thin clouds and in the outer parts of opaque clouds ($\tau \lesssim \tau_1$), the heating is mainly by the attenuated and scattered components of starlight in the UV and visible. Scattering processes dominate absorptions in the UV where the grain albedo approaches unity. In the interior of moderately opaque clouds ($\tau_1 < \tau < \tau_2$), where few photons in the UV and visible can penetrate, the grains are heated mainly by the near-infrared component of starlight. In addition, the thermal radiation emitted by grains at the outer parts of the cloud becomes significant as a heating mechanism. Finally in the central regions of extremely opaque clouds ($\tau > \tau_2$), practically all starlight, including the near-infrared component, is shielded from the cloud interior. Here only the far-infrared component of the ISRF and the thermal radiation from outer grains can penetrate. In addition to this, the thermal radiation from neighboring grains contribute to the heating, and the grain temperature approaches a limiting value. Our study indicates that, roughly independent of geometry, typically $\tau_1 \sim 5-10$ and $\tau_2 \sim 100-500$ depending on the grain composition. Due to their high albedo in the UV and visible as well as their high emissivity in the infrared, dielectric grains (e.g., silicate and ice) in general attain a lower temperature than graphite grains for a given τ_o . Using our grain opacity law, for a spherical cloud model with $\tau_o = 50$, the dust temperature decreases from ~ 24 K near the cloud surface to ~ 7 K at the cloud center. The total variation in grain temperature from the cloud surface to the center of the most opaque clouds is about a factor of 4-5, roughly independent of the grain model chosen.

In Figure 2 we plot the dust temperature distributions along the symmetry axis and along the midplane for a 1:1 disk model, and compare them with that of the spherical model

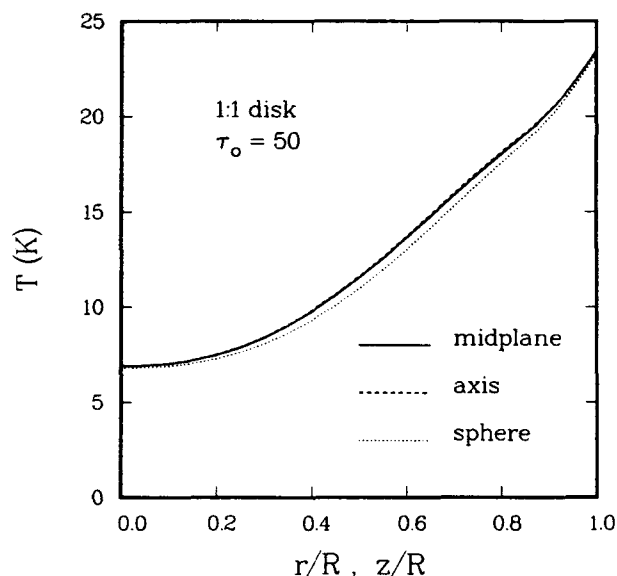


FIG. 2.—Comparison of dust temperature distributions in spherical and 1:1 disk models of the same central optical depth ($\tau_o = 50$). For the disk model, except for the slightly warmer dust at the “corners” of the disk, the overall temperature distribution remains remarkably spherically symmetric.

($\tau_o = 50$ in both models). It is clear that the radial and axial temperature distributions are virtually indistinguishable, indicating that the overall temperature distribution in the disk model remains remarkably spherically symmetric. Although the dust temperature distributions in both geometries are very similar, the temperature in the spherical case is generally somewhat lower (though by only a very small amount). We attribute this to the different effects of radiation field anisotropy in the two geometries. We also note that the dust in the edge region of the disk model is warmest, due to the shorter optical path-lengths in these regions. This edge effect has important significance in both the anisotropy of the internal radiation field and the emergent flux spectrum, as discussed below.

To study the effect of disk flattening on the temperature distribution, we compare in Figure 3 the temperature distribution for three disk models of increasing aspect ratio. First, we note that the midplane temperature distribution in the 3:1 disk model is virtually identical to that of the 1:1 disk. Jones & Skumanich (1980) argue that for a multidimensional medium, the “dominant” geometry governing the radiative transfer for a given point will be the geometry of the nearest surface. This seems not to be the case, as the planar surfaces for the disk are closer to the central parts of the midplane than the disk edge, yet they seem to have little effect on the temperature of the dust. The optical depth along the z -direction is still sufficiently high ($\tau > 20$ at $0.55 \mu\text{m}$) to keep the midplane points from communicating effectively with the disk face. The surface temperature at the center of the disk face is lower than at the rim, but the temperature gradient along the symmetry axis is steeper than along the midplane. This is because the grains at the curved edge are exposed to the external radiation from a greater solid angle than are points near the center of the planar disk face. The similarity in the midplane temperature distribution between 1:1 and 3:1 disks persists even in models with $\tau_o = 5$.

For the 10:1 disk model, the midplane temperature distribution is no longer the same as in the less flattened disks, imply-

ing that for this degree of flattening, the planar surfaces are able to effectively communicate with the midplane, and the overall temperature of the model is higher. Thus only when the optical depth along a given direction is low enough will the geometry in that direction control the overall radiation transport process. The overall dust temperature in the 10:1 disk is higher than that in either the 1:1 or 3:1 disks because the smaller opacity (by a factor of 10) along the symmetry axis allows easier penetration of heating photons. The previously noted trend, that grains close to the curved surface of the disk are warmer than those near the planar disk face, continues.

3.2. Anisotropy of Internal Radiation Field

The angular distribution of the internal radiation field is best described by the anisotropy factors. In one-dimensional spherical geometry with azimuthal symmetry, there is only one anisotropy factor, $f \equiv K/J$, where K is the second angular moment of the specific intensity I . It can be shown that $f \rightarrow 1$ if the radiation field is forward peaking (or radially streaming), $f \rightarrow 0$ if radiation is sideward peaking, and $f = \frac{1}{3}$ for isotropic radiation. In a general three-dimensional geometry, there are nine anisotropy factors, each proportional to the corresponding nine elements of the radiation pressure tensor. Of these only four are of interest in the two-dimensional disk geometry: f_{rr} , f_{zz} , $f_{\phi\phi}$, and f_{rz} (see eq. [A10] in Appendix A for definition). The first three (corresponding to the diagonal elements in the radiation pressure tensor) measure the degree of anisotropy in the respective orthogonal directions in the local coordinate system. It can be shown (Levermore 1984) that in general the sum $f_{rr} + f_{zz} + f_{\phi\phi} = 1$. Furthermore, for a completely isotropic radiation field (diffusion approximation), $f_{rr} = f_{zz} = f_{\phi\phi} = \frac{1}{3}$, and $f_{rz} = 0$. For radiation streaming along a given direction, the conjugate anisotropy factor will exceed the value of $\frac{1}{3}$ and approach unity. When radiation is peaking sideward relative to a given direction, the conjugate anisotropy factor

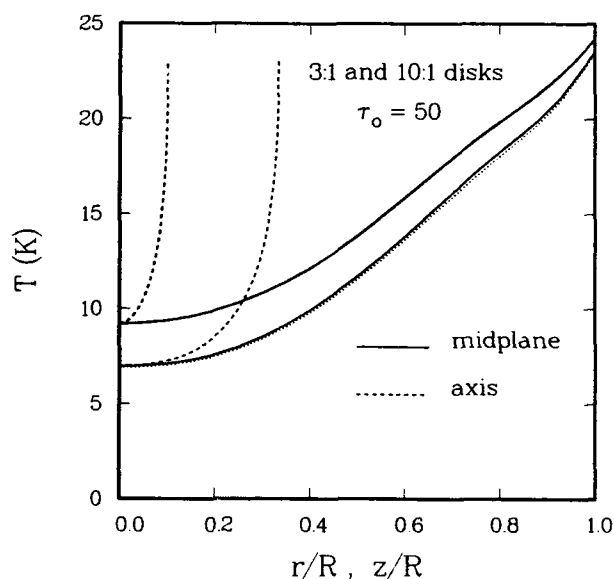


FIG. 3.—Comparison of dust temperature distributions in disk models of different aspect ratios but same τ_o . The upper set of curves is for the 10:1 disk model, while the lower set is for the 3:1 disk model. Note that for the 3:1 disk, the midplane temperature distribution is virtually identical to that of the 1:1 disk (denoted by the dotted curve). Overall dust temperature in the 10:1 disk is higher than that in either the 1:1 or 3:1 disks.

TABLE 1

PROPERTIES OF ANISOTROPY FACTORS IN DISK AND SPHERICAL GEOMETRIES

Radiation Field	Anisotropy Factors
Isotropic	$f_r = f_{zz} = f_{\phi\phi} = \frac{1}{3}, f_{rz} = 0; f = \frac{1}{3}$
Radially streaming	$\frac{1}{3} < f_r \rightarrow 1, 0 \leftarrow (f_{zz}, f_{\phi\phi}) < \frac{1}{3}, f_{rz} \geq 0; \frac{1}{3} < f \rightarrow 1$
Axially streaming or sideward peaking ...	$\frac{1}{3} < f_{zz} \rightarrow 1, 0 \leftarrow (f_r, f_{\phi\phi}) < \frac{1}{3}, f_{rz} \geq 0; 0 \leftarrow f < \frac{1}{3}$
Anisotropic	$f_r + f_{zz} + f_{\phi\phi} = 1, f_{rz} \neq 0; 0 < f < 1$

drops below $\frac{1}{3}$ and approaches zero. For the extreme cases of complete isotropy and of radiation streaming either radially or axially, $f_{rz} = 0$, but for an anisotropic radiation field, f_{rz} is nonzero in general. The behavior of the anisotropy factors under various conditions in the two geometries is summarized in Table 1.

The internal radiation field may deviate substantially from isotropy. In general, the angular distribution of the radiation field reflects the spatial variation of the source function, which depends on both density and temperature. However, since the dust temperature depends only on the mean intensity J and is also rather insensitive to changes in J , the effect of radiation field anisotropy is negligible on the grain temperature.

In Figure 4 we compare the radial anisotropy factor (f_r) and the axial anisotropy factor (f_{zz}) to the anisotropy factor (f) for the spherical model at $200 \mu\text{m}$ which corresponds to the wavelength of peak grain emission in the far-infrared. At this wavelength the spherical anisotropy factor remains close to its isotropic value of $\frac{1}{3}$ in the inner half of the cloud radius, deviating from $\frac{1}{3}$ toward the cloud surface. For the disk model, the radiation field along the symmetry axis tends to peak axially

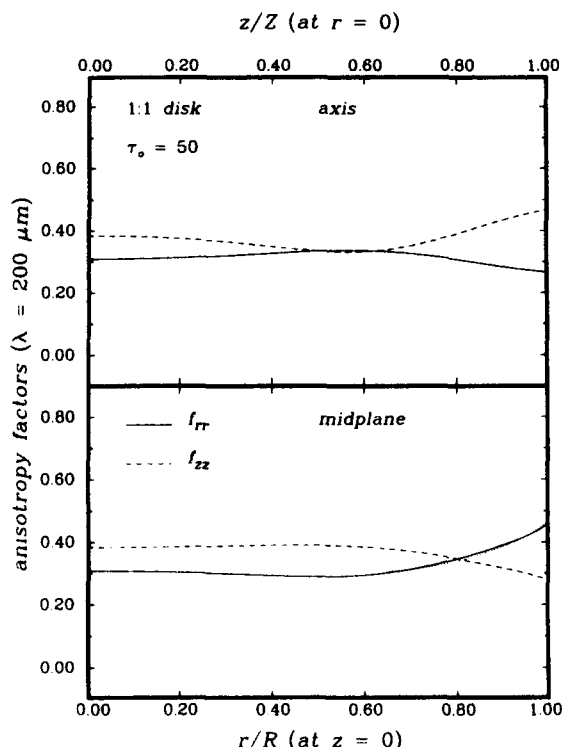


FIG. 4.—Behavior of the anisotropy factors (f_r and f_{zz}) at $200 \mu\text{m}$ along the symmetry axis (upper panel) and the midplane (lower panel) for the 1:1 disk model. Corresponding anisotropy factor for the spherical model is also plotted (dotted curve).

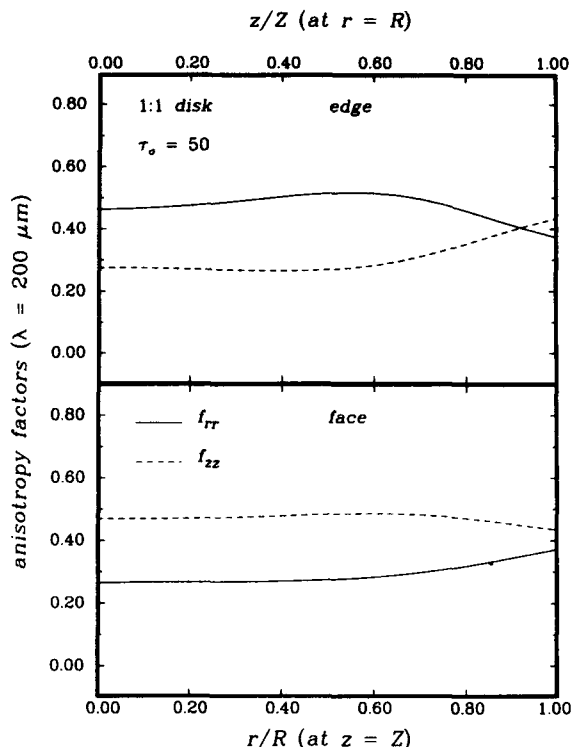


FIG. 5.—Behavior of the anisotropy factors (f_r and f_{zz}) at $200 \mu\text{m}$ along the disk edge (upper panel) and on the disk face (lower panel) for the 1:1 disk model. Along the disk curved surface, the radiation streams radially close to the midplane and becomes more axial near the disk edge. On the disk face, the radiation peaks axially at all r , but it shows an enhanced radial component near the edge.

(see upper panel of Fig. 4). In the midplane region of the disk model, f_{zz} is predominantly greater than $\frac{1}{3}$ while f_r is less than $\frac{1}{3}$ for most of the cloud volume, indicating that the radiation field is peaked along the axial direction. Our model results indicate that as the degree of disk flattening increases, the radial peaking of the radiation field is enhanced both in the midplane and along the symmetry axis. The axial streaming near the disk face is suppressed, eventually being dominated by the radial streaming.

To gain some insight into the effect of radiation field anisotropy on the observed surface brightness of the disk model in the far-infrared, we show in Figure 5 the variation of the two anisotropy factors (at $200 \mu\text{m}$), f_r and f_{zz} , for points on the planar disk face ($r, z = Z$) and on the curved side surface ($r = R, z$) of a 1:1 disk. We see that on the curved surface at $r = R$, radiation close to the midplane ($z/Z \rightarrow 0$) streams radially ($f_r > \frac{1}{3}$) and becomes more nearly isotropic as one moves away from the midplane and toward the disk face ($z/Z \rightarrow 1$). However, we note that f_r is never less than $\frac{1}{3}$ at the disk edge, and that f_{zz} becomes greater than $\frac{1}{3}$ as we approach the disk face. This suggests that radiation moving tangent to the disk edge will be predominantly parallel to the midplane near $z = 0$, and parallel to the axis near the disk face. In either case, this should make itself apparent as limb darkening when the disk is seen nearly edge-on. On the planar face of the disk ($z = Z$), radiation peaks strongly in the axial direction for all $r < R$. Only very near the edge does f_r rise above $\frac{1}{3}$ as well. This combination suggests that limb darkening should not be especially pronounced for such disks viewed nearly face-on. For disk models of higher aspect ratios, the radial streaming of the

radiation field become much more pronounced. From these results we expect that for a disk-shaped cloud heated externally, there should be no significant variations in overall brightness in the far-infrared when it is observed at different angles. This expectation is intuitively correct because the disks are optically thin to radiation at this wavelength, and it is confirmed by the calculated flux spectrum, as discussed below. Analysis of the radiation field anisotropy suggests that the enhanced radial streaming with increased aspect ratio essentially compensates for the reduced solid angle presented to the observer as one takes a nearly edge-on view of disks which are progressively flatter. Finally, we note that, at wavelengths in the visible and near-infrared, axial streaming of radiation is the predominant behavior, especially for highly flattened disks.

3.3. Emergent Flux and Energy Spectrum

To understand the effects of source geometry on the energy spectrum, we first study the results from spherical cloud models. Figure 6 shows the calculated flux spectra for a series of spherical cloud models with increasing optical depths (see Appendix A for the definition of the quantity $D^2\mathcal{F}$). As the cloud opacity τ_o increases, the grain temperature decreases, which causes the emergent flux spectrum to peak further into the far-infrared. For example, for $\tau_o = 50$, the peak flux occurs at around $200\ \mu\text{m}$. Furthermore, one notes the broadening of the emission to longer wavelengths as τ_o is increased. This is due to the emission from the cooler dust toward the cloud center. Recall that the cloud is optically thin in the far-infrared, so that at these wavelengths we are sampling the entire cloud in its emergent flux, not just the surface regions. The total thermal emission also increases with τ_o because the total dust mass increases with τ_o and more of the ambient ISRF is absorbed and reradiated. In general the peak flux is most strongly related to the mass of the warmest dust, which for optically thick clouds lies near the surface. Thus we expect that the variation in peak flux will be somewhat less as τ_o is increased, since there is relatively less warm dust near the

surface. This effect is noted when comparing the relative change in peak flux between $\tau_o = 5$ and 50, and between $\tau_o = 50$ and 500.

The effect of density gradient can be summarized as follows. For a given τ_o , a larger ρ_{cs} implies a smaller cloud mass (by roughly a factor of 3.5 between $\rho_{cs} = 100$ and $\rho_{cs} = 1$). Therefore, in a model with a density gradient, there is less total absorption of incident UV and optical photons, which results in a decrease in the total thermal emission. The emission peak, however, is slightly blueshifted because the ratio (by number density) of hot to cold dust is enhanced. Accordingly, the emergent flux profile is not a very useful observational tool for determining the presence of density gradients.

We now compare results for models with spherical and disk geometry. The dust temperature distributions in both geometries are very similar, and the emergent flux in the infrared for the disk model is found not to depend sensitively on the viewing angle. For clouds which are unresolved, one expects that the emergent flux spectrum should be characteristic only of the dust temperature and proportional to the mass of the radiating material. This expectation is reasonable, since the thermal emission is isotropic in the neighborhood of an emitting grain, and since the emission in the far-infrared is optically thin (see Appendix A for a more quantitative discussion). For isotropic radiation, one would then expect that, for an unresolved source, the emergent flux spectrum should be independent of viewing angle to the source, since the entire volume is sampled irrespective of viewing angle. Recall that even in the spherical models, the radiation does not remain isotropic. Even with complete spatial symmetry one sees a transition from isotropy to radial streaming as the surface is approached. The lack of complete spatial symmetry for disk models contributes even more to the anisotropy of the radiation field and to its variation from point to point, even at those wavelengths where the cloud is optically thin. If we consider the one-dimensional transport of radiation along a ray which passes through a cloud, then it is clear that all rays at a given impact parameter for a spherical cloud are equivalent. This is not the case for the disk-shaped clouds, where it is possible for rays at a given impact parameter to traverse widely diverse quantities of dust. Accordingly, we might not expect the emergent flux from a disk-shaped cloud to remain independent of the viewing angle unless the radiation field becomes anisotropic.

Figure 7 shows the infrared flux spectrum for a 1:1 disk model viewed at three different angles. For comparison, the flux spectrum of the spherical cloud model is also plotted. The brightness of the disk is virtually constant with viewing angle θ (angle between the disk axis and the line of sight to the observer). Since the far-infrared radiation is axially streaming (as pointed out in the previous section), the brightness of the disk seen face-on is the same as when the disk is observed edge-on, even though the disk presents a smaller solid angle. The flux is about 30% higher than the flux from the equivalent sphere although the mass of the disk is only 1.5% greater than that of the spherical model. The higher flux, the somewhat broader emission peak, and the slight shift of that peak to shorter wavelength are due to the additional dust mass lying near the "corners" of the disk, where the temperature is higher. Figure 8 is similar to Figure 7 but is for a disk model with a 3:1 aspect ratio. For the 3:1 model, the disk is still uniformly bright at all viewing angles. The $200\ \mu\text{m}$ flux is now 30% less than the value from the equivalent sphere; coincidentally, the actual dust mass is 30% less in the 3:1 disk model. Figure 9

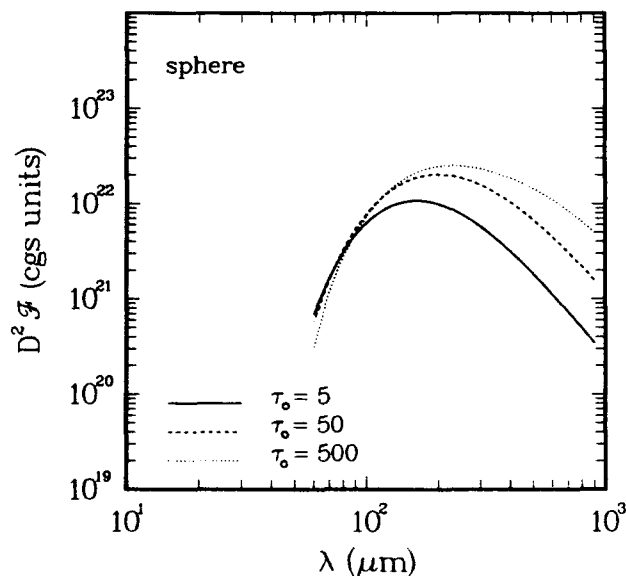


FIG. 6.—Variation of flux spectrum with central optical depth (τ_o) for a set of spherical cloud models. As τ_o increases, the shape of the flux spectrum becomes broader, and the emission peak also shifts toward longer wavelengths because of the presence of more cool dust.

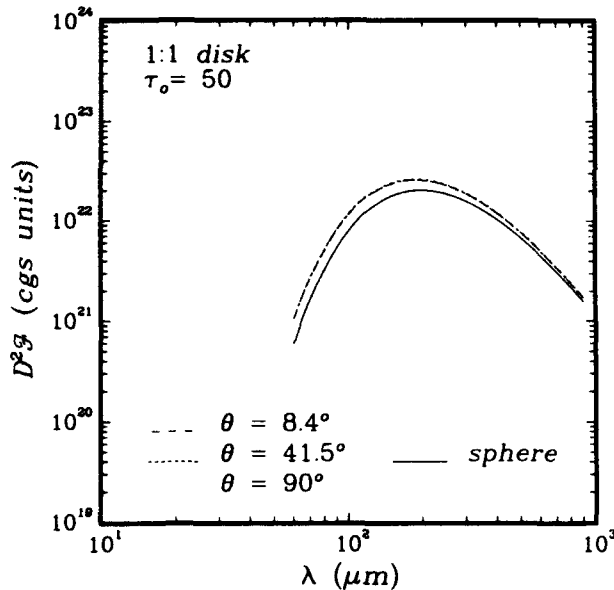


FIG. 7.—Comparison of flux spectra for spherical and 1:1 disk models of the same optical depth ($\tau_0 = 50$). Flux profile for the disk model is nearly independent of the viewing angle θ and is approximately 30% greater than that for the spherical model, although the mass is only 1.5% greater.

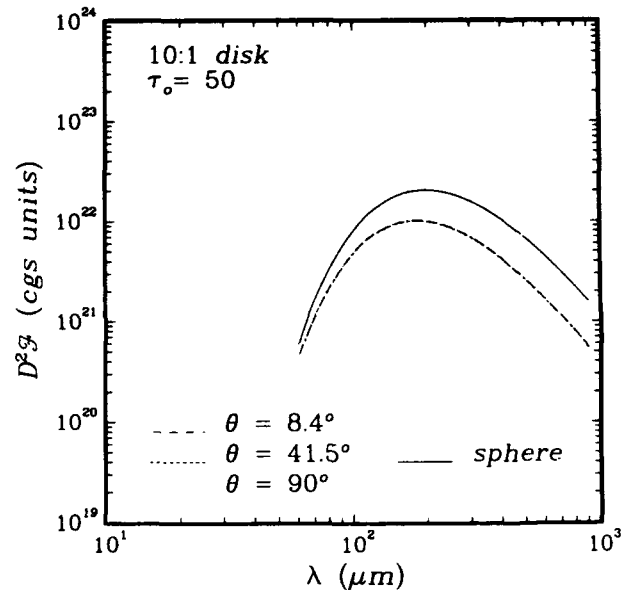


FIG. 9.—Comparison of flux spectra for spherical and 10:1 disk models of the same optical depth ($\tau_0 = 50$). Flux is approximately half that for the spherical model, although the mass is 24% of the spherical model.

shows the calculated flux spectrum for a 10:1 disk model. Like the 1:1 and 3:1 disks, the 10:1 disk shows no appreciable differences in brightness with viewing angle. The peak flux is about 50% that of the equivalent sphere, while the dust mass in the disk model is only 24% that of the spherical cloud. This may again be explained by the greater mass of warm dust in the 3:1 and 10:1 models, even though their total mass is less.

Taken together, these results seem to support the previous expectation that radiation anisotropy in disks compensates for changes in projected area when observed at different angles, since the radial streaming of radiation in the far-infrared increases with aspect ratio. There are essentially two contribu-

tions to possible variation in observed flux with viewing angle. The first is a purely geometric projection effect. For a disk of radius R , half-thickness Z , and having a uniform surface brightness, the observed flux as seen by an observer at distance D ($D \gg R$ or Z) depends on θ as (see eq. [A26] in Appendix A)

$$\mathcal{F}_{\text{disk}} \propto (\pi R^2 \cos \theta + 4RZ \sin \theta)/D^2. \quad (2)$$

This implies that for a disk with a 1:1 aspect ratio, the observed flux is larger seen edge-on than face-on, and it reaches a maximum when $\theta = 52^\circ$. Compared to a sphere with the same uniform surface brightness and radius, the ratio of observed fluxes for the two geometries is just given by the ratio of their projected areas as seen by the distant observer,

$$(\mathcal{F}_{\text{disk}}/\mathcal{F}_{\text{sphere}}) = (\pi R^2 \cos \theta + 4RZ \sin \theta)/\pi R^2, \quad (3)$$

which indicates that for $R = Z$, the flux from the disk exceeds that from the sphere for all viewing angles (by up to a factor of 1.62 at $\theta = 52^\circ$), except for the fortuitous case of face-on viewing. The second potential contribution to the variation comes from radiation field anisotropy which, as discussed above, significantly affects the surface brightness. The relative importance of these two contributions depends on such factors as the degree of disk flattening, the cloud optical depth, and the dust density distribution.

To differentiate between these two contributions, we show in the upper panel of Figure 10 the flux at the emission peak (200 μm) as a function of viewing angle for the three disk models of increasing aspect ratios. For comparison, we also plot the flux for the spherical model. It is clear from this figure that the 200 μm flux does not provide any reliable indicator that we are looking at a disk. Further, comparison of Figures 7–9 suggests that the infrared flux contains little information beyond the mass and temperature of the dust, and no information about cloud geometry. However, if the disk is optically thick, we expect observations to sample the surface regions preferentially, so that the flux would vary with angle in proportion to the projected area. Even this would probably not help, since

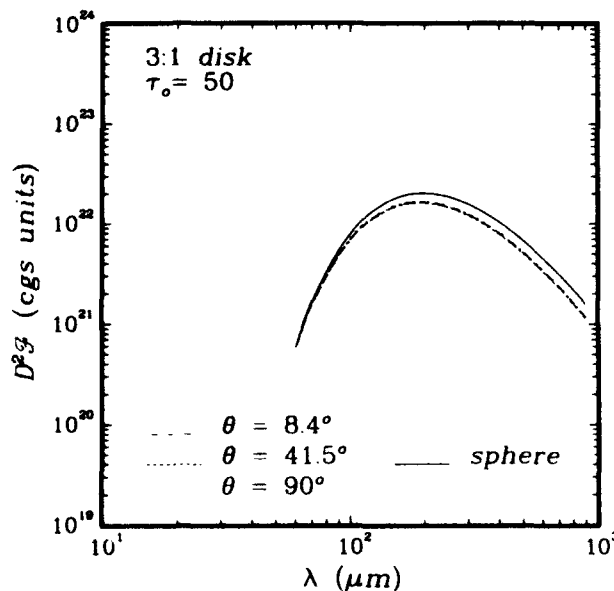


FIG. 8.—Comparison of flux spectra for spherical and 3:1 disk models of the same optical depth ($\tau_0 = 50$). Both the mass and the flux are approximately 30% less than that for the spherical model.

the shape and location of the emission peak is determined solely by the dust temperature. In the center panel of Figure 10 we show the inverse of the projected areas of sphere and disk models, that is, $(\pi R^2)^{-1}$ and $(\pi R^2 \cos \theta + 4RZ \sin \theta)^{-1}$, respectively, with $R = 1$ in all cases. The disk models are optically thick at short wavelengths, where the spectrum shows absorption rather than emission. To test whether the disk absorption could be used to determine the projected area of the disk, we calculated the absolute value of the ratio of the observed flux at $200 \mu\text{m}$, which we have shown to be independent of viewing angle, to the observed flux in absorption from the ISRF at $1.2 \mu\text{m}$, which we might expect to vary with the projected area. The bottom panel of Figure 10 shows the results, which have been normalized by the flux from a sphere, that is, $X^* \equiv X/(\pi R^2 X_{\text{sphere}})$, where $X \equiv |D^2 \mathcal{F}(200 \mu\text{m})/D^2 \mathcal{F}(1.2 \mu\text{m})|$, with $R = 1$ in all cases. The results mimic the shapes of the curves in the middle panel of Figure 10, which is expected if the absorption is proportional to projected area. In this figure we see an indication of a possible "disk signature" which could be used to determine the approximate aspect ratio and viewing angle of an unresolved, disk-shaped cloud which is heated externally.

We have concentrated our attention on the interpretation of the flux spectrum, rather than the details of the emergent intensity, since the question of source geometry is less difficult to answer for resolved sources. For a discussion of the emergent intensity variation for externally heated clouds, the reader is referred to Spagna & Leung (1985) for disk models and to Leung, O'Brien, & Dubisch (1989) for spherical models.

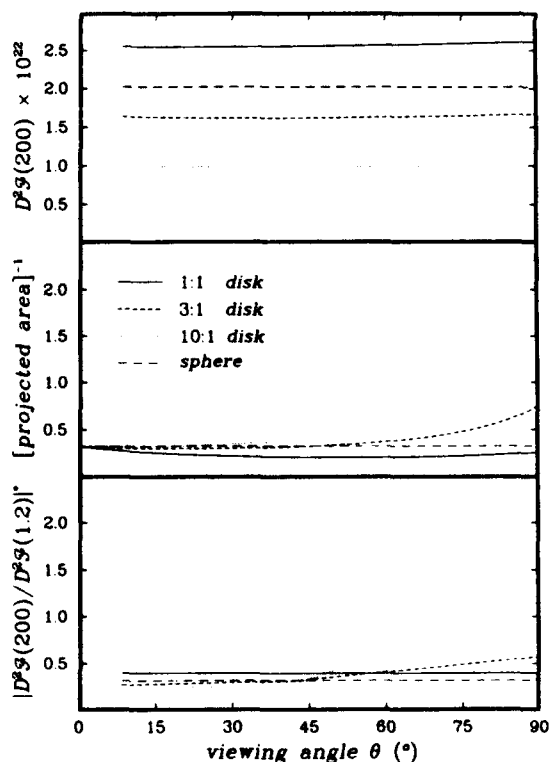


FIG. 10.—Top panel: Variation of flux at $200 \mu\text{m}$ with viewing angle θ for a sphere and a series of disk models of increasing aspect ratio. There is little variation in flux at different viewing angles. Middle panel: Normalized plot of inverse projected area of the disk and spherical models as a function of viewing angle. Bottom panel: Plot of the absolute value of the ratio of the flux at $200 \mu\text{m}$ (emission peak) to the flux at $1.2 \mu\text{m}$ (maximum absorption). The ratio is normalized by the flux ratio for a sphere.

3.4. Effects of Cloud Opacity

We ran a series of models with $\tau_o = 5, 50$, and 500 . All the models have $\rho_{cs} = 100$. Models with spherical and disk geometry were run. The effects of cloud opacity can be summarized as follows.

1.—The overall temperature distributions in both disk and spherical models decrease as the cloud opacity increases. The dust temperature in 1:1 disk models is generally higher (by at most a few percent) than that in the corresponding spherical model, the difference being larger for smaller τ_o . Similar to models with $\tau_o = 50$, the midplane temperature distributions in the 1:1 and 3:1 disk models are virtually identical for models with $\tau_o = 5$ or 500 . This implies that *only when the aspect ratio exceeds about 5:1 will the midplane temperature distribution deviate significantly from that in the 1:1 disk model.*

2.—At the wavelength of peak grain emission ($200 \mu\text{m}$), the internal radiation field becomes more isotropic as the cloud opacity increases, independent of the cloud geometry. For 1:1 disks only, the streaming of radiation along the symmetry axis is more pronounced for clouds of small τ_o . Near the cloud surface, the radiation is more anisotropic as τ_o increases, probably due to the steeper temperature gradient in the outer region when the cloud opacity increases. In particular, the radial streaming of radiation close to the cloud surface is enhanced as τ_o increases. On the other hand, at wavelengths in the visible (e.g., $0.55 \mu\text{m}$), the internal radiation field becomes more anisotropic as τ_o increases, due to the rapid decrease of energy density (fewer heating photons can penetrate into clouds of high opacity). Near the surface (within one photon mean free path), the radiation field at this wavelength is fairly isotropic, independent of τ_o , since the clouds are heated externally by the ambient ISRF.

3.—Independent of cloud geometry, the peak flux increases with cloud opacity. For disk models, the variation of flux with aspect ratio tends to become larger as τ_o increases.

4. OBSERVATIONAL IMPLICATIONS

From a conceptual standpoint, cloud models are best studied and parameterized in terms of the cloud opacity (τ_o), since τ_o controls the dust temperature distribution which in turn affects the emergent flux spectrum. From the point of view of interpreting infrared observations of dark globules, one is concerned with determining the cloud mass and dust temperature from the energy spectrum, and one would hope for some reliable "signature" which would enable at least a tentative indication of cloud geometry. A natural observational question to ask is: For an unresolved globule (externally heated by the ISRF) with disk geometry, what is the range in uncertainty in the estimates of dust mass if one incorrectly assumes that the source is a sphere? To answer this question, we must first study the relationship among the following quantities: infrared flux ($D^2 \mathcal{F}$), cloud opacity (τ_o), total dust mass (M_d), and dust temperature (T_d). To limit our consideration only to effects of source geometry and radiation transport, we assume here that we know the ISRF and the grain properties (i.e., composition, size, and extinction coefficients). First, consider the relationship between τ_o and M_d . One can easily show (see Appendix B) that for a given cloud configuration (fixed R , R/Z , and ρ_{cs}), the cloud opacity is a linear function of the total dust mass, that is, $\tau_o \propto M_d$. On the other hand, for fixed τ_o and ρ_{cs} , $M_d \propto R^2$ for spheres and $M_d \propto RZ/f(\gamma)$ for disks, $f(\gamma)$ being a slowly varying function of the aspect ratio $\gamma (\equiv R/Z)$. Likewise, for fixed M_d and ρ_{cs} , $\tau_o \propto R^{-2}$ for spheres and $\tau_o \propto f(\gamma)/RZ$ for disks. Next, consider the relationship between far-

infrared flux and cloud mass. For a cloud of *uniform density and temperature*, $D^2\mathcal{F} \propto M_d$, if the cloud is optically thin in the far-infrared (see Appendix A). Hence one might conclude that in the far-infrared, $D^2\mathcal{F} \propto M_d \propto \tau_c$. A close examination of Figure 6 indicates that this is *not* the case even for spherical geometry. Even at $1000\ \mu\text{m}$, the relationship between $D^2\mathcal{F}$ and τ_c is less than linear. Our results indicate that the same is true for spherical clouds of uniform density. This nonlinearity is due to the presence of a temperature gradient. The same situation applies to clouds of disk geometry (1:1 disks). Indeed, the incremental change in flux as τ_c increases is almost identical in the two geometries. Hence because of radiation transport effects which result in a temperature gradient, the far-infrared flux is not necessarily a very good indicator of either the cloud mass or cloud opacity, independent of the cloud geometry. Figure 7 also implies that if one naively applies the linear relationship $D^2\mathcal{F} \propto M_d \propto \tau_c$, then one could overestimate the mass of a 1:1 disk by about 30%. For a 10:1 disk, if one assumes spherical geometry in making the mass estimate, the cloud mass could be overestimated by nearly a factor of 2.

To summarize, we can say that one important observational consequence of the variation in emergent flux with aspect ratio is that it implies a large uncertainty in estimating the radiating dust mass. If spherical geometry is incorrectly assumed for an unresolved disk-shaped cloud, the estimated dust mass may easily be off by a factor of 2 or 3. In particular, one is likely to overestimate the mass of radiating dust for disks of large and small aspect ratios, with additional uncertainty because the aspect ratio itself cannot be determined from observations of the far-infrared flux. Hence due to the effects of cloud geometry and radiation transport, the estimate of dust mass (based on far-infrared fluxes) in unresolved clouds which are externally heated is fraught with uncertainties.

The second question, that of finding some disk "signature" in the observation of unresolved clouds, can be addressed once again by looking at the bottom panel of Figure 10. Here we display the absolute value of the ratio between the net flux at $200\ \mu\text{m}$, where the cloud is seen in emission, and the net flux at $1.2\ \mu\text{m}$, where the cloud is absorbing energy from the ambient radiation field. We see clearly that for disks viewed nearly face-on ($\theta < 45^\circ$) this ratio is less than its value for a sphere (0.3). For disks viewed nearly edge-on ($\theta \rightarrow 90^\circ$), this ratio is substantially greater than $\frac{1}{3}$, except for the 1:1 disk, which represents the least physically realistic model. This strongly suggests that one could identify externally heated disk-shaped clouds by comparing the (relatively easy) measurement of their far-infrared emission with the (relatively difficult) determination of their absorption in the near-infrared. It remains as a challenge to observers to test this result.

5. CONCLUSIONS AND FUTURE WORK

We now summarize the major conclusions of this paper as follows.

1.—The equilibrium grain temperature for externally heated clouds is *not* extremely sensitive to the cloud geometry or degree of disk flattening. Compared to a spherical model of the same optical depth, a 1:1 disk model shows a nearly identical temperature distribution. For disk models with aspect ratios higher than about 5:1, the central temperature is characteristic of the smallest optical depth in any direction.

2.—Compared to the spherical case, the internal radiation in the far-infrared of disk models is more anisotropic and is predominantly radially streaming for models with aspect ratios greater than 1. This radiation field anisotropy is more pronounced as the cloud opacity decreases.

3.—The observed infrared flux for unresolved disks is *not* a sensitive function of the viewing angle. Both the radiation field anisotropy and geometric projection effect contribute to keep the observed flux constant.

4.—The variation of observed flux with aspect ratio for disk models implies a large uncertainty in the estimated mass of the radiating dust. Hence even for simple sources with disk geometry, "What you see is *not* what you get"!

5.—A comparison of observed flux near the emission peak with that at the maximum absorption may be an indicator of disk geometry. It may be possible to estimate the aspect ratio and viewing angle from these observations.

The next step is to consider models with internal heat sources. This requires modest modifications in the computer code to incorporate the different boundary conditions. The effects of radiation field anisotropy and source geometry are expected to be even more important. Results from these internally heated models will be applied to the interpretation of infrared sources with disk geometry, for example, circumstellar disks, protostellar disks, and disk galaxies.

This research was partially supported by NASA under grants NAGW-577 and NAGW-1103, and under the *IRAS* Data Analysis Program (funded through the Jet Propulsion Laboratory), and by the Air Force under grant AFOSR-89-0104. G. F. S. acknowledges partial support of this research by the Thomas F. and Kate Miller Jeffress Memorial Trust. Important parts of this research were completed while C. M. L. was on sabbatical leave at the University of Calgary (UC) and at the Canadian Institute for Theoretical Astrophysics (CITA) in Canada. He is grateful to Scott Tremaine of CITA and Sun Kwok of UC for their hospitality and financial support. The authors also thank the staff (especially Beryl Lin) of the Supercomputing Service at UC and the Ontario Center for Large Scale Computation at the University of Toronto for their assistance and support. The authors thank an anonymous referee for insightful and constructive comments which led to a very significant improvement in this paper. Finally, they thank Steven D. Doty for his help in preparing Figure 11.

APPENDIX A

BASIC EQUATIONS AND BOUNDARY CONDITIONS USED IN DISK MODELS

In our discussion below, we shall use cylindrical coordinates (r, z, θ, ϕ) and omit the frequency subscript for all frequency-dependent quantities. Unless otherwise stated, we shall consider only one frequency at a time. Consider an element ds at some point (r, z) along a photon trajectory in the disk. The polar angle made with the figure (symmetry) axis is θ while the azimuthal angle to the outward radial direction is ϕ , as shown in Figure 1.

The radiation transport problem is solved as a boundary value problem by introducing two sets of auxiliary functions which describe the angular distribution of the radiation field: four anisotropy factors ($f_{rr}, f_{zz}, f_{\phi\phi}, f_{rz}$) and the configuration function ξ . Thus initially assuming the radiation field to be isotropic (diffusion approximation), that is, letting $f_{rr} = f_{zz} = f_{\phi\phi} = \frac{1}{3}$, $f_{rz} = 0$, and $\xi = 1$, we solve the nonlinear moment equation of radiation transport

$$(\partial/\partial z)\{(1/\chi)[\partial(f_{zz}J)/\partial z] + (1/r\chi)[\partial(f_{rz}J)/\partial r]\} + (1/r\chi)(\partial/\partial r)\{(r/\chi)[\partial(f_{rz}J)/\partial z] + (r/\chi\xi)[\partial(f_{rr}\xi J)/\partial r]\} = \chi J - \eta, \quad (A1)$$

with boundary conditions

$$[\partial(f_{rz}J)/\partial z] + (1/\xi)[\partial(f_{rr}\xi J)/\partial r] = -\chi H_r, \quad (A2)$$

$$[\partial(f_{zz}J)/\partial z] + (1/r)[\partial(rf_{rz}J)/\partial r] = -\chi H_z, \quad (A3)$$

where, for $\alpha = r$ or z ,

$$H_\alpha = f_{\alpha\alpha}J - 2H_\alpha^- \text{ (at the outer boundary } B), \quad (A4)$$

$$H_\alpha = 0 \text{ (along figure axis } r = 0 \text{ and along midplane } z = 0), \quad (A5)$$

under the condition of radiative equilibrium

$$\int [\eta - \chi J] dv = \int Q_{abs} \pi a^2 [B(T_d) - J] dv = 0. \quad (A6)$$

which determines the grain temperature $T_d(r, z)$ at each point in the cloud and hence the source function. From the source function, we then solve for the angular distribution of the radiation field, to update the anisotropy factors and ξ . We do this by solving the linear ray equations on an impact plane formed by parallel rays which are parameterized by their distance of closest approach (impact parameter ζ) to the figure axis and making an angle θ with the z -direction. The ray equations may be solved using a y - z coordinate system on an impact plane as (Spagna & Leung 1987)

$$(1/\chi)[\mu^2(\partial^2 u/\partial z^2) + \beta^2(\partial^2 u/\partial y^2) + 2\mu\beta(\partial^2 u/\partial y\partial z)] + \{\mu[\partial(1/\chi)/\partial z] + \beta[\partial(1/\chi)/\partial y]\}[\mu(\partial u/\partial z) + \beta(\partial u/\partial y)] = \chi u - \eta, \quad (A7)$$

where $\mu = \cos \theta$, $\beta = \sin \theta$, and $y = r \cos \phi = \sqrt{(r^2 - \zeta^2)}$. The boundary condition for this form of the ray equation is

$$\mu(\partial u/\partial z) + \beta(\partial u/\partial y) = \chi(I^- - u), \quad (A8)$$

where I^- is the specific intensity of the external radiation incident on the cloud surface. For $\mu = 0$, we impose the additional symmetry condition at $y = 0$: $\partial u/\partial y = 0$.

We have found that numerical solutions based on this differential form of the ray equation are highly sensitive to grid spacing and variations in optical depth, yielding results which are self-consistent by the internal checks built into the code but not physically meaningful at all wavelengths. In particular, variations in the emergent flux with viewing angle were exaggerated, especially at long wavelengths where one would expect these differences to be minimal because of the small optical depth in the far-infrared. Accordingly, we have adapted a short characteristic method (Kunasz & Auer 1988; Olson & Kunasz 1988) for the solution of the ray equations expressed in integral form. This method replaces the solution of the two-dimensional partial differential ray equation with a series of integrations of specific intensity along short ray segments terminating at each grid point. Because each line segment is integrated independently, variations in grid spacing do not play any significant role in delimiting the accuracy of the solution.

Following Kunasz & Auer (1988) the specific intensity at a given grid point O is obtained from

$$I_O = I_M \exp(-\Delta\tau_M) + \int_0^{\Delta\tau_M} dt S(t) \exp[-(\Delta\tau_M - t)], \quad (A9)$$

where I_M is the specific intensity at the intersection of the ray with the "upstream" grid line and S is the source function along the ray. The optical depth increment $\Delta\tau_M$ is obtained by integrating the opacity along the ray. Since the opacity and the source function are known at all points on the spatial grid, values for upstream points which are not themselves grid points may be determined by linear interpolation. As pointed out by Kunasz & Auer (1988), the advantage of this equation is that it is analytically correct, and its accuracy in this application is determined by the accuracy of the interpolation and other approximations used in its numerical evaluation.

Sweeping through the grid once beginning at the lower left corner we obtain I^+ at each point for each plane. I^- is determined by symmetry about the origin of each y - z plane; that is, the value obtained for I^+ at a given location is assigned as the value of I^- at the corresponding grid point on the opposite side of the origin. The symmetric average of I^+ and I^- is the intensity-like function u .

From the solution of the ray equations, we can evaluate the anisotropy and boundary factors in terms of u as follows:

$$f_{\alpha\beta} = \int u \Omega_\alpha \Omega_\beta d\Omega / \int u d\Omega, \quad (A10)$$

$$f_{\alpha\beta} = \int u \Omega_\alpha d\Omega / \int u d\Omega, \quad (A11)$$

for α and β denoting r , z , or ϕ . In the above equations, we have defined the following quantities

$$\Omega_r = \sin \theta \cos \phi, \quad (\text{A12})$$

$$\Omega_z = \cos \theta, \quad (\text{A13})$$

$$\Omega_\phi = \sin \theta \sin \phi, \quad (\text{A14})$$

and the integration is over the appropriate solid angles as

$$\int d\Omega = \int \int \sin \theta d\theta d\phi. \quad (\text{A15})$$

The configuration function is given in terms of the anisotropy factors by

$$\xi(r, z) = \exp \left\{ \int_0^r \left[1 - \frac{f_{\phi\phi}(r', z)}{f_{rr}(r', z)} \right] \frac{dr'}{r'} \right\}. \quad (\text{A16})$$

In principle, the incident fluxes at the outer boundary H_r^- are related to I^- by

$$H_r^-(R, z) = \left(\frac{1}{4\pi} \right) \int_{\phi=\pi/2}^{3\pi/2} \int_{\theta=0}^{\pi} I^-(R, z, \theta, \phi) \sin^2 \theta \cos \phi d\theta d\phi, \quad (\text{A17})$$

$$H_z^-(r, Z) = \left(\frac{1}{4\pi} \right) \int_{\phi=0}^{2\pi} \int_{\theta=\pi/2}^{\pi} I^-(r, Z, \theta, \phi) \sin \theta \cos \theta d\theta d\phi. \quad (\text{A18})$$

In our models, however, I^- is assumed to be isotropic and is given as an input parameter. The emergent intensity may be determined from the solution of the ray equations, that is,

$$I^+(R, Z, \theta, \phi) = 2u(R, Z, \theta, \phi) - I^-(R, Z, \theta, \phi), \quad (\text{A19})$$

or directly from the short characteristic solution.

We now express the extinction and emission coefficients, χ and η , in terms of the dust number density n_d , the grain radius a , as well as the absorption and scattering efficiency factors (Q_{abs} and Q_{sca}) from the Mie scattering theory, viz.,

$$\chi = n_d [Q_{abs} \pi a^2 + Q_{sca} \pi a^2], \quad (\text{A20})$$

$$\eta = n_d [Q_{sca} \pi a^2 J + Q_{abs} \pi a^2 B(T_d)]. \quad (\text{A21})$$

In the above expressions for χ and η , isotropic scattering as assumed.

With 41 r -points, 41 z -points, 5 θ -angles, and 51 frequency points, a typical disk model takes about 80 minutes of CPU time on a CYBER 205 supercomputer if the two-dimensional equations are used. On a CRAY XMP/24, the CPU time required is about 40 minutes. Typically less than eight iterations are required. One advantage of the short characteristic method over the differential equation method is that the CPU time is dramatically reduced, since the inversion of large matrices is no longer needed in the solution of the ray equations. Characteristic run time with this method is 800 CPU seconds on a CRAY XMP/24, with about 600 s of this time involved in a single solution of the ray equations at all wavelengths. On the other hand, a typical model with one-dimensional spherical geometry (using the same number of grid and frequency points) took only 5 s of CPU time on the CRAY. Further details of the numerical procedure can be found in Spagna & Leung (1987) for disk geometry, and in Egan et al. (1988) for spherical geometry.

The flux *emergent* from a surface element dS with its normal \mathbf{n} making an angle θ with the observer's line of sight is given by

$$dF^+ = I^+ d\Omega = I^+ (\mathbf{n} \cdot d\mathbf{S}) / D^2, \quad (\text{A22})$$

where $d\Omega$ is the solid angle subtended by the surface element and D is the distance of the source from the observer. In calculating the observed flux, it is important to recognize that for a spherically symmetric source geometry, the variation with angle of emergent intensity from a single point is sufficient to fully describe the observable quantities, since all points on the surface of a sphere are equivalent. In the case of a disk, however, the variation of emergent intensity with angle for all surface points is required for a complete description, since it is clearly not possible to map all points on the disk surface into a single point. Thus, for a spherically symmetric source of radius R , $\mathbf{n} \cdot d\mathbf{S} = 2\pi(R \sin \theta)(R \cos \theta d\theta)$, so that the flux received by a distant observer ($D \gg R$) from the visible face of the sphere is

$$F_{\text{sphere}}^+ = 2\pi \left(\frac{R}{D} \right)^2 \int_0^{\pi/2} I^+ \cos \theta \sin \theta d\theta. \quad (\text{A23})$$

For a sphere of uniform surface brightness I_o^+ , this reduces to

$$F_{\text{sphere}}^+ = (\pi R^2)(I_o^+/D^2). \quad (\text{A24})$$

For a disk of radius R , half-thickness Z , and with its symmetry axis making an angle θ with the line of sight, we can view the element

area dS as having two components: the planar surface of the disk [$\mathbf{n} \cdot d\mathbf{S}_{\text{face}} = \cos \theta (r dr d\phi)$] and the curved surface of the disk edge [$\mathbf{n} \cdot d\mathbf{S}_{\text{edge}} = \sin \theta (\cos \phi R d\phi dz)$]. Hence the total flux received by a distant observer ($D \gg Z$ or R) is given by

$$F_{\text{disk}}^+ = \left[\cos \theta \int_{\phi=0}^{2\pi} \int_{r=0}^R I_{\text{face}}^+ r dr d\phi + R \sin \theta \int_{z=-Z}^{+Z} \int_{\phi=-\pi/2}^{\pi/2} I_{\text{edge}}^+ \cos \phi d\phi dz \right] / D^2. \quad (\text{A25})$$

For a disk of uniform surface brightness I_o^+ , the above expression reduces to

$$F_{\text{disk}}^+ = (\pi R^2 \cos \theta + 4RZ \sin \theta) (I_o^+ / D^2). \quad (\text{A26})$$

We define the observed flux \mathcal{F} (above the ambient ISRF) for an unresolved source to be $\mathcal{F} \equiv F^+ - F^-$, where F^+ and F^- are calculated from equations (A23) and (A25) using I^+ and I^- , respectively. Here I^- is the ambient intensity of the interstellar radiation field and I^+ is the emergent intensity calculated from equation (A18). The quantity $D^2 \mathcal{F}$, which is independent of distance and measured in $\text{ergs s}^{-1} \text{Hz}^{-1}$, is used in Figures 6-10.

In the submillimeter region where radiation is optically thin and grain scattering is negligible, the intensity emergent from a point on the cloud surface is given by

$$I^+ = \int n_d Q_{\text{abs}} \pi a^2 B(T_d) dl, \quad (\text{A27})$$

where dl is a path length element along the line of sight. The emergent flux (defined by eq. [A22]) is

$$F^+ = \int I^+ dA / D^2 = \int Q_{\text{abs}} \pi a^2 n_d B(T_d) dV / D^2, \quad (\text{A28})$$

where we define the volume element $dV \equiv dl dA$, dA being the projected area of a surface element ($dA = \mathbf{n} \cdot d\mathbf{S}$). For an unresolved cloud of uniform density, temperature and grain composition, we get

$$F^+ = Q_{\text{abs}} \pi a^2 B(T_d) n_d V / D^2, \quad (\text{A29})$$

where V is total cloud volume. Thus for a cloud of uniform density and temperature, the flux observed at an optically thin wavelength depends only on the cloud volume and should be independent of the viewing angle or cloud geometry. In this case, the total dust mass is proportional to the observed flux and vice versa, that is,

$$M_d \propto D^2 \mathcal{F} / [N B(T_d)], \quad (\text{A30})$$

where N is the total number of dust grains in the volume V .

APPENDIX B

EXPRESSIONS FOR OPACITY AND MASS OF CLOUDS WITH A GAUSSIAN DENSITY DISTRIBUTION

Consider a dust cloud with a Gaussian density distribution given by

$$n(x) = n_c \exp(-\phi^2 x^2), \quad (\text{B1})$$

where $\phi^2 \equiv \ln(n_c/n_s)$, $n_c \equiv n(0)$, $n_s \equiv n(1)$, $x \equiv r/R$ for one-dimensional spherical geometry and $x^2 \equiv (r^2 + z^2)/R^2$ for two-dimensional disk geometry, R being the radius. It can easily be shown that the following results hold.

1.—Optical depth to cloud center:

$$\tau_{\text{sphere}} = \left[\frac{\sqrt{\pi}}{2} \frac{\text{erf}(\phi)}{\phi} \right] R \langle Q_{\text{ext}} \pi a^2 \rangle n_c, \quad (\text{B2})$$

$$\tau_{\text{disk}} = \left[\frac{\sqrt{\pi}}{2} \frac{\text{erf}(\phi L)}{\phi} \right] R \langle Q_{\text{ext}} \pi a^2 \rangle n_c, \quad (\text{B3})$$

where $\langle Q_{\text{ext}} \pi a^2 \rangle$ is the extinction cross section, a is the grain radius, and $\text{erf}(y)$ is the error function. In the expression for disk geometry, we have defined the dimensionless quantity L

$$\frac{1}{L} \equiv \begin{cases} \gamma \cos \theta & \text{for } \theta \leq \theta_o \\ \sin \theta & \text{for } \theta \geq \theta_o \end{cases}, \quad (\text{B4})$$

where $\gamma = R/Z$ is the aspect ratio (Z is the disk half-thickness), $\theta_o = \tan^{-1}(\gamma)$, and θ is the angle between the symmetry axis and the ray path along which τ_{disk} is measured. For randomly oriented disks, the average optical depth to the cloud center is given by

$$\langle \tau_{\text{disk}} \rangle = \frac{2}{\pi} \int_0^{\pi/2} \tau_{\text{disk}}(\theta) d\theta. \quad (\text{B5})$$

Note that $\langle \tau_{\text{disk}} \rangle$ depends on both γ and ϕ .

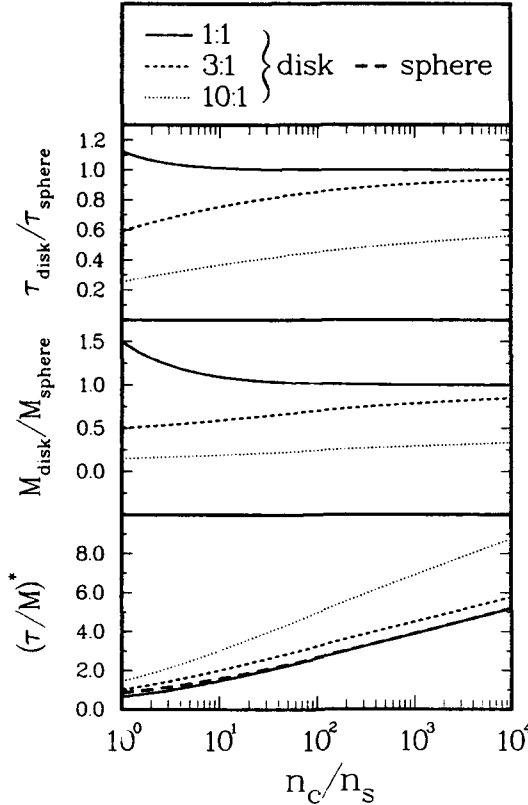


FIG. 11.—Effect of density gradient (as measured by the ratio of central to surface density, n_c/n_s) on the opacity (τ) and mass (M) for clouds with spherical and disk geometries. For models with disk geometry, different aspect ratios ($R/Z = 1, 3, 10$) are also considered. In the bottom panel, the opacity to mass ratio is scaled by some arbitrary factor.

2.—Cloud mass:

$$M_{\text{sphere}} = 3M_{\text{sphere}}^* \int_0^1 x^2 \exp(-\phi^2 x^2) dx, \quad (\text{B6})$$

$$M_{\text{disk}} = M_{\text{disk}}^* \left\{ \gamma \left[\frac{1 - \exp(-\phi^2)}{\phi^2} \right] \left[\frac{\sqrt{\pi} \operatorname{erf}(\phi/\gamma)}{2\phi} \right] \right\}, \quad (\text{B7})$$

where M^* is the mass of an equivalent sphere or disk having the same dimensions but with a uniform density equal to n_c .

In Figure 11, we plot the following quantities as a function of the density contrast (n_c/n_s) for three different aspect ratios ($R/Z = 1, 3, 10$): (1) the cloud opacity ratio ($\tau_{\text{disk}}/\tau_{\text{sphere}}$), (2) the mass ratio ($M_{\text{disk}}/M_{\text{sphere}}$), and (3) the ratio (normalized) of cloud opacity to cloud mass $[(\tau/M)^*]$ for both sphere and disk. For disks, we choose the viewing angle θ such that $\tau_{\text{disk}}(\theta) = \langle \tau_{\text{disk}} \rangle$. The ratio (τ/M) is normalized such that $[(\tau/M)_{\text{disk}}^*/(\tau/M)_{\text{sphere}}^*] = [(\tau_{\text{disk}}/\tau_{\text{sphere}})/(M_{\text{disk}}/M_{\text{sphere}})]$.

From the above expressions, one can easily show that for a given cloud configuration (fixed R , γ , and ϕ), the cloud opacity is proportional to the mass, that is, $\tau \propto M$. On the other hand, for fixed τ and ϕ , $M \propto R^2$ for spheres and $M \propto RZ/f(\gamma)$ for disks, $f(\gamma)$ being a slowly varying function of the aspect ratio γ . Likewise, for fixed M and ϕ , $\tau \propto R^{-2}$ for spheres and $\tau \propto f(\gamma)/RZ$ for disks.

REFERENCES

- Dent, W. R. F. 1988, *ApJ*, 325, 252
 Draine, B. T., & Anderson, N. 1985, *ApJ*, 292, 494
 Egan, M. P., Leung, C. M., & Spagna, G. F., Jr. 1988, *Computer Phys. Comm.*, 48, 271
 Ghosh, S. K., & Tandon, S. N. 1985, *MNRAS*, 215, 315
 Jones, H. P., & Skumanich, A. 1980, *ApJS*, 42, 221
 Keene, J. 1981, *ApJ*, 245, 115
 Kunasz, P. B., & Auer, L. H. 1988, *J. Quant. Spectrosc. Rad. Transf.*, 39, 67
 Lefevre, J., Daniel, J.-Y., & Bergeat, J. 1983, *A&A*, 121, 51
 Leung, C. M. 1975, *ApJ*, 199, 340
 ———. 1976, *J. Quant. Spectrosc. Rad. Transf.*, 16, 559
 ———. 1985, in *Protostars and Planets II*, ed. D. C. Black & M. S. Matthews (Tucson: University of Arizona Press), 104
 Leung, C. M., O'Brien, E. V., & Dubisch, R. 1989, *ApJ*, 337, 293
 Levermore, C. D. 1984, *J. Quant. Spectrosc. Rad. Transf.*, 31, 149
 Mathis, J. S., Mezger, P. G., & Panagia, N. 1983, *A&A*, 128, 212
 Mathis, J. S., Rumpl, W., & Nordsieck, K. H. 1977, *ApJ*, 217, 425
 Mathis, J. S., & Whiffen, G. 1989, 341, 808
 Olson, G. L., & Kunasz, P. B. 1988, *J. Quant. Spectrosc. Rad. Transf.*, 38, 325
 Puget, J.-L., Leger, A., & Boulanger, F. 1985, *A&A*, 142, L19
 Spagna, G. F., Jr. 1986, Ph.D. thesis, Rensselaer Polytechnic Institute
 Spagna, G. F., Jr., & Leung, C. M. 1983, *Computer Phys. Comm.*, 28, 337
 ———. 1985, *Icarus*, 61, 27
 ———. 1987, *J. Quant. Spectrosc. Rad. Transf.*, 37, 565
 Spencer, R. G., & Leung, C. M. 1978, *ApJ*, 222, 140
 Tomita, Y., Saito, T., & Ohtani, H. 1979, *Pub. Astr. Soc. Japan*, 31, 407

APPENDIX 4: PREPRINTS OF PAPERS SUBMITTED

- A4.1 Leung, C. M., "Probing Infrared Sources by Computer Modeling.", invited review paper to appear in the conference proceeding "Astronomy in New York State" (ed. A. G. D. Philip).
- A4.2 "Nagendra, K. N. and Leung, C. M., "Models of Highly Extended Dust Shells Around R C Borealis and W Hydrae.", submitted to the *Astrophysical Journal*.
- A4.3 Doty, S. D. and Leung, C. M., "A Critical Evaluation of Semi-Analytic Methods in the Study of Unresolved, Centrally Heated Infrared Sources.", submitted to the *Astrophysical Journal*.
- A4.4 Egan, M. P. and Leung, C. M., "Modeling Grain Formation in Stellar Outflows: A Master Equation Approach.", submitted to the *Astrophysical Journal*.

PROBING INFRARED SOURCES BY COMPUTER MODELING

CHUN MING LEUNG

Department of Physics, Rensselaer Polytechnic Institute

ABSTRACT. The Infrared Astronomical Satellite (IRAS) has yielded a large and uniform sample of high quality data for various infrared sources. To interpret the IRAS observations, complementary theoretical studies have been undertaken which often involve modeling in detail the scattering, absorption, and emission of photons by dust grains. In the last decade, significant progress has been made at Rensselaer in the development of radiation transport models for infrared sources. Models with increasing degree of physical realism have been constructed. We review recent progress made in the modeling of infrared sources. Directions for future research in this area are briefly discussed.

1. INTRODUCTION

Infrared radiation is the primary tracer of the dust component in the universe. Dust grains, although a minor constituent, play a very important role in the thermodynamics and evolution of young and evolved stars, nebulae, interstellar clouds, and nuclei of some galaxies. As a result of the expansion in observational facilities, new advances in instrument technology, and increased funding, there has been an unprecedented growth in infrared astronomy in the last two decades. Most recently the astronomical community has identified the 1990's to be the decade of infrared astronomy.

In the last decade, NASA has launched a number of space-based observatories: the Infrared Astronomical Satellite (IRAS), the Hubble Space Telescope (HST), and the Cosmic Background Explorer (COBE). In particular, the IRAS, launched in 1983, carried out a comprehensive infrared survey of the sky and a wide variety of astronomical objects were detected in the infrared. Thus we have discovered infrared cirrus, detected protoplanetary disks, gained access to dust-enshrouded regions of star formation, found galaxies far brighter in the infrared than in all other wavelength bands combined, probed the properties of

interstellar dust, and gained insight into the cooling mechanisms for interstellar medium. The IRAS has stimulated advances in most branches of astrophysics and the IRAS database remains a vital tool for current research in infrared astronomy.

To maximize the scientific returns of the IRAS mission, complementary theoretical studies with increasing degree of sophistication have been undertaken. A good strategy for a systematic analysis and interpretation of IRAS observations includes the following steps: a) perform statistical analyses and correlation studies, and develop classification schemes, e.g., histograms, two-color diagrams, correlation plots, classification of spectral feature profiles; b) construct *phenomenological* models for each class of objects to parameterize the observed radiation characteristics in terms of their physical source properties; c) from the phenomenological models, develop self-consistent *physical* models which can explain coherently present and future observations. The phenomenological modeling of infrared sources invariably requires solving in detail the problem of scattering, absorption, and emission of photons by dust grains, i.e., radiation transport in a dusty medium.

2. MODELING INFRARED SOURCES

To model the observed characteristics of an infrared source, one solves the equation of radiation transport in a dusty medium, subject to the constraint of radiative equilibrium. In the model the input parameters are: a) luminosity and spectral energy distribution of the central heat source, b) source geometry and dimensions, c) size, composition, and optical properties of each grain species (e.g., extinction coefficient, albedo, and scattering asymmetry parameter), d) dust density distribution, and e) other local heating mechanisms, e.g., viscosity, collision with gas particles. The model output consists of the following: a) temperature distribution of each grain species, b) combined energy spectrum of central heat source and dust cloud, and c) intensity variation across the source at each wavelength, and d) properties of internal radiation field. The choice of model parameters is guided by observations. The most important observational constraints are: a) spectral energy distribution, b) surface brightness or apparent source size as a function of wavelength, c) strength and shape of emission and absorption features, and d) color temperatures in different parts of spectrum. The interplay between observational constraints and model parameters has been considered (cf. Leung 1976b, Jones, et al. 1977), e.g., the source luminosity can be estimated from a), the dust density distribution and geometrical source size from b), the grain composition and optical depth information from c), and the dust temperature distribution from d).

The problem of radiation transport in a spherically symmetric medium containing dust grains has been considered by many authors (e.g.,

Leung 1975; Apruzese 1976; Jones and Merrill 1976; Scoville and Kwan 1976; Rowan-Robinson 1980; Wolfire and Cassinelli 1986). Among these studies, the radiation transport code developed by Leung (1975, 1976a) has been adopted by many researchers and applied successfully to the interpretation of infrared observations. The code is available for distribution (Egan et al. 1988).

In the last decade, significant progress has been made at Rensselaer in the development of radiation transport models for infrared sources. Models with increasing degree of physical realism have been constructed. In Figure 1 we summarize schematically the recent advances made. The left-hand column indicates past assumptions, in contrast with present capabilities shown in the right-hand column. Clearly models of infrared sources have become increasingly sophisticated. Below we briefly describe a few selected results to demonstrate the recent progress made in the modeling of infrared sources.

3. RECENT PROGRESS

3.1 *Modeling a Class of Infrared Sources*

The IRAS survey has made available a large and uniform sample of high-quality data from both photometric and spectroscopic observations of asymptotic giant branch (AGB) stars. In particular, IRAS data indicates that many carbon stars, especially those with optically thin dust shells, have large fluxes at 60 and 100 μm . It has been suggested that a remnant dust shell from an earlier mass-loss episode can explain the excess fluxes. Two hypotheses have been proposed to explain the origin of the remnant dust shell. First, that O-rich AGB stars may undergo a transformation to C-rich by carbon dredge-up, resulting in the formation of an inner C-rich dust shell and a remnant O-rich dust shell (Willems 1987). In the second scenario, a C-rich remnant dust shell is formed when helium shell-flashes stop the mass-loss process which resumes later (Oloffsson et al. 1990).

To test these hypotheses, radiation transport models of dust around carbon stars have been constructed: models with either a single C-rich dust shell or double shells (Egan and Leung 1991). Figure 2 shows the color-color diagrams for selected carbon stars in the IRAS-LRS catalog. The thick solid line is the blackbody line. The gray-shaded areas indicate the limits on the colors for carbon stars of various ages imposed by the models. Clearly single-shell models cannot explain the observed color distribution, while two-shell models with either a C-rich or an O-rich remnant shell can.

Thus by constructing models for a class of infrared sources and comparing the results with observations, one can identify trends and determine more reliably the physical source parameters, thereby maximizing the scientific returns of the IRAS observations.

3.2 Fractal Grains

In astrophysical environments dust grains most likely have irregular shapes formed by fractal growth processes. On the other hand, spherical dust grains are often assumed in models of infrared sources so that the dust opacity can be calculated easily from the Mie theory. A computational technique now exists for calculating the dust opacity for fractal grains of irregular geometries (Draine 1988; Bazell and Dwek 1990). The method is based on the so-called "discrete dipole approximation" in which a fractal grain is approximated by a collection of dipoles. Using these dust opacities for fractal grains, Fogel and Leung (1992) have constructed radiation transport models for circumstellar dust shells and interstellar dust clouds. Compared to models with spherical grains of the same composition and volume, models with fractal grains show a shift in the peak flux toward longer wavelengths, implying that fractal dust grains are cooler than spherical grains. These differences can be attributed to a higher ratio (p) of geometric cross section to volume for the less compact fractal grains. Figure 3 shows the results for a circumstellar shell model using three different grain shapes of the same volume: sphere, rod, and square donut. Spherical grains attain a higher temperature due to a smaller p . For the case of rod and square donut fractal grains, they have the same p and show almost no difference in the absorption cross sections and energy spectrum. This implies that, for the same p , the overall grain shape plays only a minor role.

3.3 Transient Heating of Very Small Grains

Among the unexpected results from IRAS was the discovery of excess mid-infrared emission detected in a number of infrared sources, e.g., in diffuse clouds, in dark globules, in visual reflection nebulae, and high-latitude dust clouds or infrared cirrus. It is now believed that the emission at short wavelengths ($< 30 \mu\text{m}$) comes from transient heating of very small grains (Draine and Anderson 1985) and large polycyclic aromatic hydrocarbons or PAHs (Boulanger et al. 1985; Puget et al. 1985). Temperature fluctuations in small grains occur whenever the energy input from photons or energetic particles is considerably larger than the average energy content of the grain. This non-equilibrium grain heating can significantly change the energy distribution of the radiation field in infrared sources. To properly interpret the IRAS observations, one needs a radiation transport model which takes into account self-consistently the effects of temperature fluctuations due to transient heating of small grains and PAHs.

By formulating the radiation transport problem involving transient heating in a fashion similar to a non-LTE line transfer problem involving many transitions and energy levels, Lis & Leung (1991a,b) recently developed a computer code which, for the first time, treats self-consistently the thermal coupling between the transient heating of small grains and the equilibrium heating of conventional large grains.

They have constructed models to interpret the IRAS observations of the Barnard 5 cloud (Beichman et al. 1988) and a diffuse cloud in Chamaeleon (Chlewicki et al. 1987). Figure 4 shows the relative contributions of different grain components to the emission of the Chamaeleon cloud model (Lis and Leung 1992). Longward of $100\ \mu\text{m}$, the emission is dominated by conventional large grains. Between $30\text{--}100\ \mu\text{m}$, the emission is produced mainly by very small grains. Shortward of $30\ \mu\text{m}$, both PAHs and small grains are responsible for the emission. Figure 5 compares the model results with observations (filled squares) for the surface brightness at the four IRAS bands. The agreement between the model results and observations is very good. The model also indicates that very small grains account for $\approx 15\%$ of the total opacity in the visible, and $\approx 5\%$ of the total dust mass of the cloud. On the other hand, PAHs account for $\approx 10\%$ of the cloud opacity and $\approx 20\%$ of the dust mass. Furthermore, to produce the observed infrared limb brightening at short wavelengths, the spatial distribution of small grains and PAHs must be more extended than that of large grains. Thus detailed radiation transport models now exist which incorporate both the transient heating of very small grains and the equilibrium heating of conventional large grains.

3.4 Modeling Infrared Sources with Disk Geometry

Although there is growing observational and theoretical evidence for a large number of disk-shaped or toroidal objects of astrophysical interest (e.g., circumstellar disks, protoplanetary disks, protostellar accretion disks, bipolar molecular flows, and disk galaxies), the majority of radiation transport models currently in use invoke the assumption of spherical geometry. This assumption is made because spherically symmetric geometry is the only 1-D geometry which accounts for the finite dimensions of a system in all directions. Establishing the source geometry can provide severe constraints on the origin, dynamics, and properties of infrared sources. Hence it is crucial to solve the problem of radiation transport in a dusty medium with 2-D disk geometry and apply the results to infrared observations.

A few attempts have been made to model infrared sources with nonspherical geometry. Lefevre et al. (1983) have performed Monte Carlo simulations of ellipsoidal dust shells around cool stars, while Ghosh & Tandon (1985) calculated dust temperature distributions in cylindrical clouds with embedded stars. The latter work has been extended by Dent (1988) to calculate the temperature distribution and energy spectrum of circumstellar disks around young stars. Most recently, Spagna et al. (1991) considered radiation transport in disk-shaped interstellar clouds which are heated externally by the ambient interstellar radiation field. Figure 6 shows a comparison of dust temperature distribution and flux spectra for spherical and 1:1 ($R:Z$, R is the disk radius and Z is the half-thickness of the disk) disk models of the same optical depth. For the disk model, except for the slightly warmer dust at the "corners" of the disk, the overall temperature distribution remains remarkably spherically symmetric. Furthermore, flux profile for the disk model is

nearly independent of the viewing angle and is approximately 30% greater than that for the spherical model, although the mass is only 1.5% greater. Other physical and geometrical effects of 2-D radiative transfer in various disk configurations have been studied. Thus powerful computational tools now exist for the modeling of infrared sources with a variety of geometries.

4. CONCLUDING REMARKS AND OUTLOOK

To summarize, in the last decade, much progress has been made in the development of detailed models for infrared sources. Models with increasing degree of physical realism have become available. Future research in this area will incorporate other important physical processes so that self-consistent physical models can ultimately be constructed: a) transfer of polarized radiation, b) radiation hydrodynamics, c) radiation transport in 2-D and 3-D geometries, d) grain nucleation and growth, and e) gas-phase and grain-surface chemistry. In addition, improvements in computational techniques will be made: a) better algorithms and iteration procedures, and b) automation of model fitting.

To facilitate the analysis of space-based infrared observations, a critical task is to automate the modeling process so that researchers can model infrared sources on workstations in real time. Computer modeling will then become a routine part of data analysis and be as easy as performing least-square fits to observational data. With automation researchers can perform computer experiments to test various hypotheses and determine the physical parameters for infrared sources. With such a research tool, predictions on certain observational consequences can be made which will stimulate further observations and theoretical studies, efforts which are essential to the scientific missions of the Infrared Space Observatory and the Space Infrared Telescope Facility.

ACKNOWLEDGEMENTS. At Rensselaer, research in the computer modeling of infrared sources has been supported by AFOSR (grant AFOSR 89-0104) and NASA (grants NAGW-577, NAGW-1103, NAGW-2817, and NAG 5-1182).

REFERENCES

- Apruzese, J. P. 1976, ApJ, 207, 799.
Bazell D. & Dwek, E. 1990, ApJ, 360, 142.
Beichman, C. A., Wilson, R. W., Langer, W. D., & Goldsmith, P. F. 1988, ApJ, 332, L81.
Boulanger, F., Baud, B., & van Albada, T. 1985, A&A, 144, L9.
Chlewicki, G., Laureijs, R. J., Clark, F. O., & Wesselius, P. R. 1987, in *Star Formation in Galaxies*, NASA CP-2466, ed. C. J. Lonsdale

- Persson, p. 113.
- Dent, W. R. F. 1988, ApJ, 325, 252.
- Draine, B. T. 1988, ApJ, 333, 848.
- Draine, B. T. & Anderson, N. 1985, ApJ, 292, 494.
- Egan, M. P. & Leung, C. M. 1991, ApJ, 383, 314.
- Egan, M. P., Leung, C. M., & Spagna, G. F., Jr. 1988, Computer Phys. Commun., 48, 271.
- Fogel, M. E. & Leung, C. M. 1992, in preparation.
- Ghosh, S. K. & Tandon, S. N. 1985, MNRAS, 215, 315.
- Jones, T. W., Leung, C. M., Gould, R. J., & Stein, W. A. 1977, ApJ, 212, 52.
- Jones, T. W. & Merrill, K. M. 1976, ApJ, 209, 509.
- Lefevre, J., Daniel, J.-Y., & Bergeat, J. 1983, A&A, 121, 51.
- Leung, C. M. 1975, ApJ, 199, 340.
- Leung, C. M. 1976a, J. Quant. Spectrosc. Rad. Transf., 16, 559.
- Leung, C. M. 1976b, ApJ, 209, 75.
- Lis, D. C. & Leung, C. M. 1991a, Icarus, 91, 7.
- _____ 1991b, ApJ, 372, L107.
- _____ 1992, in preparation.
- Olofsson, H., Carlstrom, U., Eriksson, K., Gustafsson, B., & Willson, L. A. 1990, A&A, 230, L13.
- Puget, J. L., Leger, A., & Boulanger, F. 1985, A&A, 142, L19.
- Rowan-Robinson, M. 1980, ApJS, 44, 403.
- Scoville, N. Z. & Kwan, J. 1976, ApJ, 206, 718.
- Spagna, G. F., Jr., Leung, C. M., & Egan, M. E. 1991, ApJ, 379, 232.
- Willems, F. J. 1987, Ph. D. thesis, Universiteit van Amsterdam.
- Wolfire, M. G. & Cassinelli, J. P. 1986, ApJ, 310, 207.

FIGURE CAPTIONS

- Fig. 1 - Comparison of past (left column) and present (right column) capabilities in models of infrared sources.
- Fig. 2 - Color-color diagrams for selected carbon stars in the IRAS data (filled circles). The shaded areas indicate regions occupied by single and double shell models.
- Fig. 3 - Left panel: absorption cross sections for amorphous carbon grains of same volume but different shapes. Right panel: energy spectrum from a circumstellar dust shell model.
- Fig. 4 - Relative contributions of different grain components to the emission for a model of the Chamaeleon diffuse cloud.
- Fig. 5 - Comparison of model results (solid line) with the IRAS observations (filled squares) of the Chamaeleon diffuse cloud.
- Fig. 6 - Comparison of dust temperature distribution (left panel) and flux spectra (right panel) for spherical and disk models of the same optical depth.

MODELING INFRARED SOURCES PAST & PRESENT

MODELING APPROACH

- analytical
- single source
- numerical
- single source, class of sources

GRAIN PROPERTIES

- grey opacity
- single grain type
- single size grain
- spherical shape
- non-grey opacity
- multiple grain types
- size distribution
- arbitrary shapes

PHYSICAL PROCESSES

- isotropic radiation
- single or no scattering
- equilibrium heating
- temp.-independent opacity
- anisotropic radiation
- anisotropic multiple scattering
- equilibrium + transient heating
- temp.-dependent opacity

SOURCE GEOMETRY

- 1-D slab or sphere
- 1-D sphere, 2-D disk

Figure 1

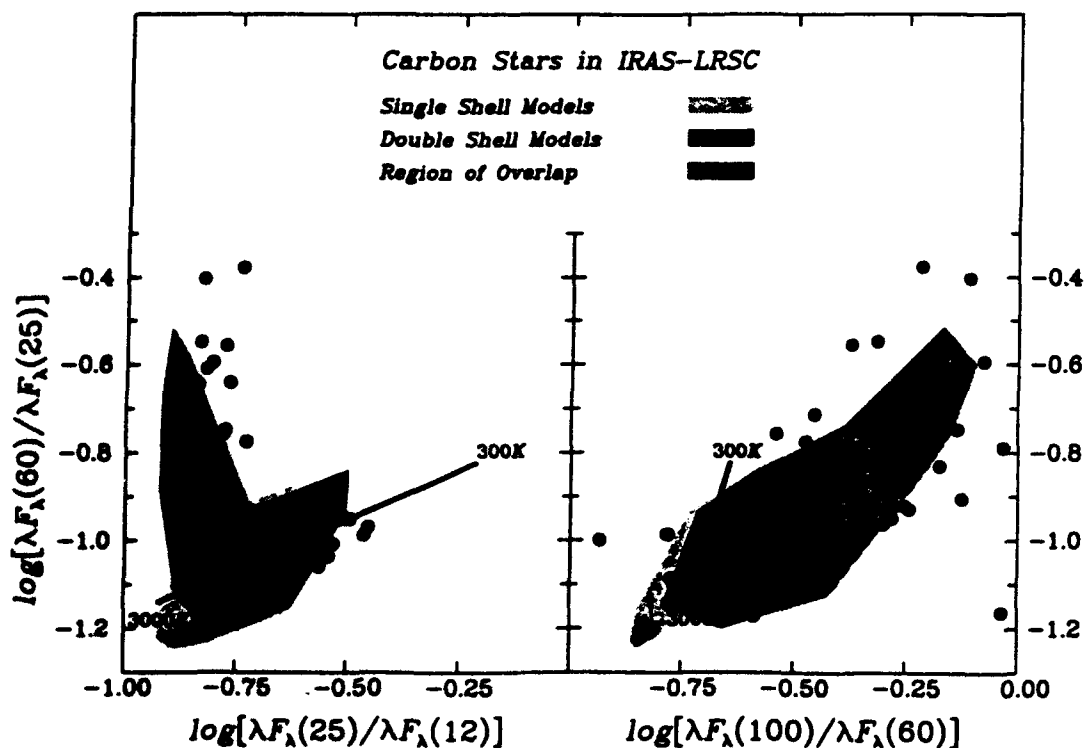


Figure 2

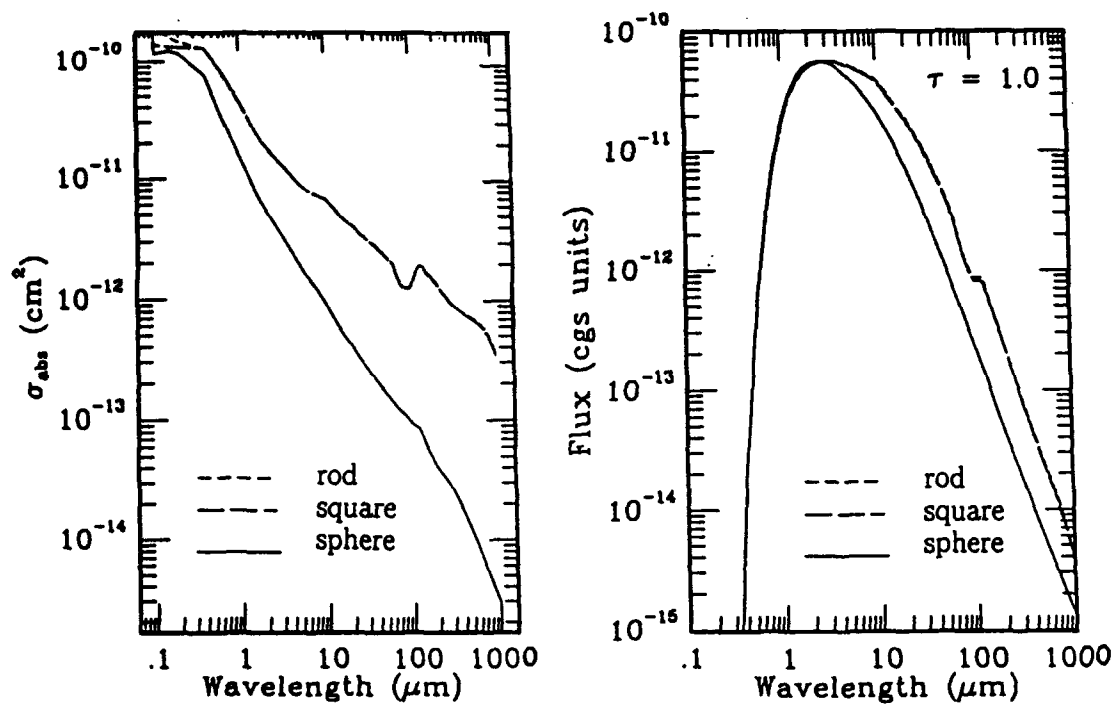


Figure 3

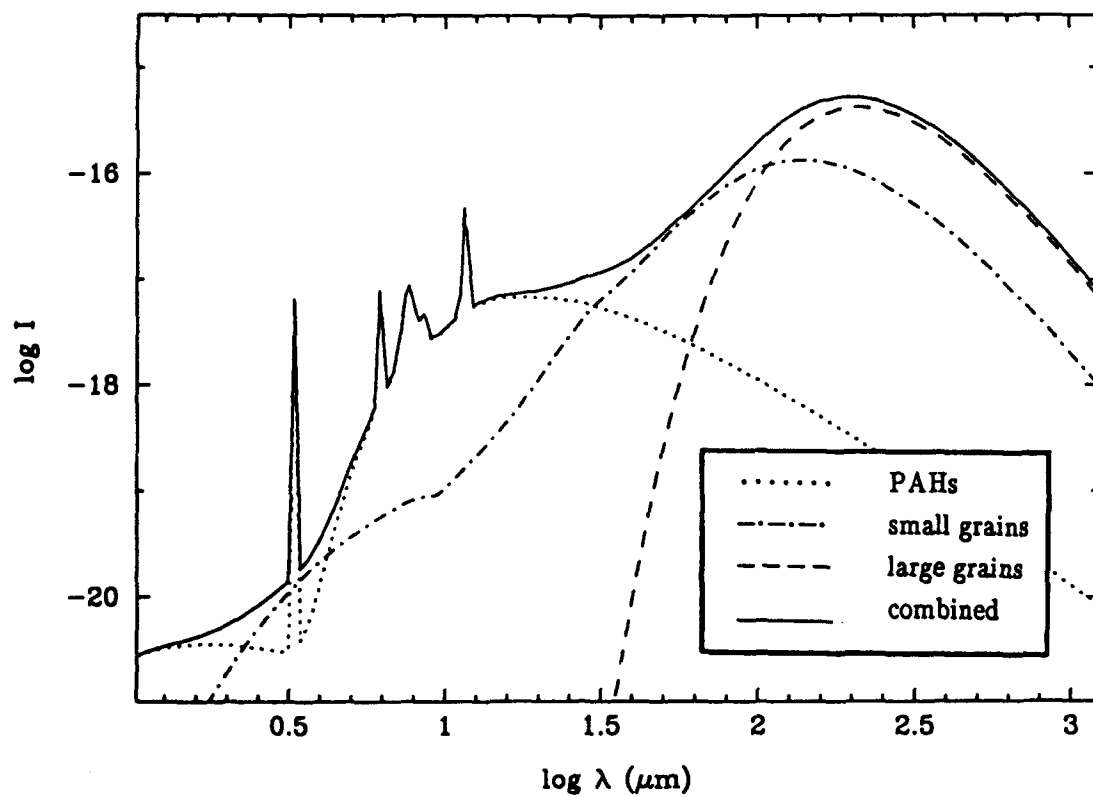


Figure 4

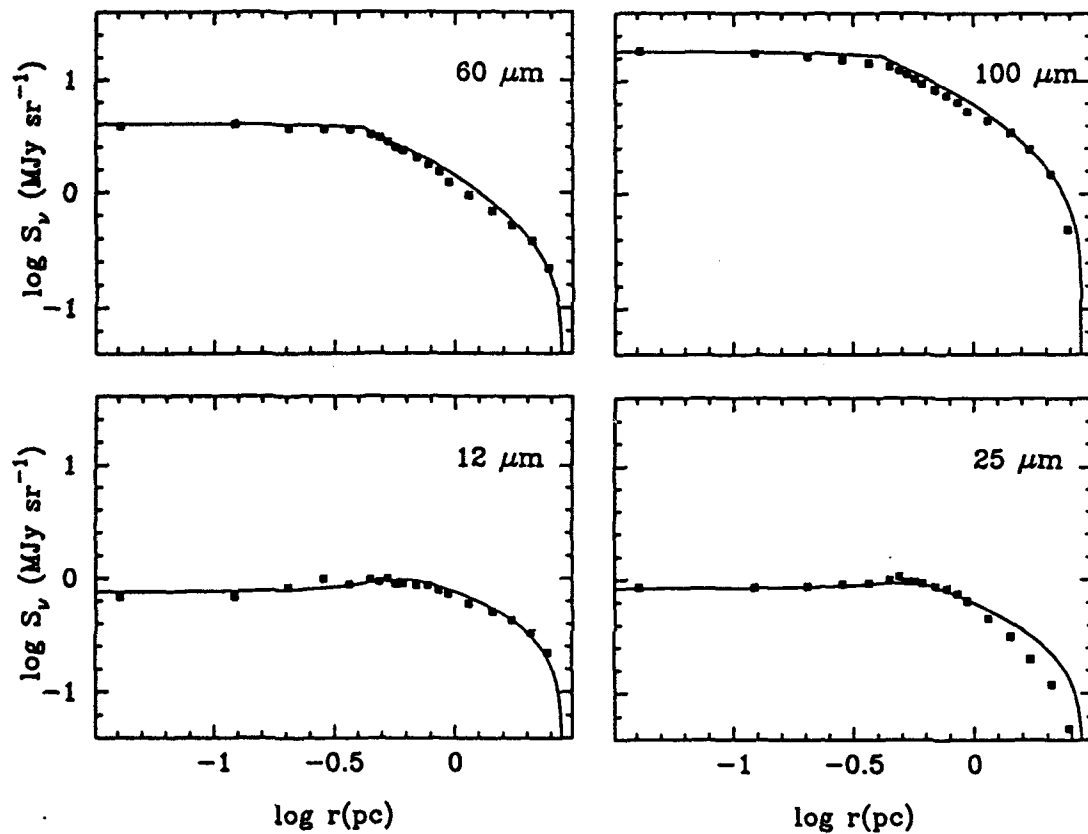


Figure 5

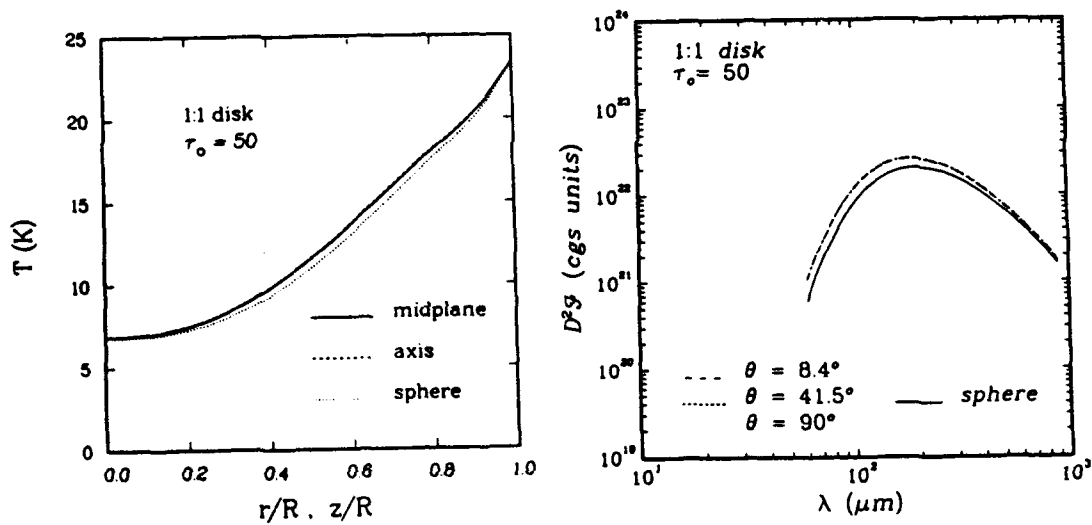


Figure 6

**MODELS OF
HIGHLY EXTENDED DUST SHELLS AROUND
R CORONAE BOREALIS AND W HYDRAE**

K. N. NAGENDRA AND CHUN MING LEUNG

Department of Physics, Rensselaer Polytechnic Institute, Troy, NY 12180-3590

Submitted to The Astrophysical Journal

ABSTRACT

Schematic models are presented for the dust shells of hydrogen deficient supergiant star R Coronae Borealis, and the oxygen rich red giant W Hydrae. IRAS observations of R CrB are used as constraints in selecting the parameters for the radiative transfer modeling of this system. Based on suggestions from earlier work a *double shell model* is employed as a standard scenario for R CrB. The first shell is a hot dust inner shell of radius 6" surrounding the central star. The second shell is the cooler remnant dust shell, which is highly extended with a radius 10' at a source distance of 1.6 kpc from earth. The two shells can be spatially well *separated* from each other, and can have completely different mechanisms responsible for heating of their dust grains. A comparison of '*analytic models*' and the '*radiative transfer models*' is made, in order to clarify usefulness of both, in modeling far infrared IRAS flux density and surface brightness data. Since it is difficult to give a unique best fit model using radiative transfer models based on simple power law type density, opacity distributions, and single size grain models, a detailed parametric study of the system is undertaken. The extended shell of W Hya, has a radius of 20' at a source distance of 130 pc from earth. The IRAS data is used to constrain the models of W Hya. The models are based on the scenario of *single* large circumstellar dust shell, much like the familiar dust shells around late type giants. We find that somewhat higher density of hot dust is required in the hot core of the shell, compared to extended part of the shell (which is not separated) starting very near this core, in order to fit the near infrared ($< 25 \mu\text{m}$) flux densities. A comparison of analytic approach and radiative transfer approach is also made. A parametric study of this system is presented on the same lines as R CrB, although these two systems are essentially different in nature. The models of R CrB clearly point to the configuration of a large well separated cool shell surrounding a tiny hot dust shell, which support existing view about this extended shell to be a *fossil shell*. However the distance to which such an extended shell has moved as a whole,

leaving a cavity in between the two shells, can not be fixed from radiative transfer analysis. Thus it can be treated as an unknown parameter of the system for modeling purposes. The ISRF incident on outer boundary plays a considerable role in modeling the IRAS 60 μm and 100 μm surface brightness data of R CrB. The observed isothermal temperature of R CrB fossil shell poses serious problems. We favour models in which the density varies as $r^{-\gamma}$ ($\gamma = 1.0 - 1.5$) over inverse square law ($\gamma = 2$) models. The source of dust heating in such models is an even combination of central star radiation and ISRF. Our models of W Hya indicate on the other hand, that its enormous cool shell is heated predominantly by the central star radiation (in conformity with earlier suggestions). No excess ISRF is required to model the IRAS 60 μm and 100 μm surface brightness profiles of W Hya. The density distribution in W Hya shell is possibly of the form $r^{-\gamma}$ ($\gamma = 0.5 - 1.0$). It is not clear from our models if this shell is a remnant shell. The amorphous carbon in the case of R CrB and amorphous silicate in the case of W Hya give better fits to the IRAS data, than crystalline dust grains.

Subject headings: infrared:sources-stars:circumstellar shells-stars:R Coronae Borealis-stars:W Hydrae-models:Radiative Transfer

1. INTRODUCTION

It is well known that supergiant stars with an active mass loss are also associated with large dust shells. The existence of dust in the envelopes of several giant and supergiant stars is confirmed by large infrared excess in the continuous spectrum of these stars. The dust grains in the shell are basically formed by condensation of molecular gas at large distances from the central star photosphere. For this reason, the temperatures of dust shells are rather small (nearly 1000 K at the dust condensation radius down to 20 K at the shell boundaries). There is always a momentum transfer from the dust grains to the ambient gas through collisional processes. Thus the dust shells contain large amounts of gas dragged in along with the radiatively driven expanding dust shells. However infrared continuum radiation arises mainly due to the emission by grains. Hence infrared ($\lambda > 3 \mu\text{m}$) continuum observations are sensitive indicators, not only of the total amount and radial distribution of dust grains in the shell, but also of their composition. Depending on the massloss rate in the photospheric levels, there is a wide range of characteristics and peculiarities associated with these dust shells. For example, stars with smaller massloss rates usually have optically thin shells and are not geometrically extended. There are some exceptions to this. The two stars that we have selected here for study - R CrB and W Hya are, for instance, systems with low massloss rate, having optically thin but geometrically highly extended dust shells. The dust massloss rate in R CrB extended shell is $\dot{M}_d(1.4') \approx 1.5 \cdot 10^{-6} M_{\odot}/\text{yr}$ with dust mass in the range $M_d \approx 10^{-3} - 10^{-2} M_{\odot}$ assuming amorphous carbon dust. The corresponding quantities for W Hya are $\dot{M}_d(3') \approx 5 \cdot 10^{-9} M_{\odot}/\text{yr}$ and $M_d \approx 1 \cdot 3 \cdot 10^{-4} M_{\odot}$ assuming silicate based grains. For this reason, the modeling of infrared emission in these objects is interesting. The Infrared Astronomical satellite (IRAS) observed several such objects, characterised by large $100 \mu\text{m}$ flux, and unusually large $100 \mu\text{m}$ extended emission (meaning strong $100 \mu\text{m}$ intensity distribution upto very large distances from the central star).

It is important to note that detection of such extended emission (extended shell) was only

due to disk resolved observations, made with much smaller beam sizes compared to those normally used in disk integrated flux measurements. It is more common that the theoretical modeling efforts were concerned mainly with fitting the flux data. With the availability of disk resolved data obtained from IRAS and subsequent observational efforts, it is now important to model intensity (commonly called surface brightness) data whenever possible. Surface brightness data severely constrains the otherwise very large number of possible models that can easily fit a single piece of flux density (spectrum) data. The extended shell of R CrB was modelled by Gillett et. al (1986) employing mainly surface brightness data to derive the parameters such as total dust mass and massloss rate in the shell. A similar approach was employed by Hawkins (1990) to explore the properties of highly extended dust shell of W Hya. The question (at least in the case of W Hya) of whether these extended shells are part of the ongoing massloss process, or simply constitute cooler remnant (fossil dust) of earlier *episodic massloss* events is still not clear. Detailed radiation hydrodynamic modeling, starting with evolutionary status of asymptotic giant branch stars is required in this direction. Our purpose in this paper is to reexamine the modeling the R CrB and W Hya data obtained by IRAS, through a self consistent radiative transfer approach. We do not attempt to provide best fits to the observed data, but concentrate on general characteristics of modelling such unusually large shells, and on the procedures required and difficulties that arise in modeling highly extended shells. However, we confirm qualitatively the conclusions reached by above mentioned authors as regarding the nature and physical properties of the dust shells in these two stars, through our independent approach.

The paper is organised in three sections. The next section (section 2) deals only with the *analytic* modeling (abbreviated as AM), an approach similar to that used by Gillett et. al (1986) and Hawkins (1990). But the beam convolution procedures used by us are different. We present this section basically (a) to show the equivalence of the earlier approaches and the one used in this paper and (b) to indicate the correctness of our convolution procedures, which are used in exactly identical way in the subsequent *Radiative Transfer* (abbreviated as RT)

modeling also discussed in section 3. In section 3 we present the modeling of systems such as R CrB, having possibly detached shells, through the two shell model approach. We also discuss in this section the modeling of W Hya through the single shell model approach. We show the dependence of results (flux density in all the IRAS bands and intensity in 60 μm and 100 μm) on several important parameters. This is done to demonstrate the way in which the fit to surface brightness constrains the free parameters to narrow ranges, unlike a fit only to the flux density. Each subsection deals with the effect of variation of a single parameter. But one common (best fit or reasonable fit) model runs through all the subsections as a *median model* and only the parameter specific to that subsection is varied, in each case. In section 4 we describe the physical implications of our model results. In section 5, we summarise the main results of our studies.

2. ANALYTIC APPROACH - OPTICALLY THIN APPROXIMATION

In this section we will discuss the computation of flux and surface brightness across the visible disk offered by a dust cloud. We have utilised the expressions for flux density $F_{\nu}(\lambda)$ and intensity distribution $I_{\nu}(\lambda, P)$ on the disk as a function of P , given in Gillett et. al (1986). Various approximate forms of these expressions are employed by different authors (see e.g Sopka et. al., 1985, and references therein). Basically these formulae are derived assuming that the dust medium is optically thin in the wavelength under consideration.

2.1 Estimation of flux density in optically thin limit

The flux density at earth from an optically thin spherical shell medium is given by (in units of $\text{ergs s}^{-1} \text{cm}^{-2} \text{Hz}^{-1} \text{sr}^{-1}$)

$$F_{\nu}(\lambda) = \frac{4 \pi \kappa(\lambda) m_d n_0 r_0^{\gamma}}{D^2} \int_{r_{\min}}^{r_{\max}} r^{2-\gamma} B_{\nu}[\lambda, T(r)] dr, \quad (1)$$

where $B_{\nu}[\lambda, T(r)]$ is the Planck function at the local temperature $T(r)$ of the dust particles, at a distance r from the central star of radius r_* and effective temperature T_* . D is distance to the shell from the earth, m_d is the mass of a dust particle and $\kappa(\lambda)$ its opacity at wavelength λ . In

equation (1) it is assumed that the dust number density varies in the shell according to a power law

$$n(r) = n_0 (r_0 / r)^\gamma \text{ cm}^{-3}, \quad (2)$$

between the inner boundary of the shell r_{\min} and the outer boundary r_{\max} . The quantity γ is the index of power law density distribution. The reference density n_0 is the normalising density at some reference distance r_0 . A rough estimate of n_0 can be made using the expression (Sopka et. al., 1985)

$$n_0 = \frac{3 \dot{M}_d(r_0)}{16 \pi^2 a^3 \rho_d V_d r_0^2} \text{ cm}^{-3}, \quad (3)$$

which depends on the massloss rate \dot{M}_d in the dust wind at reference radius r_0 . Other quantities in equation (3) are a , ρ_d , and V_d respectively the dust particle radius, the mass density of the dust particle, and the velocity of dust wind at r_0 . For rough estimates of $\dot{M}_d(r_0)$ one can use the expression given in Sopka (1985)

$$\dot{M}_d(r_0) = 2 f_v^{\text{obs}}(\lambda) V_d D^2 / [\kappa(\lambda) \xi(\lambda)], \quad (4)$$

where

$$\xi(\lambda) \approx \frac{4 k T_0}{\lambda^2} r_0 \frac{(r_{b,\lambda} / r_0)^{1-\beta}}{1 - \beta}, \quad (5)$$

with $\beta = 2/(4+m)$, and $r_{b,\lambda}$ the linear radius of the telescope beam at the source. In deriving equation (5), a box type beam (meaning a beam of uniform response) is employed. Similarly for a rough estimate of V_d , one can use the terminal velocity of the dust wind itself, given by

$$V_d \approx \left[\frac{\beta L_*}{M_t c} (r_{\max} - r_{\min}) \right]^{1/2}, \quad (6)$$

where $M_t = M_d + M_g$. An upper limit on total mass of the shell $M_t = 1-2 M_O$ is usually employed in theoretical modeling of circumstellar shells with larger massloss rates. At least for extended emission from nearly isothermal dust clouds, a rough estimate of M_d in the extended shell can be obtained using integrated extended emission (see Gillett et. al., 1986)

$$M_d = \Omega_d(\lambda) D^2 / k(\lambda) , \quad (7)$$

with

$$\Omega_d(\lambda) = f_v(\lambda) / B_v(\lambda, T) , \quad (8)$$

where $\Omega_d(\lambda)$ is the effective solid angle subtended by the emitting cloud with a dust temperature T . The nominal values of the dust particle radii used here are $a = 0.05 \mu\text{m} - 0.1 \mu\text{m}$. Dust mass density of $\rho_d = 3 \text{ gm cm}^{-3}$ is generally employed for interstellar dust particles.

If $\dot{M}_d(r_0)$ and V_d are known, then equation (3) can be used to compute n_0 . The absorption coefficient of dust particles can be assumed to vary according to a power law

$$\kappa(\lambda) = \kappa_0 (\lambda_0/\lambda)^m \text{ cm}^2 \text{ gm}^{-1} , \quad (9)$$

to a good approximation. The absorption coefficient $\kappa_0 = \kappa(\lambda_0)$ at λ_0 is then required to be specified as a free parameter.

$$\kappa(\lambda_0) = Q_{\lambda_0} \pi a^2 / \rho_d (4 \pi a^3/3) \text{ cm}^2 \text{ gm}^{-1} , \quad (10)$$

can be computed using the absorption efficiency Q_{λ_0} of the dust particle at wavelength λ_0 .

The temperature that a dust particle attains in '*thermal equilibrium*' condition with the central star radiation is given by the equation of thermal balance

$$T(r) = T_* \left[(r_*/2r)^2 + C \right]^{1/(4+m)} , \quad (11)$$

written for an isolated grain. The quantity m in equation (9) and (11) is the exponent of the power law type variation of opacity. It is an important free parameter in our models.

Generally $m = m(\lambda)$, but in a smaller range of wavelengths m can be assumed as constant. We have also assumed inherently that $Q_{\lambda, \text{abs}} = Q_{\lambda, \text{emis}}$. The constant C in equation (11) is a radially independent function in the first approximation. It represents the heating of dust from a radiation field which is spherically symmetric and isotropic. Notice that if this radiation field is assumed as *interstellar radiation field* (ISRF) then basically only half of the mean intensity of ISRF goes to heating the dust. Gillett et. al (1986) employ $C = 6.9 \cdot 10^{-13}$

$[\dot{H}_c / \dot{H}_*(r_0)]$ where \dot{H}_c is the rate of dust heating due to this constant source mentioned above.

and $\dot{H}_*(r_0)$ is the rate of heating due to central star, at a radial point r_0 , and is given by

$$\dot{H}_*(r_0) = \int_0^\infty < Q_{\text{abs}} \pi a^2 >_v J_v(r_0) dv, \quad (12)$$

where $J_v(r_0)$ is the mean intensity of central star radiation field, given by

$$J_v(r_0) = W B_v(T_*) / 2 = B_v(T_*) / 2 \left[1 - \sqrt{1 - (r_*^2 / r_0^2)} \right], \quad (13)$$

with W being the dilution factor in vacuum. For computing a spatially independent heating rate we can use

$$\dot{H}_c = \int_0^\infty < Q_{\text{abs}} \pi a^2 >_v J_{v,c} dv. \quad (14)$$

One obvious source of such radiation field is ISRF itself ($J_{v,c} \equiv J_{v,\text{ISRF}}$). For simplicity one can use ratio $[\dot{H}_c / \dot{H}_*(r_0)]$ as a free parameter with values in the range ($C = 0-10$). Notice from expression (11) that the *external heating* leads to a nearly isothermal temperature distribution for positions far from the central star, if large values of C are used. Using equation (11) in equation (1), and after a change of variable of integration from r to T , we get

$$F_v(\lambda) = \left[\frac{4 \pi \kappa(\lambda) m_d n_0}{D^2} \right] A_1 \int_{T_{\min}}^{T_{\max}} A_2(T) B_v(\lambda, T) dT, \quad (15)$$

where,

$$A_1 = r_0^\gamma (1/16) 2^\gamma r_*^{3-\gamma} (4+m) T_*^{-(4+m)}, \quad (16)$$

$$A_2(T) = \left[\frac{[T(r)]^{3+m}}{[(T(r))^{4+m} T_*^{-(4+m)} - C]^{(2.5-0.5\gamma)}} \right]. \quad (17)$$

The function $A_2(T)$ is rather insensitive to the magnitude of C when the dust shell is compact, meaning that all radial points in the shell are closer to the central star. Thus for example, in a compact shell with $\gamma = 2$, equation (15) goes to equation (4) of Gillett et.al (1986). For extended shells, $A_2(T)$ depends on C significantly.

2.2 Estimation of surface brightness $I_V(\lambda, P)$ in the optically thin limit:

We employ the expression given in Gillett et al (1986) for estimating the intensity distribution, also referred to in their paper as *intrinsic profile*. The intensity distribution $I_V(\lambda, P)$ at any impact parameter P is given by

$$I_V(\lambda, P) = 2m_d \kappa(\lambda) n_0 r_0^\gamma \int_P^{r_{\max}} \frac{B_V[\lambda, T(r)] dr}{r^{\gamma-1} (r^2 - P^2)^{1/2}} \quad \text{for } r_{\min} \leq P \leq r_{\max}. \quad (18)$$

When $P < r_{\min}$, the lower limit of integration has to be taken as r_{\min} . For an *isothermal* temperature distribution $T(r) = T_c = \text{constant}$, equation (18) further simplifies to

$$I_V(\lambda, P) = 2m_d \kappa(\lambda) n_0 r_0^2 B_V(\lambda, T_c) \frac{1}{P} \begin{cases} [\cos^{-1}(P/r_{\max}) - \cos^{-1}(P/r_{\min})] & \text{for } P < r_{\min}, \\ \cos^{-1}(P/r_{\max}) & \text{for } r_{\min} \leq P \leq r_{\max}. \end{cases} \quad (19)$$

2.3 Spectral and Spatial convolutions on the intrinsic intensity distribution:

For a comparison of the theoretically calculated flux density and surface brightness with IRAS observed data, we need to perform a spectral (or frequency) convolution on the theoretical fluxes $F_V(\lambda)$ and the combined spectral and spatial (or beam) convolution using intrinsic intensities $I_V(\lambda, P)$. The IRAS passband filters are substantially wide (widths: 8 μm , 16 μm , 60 μm , and 75 μm centered approximately at 12 μm , 25 μm , 60 μm , and 100 μm respectively). Hence the flux density observed at 60 μm for instance, has contributions from emission at other frequencies in the band, and vice versa. In other words, we have to convolve the flux density function in the 60 μm band with the 60 μm band '*spectral response function*' to get the true flux density at 60 μm and to compare directly with the observed flux density. The spectral response functions of all the four IRAS bands have been tabulated in the IRAS supplementary catalogue. We have convolved the flux density spectrum and intensity spectrum in the individual IRAS bands, with respective response functions. The flux density in the IRAS bands are measured using telescope beam sizes larger than the source size. For example, the IRAS flux densities from R CrB are measured with a 24' diameter beam, and the

source diameter is approximately 18'. In principle, we need to observe using a much larger beam size, to see the entire source as a point source. As such the observations are made with beams of sizes comparable to the source size, we are required strictly speaking, to convolve our theoretical fluxes also, with a relevant beam pattern of the 24' diameter beam centered on the source. This will take care of finite beam size effect which is present in flux density measurements. In practice however, it is not necessary to do such a convolution, as long as strongly emitting region of the dust cloud has an effective radius smaller than the radius of the beam employed in integrated flux density measurement.

The brightness distribution on the surface of the cloud is measured with a beam size much smaller than the source size. In fact, smaller the beam size, larger is the information content for individual beam positions. The IRAS beam sizes in the four bands mentioned above, are reasonably smaller to allow good disk resolved measurements to be made. The 60 μm and 100 μm beam sizes are respectively, (1.5'x5') and (3'x5'), with short axis parallel to the in-scan direction. The *convolved brightness* $\tilde{I}_v(\lambda, p)$ is measured by centering such small beams at several positions p (different from the P used in the discussions so far, see equation 24) across the disk. The 60 μm brightness of R CrB for instance is measured at 17 positions (p) on the visible disk of the source. The expressions we give below for *beam pattern* assume a circular cross section of the beam, at the source. The total convolution integrals characterised by a tilde (\sim) above respective symbols are written as

$$\tilde{F}_v(\lambda_i) = \int_{A_{\lambda_i}}^{B_{\lambda_i}} G(\lambda_i, \lambda) F_v(\lambda) d\lambda, \quad i=1,4., \quad (20)$$

involving only a spectral convolution on the flux density, and a spectral+spatial convolution

$$\tilde{I}_v(\lambda_i, p) = \int_{A_{\lambda_i}}^{B_{\lambda_i}} G(\lambda_i, \lambda) I_v^c(\lambda, p) d\lambda, \quad i=1,4., \quad (21)$$

on the intrinsic intensity. The spatially convolved intensity profile is obtained from

$$I_v^c(\lambda, p) = \int_0^{2\pi} d\theta \int_0^\infty R(\lambda, r, \theta) \left[I_v(\lambda, r, \theta) - C I_{v, \text{ISRF}}(\lambda) \right] r dr. \quad (22)$$

In the above equations, the functions $G(\lambda_i, \lambda)$, $i=1,4$ represent the normalised spectral response functions of the four IRAS bands ($\lambda_1 = 12 \mu\text{m}$, etc.). These functions are roughly centered around λ_i and depend upon the transmission characteristics of the IRAS filters of width $[A_{\lambda_i}, B_{\lambda_i}]$ centered around λ_i . The function $R(\lambda, r, \theta)$ is the normalised *spatial response function* of the beam, or simply called as beam pattern. For the applications in this paper, we have used angle independent beam patterns given by

$$R(\lambda, r, \theta) = R(\lambda, r) = \begin{cases} (1/2 \pi \sigma_\lambda^2) e^{-r^2/2\sigma_\lambda^2} & \text{for Gaussian beam} \\ (1/2 \pi \sigma_\lambda^2) \delta(r - \sigma_\lambda) & \text{for uniform beam} \end{cases} \quad (23)$$

where $\delta(r - \sigma_\lambda) = 1$ for $|r| < \sigma_\lambda$ and $\delta(r - \sigma_\lambda) = 0$ for $|r| > \sigma_\lambda$, namely a step function of width $2\sigma_\lambda$. The half width of the beam is given by $\sigma_\lambda = (r_{b,\lambda}/R)$ in dimensionless units where R is the radius of the source and $r_{b,\lambda}$ is the radius of the beam at the source. We compute the intrinsic profiles $I_v(\lambda, P)$ as a function of impact parameter P (the projected radius) using the analytic model or the radiative transfer program, as the case may be. For the quantities $I_v(\lambda, r, \theta)$ required on a fine (r, θ) mesh centered around specified position p of the beam, we do interpolation on $I_v(\lambda, P)$ computed earlier on P grid. The following expression is useful

$$P = [r^2 + p^2 - 2 r p \cos(\pi - \theta)]^{1/2}, \quad (24)$$

where p is the distance of the beam center from the center of the visible disk. Notice from equations (21) and (22) that in order to get $I_v(\lambda, p)$ we have to perform spatial (beam) convolution on a large number of frequency points in each *frequency band* characterised by λ_i . This is disadvantageous, since performing accurate spatial convolution is computationally expensive. Basically the actual wavelength dependence of the beam sizes is not known (it depends on instrumental characteristics). It is acceptable however to assume $[\sigma_\lambda]_i = \sigma_{\lambda_i}(\lambda/\lambda_i)$, $i = 1,4$ based on a diffraction limited wavelength dependence. It is not a bad approximation, even to assume that, in a given bandwidth $[A_{\lambda_i}, B_{\lambda_i}]$, the beam width remains at certain

constant level. We have selected $[\sigma_\lambda]_i = \sigma_{\lambda_i}$, $i = 1, 4$. Notice that with this assumption, the order of integration (spatial + spectral) can be *reversed* to get (spectral + spatial) convolution integral (see equations 21 and 22). This has great advantages computationally, since we now need to perform only 4 spatial convolutions ($i = 1, 4$) to get $\tilde{I}_v(\lambda_i, p)$ at any one position p on the disk (compared to hundreds of spatial convolutions to be performed for each p otherwise). The intensity of interstellar radiation field is given by $I_{v, \text{ISRF}}(\lambda) = 4 F_{v, \text{ISRF}}(\lambda)$. The ISRF in the neighborhood of the Sun can be used as a good approximation.

2.4 Application of AM for the analysis of IRAS flux and surface brightness data:

Now we will discuss some results obtained from Analytic modeling (AM) where the expressions given above (equations 1-24) are utilised. We discuss here the AM approach in some detail with two purposes in mind: (1) To show the similarity of AM approach to Radiative Transfer (RT) approach. In fact, AM solutions, which are much less expensive to compute, can be used to establish bounds on a number of free parameters beforehand, so that expensive trial and error process employing RT approach can be avoided. In this way AM can act as a preprocessor routine to any major RT code. (2) To show that for optically thin dust shells, both give qualitatively same results, although one can obtain a self consistent temperature structure only in the case of RT, carefully considering the dust heating by radiation of all frequencies in the stellar spectrum.

2.4.1. *R Coronae Borealis (R CrB)*

For the purpose of study, we select a set of model parameters close to the actual best fit model parameters suggested by Gillett et. al (1986) for R CrB. We made no attempts to fine tune the parameters further, to provide a "best fit". Our interest is a comparison of AM and RT approaches, than providing independent best fits. In Figure 1a we show the observed flux density $\tilde{F}_v(\lambda)$ in the IRAS bands measured in the point source processing mode (using beam sizes in which R CrB looks a point source in 12 μm and 25 μm bands), by triangles. The flux density $\tilde{F}_v(\lambda)$ measured with a 24' diameter beam, centered on R CrB is shown by circles.

There is no significant difference between these two sets of data in the $12\ \mu\text{m}$ and $25\ \mu\text{m}$ bands. The dotted line shows the theoretical AM flux density spectrum computed using equation (15) after being convolved as in equation (20). The model parameters used in this case are as follows: $T_* = 7600\ \text{K}$, $L_* = 1.04\ 10^4\ L_\odot$, the dust condensation temperature of graphite grains at first radial point being $T_{\text{max}} = 900\ \text{K}$, and $T_{\text{min}} = 90\ \text{K}$ at the surface of the hot shell. A temperature of $90\ \text{K}$, when used in equation (11), with $C = 0$, and $m = 1$, gives the radius of this compact hot shell to be approximately $5''$. This shell extending between $[900\ \text{K} - 90\ \text{K}]$ in temperature scale, is the shell detected in the near infrared ground based measurements made two decades ago. Even being so compact, this shell accounts for almost complete flux density in $12\ \mu\text{m}$ and $25\ \mu\text{m}$ bands, and for nearly half of the flux density at $60\ \mu\text{m}$. These fluxes are much in excess of the photospheric values of the central star. Hence they truly represent the IR excess and are emitted by dust particles present in this compact shell. Other parameters employed in figure 1a are further, $\gamma = 2$, namely the inverse square density variation in the shell; the normalising temperature $T_0 = 30\ \text{K}$ at $r_0 = 0.14\ R$ cm; $n_0 = 1.38\ 10^2\ \text{cm}^{-3}$; $\kappa_0 = 400\ \text{cm}^2/\text{gm}$; mass density of dust material $\rho_d = 3\ \text{gm cm}^{-3}$; $a = 0.05\ \mu\text{m}$; and $m = 1$. R is the radius of the source $= 1.54\ 10^{19}\ \text{cm}$ corresponding to the angular diameter of $20'$ at a distance of $1.6\ \text{kpc}$. In Figure 1b we show the $(60\ \mu\text{m}/100\ \mu\text{m})$ observed intensity ratio data plotted as a function of impact parameter p on the disk. It is interesting to note that the ratio remains nearly *constant* across the extended cool shell. in the region of $r > 1'$. The lines show AM intensity ratios $\bar{I}_v(60\ \mu\text{m}, p) / \bar{I}_v(100\ \mu\text{m}, p)$. The ratio remains nearly constant across the entire apparent disk for the AM. The constancy of any intensity ratio means that, in an optically thin medium, the *dust temperature* is independent of distance from the central star. This peculiarity is the most important part of R CrB surface brightness data, since if the dust in the extended shell is heated by central star radiation, the temperature never remains constant due to geometric dilution of stellar radiation as a function of radial distance from the central star. In Figure 1c we show the $60\ \mu\text{m}$ brightness distribution across the disk. The filled triangles represent unprocessed in-scan data measured with $(1.5' \times 5')$ beam. In

Figure 1d analogous measurement made with (3'x5') beam size in the 100 μm band are shown by filled squares. The open triangles and squares represent corresponding point source processed data in these two bands. Only right half of the *brightness profile* is shown. The vertical error bars show difference between left and right half segments of the profiles. The point source processed data is obtained by subtracting the *point source response function* (PSR) from the original unprocessed in-scan data. The PSR is computed employing the theoretical $F_{\nu}(\lambda)$ estimated using equation (15). The point source component of intensity profile computed for the 5" radius point source (the inner hot shell) is then 'subtracted' from the original in-scan data. This results in surface brightness data profiles that are formed by contributions to any given line of sight *from mainly the extended shell*. Further the theoretical *intrinsic intensity profiles* computed from equation (18) or (19) are 'convolved' with this PSR function at each individual impact parameter to take care of the '*point source response of telescope beam pattern*' approximately, when observing the extended component of emission (see Gillett et. al., 1986 and Hawkins, 1990 for discussion on this matter).

However we have taken a different approach in computing our AM brightness profiles. We do not compute PSR and convolve it with intrinsic intensities (as mentioned already the intrinsic profiles are obtained either from AM or from RT). Instead we do the beam convolution as discussed in equations (21)-(23) on intrinsic profiles. It can be seen that for a Gaussian beam pattern, our approach is somewhat equivalent to the approach just mentioned above, since clearly PSR function resembles our Gaussian beam function in shape and width (see Gillett et. al, 1986, Fig.3). The curves in Figure 1c represent intrinsic (= spectrally and spatially unconvolved) profiles. The three curves correspond to three different constant temperatures of the extended shell. In obtaining these profiles, we have used $10 n_0$ as the normalising density. In other words, we have enhanced the density contrast all over the extended shell ($1.4' < p < 10'$) as compared to the extrapolated density distribution from the 5" inner shell, which was employed to model *only* 12 μm and 25 μm fluxes (see Gillett et. al, 1986 also). This *density contrast* in the extended shell of R CrB seems to be conspicuous,

since as we see later it is always required (even in RT models) to fit the IRAS data, particularly the $100\ \mu\text{m}$ brightness data. It simply means that if the extended shell has moved out from the inner hot shell ever since the termination of last episodic mass loss event, and has an independent existence now continuously expanding with same velocity and massloss rate, then the dust density in this shell is substantially higher (≈ 10 times) than obtains in the scenario of single large shell with a single density power law. This is the *fossil shell* scenario suggested by Gillett et. al (1986). It is likely that a density enhancement may be caused by accumulation of dust by subsequent mass loss events. It can also arise from a slow dispersion of large discrete dust clouds ejected during massloss. The fossil shell maintains a constant mass loss rate *as many* (= density enhancement factor) times smaller than the ongoing mass loss rate prevalent in the inner hot shell. As we see later, this scenario although plausible is not standard, since the *position* of remnant shell (meaning its inner edge) should depend upon actual evolutionary details of the system, and not be fixed arbitrarily to fit the surface brightness data. In this paper, we have employed this "position" of the remnant shell as a free parameter, and show that a series of models are possible depending on this parameter alone. In Figures 1e,f we show the corresponding cases of Figures 1c,d but after those intrinsic profiles are (spectrally + spatially) convolved with respective spectral response (G) and beam response (R) functions. The magnitude and shape of the brightness profiles are quite different from the intrinsic profiles after they are convolved. It happens because the spectral convolution involves the intrinsic profiles (at several other wavelengths in the spectral band) which have very different and strong spatial dependence. The spatial convolution obviously smoothens the spatial features such as the one at the inner boundary of the fossil shell (the kink at $1.4'$), due to spatial coupling of the emission in nearby lines of sight, covered inside the beam integration. In Figure (2), we show the cases in which all other parameters are same as in Figure (1), and with $T_1 = 30\ \text{K}$, but for the *opacity index* m being treated as a free parameter. The values of m selected are $m = 0.9, 1.0, \text{and } 1.2$ namely those representative of highly amorphous dust grains. Notice that the effect of m on $100\ \mu\text{m}$ brightness is

insignificant in this position of the fossil shell. The $60\ \mu\text{m}$ brightness is somewhat affected, because a change in m produces significant changes in the radius of inner boundary of the shell, as well as changes the wavelength dependent emission efficiency of the grains in a shell, which is deliberately tuned for peak emission at $100\ \mu\text{m}$ ($\lambda_{\text{max}} T_c \approx 0.3$ with $T_c = 30\ \text{K}$). The models shown in Figures (1) and (2) can be grouped as *isothermal models* where we have directly 'prescribed' the temperature as constant at certain level, without being concerned about the dust heating mechanism involved etc. These models are thus too simplistic. When the dust temperature distribution is computed using actual *thermal equilibrium relation* (equation 11), with a contribution to heating from external ISRF and the stellar radiation, then the free parameters required to fit the observed $\tilde{I}_\nu(\lambda, p)$ are somewhat different. In this later case, the values of temperatures in the outer layers of fossil shell are smaller compared to our prescribed value of $30\ \text{K}$ of isothermal models. In order to heat the dust in the outermost layers to such temperatures so that we get required $100\ \mu\text{m}$ emission, a position independent heating source characterised by parameter $C = 4$ is employed. The parameters used for *thermal equilibrium models* (Figures (3)) are same as the isothermal models except $n_0 = 6.2 \times 10^5\ \text{cm}^{-3}$ at $r_0 = 1.4'$ in the computation of intrinsic profiles. Opacity index m is now the free parameter. Such a high density in the inner parts of fossil shell, is necessary in order to obtain required amount of brightness in this region. Another reason for requiring high densities is rather small size of the dust particles we have selected to represent amorphous carbon. The three model profiles in Figures 3e,f correspond to three different values $m = 0.9, 1.0, 1.1$. The first two cases do not differ much. $m = 1.1$ leads to large $60\ \mu\text{m}$ and slightly larger $100\ \mu\text{m}$ emission in the fossil shell compared to observed brightness. We see that brightness profiles in these thermal equilibrium models depend sensitively on m unlike the isothermal case. In Figure (4) we present the dependence of AM results on external heating parameter C , which specifies how many times the ISRF in the solar neighbourhood is being employed. From the Figures, it is clear that brightness profiles sensitively depend on this parameter. If the density of dust in extended shell is smaller, then more and more of this isotropic heating is required in order to

maintain the local radiation density which is responsible for heating the dust. In Figure (5) we present the AM results for different values of density exponent γ . The brightness profiles depend quite sensitively on the density variation in the extended shell. The fossil shell is quite far from the central star ($T_1 \approx 30$ K). For a given amount of dust mass in this fossil shell, an inverse square ($\gamma = 2$) power law seems to provide a good fit. It is important to note that the disk integrated flux density computed for $60 \mu\text{m}$ and $100 \mu\text{m}$ bands, employing the (spectrally + spatially) convolved profiles, provides a good fit to the observed flux density data also (the open circles at $60 \mu\text{m}$ and $100 \mu\text{m}$ in the flux density plots). The fits are not shown here because they are fully independent of $12 \mu\text{m}$ and $25 \mu\text{m}$ flux density calculation.

2.4.2. *W Hydrae (W Hya)*

We present the analytic model results of W Hya in Figures (6) - (7). In Figure 6a, the analytic fit to $12 \mu\text{m}$ and $25 \mu\text{m}$ flux densities are shown. The filled dots represent flux densities observed in the point source processing mode. The open circles refer to the observations made with a $30'$ diameter beam. The source diameter is approximately $20'$. The source size is much smaller in $12 \mu\text{m}$ and $25 \mu\text{m}$ bands. In Figure 6b, we show the $60 \mu\text{m}/100 \mu\text{m}$ intensity ratio. The filled circles and open circles show respectively the unprocessed and point source processed data. In the AM the geometry employed for W Hya is similar to that of R CrB (it is not so when we model these two sources employing RT approach). The common model parameters used in all the W Hya analytic models are as follows: $T_* = 2700$ K; $L_* = 1.2 \cdot 10^4 L_\odot$; $T_{\text{max}} = 1000$ K; $T_{\text{min}} = 250$ K at the surface of compact hot shell; $D = 130$ pc; $R = 0.5$ pc; $\rho_d = 3 \text{ gm cm}^{-3}$; $a = 0.10 \mu\text{m}$; The normalising quantities $T_0 = 240$ K; $n_0 = 5.77 \cdot 10^6 \text{ cm}^{-3}$; $r_0 = 0.005 R (= 6'')$; and $\kappa_0 = 60 \text{ cm}^2 \text{ gm}^{-1}$ corresponding to amorphous silicate grains. The radius of the compact shell is roughly $5''$ corresponding to $T = 250$ K and $m = 1.2$. Also, the density exponent $\gamma \approx 2$ is used in this tiny hot core. All the symbols have same meaning as in case of R CrB, unless mentioned otherwise. This core of hot dust is responsible for almost all of the $12 \mu\text{m}$ and $25 \mu\text{m}$ fluxes and part of the $60 \mu\text{m}$ and $100 \mu\text{m}$ fluxes. For Figure (6) the following specific parameters which are only to do with the

extended (we still do not call it *fossil*) shell, are used along with those just given above: $r_1 = 6''$; and $T_1 = 240$ K. The density law exponent γ is a free parameter for these three figures. Corresponding to $\gamma = 0.0, 0.5$, and 1.0 in the extended shell, the specific renormalising factors (which multiply n_0) are respectively $1.92 \cdot 10^{-3}$, $1.92 \cdot 10^{-2}$, and $0.96 \cdot 10^{-1}$. Such large differences in normalising factors between the compact shell and the extended shell arises partly because we employ $\gamma \equiv 2$ in the core and $\gamma \leq 1$ in the extended shell. There is no external heating by ISRF in W Hya models i.e. $C = 0$. The sizes of the Gaussian beams used in spatial convolution are same as those employed for R CrB, namely $\sigma_{100 \mu m} = 0.1125$ and $\sigma_{60 \mu m} = 0.0650$. Notice that in case of W Hya, the extended shell begins very close to the surface of the compact shell. This is in contrast with the R CrB extended shell which starts quite far from the surface of inner compact shell (in good analytic model fits). Because of this proximity of the fossil shell to the central star, the dust near its inner boundary is hot, leading to a sharp increase in $\tilde{Y}_\nu(60 \mu m, p)$ for $p < 0.3$, in all the model brightness profiles of W Hya. In Figures 6c,d we show intrinsic profiles at $60 \mu m$ and $100 \mu m$. The filled triangles/squares and open triangles/squares correspond respectively to unprocessed/point source processed data. The shape of the cusp at r_1 which is clearly seen in Figures 3c,d for instance is not resolved in the adapted ordinate scale, because the two shells are extremely close. The intrinsic profiles at $60 \mu m$ and $100 \mu m$ have similar shape as those of R CrB but there is a sharp increase in intensity at r_1 due to larger amount of central condensation of dust in that region of W Hya extended shell, which strongly saturates the beams. In Figures 6e,f we show the corresponding profiles obtained after performing the convolutions. For this "position", meaning inner boundary radius of the extended shell, it appears that $\gamma = 0.0$ provides a reasonable fit to the surface brightness data at least in the region $0.3 \leq p \leq 1.0$ and $0.5 \leq \gamma \leq 1.0$ provides better fit to the $100 \mu m$ data, in regions $0 \leq p \leq 0.3$. We stress once again that the position of the extended shell is a crucial parameter even for W Hya, and one can generate a series of best fit models based on this parameter T_1 alone. The main conclusion from Figure (6) is that the extended shell is *not* a continuation of the inner compact shell, despite being very close, as

seen through different density contrast parameters required for each shell, and the necessity to use different density laws in each shell. Whether this points to the *remnant (or fossil)* nature of the extended shell is not clear at this point. In Figure (7) we show the effect of opacity index m on flux and surface brightness, in $\gamma = 0.5$ density model. All other model parameters are same as those employed for Figure (6). Increasing or decreasing the value of spectral index m about a best fit value (say, $m = 1.2$), correspondingly changes the flux and surface brightness. The parameter m strongly affects the dust emission and also the temperature gradient in the dust cloud. The temperature gradient is mapped almost directly onto the frequency gradient of a flux density spectrum and the spatial gradient of intensity in an optically thin medium. From these figures it is clearly seen that a range of density laws with $\gamma = 0 - 1$ can fit the data, and m can be used to fine tune the fit. Since employing different γ 's means very different mass loss rates for a given expansion velocity ($\dot{M}_d = 4 \pi r^2 \rho(r) v(r)$, $\rho(r)$ being the dust density in the atmosphere), it is not useful to model the extended shells, using single power laws throughout the shell unless we can narrow down the range $\Delta\gamma$ and Δm based on observations or more detailed modeling.

3. RADIATIVE TRANSFER ANALYSIS OF IRAS DATA

In the previous section on analytic modeling we examined the physical quantities involved and the influence of independent parameters in the problems at hand. The radiative transfer (RT) analysis is not much different from AM analysis as far as handling the free parameters of the problem namely γ , m , T_1 , r_1 , C etc. is concerned. Indeed the convolutions are performed in exactly the same manner in both the cases on intrinsic (specific) intensities. The following difference between AM and RT has then to be understood before going on to details of RT models: (1) the temperature structure $T(r)$ is assumed in AM, as that given by thermal equilibrium condition (equation 11). On the other hand, $T(r)$ is computed as an end product of the modeling in RT approach. Since $T(r)$ is non-linearly coupled to the local radiation field,

we need to solve RT equation and energy balance equation simultaneously and iteratively. The rate of convergence of iteration depends on the goodness of initial guess for $T(r)$. See Leung (1976) and Egan et. al. (1988) for a discussion of the method of solution and details of coding respectively. The $T(r)$ computed using equation (11) can be used for this purpose, with m and C values *derived* approximately by the corresponding best fit AM. We have found this procedure to be very useful in practice. (2) In the AM although a spatially independent dust heating source can be assumed through a choice $C \neq 0$, no details such as the relative strength and frequency dependence of this source is relevant. However in RT approach, this external heating source is assumed to be the ISRF incident on the outer boundary and since it is a boundary condition, flux and surface brightness results depend quite sensitively on its strength and frequency dependence. The dust heating from ISRF is mainly due to its UV component. (3) The normalisation quantities n_0 , r_0 , T_0 derived in AM can be advantageously used in the RT approach also. However the total optical depth defined as

$$\tau_\lambda(r) = \int_R^r Q_\lambda \pi a^2 n(r) dr \quad (25)$$

is a more practical free parameter in the RT approach. (4) In computing brightness profiles in AM we inherently assume that the emission originates locally in the self emitting extended shell surrounding a hollow cavity. Secondly, at the inner boundary no radiation input is given. An inner hot dust shell of radius $6''$ is employed to model the point source processing flux densities. Hence both these shells are treated as absolutely independent. In RT approach, the *diffuse radiation field* at every point within the system is included and hence central star, the inner hot shell and extended shell parameters enter more sensitively in to the modeling effort and are taken care consistently. (5) The difference between AM and RT solutions increases as the dust optical depth increases. This is due to inapplicability to the optically thick media, of many expressions employed in AM based on optically thin approximations.

3.1 RT models of R CrB

We now discuss the RT models computed by us. In modeling the R CrB data we have

employed the *two step* (or two-component) model approach. It is not same as the *combination* of solutions obtained for inner compact shell and the extended remnant shell separately, as is done in AM. Here the RT problem is solved twice. The first [component] solution is to compute the radiation field in the inner compact shell constituting the densest part of the circumstellar shell. This shell is formed partly due to current massloss. Almost the entire optical depth occurs in this shell. The emergent net flux and the intensity distribution across this compact disk are computed employing the central star radiation as inner boundary condition and no radiation incident on the outer boundary as the outer boundary condition. This outer boundary condition should in principle, take care of inward emission (back warming) from the external cool dust shell surrounding it. In practice since the extended shell, being much cooler ($T \approx 30 \text{ K} - 10 \text{ K}$) emits weakly in the optical and near IR regions of the spectrum, the effect of external illumination on the compact hot dust shell ($T \approx 900 \text{ K} - 90 \text{ K}$) is small and hence can be ignored in the first approximation. The second [component] solution involves computing the radiation field in extended cool shell, employing the emergent diluted radiation of the compact shell, as inner boundary condition and the external ISRF as outer boundary condition. It is important to note that, although the two concentric shells are separated, and there is no dust in between them, a continuity of the solution exists across the shell boundaries. This also means that the net flux remains constant at all the radial mesh points encompassing both the dust shells. Thus the extended shell is (artificially) separated from the compact shell, without affecting the generality and self-consistency of the RT solution. The best check for verifying the correctness, continuity and accuracy of the final solution, is an intercomparison of intensities and fluxes computed employing a '*single shell model*' and a '*two shell model*' with identical parameters except for separation of the shells. There are two reasons for our using this two step approach. (1) Since the extended shell can be positioned arbitrarily and can have arbitrary physical parameters completely independent of the inner compact shell, it provides a natural leverage to deal with the scenario of detached remnant shells such as in the case of R CrB. (2) It is rather easy to separate the hot dust

emitting regions (responsible for 12 μm and 25 μm emissions) and the cool dust emitting regions (responsible for 100 μm and partly 60 μm) without significantly affecting the total emergent flux in all the IRAS bands. The problems we encounter employing a two step approach is that there are more number of free parameters to handle, and hence more observational constraints are needed in fixing some of the parameters. The physical properties of inner shell are relatively better known, so that our modeling basically involves varying the parameters of the outer extended shell.

3.1.1. Effect of variation of opacity exponent m

In Figure (8) we present one of the series of schematic RT models of R CrB and discuss the results in comparison with results of AM. In Figure 8a we show the flux density data. The data points have same meaning as in Figure 1a. The model parameters used for the Figure (8) are given below. Inner compact shell has the following parameters: $T_* = 7000$ K; $L_* = 1.04 \cdot 10^4 L_O$; $R = 6''$; $D = 1.6$ kpc; solid angle subtended by the entire source at earth $\Omega = 2.6 \cdot 10^{-5}$ sr; $T_1 = 900$ K; $\rho_d = 3 \text{ gm cm}^{-3}$; $a = 0.05 \mu\text{m}$; $\kappa_0 = 400 \text{ cm}^2 \text{ gm}^{-1}$; $\gamma = 2$; total optical depth $\tau_{0.55\mu\text{m}} = 0.22$; density enhancement parameter $C_2 = 1$; and external radiation parameter $C = 0$. The cool extended shell has the following parameters: $r_1 = 1.4''$; $T_1 = 30$ K; $\gamma = 1.9$; $\tau_{0.55\mu\text{m}} = 10^{-3}$; density enhancement parameter $C_2 = 5.0$ (implying the use of $C_2 n(r)$ for $r > 1.4''$); and external radiation parameter $C = 15$ (meaning the external boundary condition is $= C * I_{\nu, \text{ISRF}}(\lambda)$); and the beam size parameters $\sigma_{100\mu\text{m}} = 0.225$ and $\sigma_{60\mu\text{m}} = 0.125$ with a Gaussian beam pattern. The inner boundary condition for this shell is, as mentioned earlier, the diluted net flux $F_{\nu}^I(\lambda) [R^1/r_1]^2$ of the compact shell (superscripted here as I). The 12 μm and 25 μm fluxes are almost entirely due to this compact shell. It also emits flux densities of 3 Jy and 0.8 Jy at 60 μm and 100 μm respectively. Thus nearly half of the integrated flux observed at 60 μm band arises in this compact shell itself, with the rest of the flux contributed by the extended shell. On the other hand, more than 90% of 100 μm flux arises in the extended shell, and only 10% or less is due to emission in the compact shell. If we increase the size of the compact shell for instance, the long wavelength flux density slowly

increases. The geometry we have employed for RT in this subsection is similar to that used in AM (since $T_1 = 30$ K for the extended shell). However other parameters are different, because in RT approach we model both shells together. The model parameters used for this series of three models are closer to best fit model parameters suggested by Gillett et. al (1986). It can be seen that the results are quite sensitive to the opacity index m . Some physical parameters of this two component model are plotted in Figure 8e. We find that only when the dust temperature in the extended shell is nearly constant in the range 30 K - 25 K, do we get qualitative fits to the data, in any model of R CrB. To maintain this near constancy of $T(r)$ across such a large shell, we always require very strong ISRF (namely $C = 10 - 30$). Since the models depend sensitively on various physical and geometrical parameters of both the shells, we consider that it is useful to understand the dependence of the model fits by varying one parameter at a time for the sake of clarity. The parameters are also not varied over a large range as is the practice in pure theoretical modeling employing RT. Rather we select the set of parameters which approximately fit the data, and then vary the parameter under question around that value. In this manner, the effect of this parameter on two component modeling in general, and on the R CrB models in particular is understood. In all the models of R CrB presented in this paper, the characteristics of compact shell are fixed, and only the parameters of the extended shell are varied. This is done essentially to study extended shell in more detail. However to avoid confusion, we specify quantities related to extended fossil shell by *ext* and those related to inner shell by *inn* whenever necessary.

3.1.2. Effect of position [$r_1(\text{ext})$] of the extended shell

This series of models is run by changing the parameter $T_1(\text{ext})$, the inner boundary temperature of the extended (fossil) shell. The radius $r_1(\text{ext})$ is computed from $T_1(\text{ext})$ given as input. In Figure (9) we show the results for models in which the extended shell starts (not condensates) at three different positions. We select three values of temperature $T_1(\text{ext}) = 30$ K, 50 K, and 80 K for this purpose. Corresponding positions of the extended shell are respectively $r_1(\text{ext}) = 1.4'$, $0.4'$, and $0.12'$. It can be seen clearly that for a given set of model

parameters (in this Figure (9) we have $T_1(ext) = 50$ K model as a close fit model), moving out the extended shell (by a choice $T_1(ext) = 30$ K), leads to a decrease in $12\ \mu\text{m}$ and $25\ \mu\text{m}$ fluxes because of rapid decrease of radiation field in these two bands, away from the compact shell surface. As we move away from the compact shell, the dust at the inner edge of fossil shell can not be heated sufficiently to emit in $12\ \mu\text{m}$ and $25\ \mu\text{m}$ bands. Although rather diluted infrared spectrum of the hot shell is subsequently absorbed in the fossil shell, the dust emission mainly occurs in $100\ \mu\text{m}$ band. When the fossil shell is moved inwards ($T_1(ext) = 80$ K), the $12\ \mu\text{m}$ and $25\ \mu\text{m}$ fluxes do not differ from those of $T_1 = 50$ K case, since these near infrared photons are intercepted before diluted, at the high density inner regions of fossil shell and reemitted in the same bands, due to dust being sufficiently hot. Since the column density for longer wavelength emission is substantially smaller in this case (see Fig. 9e), the $60\ \mu\text{m}$ and $100\ \mu\text{m}$ fluxes and intensities are smaller. Thus although the dust temperature in the cloud is not much affected relative to $T_1 = 50$ K case, by moving the shell in ($T_1 = 80$ K) or out ($T_1 = 30$ K), the $60\ \mu\text{m}$ and $100\ \mu\text{m}$ fluxes and intensities increase or decrease respectively, due to increase or decrease of long wavelength optical depth in the outer parts of the fossil dust cloud. The different positions of the fossil shell basically represent how far the shell has moved since the termination of massloss (see section 4.1 for discussions)

3.1.3. Effect of variation of density exponent $\gamma(ext)$

This series of models is run by changing the parameter $\gamma(ext)$ in the density distribution of the fossil shell. In Figure (10) we show the results for a model which is one of the best fit models for *that position* ($T_1 = 30$ K) of the extended shell. We select $\gamma(ext) = 1.5, 1.9$, and 2.3 for this purpose, with $\gamma = 1.9$ being the median best fit model and also serving as link with models in other subsections of 3.1. Density exponent is a sensitive parameter. For smaller values of γ , namely $\gamma = 1.5$, the amount of dust is large throughout the extended shell (particularly in the regions $p > 3'$). Hence both $60\ \mu\text{m}$ and $100\ \mu\text{m}$ flux density as well as surface brightness are larger as compared to $\gamma = 1.9$ or 2.3 models. For $\gamma = 2.3$ the dust density in most part of the extended shell is small. Hence the $60\ \mu\text{m}$ and $100\ \mu\text{m}$ flux density

and intensity are also small. However for lines of sight crossing the shell in the inner parts ($p < 3'$) the intensity distribution does not depend very much on the kind of density distribution in outer parts of the shell, because the different density profiles $n(r)$ nearly merge in this region. It can be noticed also from Figure 10e that $p \approx 3'$ is the position where the density profiles cross over each other. This happens because we constrain the models with a given input value of optical depth $\tau_{0.55 \mu m}$ for all these density laws, which basically redistributes the dust density in such a way as to attain this value of optical depth. All the model parameters employed for Figure (10) are same as in the previous section 3.1.2 except for $r_1(ext) = 1.4'$ (i.e. $T_1(ext) = 30$ K) and $m = 1$, with γ being treated as the free parameter. It is clear that the brightness fit for the central positions is dictated by very strong emission from the inner shell, at shorter wavelengths ($\leq 30 \mu m$), than by the physical properties of the extended shell itself. In Figure (11) we show the corresponding results for another position of the shell represented by $r_1(ext) = 0.4'$ ($T_1(ext) = 50$ K). Qualitatively same behaviour as discussed above for the position $r_1(ext) = 1.4'$ of the shell, holds good in this case also. As the extended shell inner boundary approaches the inner hot shell, brightness profiles for $p > 2'$ begin to get weaker for $\gamma = 2.3$ and $\gamma = 1.9$ due to larger overall heating of the extended shell, resulting in a drop in the volume emission in $60 \mu m$ and $100 \mu m$ bands. Thus only a less steeper density distribution such as $\gamma < 1.5$ may fit the data now, since the drop in volume emission is compensated for by increased dust density. Figure (12) shows the behaviour of brightness profiles when the two shells are very close ($T_1(ext) = 80$ K). Thus, although the 'cavity' between the two shells is now replaced with large amount of dust, it does not decrease the $60 \mu m$ and $100 \mu m$ intensities for the rays within $p < 3'$. This is because the shell is optically thin, and the line of sight rays for $p < 2'$ are not sufficiently attenuated inspite of having the largest path lengths. In fact there is a slight increase of $60 \mu m$ brightness due to increased dust column density in $p < 2'$ region which can be seen by comparing Figures 10c, 11c, and 12c. More importantly, we can notice that if the shells are close (or in fact form a single *continuous* shell as with W Hya), then $\gamma = 1$ models provide a better fit than $\gamma = 2$ models if the total optical depth is kept as a constant

irrespective of position of the extended shell. If the dust massloss rate in the shell is small, then optical does not strongly differ for three different positions of the shell. But $\tau_{(ext)}$ decreases slowly with the age of the shell if there is no interaction. This conclusion is in general conformity with the best fit models suggested for W Hya, employing $\gamma \equiv 1$ density law (see Hawkins, 1990 and W Hya models presented in 3.2). The total optical depth is proportional to the total amount of dust of given type, in the extended shell. It is possible to constrain it to a somewhat narrow range through simple estimates of gas to grain density ratio and through models of molecular line features. Thus a single continuous shell models may be employed to model the R CrB data, even with 3 - 10 ISRF environment around the shell, if we employ $\gamma = 1$ density distribution (variable rate of massloss in the uniformly expanding shell). If $\gamma = 2$ density law is employed (constant rate of massloss with constant velocity) we require a stronger (10 - 30 ISRF) since the temperature gradient is steeper in this case. Secondly, although increasing $\tau_{(ext)}$ has similar effect as increasing the magnitude of ISRF for $p > 2'$, it leads to undesirable enhancement of intensity in the region $p < 2'$, due to a larger concentration of dust grains near the inner boundary. As such the range of optical depths we have used are appropriate and are of the same magnitude as suggested in the best fit models of Gillett et. al (1986). Thus our models are represented by similar values of the total dust mass M_d and massloss rate $\dot{M}_d(r_0)$ as in Gillett et. al (1986) models.

We realize that the '*position*' of the remnant shell in the system is a non-trivial parameter. It has important consequences in terms its direct relation to the evolutionary models of asymptotic giant branch phase (Schonberner, 1977). Our models of R CrB are too simplistic to give a definite idea about exact position of the fossil shell, which fits the IRAS data best, since all the model parameters are not strongly constrained. However we point to the importance of this parameter in more realistic modeling. The fact that we can fit the observed data with a model choosing a certain value for the position of the fossil shell, does not help much, since as can be seen from Figures (10), (11), and (12), just a 20 % variation in the

density exponent with small fine tuning using spectral index m , can fit the IRAS data even for such largely different positions as $r_1(ext) = 1.4', 0.4', \text{ and } 0.12'$. Whereas an uncertainty of this magnitude in density exponent γ is acceptable, such a wide difference for the *position* of the fossil shell is not, since the later is connected closely with the evolutionary status of R CrB which is not yet established accurately. Since somewhat narrow range in dust parameters (m , a , and κ_0) as well as density exponent γ , is established, the *positions* of R CrB fossil shell substantially closer than $r_1(ext) = 1.4'$, may well be possible.

3.1.4 Effect of variation of the incident ISRF on temperature structure

In the series of models shown in Figures (13) - (15), we show the effect of ISRF on the flux density and brightness profiles when the extended shell is situated in three positions corresponding to $T_1(ext) = 30 \text{ K}, 50 \text{ K}, \text{ and } 80 \text{ K}$. Figure (13) shows the results for $T_1(ext) = 30 \text{ K}$ case. Although external radiation used is very strong, fluxes at wavelengths shorter than $30 \mu\text{m}$ are not affected because ISRF used is not strong enough to heat the dust to temperatures greater than 100 K in the extended shell. Keeping all other parameters constant, an increase in ISRF increases only the fluxes longward of $30 \mu\text{m}$. The intensity ratio also shows a similar behaviour (larger the ISRF, larger is the ratio), for $p > 3'$. For $p < 3'$, a reversal of this characteristic is seen, i.e the $60 \mu\text{m}$ brightness increases slowly compared to $100 \mu\text{m}$ brightness as the ISRF is increased. This happens because of the competing influence of inner shell radiation field on the $60 \mu\text{m}$ emission and more due to large short wavelength ($\lambda < 30 \mu\text{m}$) radiation density in the cavity, which slowly gives way to the influence of ISRF for $p > 3'$. The $100 \mu\text{m}$ intensity however depends on ISRF more sensitively since ISRF spectrum itself has a sharp increase longward of $60 \mu\text{m}$. Therefore $100 \mu\text{m}$ intensity all across the disk is affected with equal strength as $100 \mu\text{m}$ ISRF can transfer easily into deeper layers in the cloud and also because it is easier to heat the dust to $T \approx 30 \text{ K}$ with the strength of ISRF we have employed here. The $100 \mu\text{m}$ beam width being twice larger than the $60 \mu\text{m}$ beam width, the effect of ISRF gets included even for centered position of $100 \mu\text{m}$ beam. In Figure (14) the effect of ISRF is shown for an intermediate position (represented by $T_1(ext) = 50 \text{ K}$) of the

fossil shell. The impact of ISRF on $60\ \mu\text{m}$ flux is weaker as compared to $T_1(\text{ext}) = 30\ \text{K}$ position. Due to relatively larger increase of $60\ \mu\text{m}$ intensity in the $p < 2'$ region, the intensity ratio also is larger due to which a fit to the observed data is better only in the extended part of the cloud ($p > 4'$). When the extended shell is still closer to the star ($T_1(\text{ext}) = 80\ \text{K}$) the impact of ISRF is rather small (see Fig. 15). For this position, ISRF itself is diluted gradually through interaction with cold dust distributed over a large volume of space in the extended shell. The $100\ \mu\text{m}$ fluxes are too small because of larger heating from the stellar radiation. The general effect of ISRF on dust temperature in the extended shell is that, larger the ISRF, larger is the dust temperature in a large part of the extended shell. In conclusion we can say that use of somewhat strong ISRF environment is inevitable in modeling the IRAS data of R CrB because of the *isothermal nature* of the extended shell, in contrast to the modeling of W Hya presented in section 3.2.

3.1.5. Effect of variation of total optical depth $\tau(\text{ext})$

In Figures (16) -(18) we show the usual position dependent series of models corresponding to three positions of the extended shell. Notice that optical depth $\tau(\text{ext})$ has a strong effect on the distribution of radiation field in the fossil shell. Since we use a nearly inverse square ($\gamma = 1.9$) power law density distribution in these models, the effect of changing $\tau(\text{ext})$ is to basically change the amount of dust at all the radial points of the shell. The change in dust density in extended part of the shell is in direct proportionality to corresponding change in total optical depth. Hence the intensity ratio remains a constant irrespective of the change in optical depth in the extended part of the shell. However in the inner regions, the intensity ratio decreases when we increase the optical depth. This is due once again to larger increase of $60\ \mu\text{m}$ brightness for $p < 4'$ as compared to $100\ \mu\text{m}$ brightness. The change in $60\ \mu\text{m}$ flux as a function of $\tau(\text{ext})$ is slightly smaller because the $60\ \mu\text{m}$ emitting volume is smaller compared to $100\ \mu\text{m}$ emitting volume. The optical depth effect is significant near inner boundary of the shell for all the positions ($T_1(\text{ext}) = 30\ \text{K}, 50\ \text{K}, 80\ \text{K}$), since large contribution to $\tau(\text{ext})$ comes only from these parts of the shell when inverse square density variation is employed.

The dependence of flux density and intensity on the total optical depth is clearly linear because of the extended shell being optically thin for the radiation of all frequencies in the spectrum. If the optical depth is large or the dust is scattering dominated, then this conclusion does not hold. The behaviour of long wavelength diffuse radiation in cold dust shells, heated by central star radiation and by a strong ISRF, is not easy to understand even in a situation involving truly absorbing dust particles (neglecting scattering). It is because of the basically non-local nature of the physical process involved in the highly efficient absorption of short wavelength photons (optical and UV) and the subsequent emission of isotropic thermal radiation almost entirely at much longer wavelengths, characterising the local dust temperature. The process is similar to reprocessing of a high energy spectrum by a cloud of cold electrons, through the process of Comptonisation. When photons of shorter wavelength are absorbed and emitted at longer wavelength, the emitted photons can travel a longer distance in the dusty atmosphere because of the increased mean free path ($l_\lambda \approx \kappa_\lambda^{-1}$) compared to original photons. Hence the infrared photons arising due to absorption of central star radiation by cold dust, travel longer distances in the spherical layers, thereby coupling different geometrical positions (which are characterised by dust particles of different temperatures and curvature factors). This non-local coupling is very similar to transfer of γ -rays in a cold electron atmosphere, or to the transfer of line radiation in the coherent wings of a scattering dominated line. This characteristic of transfer of radiation in a dust cloud, coupled with regular peculiarities of radiative transfer in spherical geometry (see e.g. Nagendra, 1988), make even a simple problem of transfer of continuum radiation in an absorbing dust cloud, obscure to straight forward interpretation. This difficulty persists for optically thin dust shells also to some extent.

3.1.6. Effect of change in density contrast in the $r > 1.4'$ region

We mean by this density enhancement, an artificial increase of dust density beyond certain radius, over and above that given by the regular power law applied to both compact and the fossil shell. In all our models of R CrB we have employed this density enhancement at $1.4'$ irrespective of where the extended shell is positioned. A density enhancement of this type is

equivalent to concentration and settling of cold dust due to some reason. A possible reason could be a drop in the velocity of dust wind around this radius., due to collision with a preexisting fossil shell having smaller but constant mass loss rate. Such a density enhancement (contrast) has been employed even in the optically thin models of Gillett et. al (1986) (see also the analytic modeling in this paper- section 2.4.1). However in their models, the extended shell starts at this position 1.4' itself. *But we have explored models with smaller value of inner radii also (0.4' and 0.12'). This enhancement is also equivalent to the occurrence of large sized grains compared to the cloud interior, in the cooler ($T < 30$ K) layers. Figure (19) shows this effect for the position $T_1(ext) = 30$ K of the dust shell. The amount of cold dust and optical path length (in the extended shell) for all the lines of sight is larger in this position of the fossil shell, compared to closer positions (compare e.g Figs. 19e and 21e). Due to this the $60\ \mu\text{m}$ and $100\ \mu\text{m}$ fluxes which are formed mainly in the extended shell, are slightly larger in the $T_1 = 30$ K case. Also when there is no density enhancement ($C_2 = 1$) the $12\ \mu\text{m}$ and $25\ \mu\text{m}$ fluxes undergo smaller amount of absorption and reprocessing (smaller amount of cool dust), resulting in higher emergent fluxes in these two bands. As the dust concentration is increased ($C_2 \neq 1$), the $12\ \mu\text{m}$ and $25\ \mu\text{m}$ fluxes decrease, due to absorption by cool dust ($T < 30$ K) which can emit only in longer wavelengths ($> 100\ \mu\text{m}$) due to smaller temperatures attained by these dust particles. The $60\ \mu\text{m}$ and $100\ \mu\text{m}$ fluxes are not much affected however, since the effect of change in the cool dust (< 30 K) density is overshadowed by the dominating influence of ISRF in these dust layers. It is difficult to perceive this change in the dust density contrast since a diluted radiation field in $60\ \mu\text{m}$ and $100\ \mu\text{m}$ bands is intercepted by these cold dust layers. The smaller effect for this position of the fossil shell is also seen from Figure 19c,d. Figure (20) shows the density enhancement effect for intermediate ($T_1(ext) = 50$ K) position of the extended shell. There is no significant effect on $12\ \mu\text{m}$ and $25\ \mu\text{m}$ fluxes, for this and any closer position, the reason for which is discussed earlier. The $60\ \mu\text{m}$ and $100\ \mu\text{m}$ fluxes as well as intensities increase as the contrast factor is increased since now the density contrasted layers of dust ($p > 1.4'$), intercept already*

processed high photon density in 60 μm and 100 μm bands. A similar behaviour is seen for the position much closer to the star (Figure (21)) except that the fluxes and intensities are smaller than required, for obvious reasons. The 60 μm and 100 μm extended emission does not linearly depend on the increase of density contrast. In fact as contrast is increased ($C_2 > 10$), a saturation of brightness is soon reached.

3.1.7. The effect of beam dilution on the surface brightness

Finally we discuss in this section the effect of beam sizes on the computed surface brightness profiles. It is well known that in the limit of infinitely small beam sizes, the intensity measured on any position p on the visible disk is the local specific intensity itself. However when the beam sizes are larger, what is actually measured at p , is a spatial convolution of the intensity distribution in a small area surrounding p , with the beam response function. In other words, what is observed in practice is a mean value, which depends on the beam size (beam radius $r_{b,\lambda}$; $\sigma_\lambda = r_{b,\lambda}/R$) and on the beam response function G (Gaussian or uniform). As in the case of optically thin modeling, we use a Gaussian beam of half width $r_{b,100\ \mu\text{m}} = 2.25''$ and $r_{b,60\ \mu\text{m}} = 1.25''$ at the source. They correspond roughly to the radii of circles whose areas at full width are equal to beam areas of the (3''x5'') and (1.5''x5'') rectangular beams of IRAS. The IRAS beams in principle are supposed to have uniform response. Since we find that the difference between uniform beam pattern (square beam) and Gaussian beam pattern is $< 1 - 10\%$ depending on beam position, we have always used a Gaussian beam pattern in this paper, which is more realistic and general. The choice of beam sizes mentioned above, gives a *disk integrated flux* (obtained by integrating on the beam convolved 'mean brightness' at several p on the visible disk) to an accuracy of $\pm 5\%$ of observed fluxes. This simultaneously confirms the consistency of model flux fits and model surface brightness fits to the same level of accuracy. In Figure (22) we show the effect performing the beam convolution using different beam sizes choosing for illustration the intermediate position $T_1(\text{ext}) = 50\text{ K}$ for the models. The three cases correspond to $2r_{b,100\ \mu\text{m}} = (4.05''; 4.5''; 4.95'')$ and $2r_{b,60\ \mu\text{m}} = (2.25''; 2.5''; 2.75'')$ taken in corresponding pairs respectively. This choice

represents a $\pm 10\%$ variation around the regular beam sizes used every where in this paper. Notice that results differ from few percent at the limb to a maximum of 15% at the disk center. A part of this difference can be ascribed to numerical error in performing the convolution integral on different beam sizes but employing same number of grid points. Thus an uncertainty of $\pm 10\%$ in beam sizes results in deviation of same magnitude in model results. Essentially similar conclusions hold for other two positions of the extended shell $T_1(ext) = 30\text{ K}$ and 80 K and hence not shown here. When the extended shell is very close to the inner hot shell ($T_1(ext) = 80\text{ K}$), the convolutions are slightly more accurate for the same resolution in the radial grid. This is because intensity distribution across the interfacing shell boundaries is not very sharp unlike the situation when the shells are well separated (as in the case of $T_1(ext) = 30\text{ K}$). To deal with the strongly coupled variation of specific intensity $I_\nu(\lambda, P)$ as a function of frequency (since we do perform spectral convolution) and space, we use 340 carefully placed radial grid points (340 lines of sight) in solving the transfer equation to get a good P-grid resolution (see equation 24) to start with, before performing the convolution. In performing convolution integral we take further care by employing an r grid that depends on beam position p on the disk and on the scan angle θ measured in the beam coordinate system. For single shell models, normally a smaller number of points (100 to 50 points) in P grid are sufficient (see discussion on W Hya) in computing the line of sight specific intensities in the radiative transfer code. In any case performing convolution integral on an intensity distribution, where the central heat source (star) emits strongly than the fuzzy extended shell, but occupies a very small region of space than the shell itself, poses considerable numerical difficulties.

3.2 RT models of W Hya

In this section we discuss the radiative transfer models computed to fit the W Hya data. Once again we emphasise that obtaining a best fit model is not our criterion, although it can be achieved through a variation of parameters relevant to the source and running a large number of models. That approach is useful when the number of observational constraints are more

(implying a smaller number of free parameters in theoretical modeling). In the schematic models we present, involving single power law variations of density and opacity, a parametric study is more meaningful than a best fit model, since possibly we can systematically narrow down the range of model parameters in subsequent detailed and realistic modeling efforts. For W Hya modeling we use a *single shell model* approach, which is same as conventionally used circumstellar dust shell modeling. In all other respects the modeling is similar to that of R CrB. In fact W Hya modeling is easier since we deal with just one set of model parameters.

3.2.1. Effect of variation of opacity exponent m

In Figure (23) we present the models for three values of m ($= 1.0; 1.1; 1.2$). The open circles represent the integrated flux measured with a 30' beam. The filled triangles represent the point source processing flux density data. The model parameters employed in obtaining these results are as follows: $T_* = 2700$ K; $L_* = 1.2 \cdot 10^4 L_\odot$; source radius $R = 20'$; $D = 130$ pc; $T_1 = 1000$ K; $\rho_d = 3 \text{ gm cm}^{-3}$; $a = 0.1 \text{ } \mu\text{m}$; $\kappa_0 = 60 \text{ cm}^2 \text{ gm}^{-1}$; $\gamma = 1.1$; $\tau_{0.55 \text{ } \mu\text{m}} = 3.2$; density enhancement parameter at 1' radius $C_2 = 1$; and external radiation field parameter $C = 1$. The normalising quantities are $r_0 = 1'$, $T_0 = 102$ K, and $n_0 = 9.23 \cdot 10^3 \text{ cm}^{-3}$. The beam size parameters are $\sigma_{100 \text{ } \mu\text{m}} = 0.1125$ and $\sigma_{60 \text{ } \mu\text{m}} = 0.0625$. The inner boundary condition is the diluted central star radiation field. In addition we have enhanced the density in the tiny central core region of radius 5" by a factor of 2. All these parameters are common for all the models of W Hya unless otherwise stated. From the Figure (23) we can see that, larger the value of m , larger is the flux in all IRAS bands since the dust temperature gradient becomes steeper with an increase of spectral index m and we find as a result, relatively cooler dust in a larger region of the extended shell. The 100 μm flux can be increased by increasing the density of cool dust in the extended part ($p > 2'$) of the W Hya shell. As in the case of R CrB, the fit to the surface brightness data in the region $p < 4'$ (i.e $p < 0.2$ in dimensionless units), is not good. *The reason for discrepancy is once again the failure of single power law density distribution in the inner parts of this highly extended (possibly fossil) shell of W Hya.* We can improve the fit in this region by slowing down the rapid increase of density towards the inner

edge, which occurs within a small distance from the inner edge. A composite power law density in the inner parts of the shell is useful in this effort. Since it is an arbitrary adjustment depending actually on the given set of other model parameters, we have not attempted doing it. Realistic modified power law type density distribution can be generated using a simple treatment of hydrodynamics in radiation driven dust winds (Shutte et. al, 1989). It can be seen from Figure 23e that there is no significant effect on dust density and optical depth distribution as a result of variation of m . The small variation in $T(r)$ in the outer layers depending on the value of m employed, is due to slightly different dust condensation radii for different values of m . A comparison with corresponding models AM (see Figure (7)) shows that the effect is weaker for $60 \mu m$ and in particular for $100 \mu m$ in the AM. The reason for this is relative insensitivity of $100 \mu m$ flux to variation of m , when it is computed using optically thin approximation which does not involve ISRF sensitively into the problem unlike the RT approach. The effect is also similar to that in R CrB models shown in Figure (8).

3.2.2. *Effect of dust condensation temperature T_1*

In radiative transfer modeling it is customary to prescribe the dust condensation temperature as a free parameter. Using the thermal equilibrium condition (equation 11), we can then get the dust condensation radius $r_1(T_1)$. The effect of this important parameter is shown in Figure (24). The three condensation temperatures selected are 900 K, 1000 K, and 1100 K. W Hya dust shell is known to have an oxygen rich composition and hence predominantly silicate based grains in its dust shell. Due to smaller opacity of silicate dust particles, we require a large optical depth value $\tau_{0.55 \mu m} = 3 - 5$ in order to get a sufficient dust density in the inner most parts (hot dust region) of the shell. Smaller optical depths can not reproduce $12 \mu m$ and $25 \mu m$ fluxes in the models we discuss. It can also be seen from Figure 24b that variation of T_1 has almost insignificant effect on intensity ratio. Except the peak intensity at $p = 0$, the surface brightness profiles show the expected behaviour of decrease in the brightness distribution all across the dust shell as T_1 is increased which because of higher temperatures of the dust when the shell is closer to the central star. The corresponding

models of R CrB are presented in Figure (9).

3.2.3. Effect of variation of density exponent γ

The density variation in the dust shell of W Hya has a significant effect on the results. From Figure 25a it can be seen that a slow density law (meaning $\gamma = 0.8$) can be used to fit the $100\ \mu\text{m}$ flux density since it leads to larger amount of dust in cooler parts of the shell. As will be clear in further discussions, we can improve the fit to the surface brightness data also, without affecting this flux fit significantly. In case of W Hya the intensity ratio is a more sensitive function of spectral index m , than the dust density distribution law. This is the usual characteristic observed in circumstellar dust shells which are optically thin to the far infrared radiation. A comparison with corresponding cases in R CrB Figure (10) shows that in spite of larger optical depth of W Hya ($\tau = 3$) as compared to that of R CrB ($\tau = 0.3$), the long wavelength intensities and fluxes still show similar character as regards the variation of γ . As in the case of true emission models, smaller values of γ (relatively larger local dust density in the outer parts) results in larger surface brightness at every point on the visible disk. The $60\ \mu\text{m}$ and $100\ \mu\text{m}$ brightnesses vary linearly with respect to γ . The temperature structure is not affected, as can be seen from Figure 25e. Since the shell is substantially optically thick, it is the transferred radiation density that controls the $T(r)$. When the medium is optically very thick, $T(r)$ is governed by the local dust density through thermalisation of short wavelength radiation.

3.2.4. Effect of variation of the incident ISRF

In the Figure (26), we have shown the effect of external ISRF on the dust heating in the extended shell of W Hya. The three cases correspond to $C = 0, 1$, and 20 . It is interesting that the amount of ISRF incident on the outer boundary of W Hya shell is not an important factor as far as modeling the IRAS data is concerned. In fact, there is no need to employ ISRF contribution to dust heating. Thus we agree with the conclusion drawn by Hawkins (1990) that the highly extended shell of W Hya is mainly heated by central star radiation field. In general, as in the case of R CrB large values of ISRF can enhance the $100\ \mu\text{m}$ flux by heating

the dust to relevant temperature range 25 K - 30 K in the outer layers of dust shell by absorption of short wavelength components of ISRF. This characteristic can be used to improve the 100 μm flux density fit. However unlike the case with R CrB, it is not a basic requirement in modeling the IRAS surface brightness data of W Hya.

3.2.5. *Effect of variation of the total optical depth τ*

The total optical depth clearly characterises the spatial correlation between absorption and emission processes over distances of a photon mean free path. Hence media with larger optical depths basically require a careful consideration of transfer problem. In the present case, however we are dealing with intermediate optical thickness of the shell. Hence the optical depth effects (conventionally called RT effects) are not very strong when compared to the role played by other parameters (m , γ etc) of the problem. From Figure (27) one can see that an increase in τ increases the flux density in all the IRAS bands. In this way it is similar to the effect of varying the opacity exponent m (see the analytic expression (1) or (15) in section 2). But there are basic differences between the two mechanisms. The change in opacity index changes the entire temperature scale itself in the extended shell (see the intensity ratio in Fig. 23b) brought about by changes in dust emission/absorption coefficient at all the points in the medium. Because of this it affects 60 μm and 100 μm radiation fields differently. A change in total optical depth τ grossly changes the number density at all the radial points, and particularly near the inner boundary. For clouds of small optical depths, this does not affect the overall temperature distribution (see section 3.2.3). So a change in τ affects the 60 μm and 100 μm local intensity to nearly the same extent, because of which intensity ratio does not change significantly when τ is changed. The $T(r)$ is strongly coupled to the local dust density only in optically very thick dust shells.

3.2.6. *Effect of density enhancement in the $p > 1'$ region of the dust shell*

We have presented these results to give an analogy with the modeling of R CrB extended shell. Whereas in R CrB, it is almost a necessity to have a dust enhancement in cooler regions ($T \leq 30$ K) of the extended shell 'positioned' anywhere with respect to the hot shell, it is not so

in the case of W Hya. This behaviour once again strongly supports the scenario of fossil shell in R CrB, which accumulates dust beyond certain radius ($1.4''$) through a reduced local mass loss rate compared to inner parts of the fossil shell. But it is not clear whether the extended shell of W Hya is really a fossil shell in the same sense - because W Hya data can easily be modelled without any such arbitrary change in density distribution. In Figure (28), we have shown three cases: a density decrement by a factor of 2; no change from the regular power law; and a density increment by a factor of 2, the density contrast starting at the radial point corresponding to $1''$ from the center of the dust cloud. These changes, as expected affect mainly $60\ \mu\text{m}$ and $100\ \mu\text{m}$ fluxes and intensities. The brightness increases or decreases depending on an increase or decrease of C . It can be seen that qualitatively similar effect on brightness distribution occurs even through normal changes in optical depth and hence there is no necessity from the modeling point of view to assume a density contrast anywhere in the extended shell of W Hya. As mentioned in the beginning, we have increased the dust density in the tiny core of radius $6''$ in the W Hya shell, only to obtain a better fit to $12\ \mu\text{m}$ and $25\ \mu\text{m}$ flux densities. Thus if we assume that expansion velocity is constant in the whole shell, then we indirectly have a mass loss rate twice larger in the core region compared to positions in the immediate neighbourhood. Since we basically have a variable mass loss rate in the W Hya shell ($\gamma \approx 1$, in best fit models), it is possible to visualise that the mass loss rate can be larger in the inner hot shell by this factor.

In order to emphasise the necessity of computing surface brightness and the flux density together in modeling the IRAS data, we have presented a set of models in Figure (29). The models are computed in the same way as discussed in detail in section 3.1 on R CrB. We designate the three models which are arbitrarily selected, as models 1- 3 (dotted, dashed, and full lines respectively) in all the Figures 29a-e. In Table 1 we list some of the input parameters. All the symbols have same meaning as in section 3.1. Rest of the input parameters are exactly same as those mentioned in section 3.1.1, and are common to all the three models presented in Figure (29). From Table 1, it can be clearly seen that the models

are completely random. However as shown in Figure 29a, all these models approximately fit the flux density data. Indeed model 1 (dotted line), and model 2 (dashed line) give nearly identical fluxes in spite of being so much different. The intensity ratio however resolves models 1 and 2. Still, all the three models appear to fit the intensity ratio also, seen independently, fairly well (Fig. 29b). Only the individual surface brightness fits in Figures 29c,d help eliminate model 1 and model 3 as less suitable. Model 2, possibly with small improvement, can be one of the better models since it fits the flux density, intensity ratio, and surface brightness simultaneously. Thus if the constraint of observed surface brightness is not utilised (at least when available), then it is hard to narrow down the possible range of physical parameters. The gross parameters derived from these three models are shown in Table 2. It is useful to calculate the absolute brightness in all the IRAS bands and the mutual intensity ratios, in order to constrain the large number of possible models which emerge from the radiative transfer analysis of IRAS data.

4. CONCLUSIONS

Our schematic radiative transfer models based on self-consistent temperature structure calculation lead to following specific conclusions:

(1) The identification of extended shell of R CrB as a fossil shell by Gillett et. al (1986) is essentially correct, since our models also require a considerable detachment of fossil shell from the inner hot shell. A constant but smaller massloss rate than required in the single shell scenario with no differential massloss rate anywhere in the shell, is appropriate. We find that rather high values of ISRF are necessary to fit the IRAS data if we prefer to retain the picture of constant massloss rate ($\gamma \approx 2$) with constant velocity of expansion through both the dust shells. The ISRF required is larger than suggested by Gillett et. al (1986). It appears that ISRF heating may thus be contributing only to a smaller extent in establishing a constant dust temperature in the shell, and the shell may have a density distribution with a power law index $\gamma \approx 1.0 - 1.5$. From our studies, it is difficult to identify any additional mechanism which can

lead to this isothermal temperature of the fossil shell. However temperature structure also depends sensitively on composition and emission efficiency of the dust grains. The local heating by small grains for instance, which emit strongly in $12\ \mu\text{m}$ and $25\ \mu\text{m}$ bands is one possibility. This can affect the $60\ \mu\text{m}$ fit and $60\ \mu\text{m}$ to $100\ \mu\text{m}$ intensity ratio in the inner parts of the extended shell indirectly. There is no difficulty in modeling the $100\ \mu\text{m}$ surface brightness arising in outer layers by employing usual large grains model. The heating of large grains in the outermost layers by regular (or even smaller multiples of) ISRF is still a reasonable assumption. The grains are more likely to be amorphous carbon or carbon based grains in R CrB fossil shell.

(2) The variable mass loss scenario for W Hya suggested by Hawkins (1990) is reasonable for this star. Although it is difficult to identify the extended shell as a remnant shell, unlike the straightforward case of R CrB, a clear distinction between the mass loss rate in the small $6''$ core region (with density exponent $\gamma = 2$) and the rest of the $1200''$ shell (with $\gamma = 1$) seems to point to a separate identity to the extended shell. There is no need to employ excess ISRF for dust heating in order to fit the surface brightness data. This is in conformity with low radiation, low ISM environment around this system. The heating of the dust grains in W Hya is almost entirely due to stellar radiation field. The oxygen rich composition of W Hya red giant atmosphere leads to a likelihood of silicate based grains in the circumstellar dust shell.

The general conclusions from our models are:

(1) No single power law density distribution can fit the IRAS surface brightness across the entire source, in $60\ \mu\text{m}$ and $100\ \mu\text{m}$ bands. The density distribution near the inner boundary of extended shell of both R CrB and W Hya is certainly of a composite power law type. It is obvious that the dust shell inner boundary is a transition zone in terms of spatial dependence of gas to dust ratio, grain temperature, and grain size distribution. Hence a complex density structure in this region compared to other regions of the shell is quite possible. Some of our models not discussed in this paper show that a Gaussian density distribution in the even smaller ($r = 1''$) core region can improve the fit to brightness data in the inner $p < 3'$ region.

(2) Our analysis procedure of modeling the *integrated flux density* data and the *unprocessed surface brightness* data in the IRAS bands, using a *single set* of model parameters for the system as a whole seems to be correct and almost equivalent to the modeling of *point source processed flux* and *point source profile convolved brightness*, as is done in earlier studies of R CrB and W Hya.

(3) The *two shell model* employed for R CrB modeling is an artifact that can be used conveniently to model fossil shells, since two entirely different sets of physical parameters can be employed for the inner hot core (shell) and the extended shell, without affecting in any way the generality or self consistency of the radiative transfer solution. In practical terms however, this is quite expensive to do since large number of radial grid points are required to ensure good solution of the transfer problem as well as accurate convolution results.

(4) Except for the temperature structure, which is derived in a realistic manner, it is clear that no greater insights can be obtained from the pure radiative transfer modeling than from a simple analytic modeling, when the dust shells are optically thin in the relevant wavelengths of interest. It is always useful to construct full analytic models (as we have done in this paper), which act as preprocessors to the more involved transfer calculations. Basically analytical models narrow down almost all the free parameters fairly well, before the more expensive radiative transfer modeling is undertaken.

Acknowledgement:

This work has been partially supported by the U. S. Air Force under grant AFOSR 89-104.

REFERENCES

- Egan, M.P., Leung, C.M., & Spagna Jr. G.F. 1988, *Comp. Phys. Comm.*, **48**, 271
- Gillett, F.C., Backman, D.E., Beichman, C., & Neugebauer, G. 1986, *ApJ*, **310**, 842
- Hawkins, G.W. 1990, *A&Ap*, **229**, L5
- Hecht, J.H. 1991, *ApJ*, **367**, 635
- Hrivnak, B.J., Kwok, S., & Volk, K.M. 1989, *ApJ*, **346**, 265
- Leung, C.M. 1976, *JQSRT*, **16**, 559
- Nagendra, K.N. 1988, *ApJ*, **335**, 269
- Pollacco, D.L., Tadhunter, C.N., & Hill, P.W. 1990, *MNRAS*, **245**, 204
- Pollacco, D.L., Hill, P.W., Houziaux, L., & Manfroid, J. 1991, *MNRAS*, **248**, 1p
- Rao, N.K., & Nandy, K. 1986, *MNRAS*, **222**, 357
- Rowan-Robinson, M. 1982, *MNRAS*, **201**, 281
- Schonberner, D. 1977, *A&Ap*, **57**, 437
- Wright, E.L. 1989, *ApJ*, **346**, L89
- Sopka, R.J., Hildebrand, R., Jaffe, D.T., Gatley, I., Roellig, T., Werner, M., Jura, M., & Zuckerman, B. 1985, *ApJ*, **294**, 242

TABLE 1

SOME INPUT PHYSICAL PARAMETERS FOR MODELS SHOWN IN FIGURE 29

Parameter	Model 1	Model 2	Model 3
T_1 (K)	80	50	80
γ	0.5	1.9	2.3
C	25	15	10
C_2	25	05	30
$\tau(ext)$	$2.5 \cdot 10^{-4}$	$1.0 \cdot 10^{-3}$	$2.0 \cdot 10^{-3}$

TABLE 2

SOME DERIVED QUANTITIES FROM MODEL FITS SHOWN IN FIGURE 29

Quantity	Model 1	Model 2	Model 3
T (3') (K)	29.4	27.3	26.0
n(3') (cm ⁻³)	1.3 10 ²	4.2 10 ²	6.6 10 ³
$\pi(3')$	1.8 10 ⁻⁴	2.6 10 ⁻⁴	3.4 10 ⁻⁴
$\dot{M}_d(3') (M_O/Yr)$	2.4 10 ⁻⁹	8.1 10 ⁻⁹	1.3 10 ⁻⁸
$M_d (M_O)$	2.5 10 ⁻⁴	7.4 10 ⁻⁴	9.1 10 ⁻⁴

FIGURE CAPTIONS

- FIG. 1 - Analytic *isothermal* models of R CrB. (a) IRAS flux density spectrum. Triangles: point source processed flux density. Circles: integrated flux density observed in 24' beam. (b) unprocessed 60 μm to 100 μm intensity ratio. The lines represent *isothermal* analytic model fits. (c) 60 μm surface brightnesses. Open triangles: Point source processed data. Filled triangles: unprocessed data. (d) 100 μm surface brightness. Open squares: point source processed data. Filled squares: unprocessed data. Models are *intrinsic (unconvolved)* profiles for a prescribed T_c . (e) and (f) Same as (d) and (e) except for (*spectral + spatial*) convolution on the intrinsic profiles. (g) Physical parameters of isothermal models. $n(r)$ is in arbitrary units.
- FIG. 2 - Same as Fig.1 but for $T_c = 30$ K, and different values of *opacity index* m . (c) and (d) Intrinsic brightness profiles. (e) and (f) convolved profiles. (g) Physical characteristics of the model.
- FIG. 3 - *Thermal equilibrium* models of R CrB. The models correspond to different values of spectral index m . These models need a larger density contrast in the extended shell as compared to the *isothermal* case to fit the data (see the text). The sharp drop in brightness in the *cavity region* ($0 < p < 1.4'$) in (c) and (d) is due to non-isothermal nature of $T(r)$ in the extended shell.
- FIG. 4 - Thermal equilibrium models showing the *effects of ISRF*. Flux density computation does not involve ISRF. The free parameter is C which represents how many times (*solar neighborhood*) ISRF is employed in computing $T(r)$. (c) and (d) The effect of external ISRF on intrinsic profiles. (e) and (f) Convolved brightness profiles. It is difficult to fit the brightness data unless substantially strong ISRF is employed in R CrB modeling.
- FIG. 5 - Thermal equilibrium models for different values of exponent γ in power law

density variation in the shell.

FIG. 6 - Analytic *thermal equilibrium* models of W Hya. (a) IRAS flux density spectrum. Filled circles: point source processing flux density. Open circles: flux density measured with 30' diameter beam. (b) Unprocessed 60 μm to 100 μm intensity ratio. Compare with Fig.1a,b. The lines represent model fits. Density exponent γ is the free parameter. (c) and (d) IRAS 60 μm and 100 μm surface brightnesses of W Hya. Open triangles and open squares: point source processed data. Filled triangles and squares: unprocessed data. Models correspond intrinsic profiles. (e) and (f) Convolved model profiles. The profiles steepen as γ is increased. (g) Variation of dust density, temperature and optical depth as a function of radius.

FIG. 7 - Analytic models for W Hya showing the effects of *spectral index* m . A density exponent of $\gamma = 0.5$ is employed for this series of models. The variation of m uniformly affects the brightness at all the lines of sight p , unlike density exponent γ . The radiation in 60 μm and 100 μm bands are affected to different extent.

FIG. 8 - *Radiative Transfer* models for IRAS observations of R CrB. The symbols and data points have same meaning as in Fig.1. (a) and (b) The effect of opacity index m on flux density and intensity ratio. (c) and (d) The radiative transfer models of R CrB surface brightness in 60 μm and 100 μm bands. The models represent (*spectrally + spatially*) convolved profiles. (e) Physical quantities namely the $n(r)$, $\tau(r)$ and temperature structure $T(r)$ are shown.

FIG. 9 - Models of R CrB when extended shell is *positioned* at different distances from the central star. $T_1(\text{ext})$ (= 30 K, 50 K, and 80 K), is the free parameter of the problem. Farther the shell, smaller is the 100 μm flux density. (c) and (d) Surface brightness profiles showing the effect of moving the fossil shell farther and closer through a variation of $T_1(\text{ext})$. (e) The physical parameters of the

models.

- FIG. 10 - Effect of variation of density exponent $\gamma(\text{ext})$. The position of the shell is $r_1(\text{ext}) \equiv 1.4'$ ($T_1(\text{ext}) = 30$ K). Note: Figs.(10)-(12) show the same effect, but for different *positions* of the fossil shell thus forming a sequence. (c) and (d) Surface brightness profiles for a *far off position* $r_1(\text{ext}) \equiv 1.4'$ of the fossil shell. The case with $\gamma = 1.9$ represents common link with other Figures. (e) Physical parameters of the models.
- FIG. 11 - Same as Fig.(10), but for an *intermediate position* $r_1(\text{ext}) \equiv 0.4'$ of the fossil shell corresponding to $T_1(\text{ext}) = 50$ K. Notice the resolution of intensity ratios for $p < 3'$ location on the visible disk.
- FIG. 12 - Same as Figs.(10) and (11) except for a *close position* $r_1(\text{ext}) \equiv 0.12'$ of the fossil shell corresponding to $T_1(\text{ext}) = 80$ K. Only $\gamma \approx 1.5$ can fit the flux density data for such a close position of the fossil shell to the central star. The geometry is similar to that of W Hya in this respect, except for a density contrast (see Fig.12e). $\gamma = 1.5$ implies a considerable amount of variable massloss in the shell.
- FIG. 13 - A study of the role of ISRF in radiative transfer models. C is the free parameter of this series of models which run from Figs.13-15, once again based on the *position* of the fossil shell selected through $T_1(\text{ext}) = 30$ K, 50 K, and 80 K.
- FIG. 14 - Same as Fig.13 but for an *intermediate position* $r_1(\text{ext}) = 0.4'$ of the extended fossil shell corresponding to $T_1(\text{ext}) = 50$ K. Notice the nearly uniform decrease of brightness across the entire fossil shell, for all the models. $C = 20$ provides a reasonable fit.
- FIG. 15 - Same as Figs.13 and 14 but for a closer position of the fossil shell $r_1(\text{ext}) = 0.12'$. It is clear that an even larger amount of ISRF is required to fit the IRAS flux density and brightness data. Such a strong radiation environment is unreasonable.

- FIG. 16 - A study of *variation of total optical depth* $\tau(ext)$ on the R CrB model results. The model series is presented once again for three successive positions of the fossil shell in Figs.16-18. Optical depth is an important parameter which signifies dust luminosity. Larger the $\tau(ext)$, larger is the $60\ \mu\text{m}$ and $100\ \mu\text{m}$ brightness. Since fossil shell is optically thin, brightness variation is linear in both these IRAS bands.
- FIG. 17 - Same as Fig.16 except for $T_1(ext) = 50\ \text{K}$. It can be seen that τ effect changes the intensity ratio only for $p < 3'$, since dust density is large in this region. $\tau(ext) = 10^{-3}$ corresponds to the median model in Figs.16-18 and also is the link with other Figures. The effect of $\tau(ext)$ on $T(r)$ is insignificant.
- FIG. 18 - Same as Figs.16 and 17 except for a closer position $T_1(ext) = 80\ \text{K}$ of the fossil shell. A large optical depth in the fossil shell, but a higher density of cool dust in its outer layer are required to model the IRAS data, for this position of the shell (since $\gamma = 1.9$). The other alternative is a slow density law ($\gamma = 1.5$, see Fig.12).
- FIG. 19 - Effect of changing the *density contrast* parameter C_2 of the fossil shell. Figs.19-21 show this series of models. The density scaling up is done only beyond the location $p > 1.4'$ ($T_1 \approx 30\ \text{K}$). The free parameter of this series of models is C_2 . The flux density in $12\ \mu\text{m}$ and $25\ \mu\text{m}$ are significantly affected, due to obscuration by cool dust. However this factor C_2 has a minor effect on brightness profiles for this position, $T_1(ext) = 30\ \text{K}$ of the fossil shell, except near the inner edge.
- FIG. 20 - Same as Fig.19 except for the intermediate position $T_1(ext) = 50\ \text{K}$ of the fossil shell. Since the shell as a whole is sufficiently warm in this position, the density contrast does not affect the $12\ \mu\text{m}$ and $25\ \mu\text{m}$ flux density strongly (see Fig.19a). The brightness profiles are significantly affected.
- FIG. 21 - Same as Figs.19 and 20, but for $T_1(ext) = 80\ \text{K}$. A larger density contrast C_2 is

needed for this position of the extended shell in order to fit the flux density and surface brightness data. Compare this characteristic with the effect of density exponent γ (see Fig.12) and optical depth $\tau(ext)$ (see Fig.18).

- FIG. 22 - The effect of beam size uncertainty on the model results are shown, for the position $T_1(ext) = 50$ K of the fossil shell. The three cases correspond to a variation of ± 10 % about the standard beam sizes $r_{b,100 \mu m} = 2.25'$ and $r_{b,60 \mu m} = 1.25'$ employed in all the results on R CrB in this paper. The beam size variation can significantly affect the surface brightness profiles and the intensity ratio. The effect is of similar nature for other two positions of the fossil shells also.
- FIG. 23 - *Radiative Transfer* models for IRAS data of W Hya. The symbols for the observed data points have same meaning as in Fig.6. The curves show the effect of variation of the *opacity index* m . The W Hya is modelled in the scenario of a single shell. Compare with Fig.8 on R CrB. $I_V(60 \mu m, 0)$ is obtained by linearly extrapolating intensity ratio given in Hawkins(1990), and is uncertain.
- FIG. 24 - Effect of variation of dust *condensation temperature* T_1 on the model results of W Hya. Compare with Fig.9 on R CrB. $T_1 = 1000$ refers to the median model and employed in all the models of W Hya.
- FIG. 25 - Effect of variation of *density exponent* γ in the modeling of the W Hya data. Compare with Figs.10-12 on R CrB, particularly Fig.12. The data can be fitted employing such variable massloss models, except in a very small region at inner edge of the shell. $\gamma = 1.1$ refers to the median model.
- FIG. 26 - Effect of *external radiation* (ISRF) on models of W Hya. Compare with Fig.15 on R CrB. It is clear that large ISRF is not required to model IRAS observations of this star. $C = 1$ refers to the median model.
- FIG. 27 - Effect of *optical depth* τ variation in the models of W Hya. Compare with

Fig.18 on R CrB. Although the dust optical depth is substantially large in W Hya shell, its variation still has a linear effect on the bightness profiles, as in the case of R CrB. $\tau = 3.2$ refers to the median model.

FIG. 28 - Effect of *density scaling (contrast)* parameter C_2 in the models of W Hya. The density scaling is done only for locations $p > 1'$ in the shell. Compare with Figs.19-21 on R CrB. The model results sensitively depend on C_2 . The value $C_2 = 1$ refers to the median model

FIG. 29 - Some miscellaneous models of R CrB shown here to demonstrate the need to model the IRAS flux density, and surface brightness together, in order to provide a better constraint on the model parameters. Some model parameters for these arbitrary set of models, are given in Table 1. The rest of the parameters are same as the standard set (see section 3.1.1).

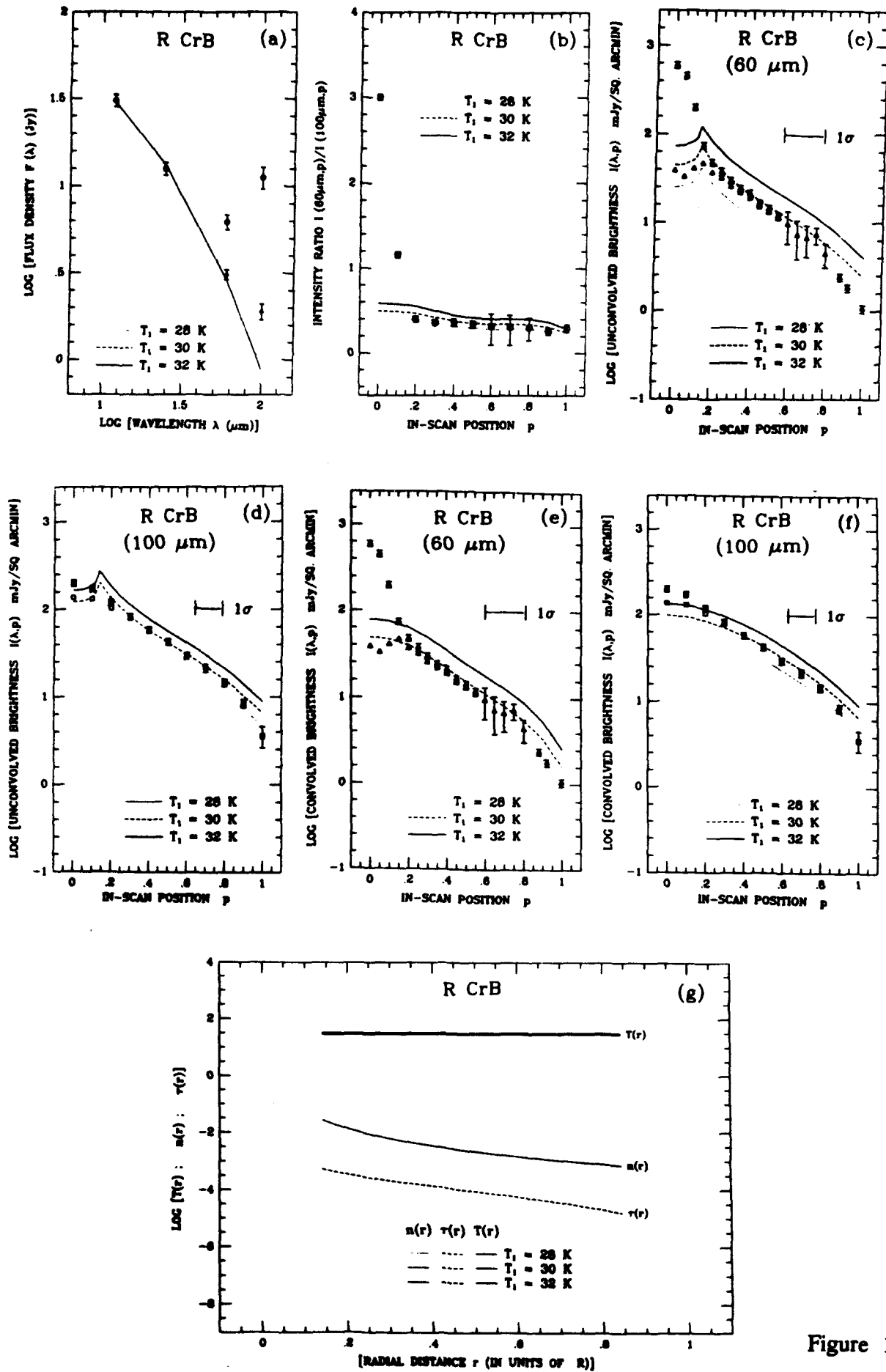


Figure 1

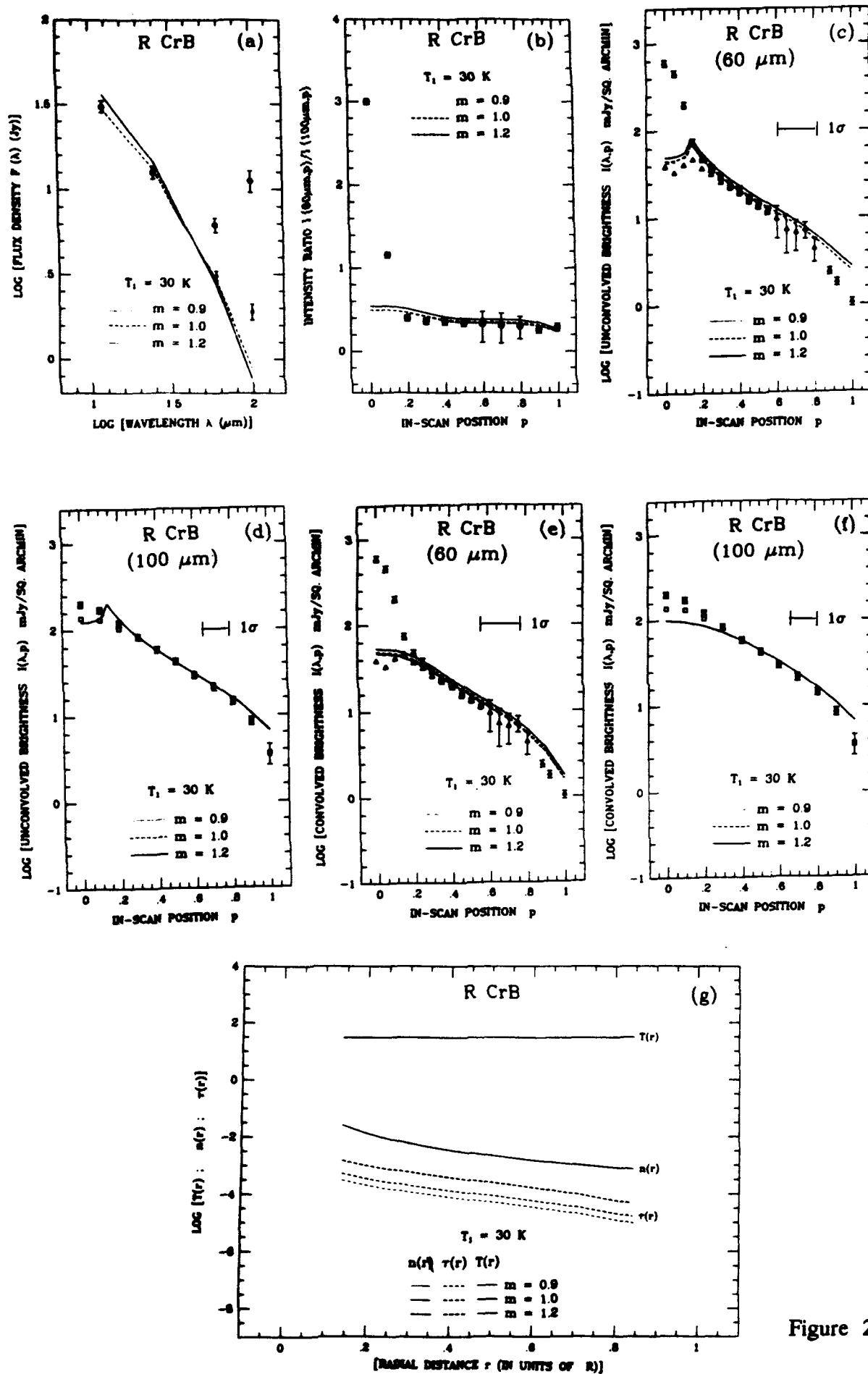


Figure 2

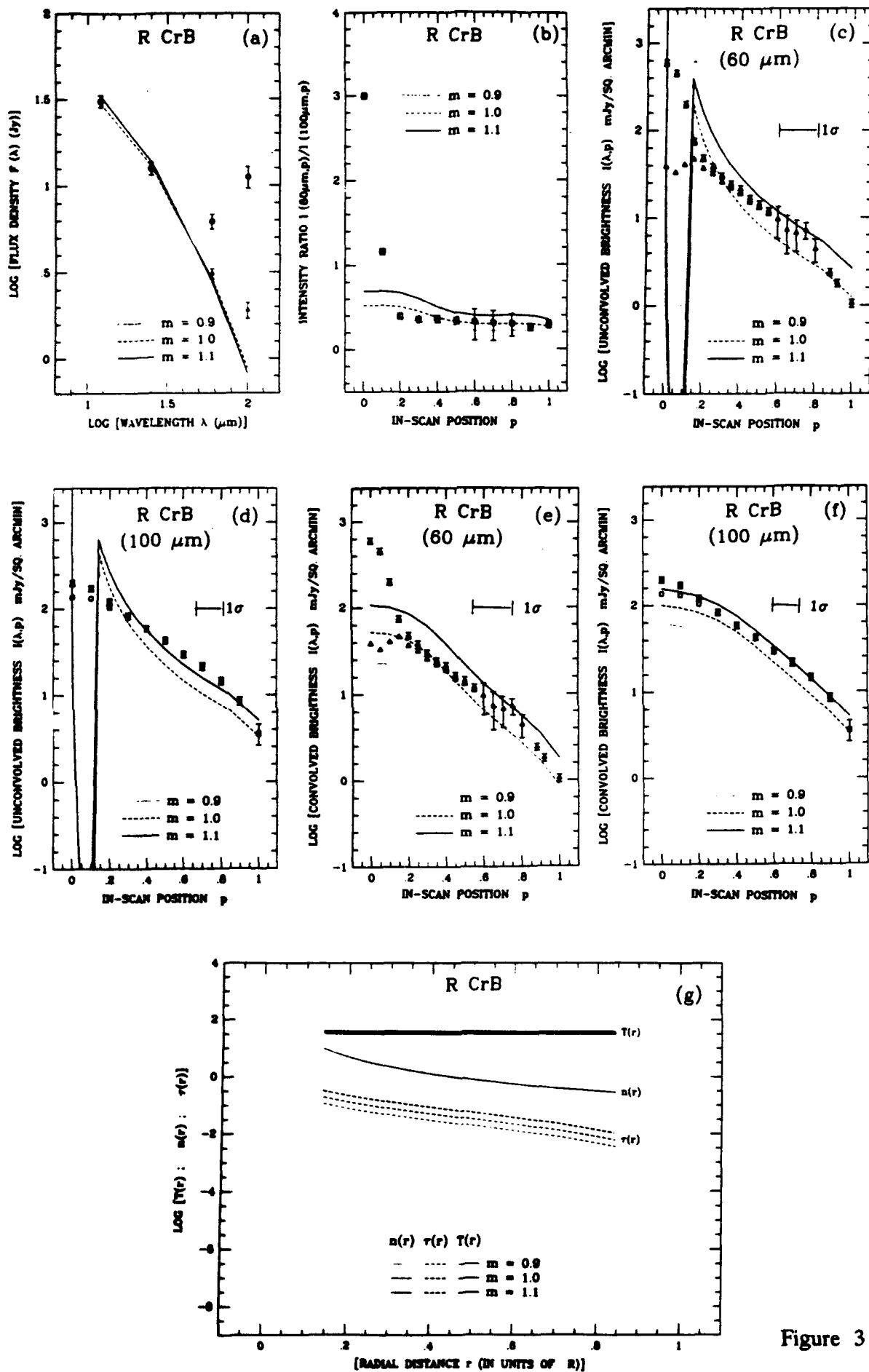


Figure 3

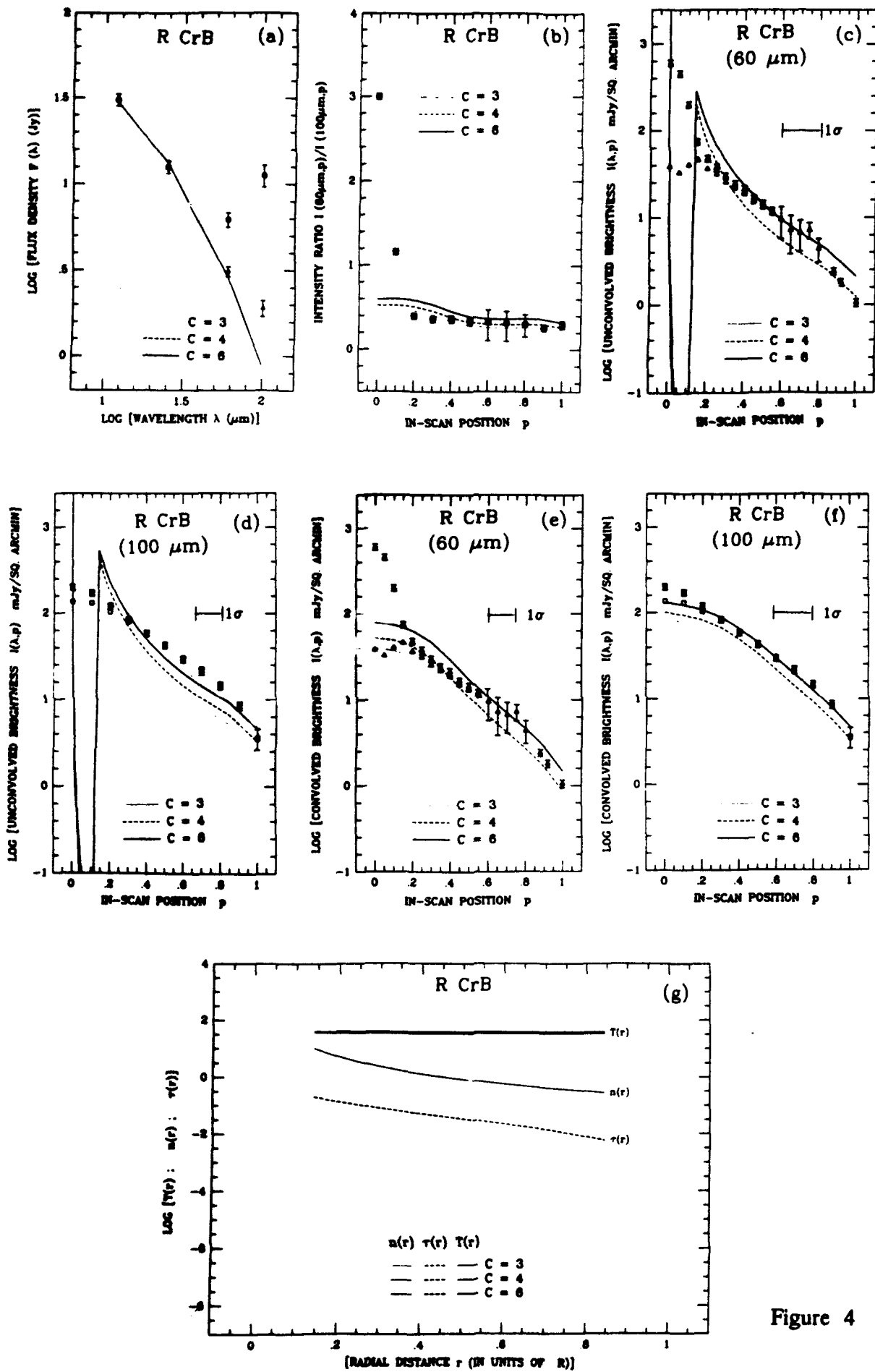


Figure 4

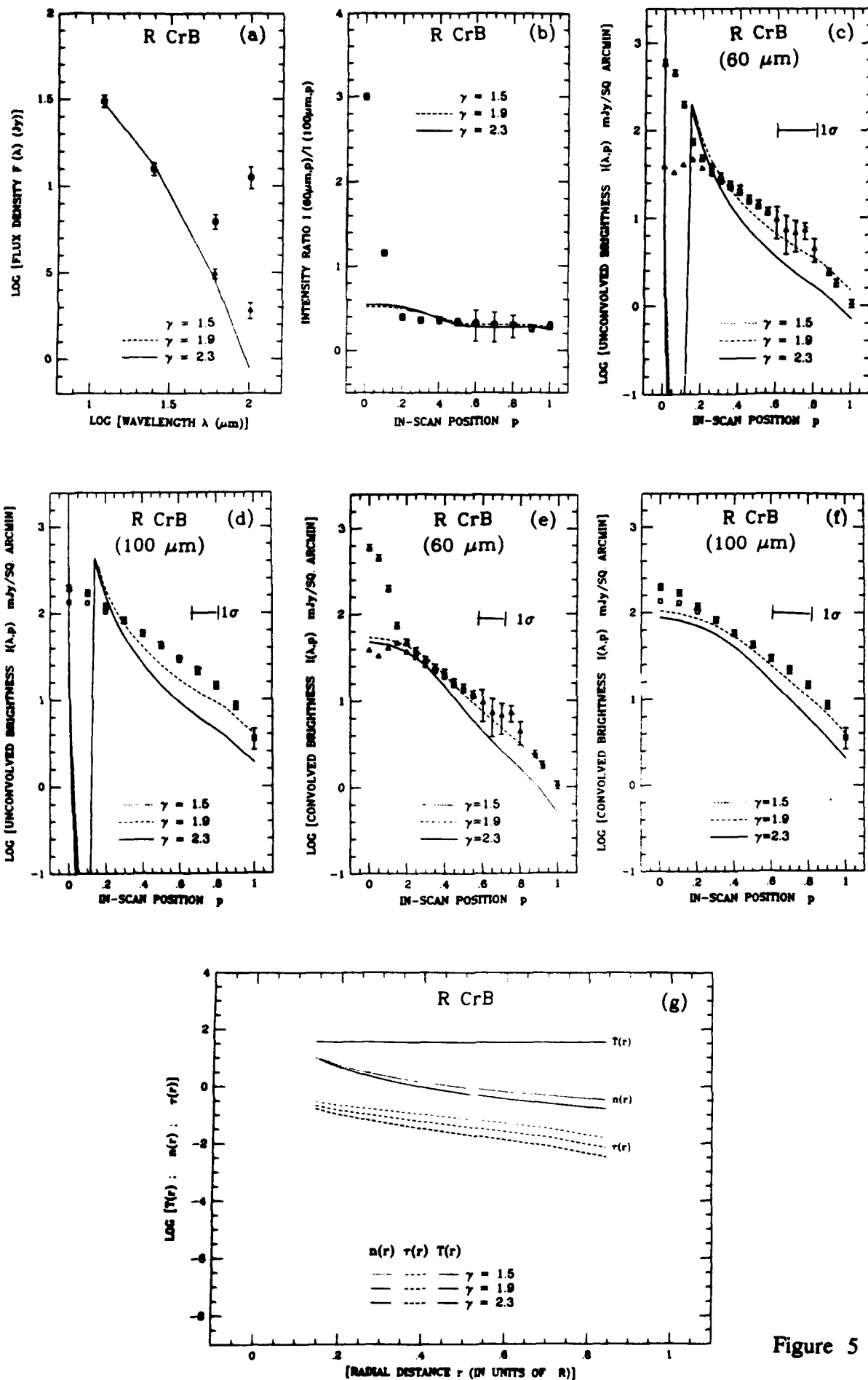


Figure 5

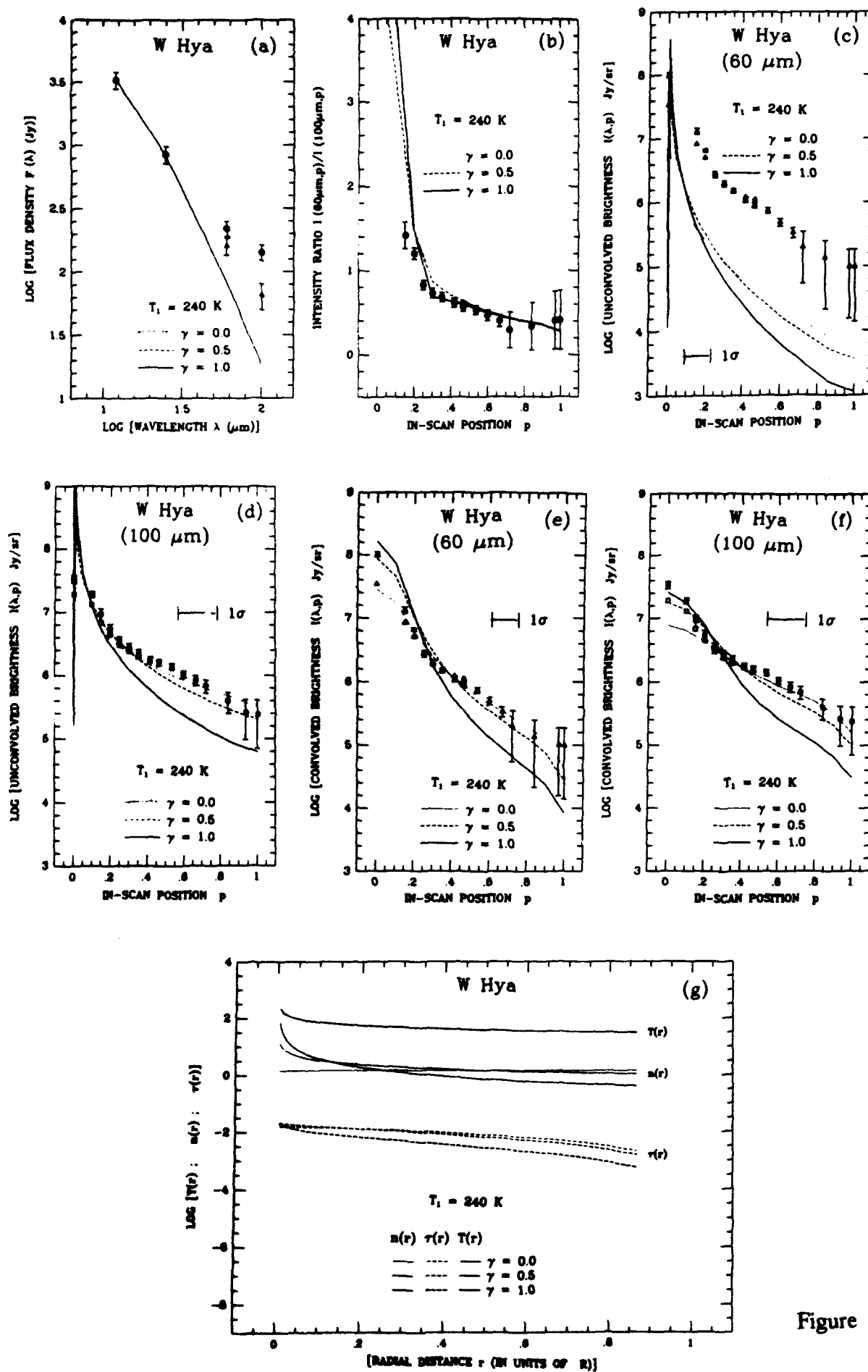


Figure 6

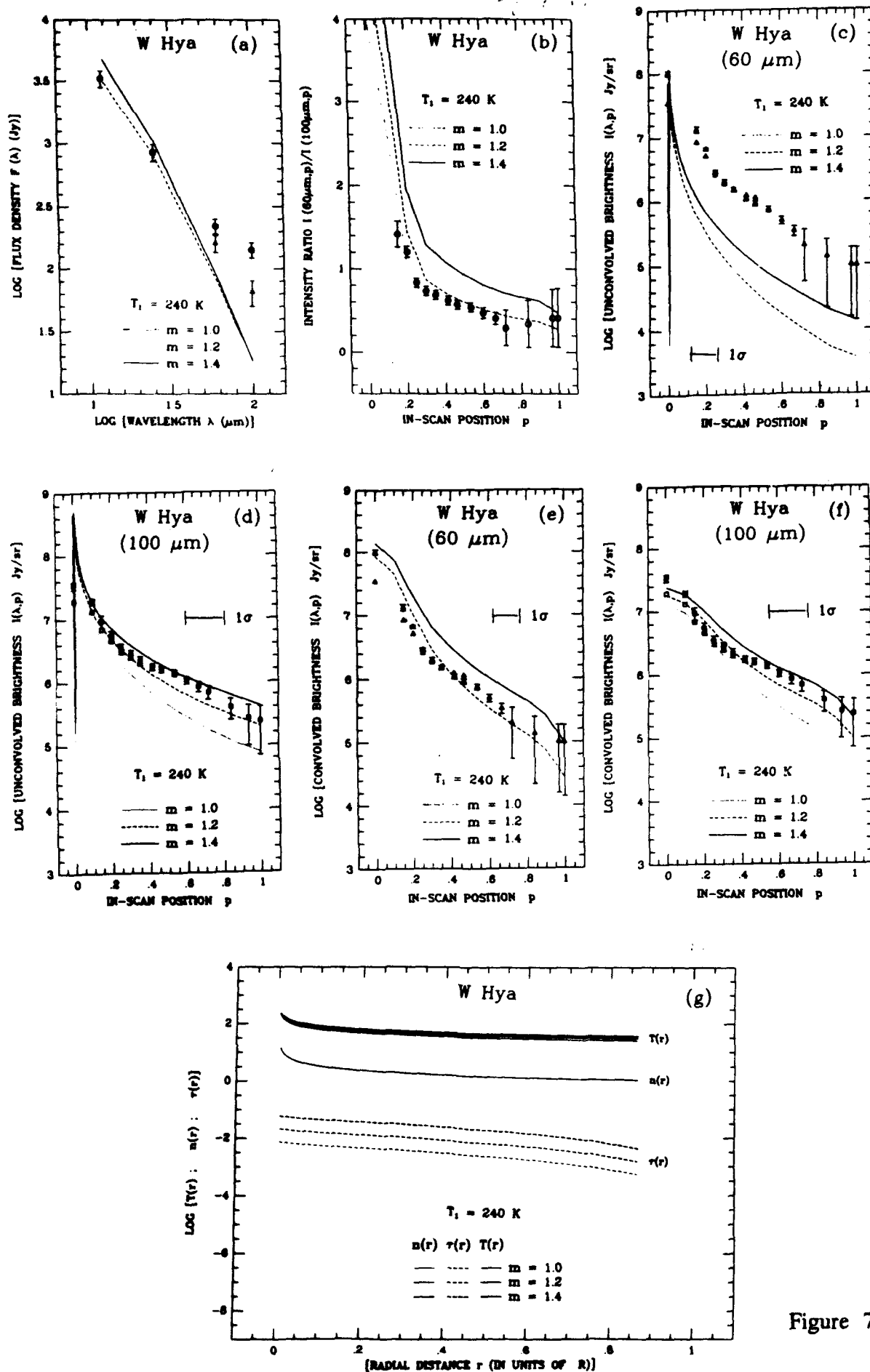


Figure 7

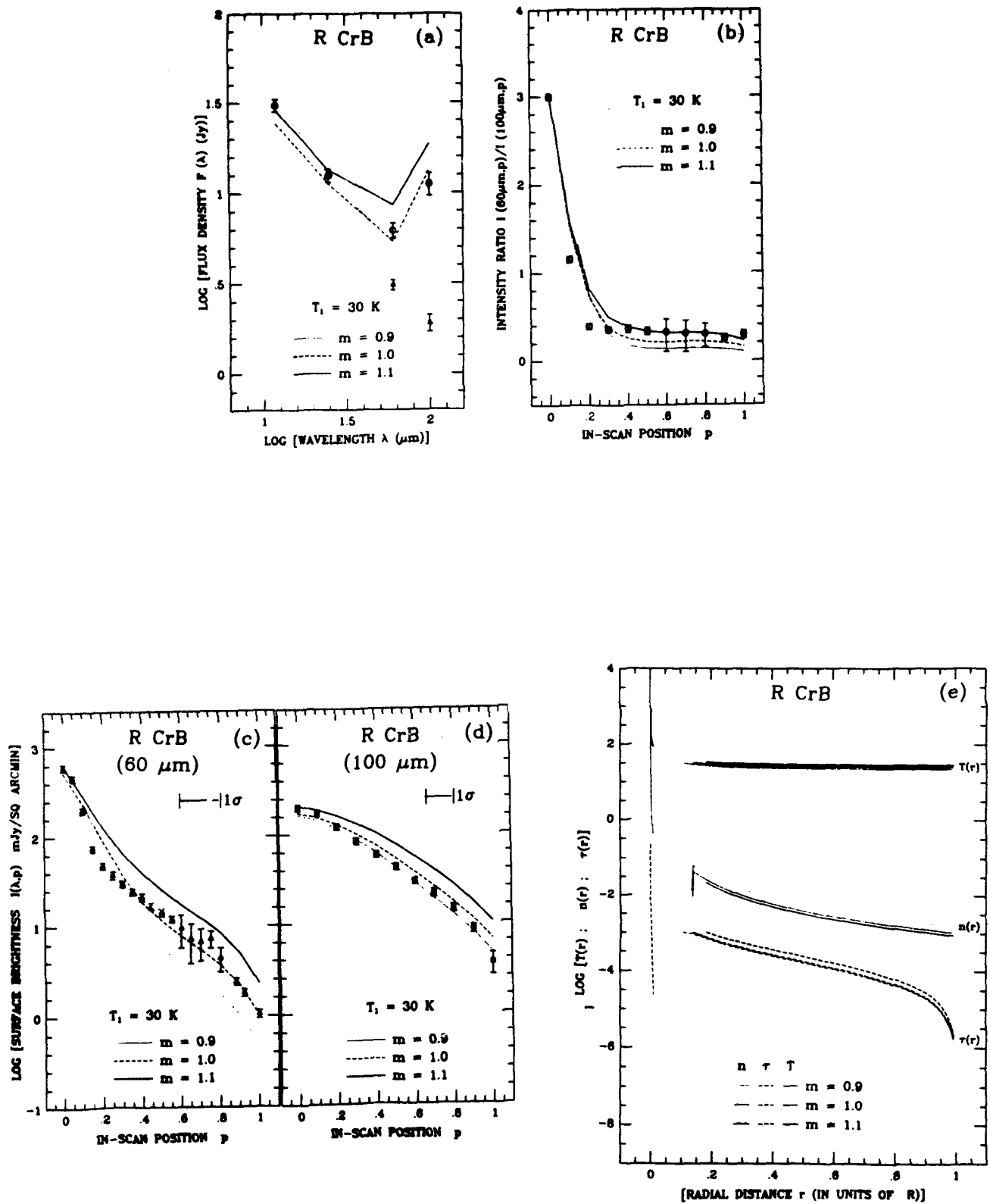


Figure 8

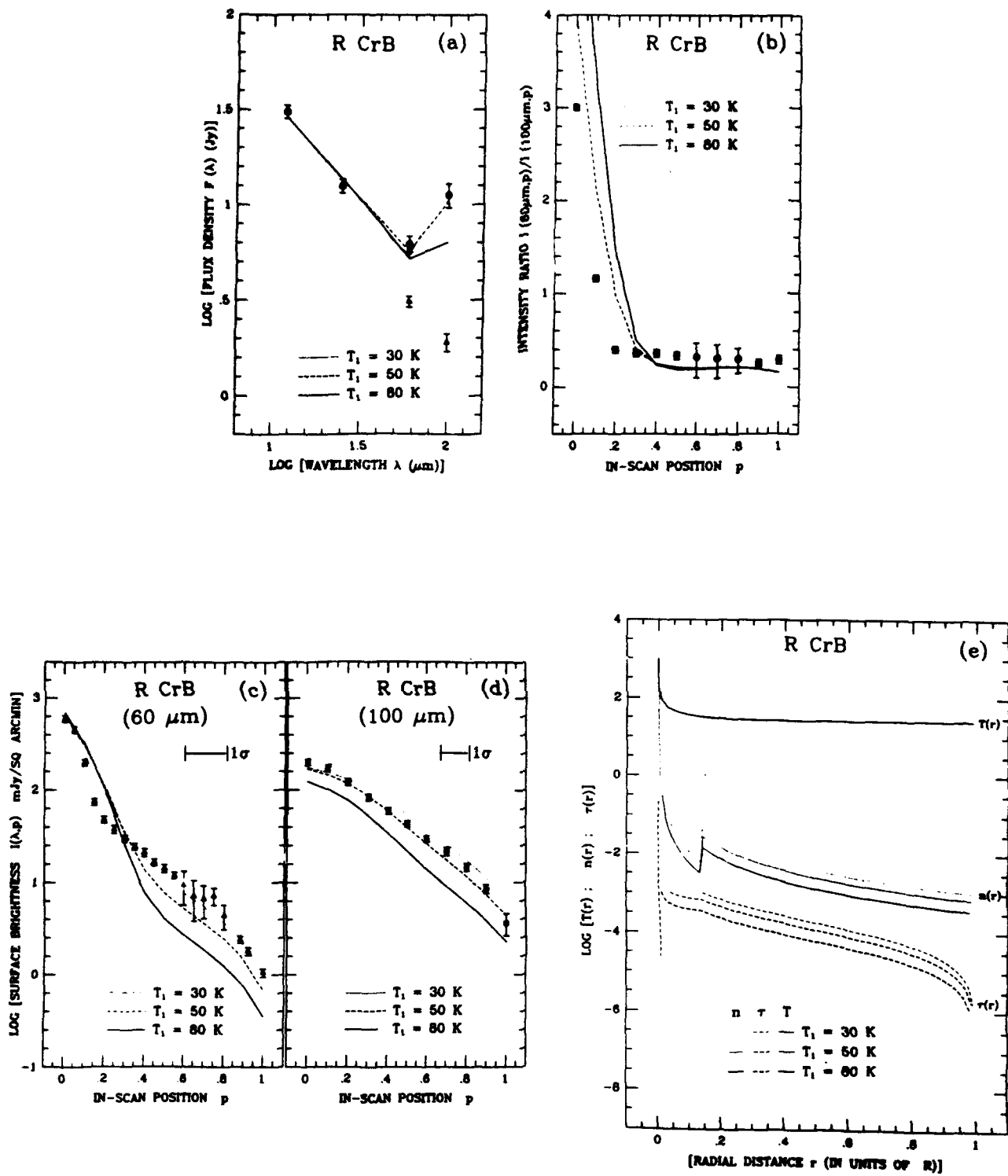


Figure 9

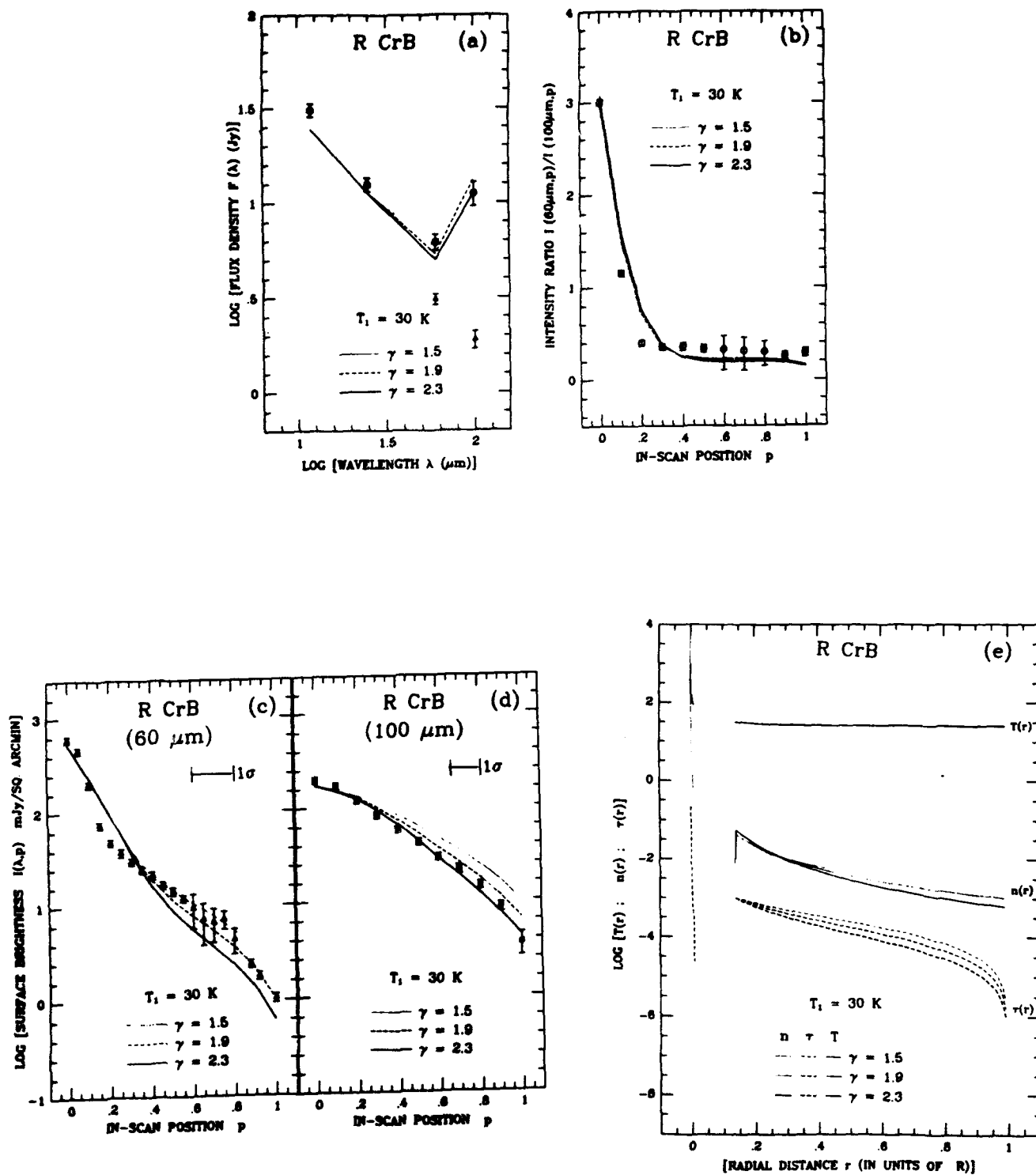


Figure 10

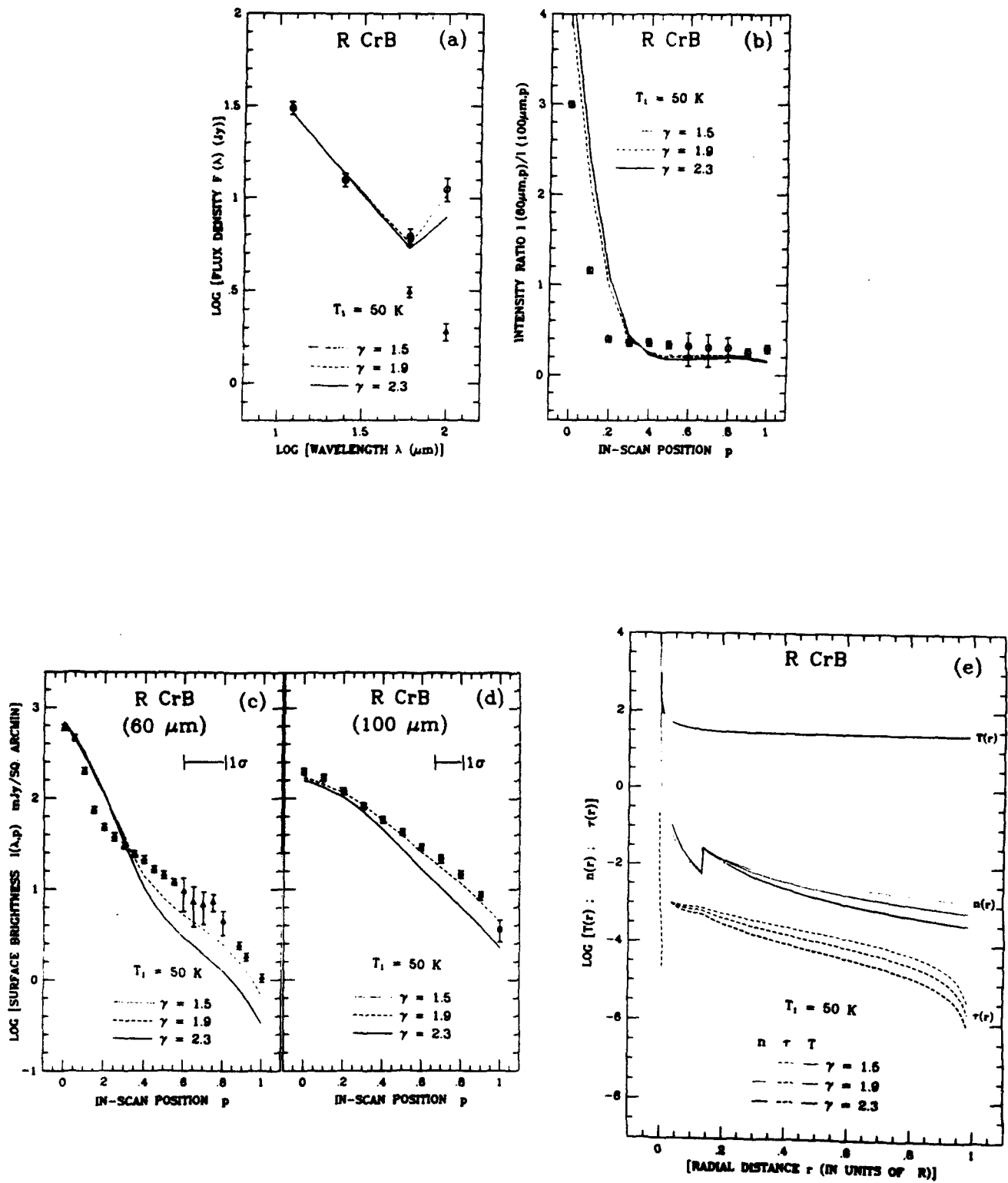


Figure 11

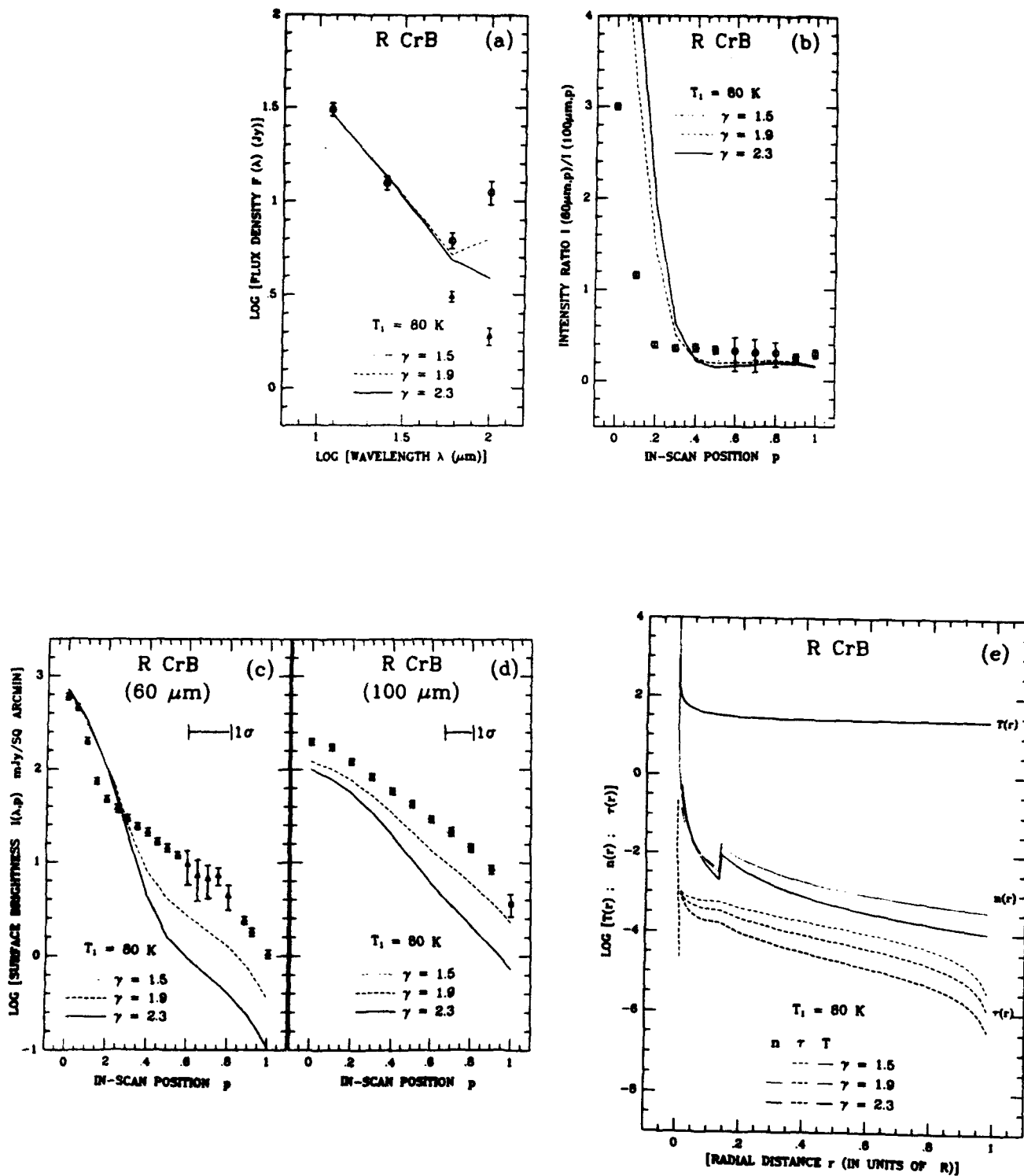


Figure 12

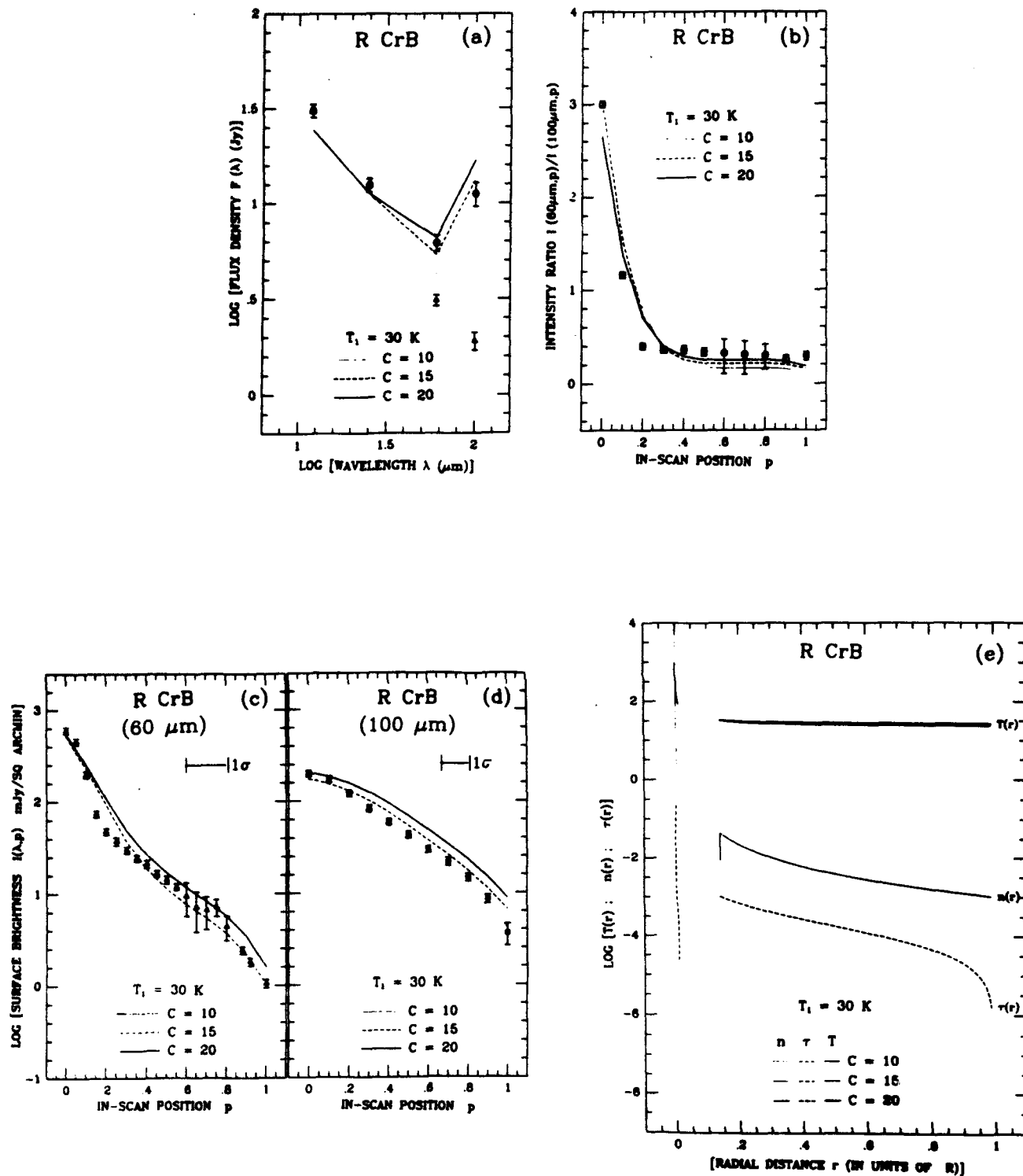


Figure 13

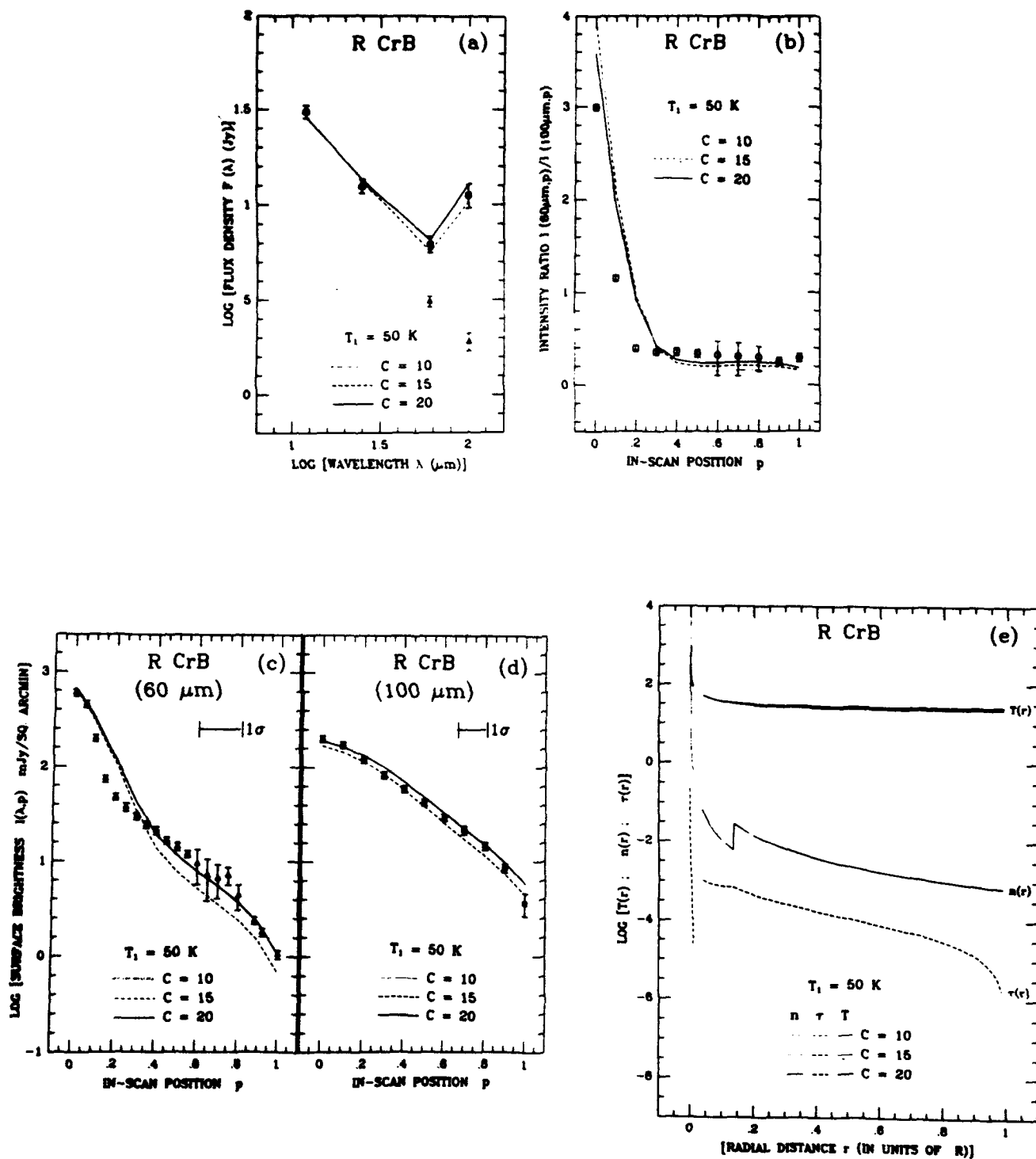


Figure 14

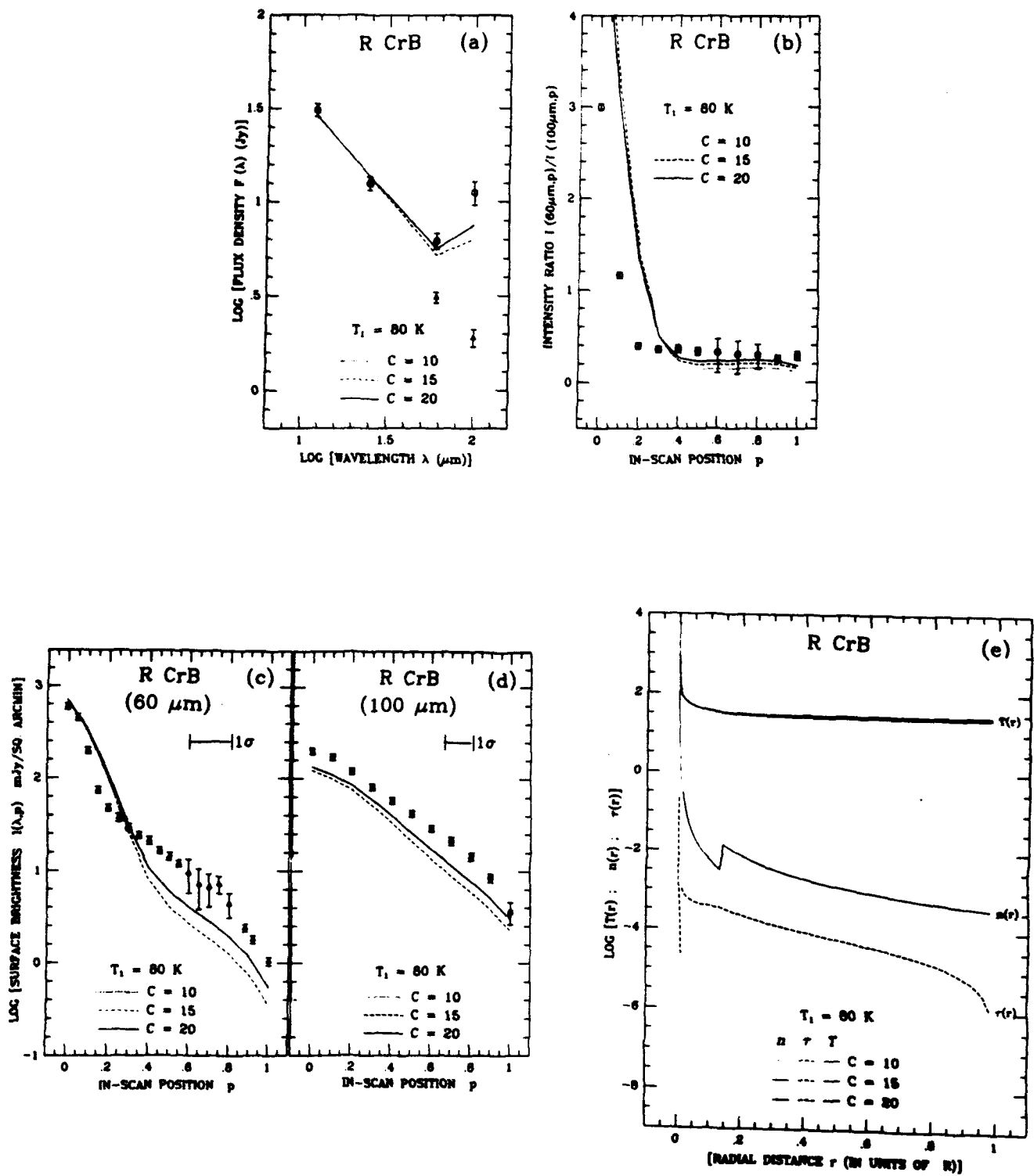


Figure 15

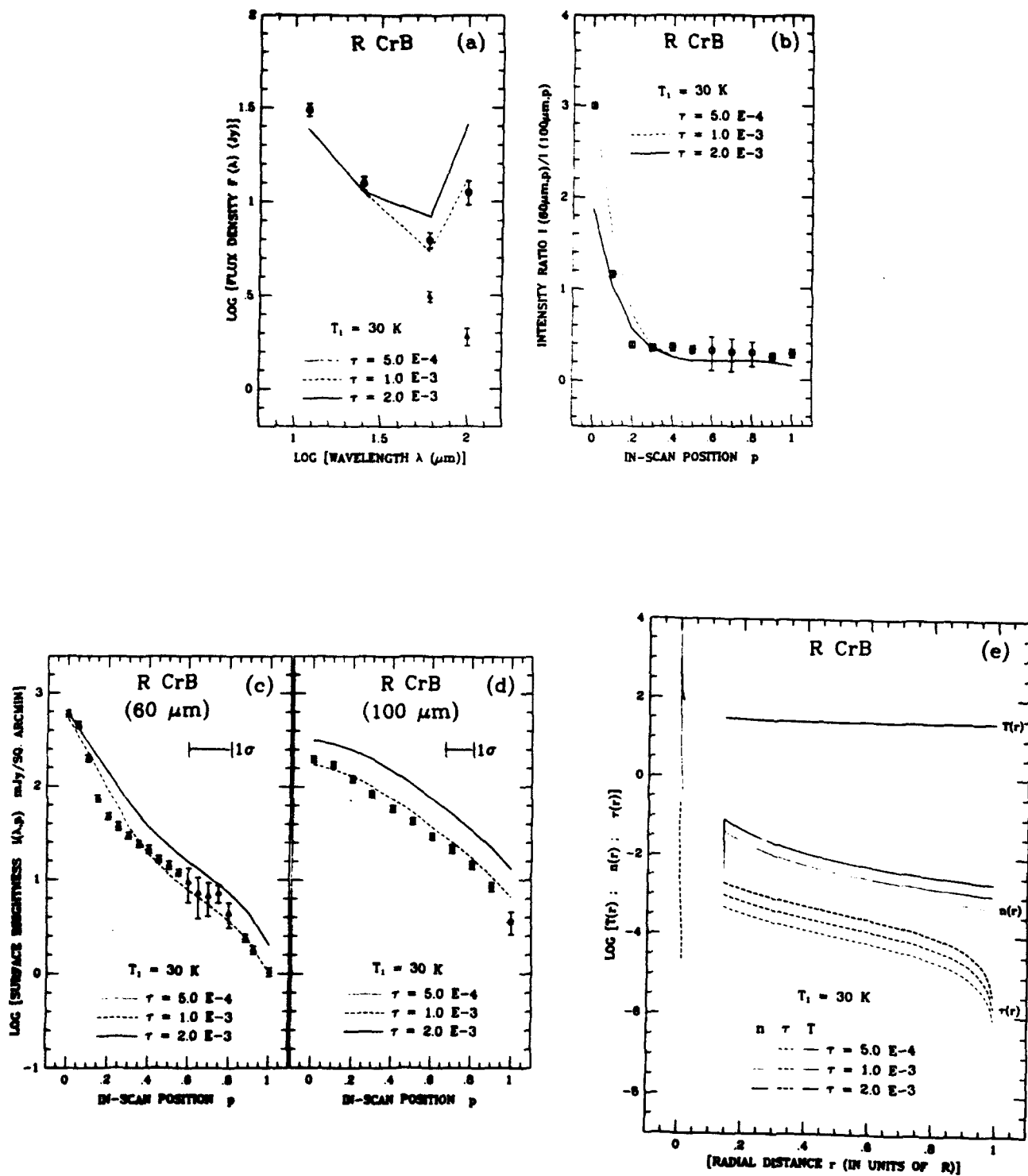


Figure 16

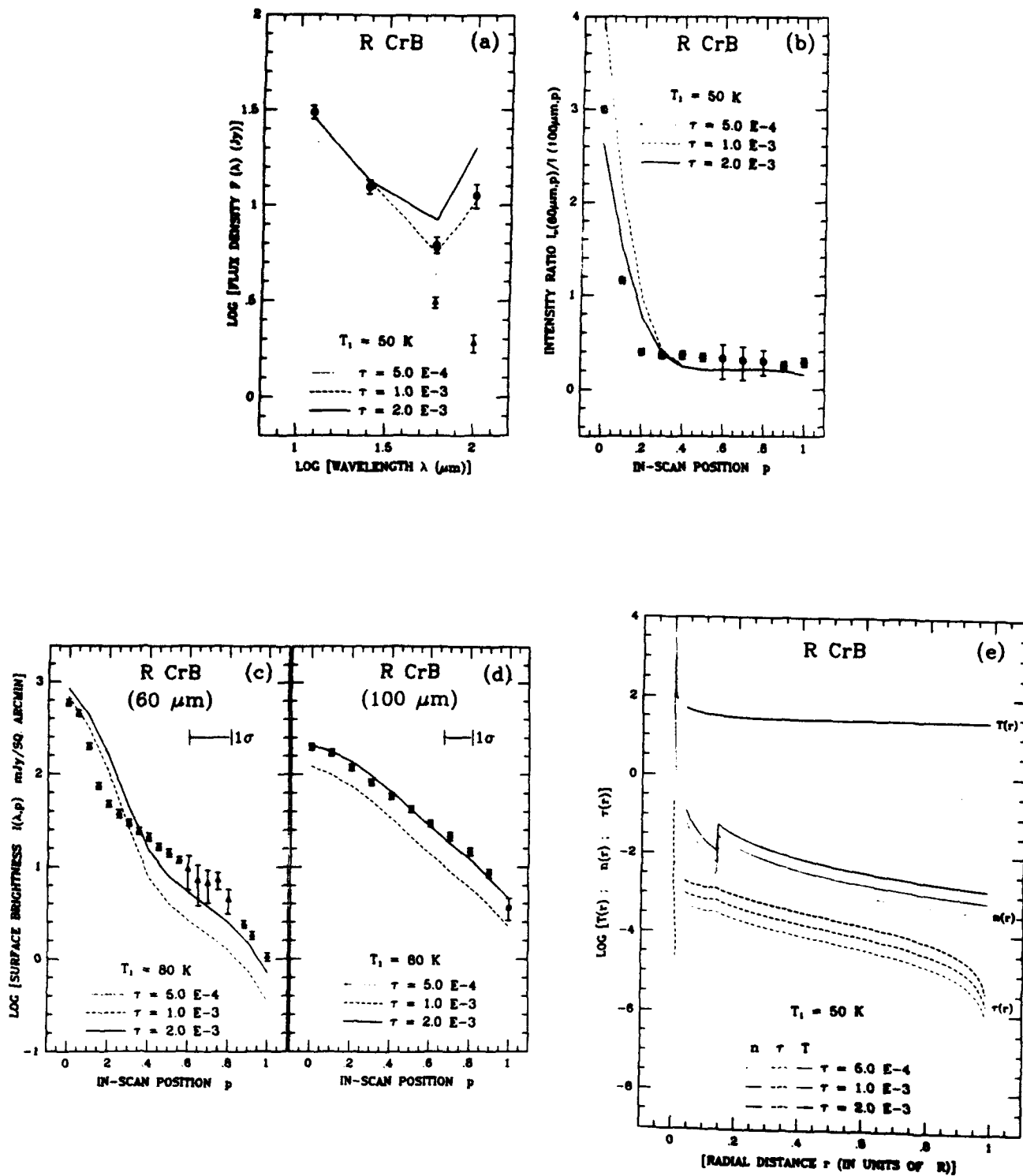


Figure 17

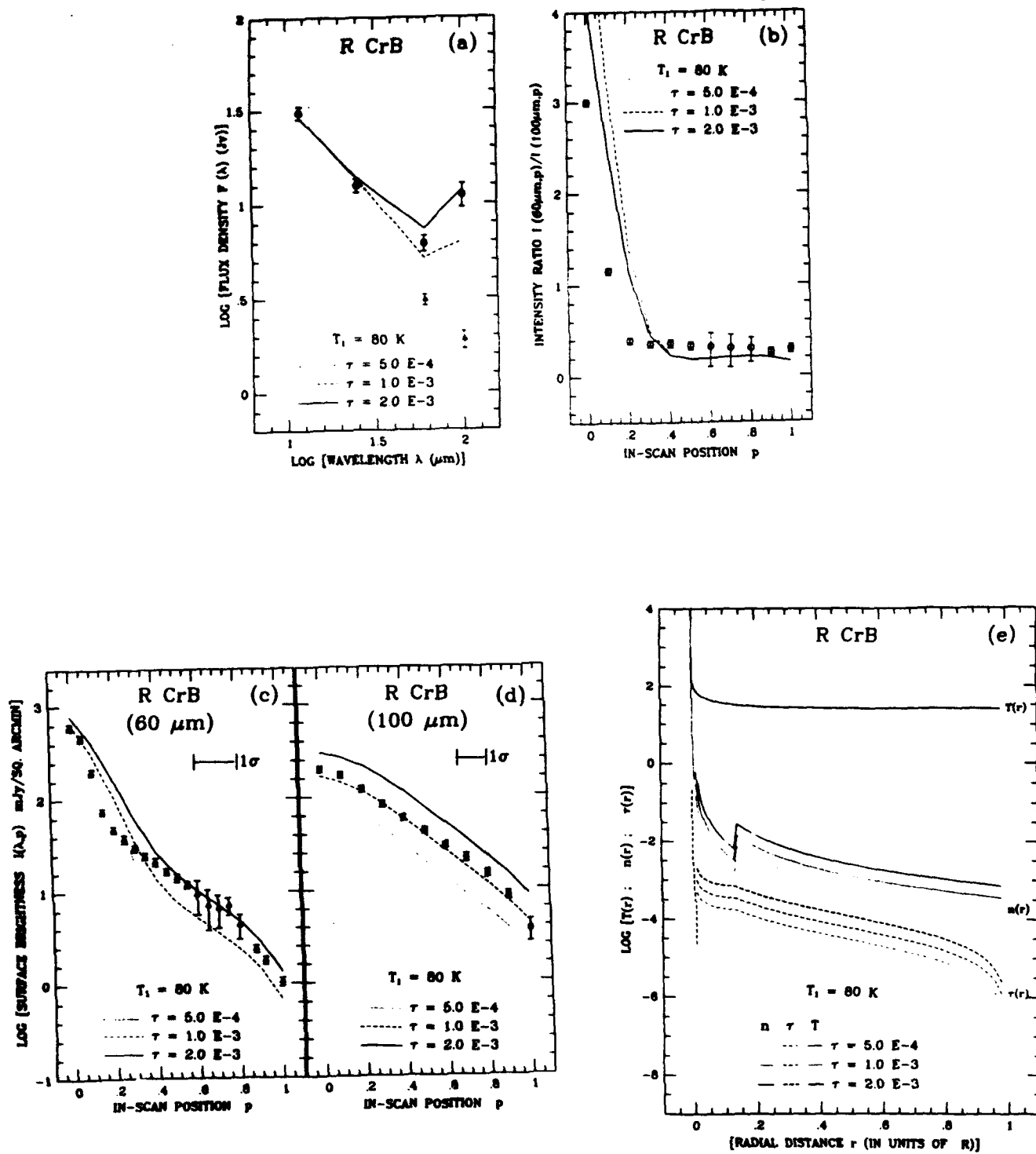


Figure 18

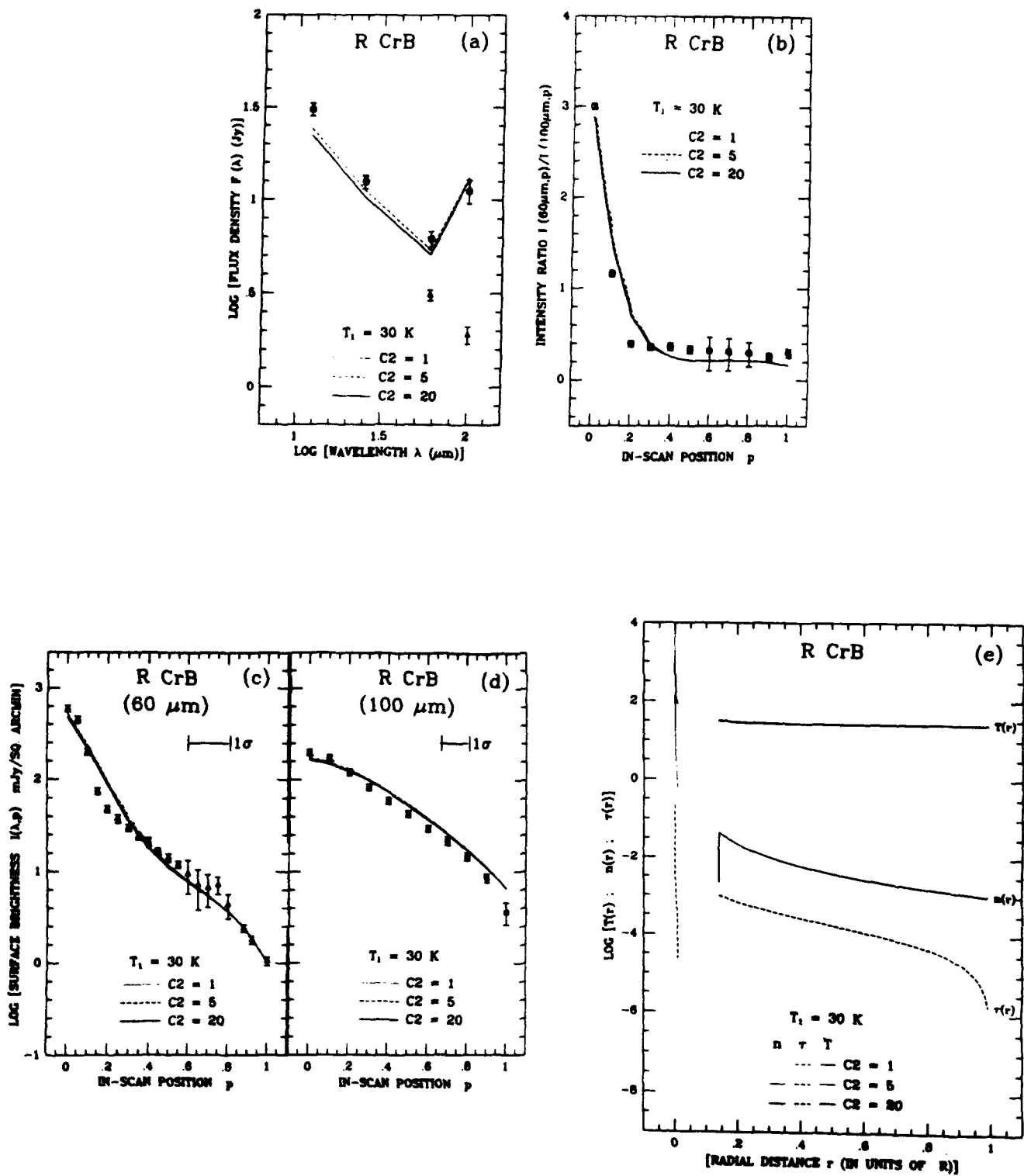


Figure 19

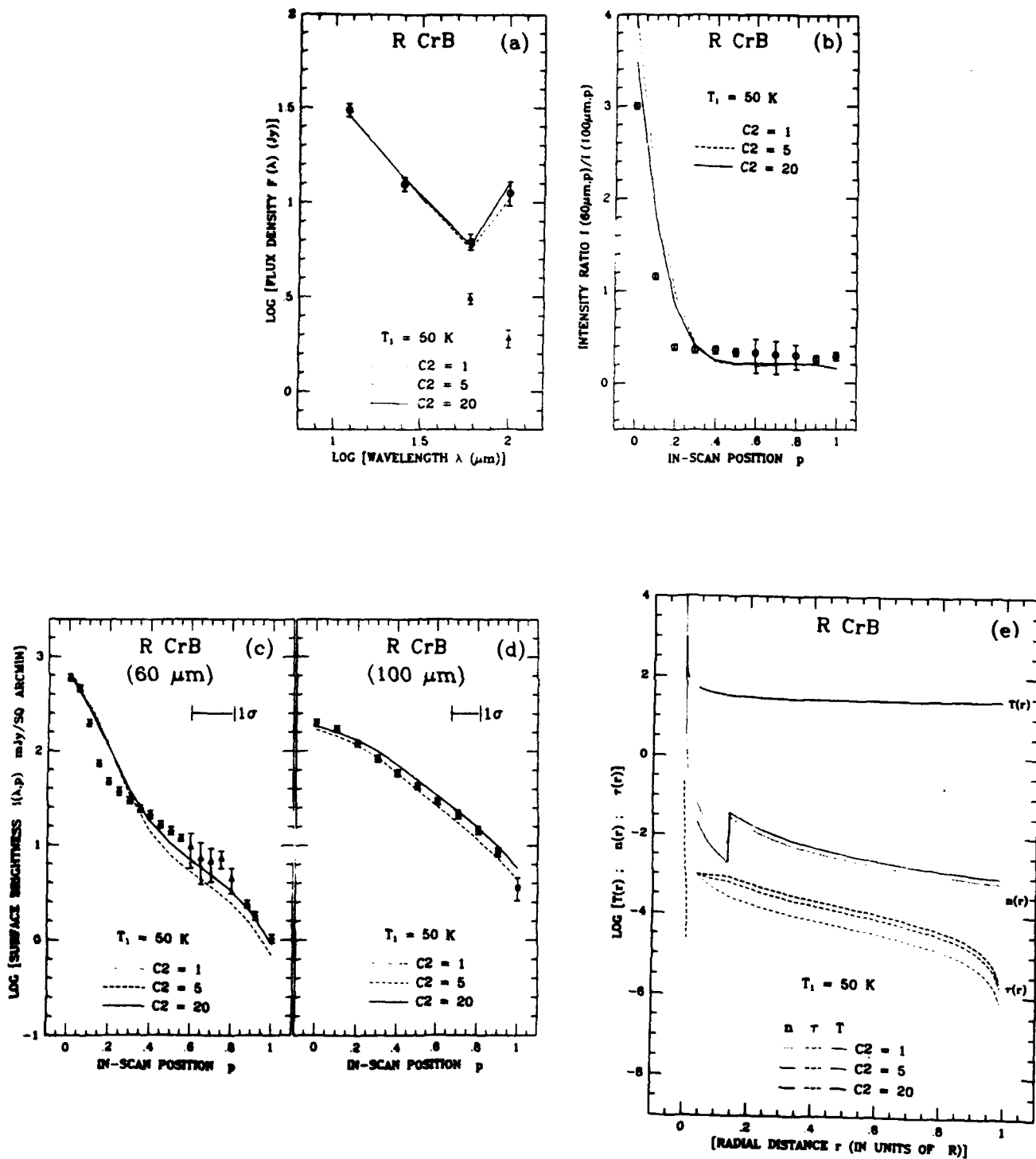


Figure 20

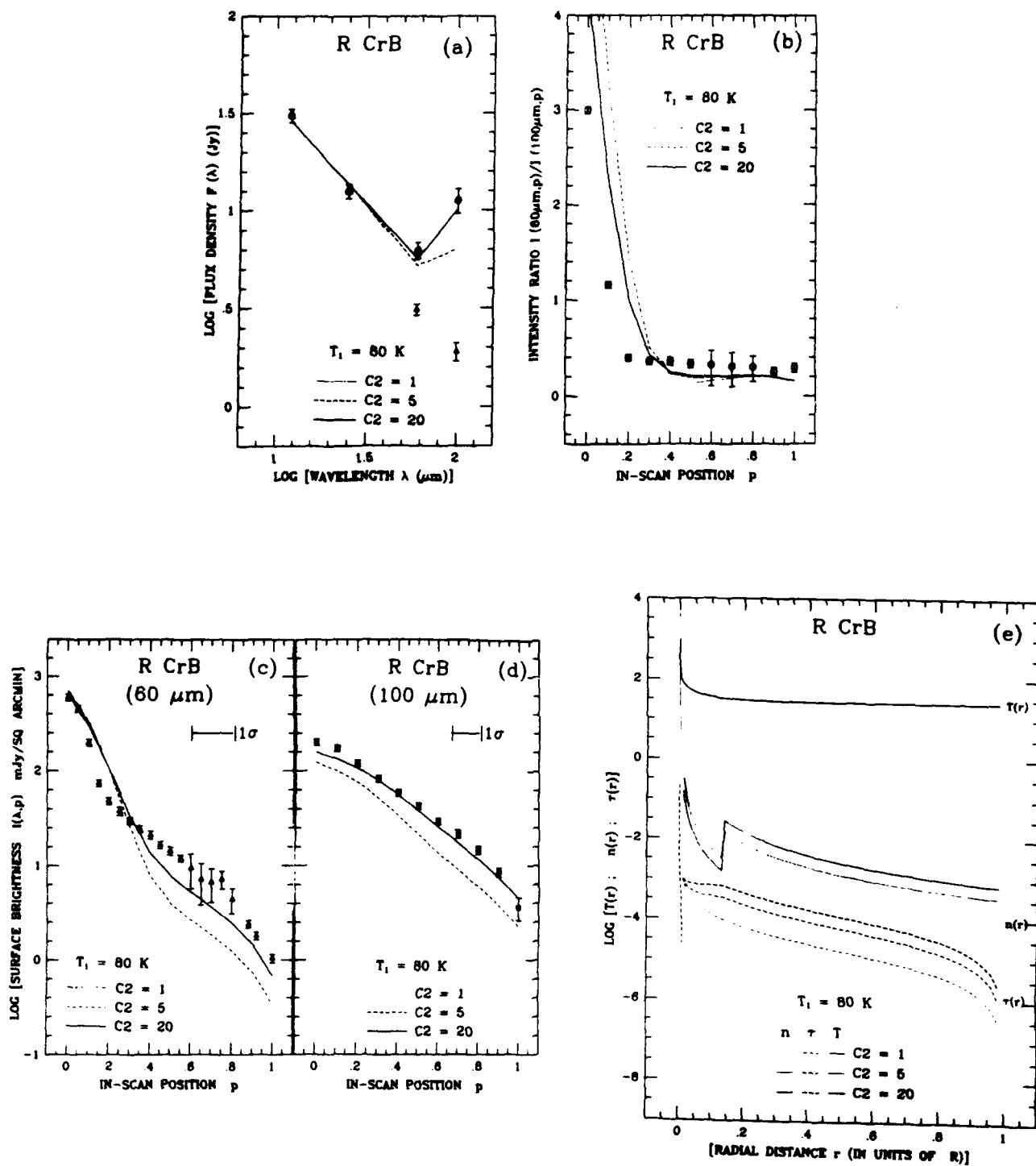


Figure 21

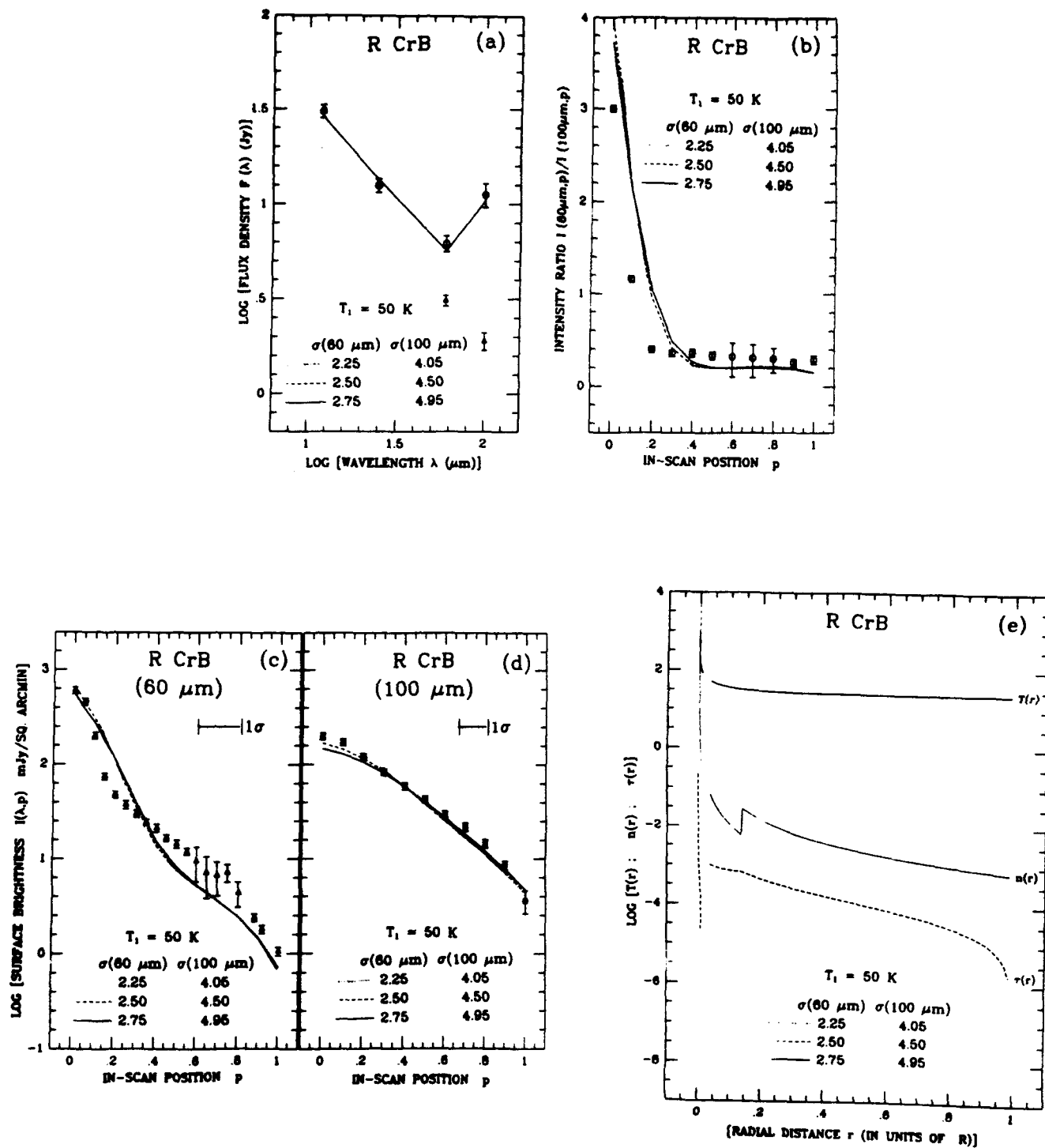


Figure 22

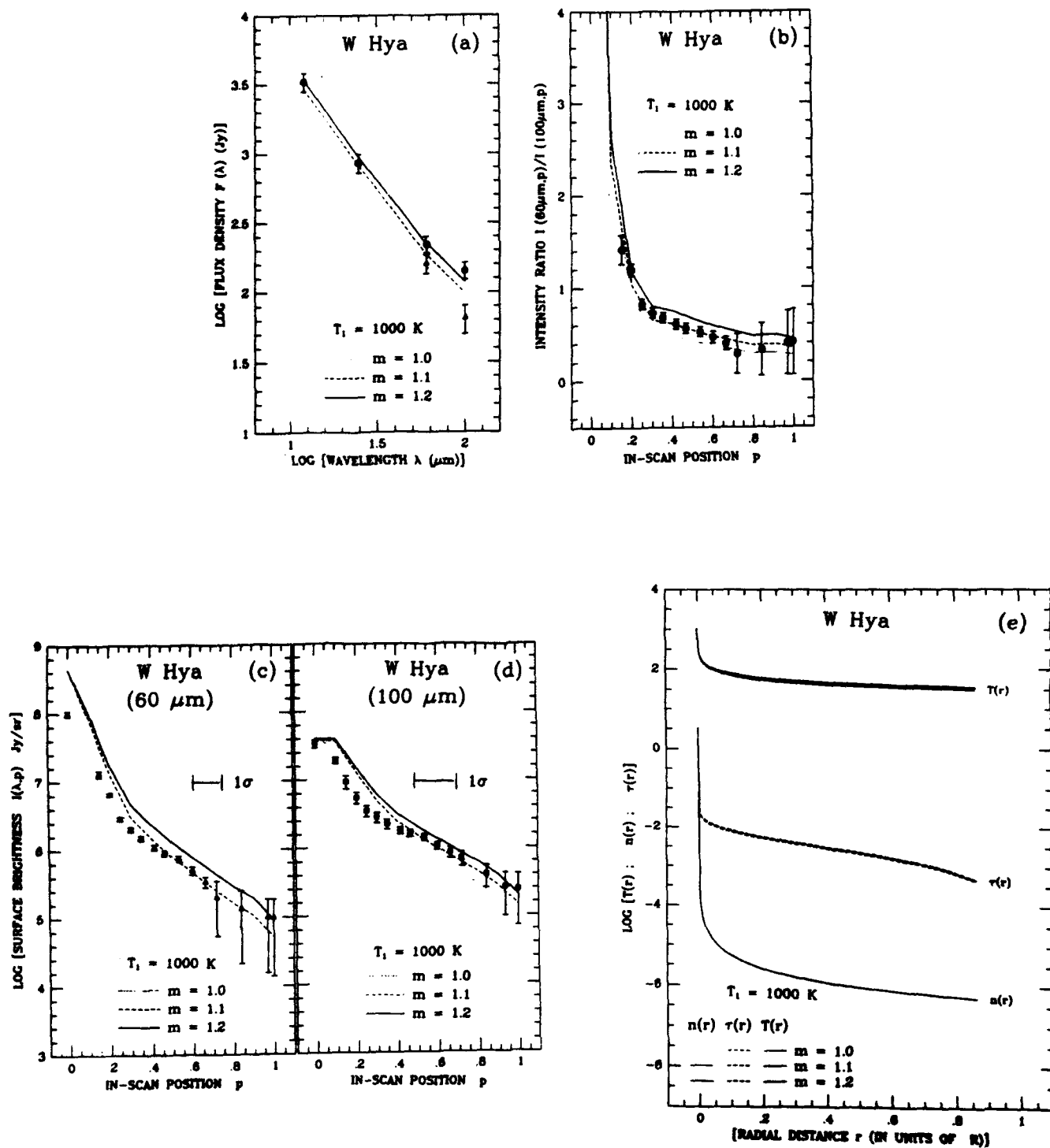


Figure 23

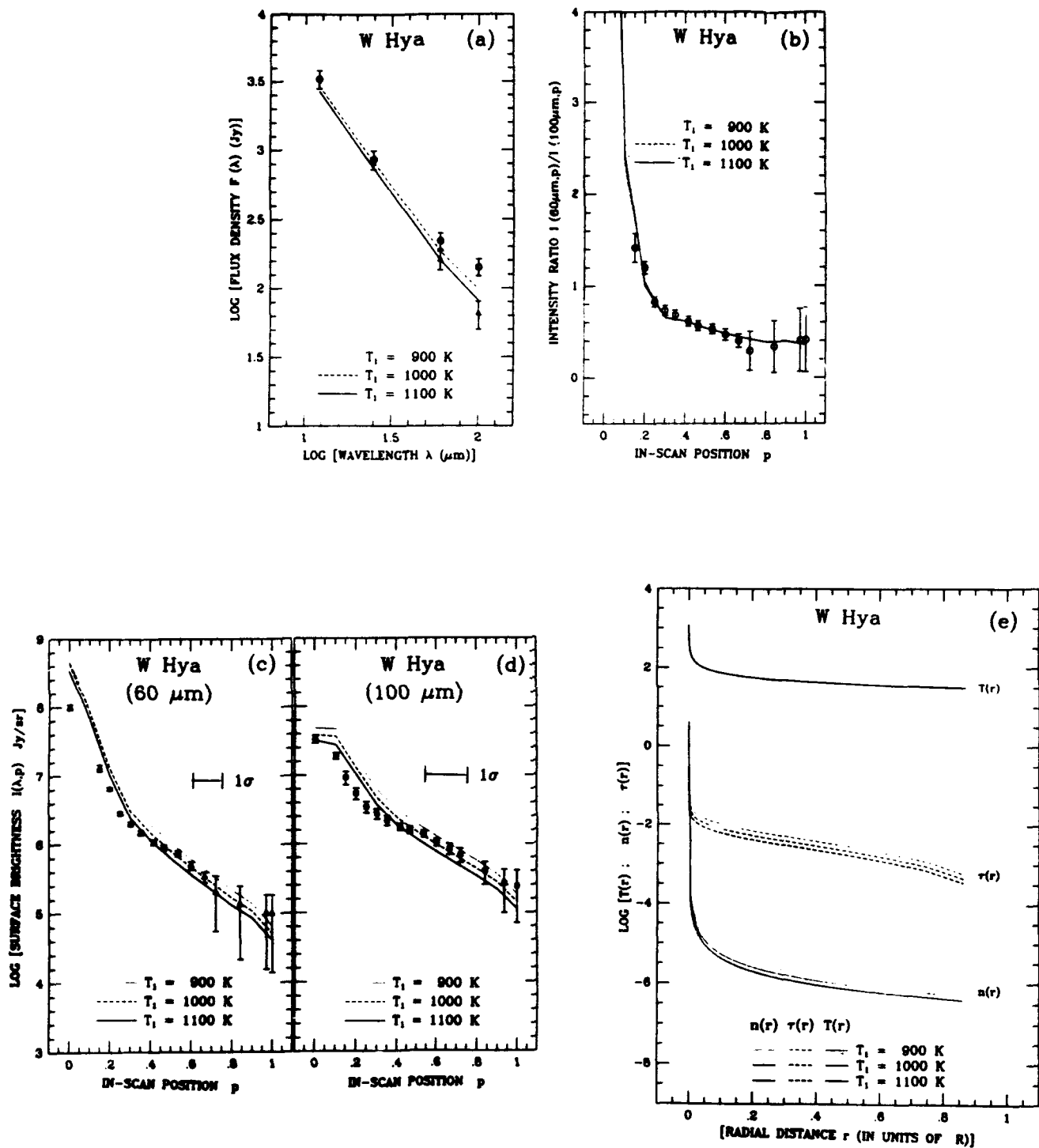


Figure 24

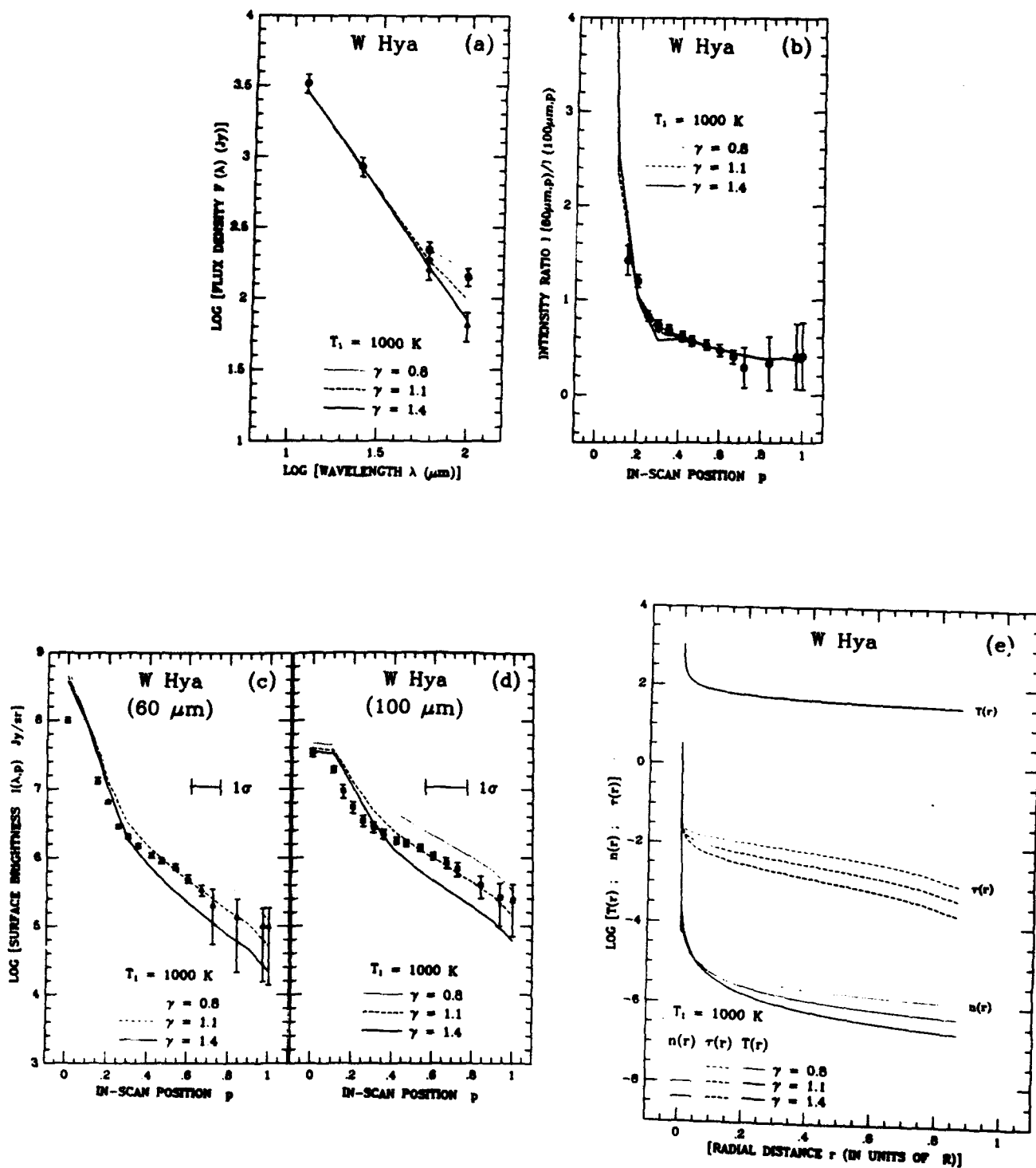


Figure 25

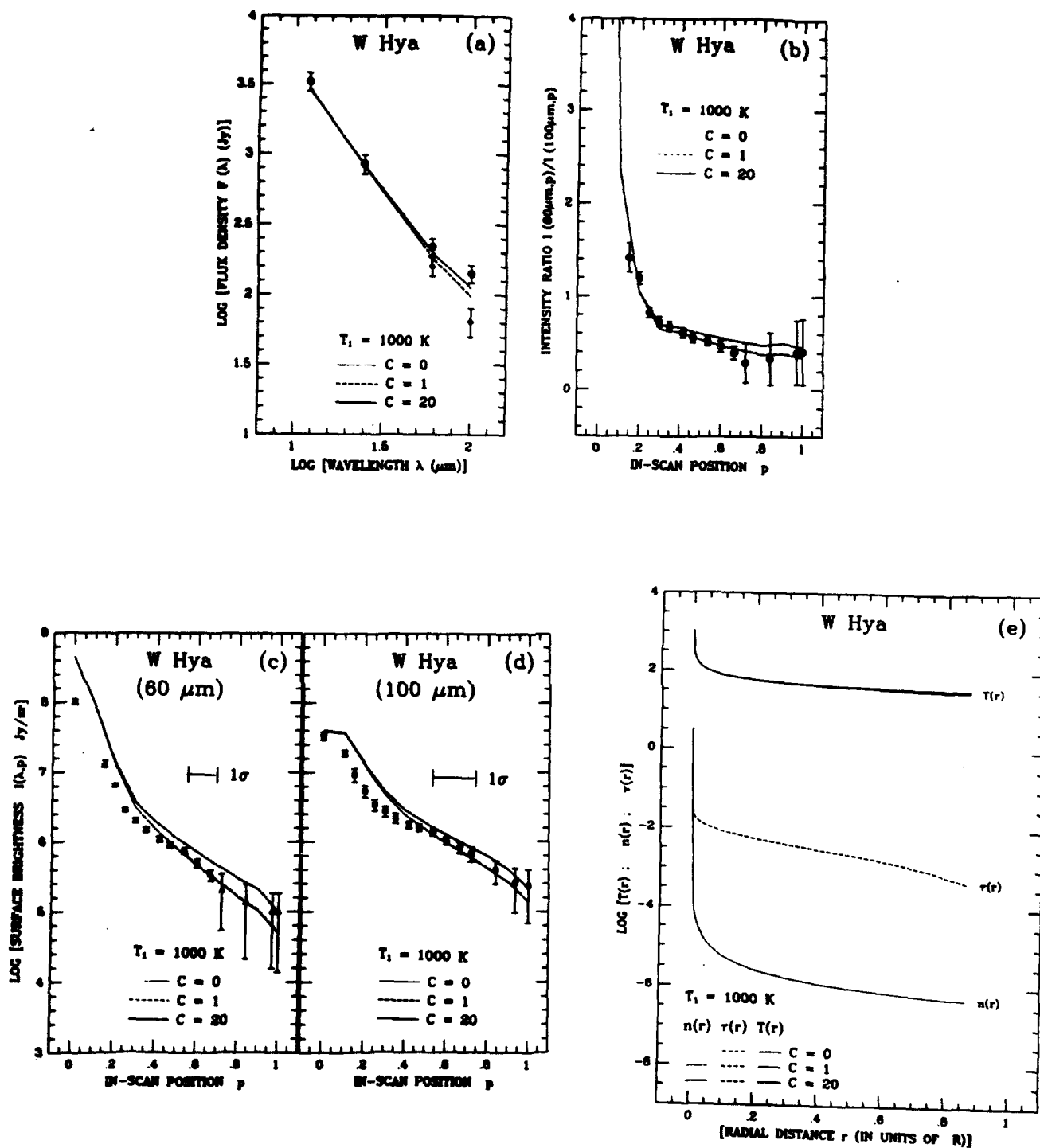


Figure 26

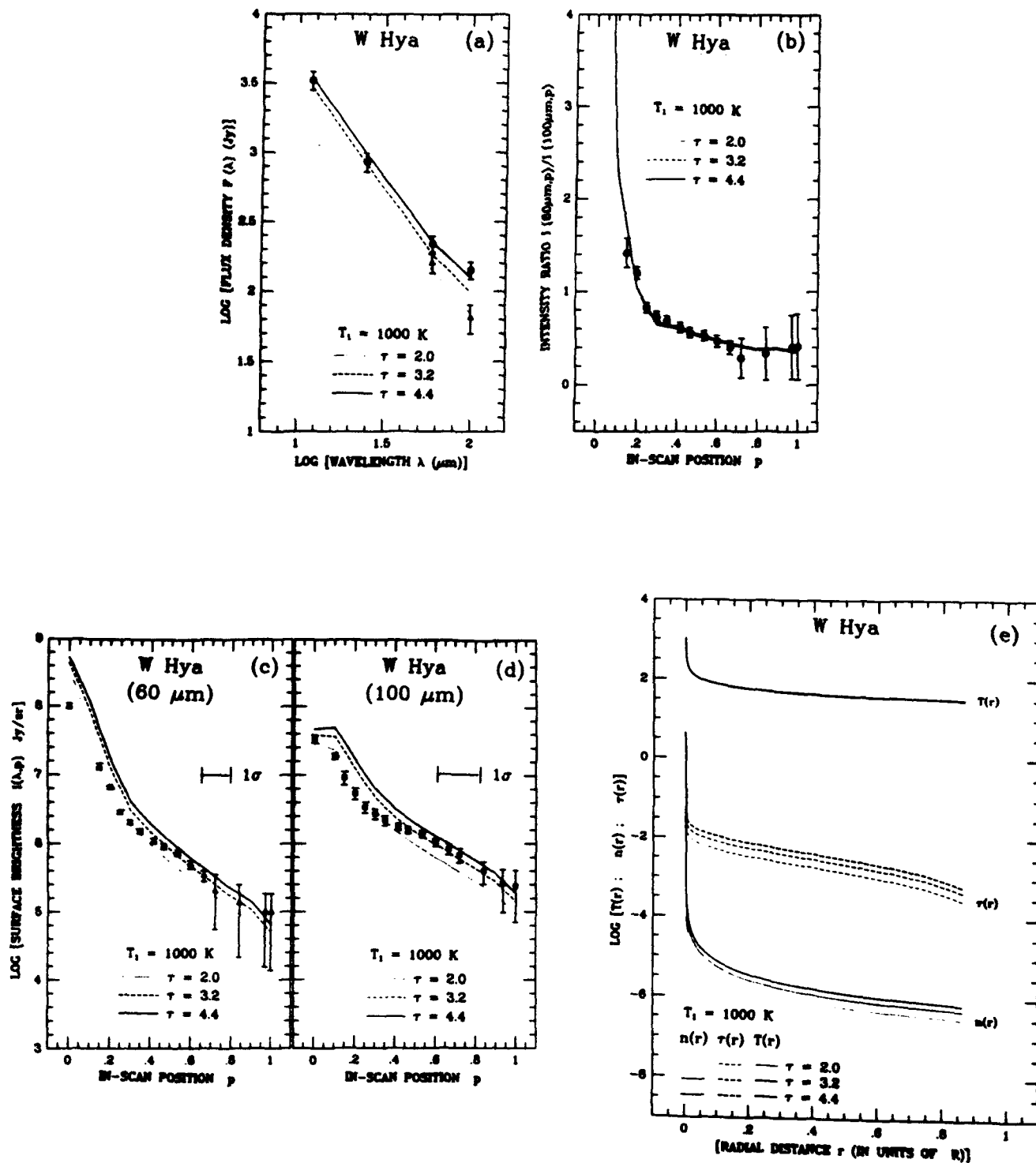


Figure 27

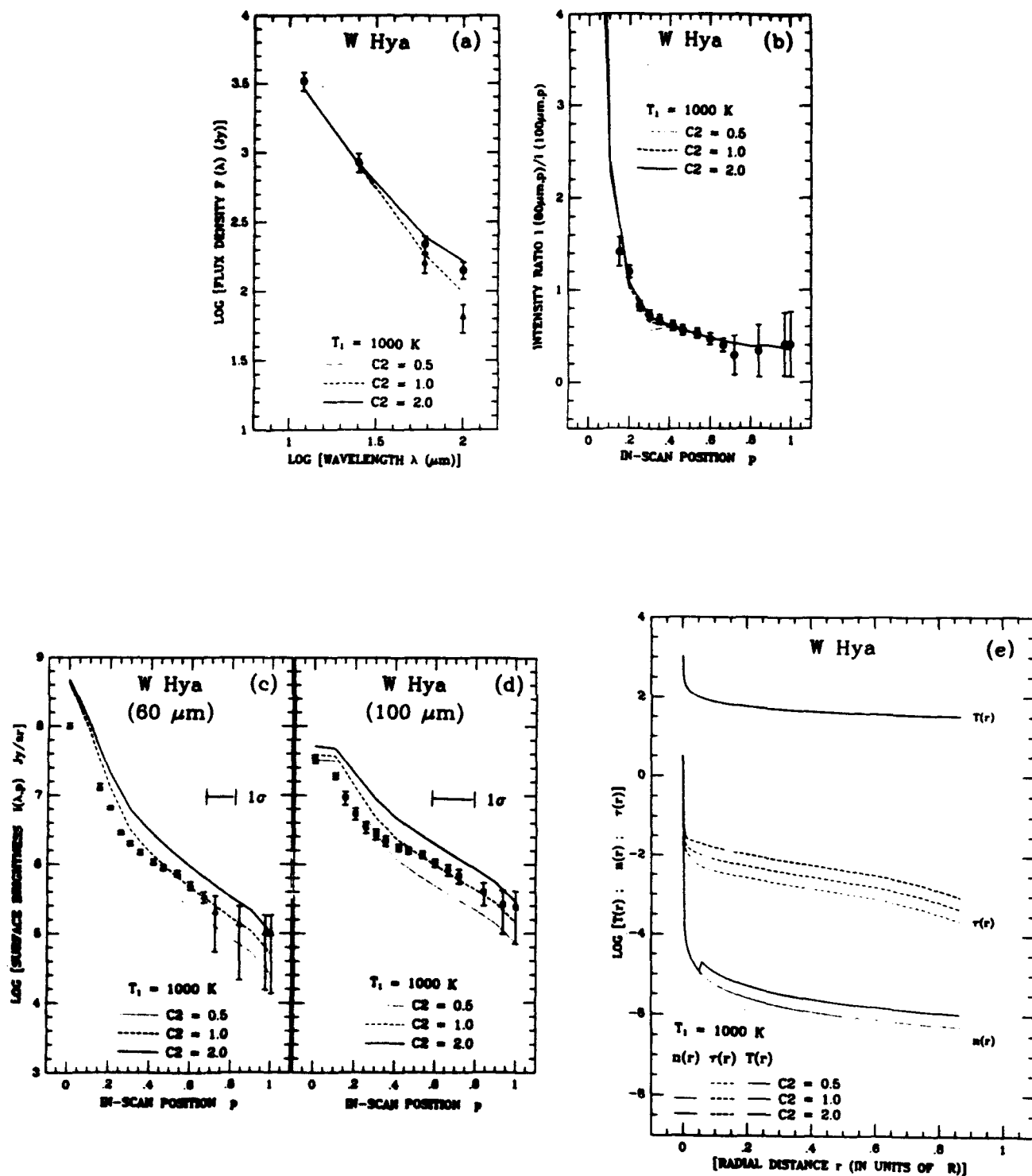


Figure 28

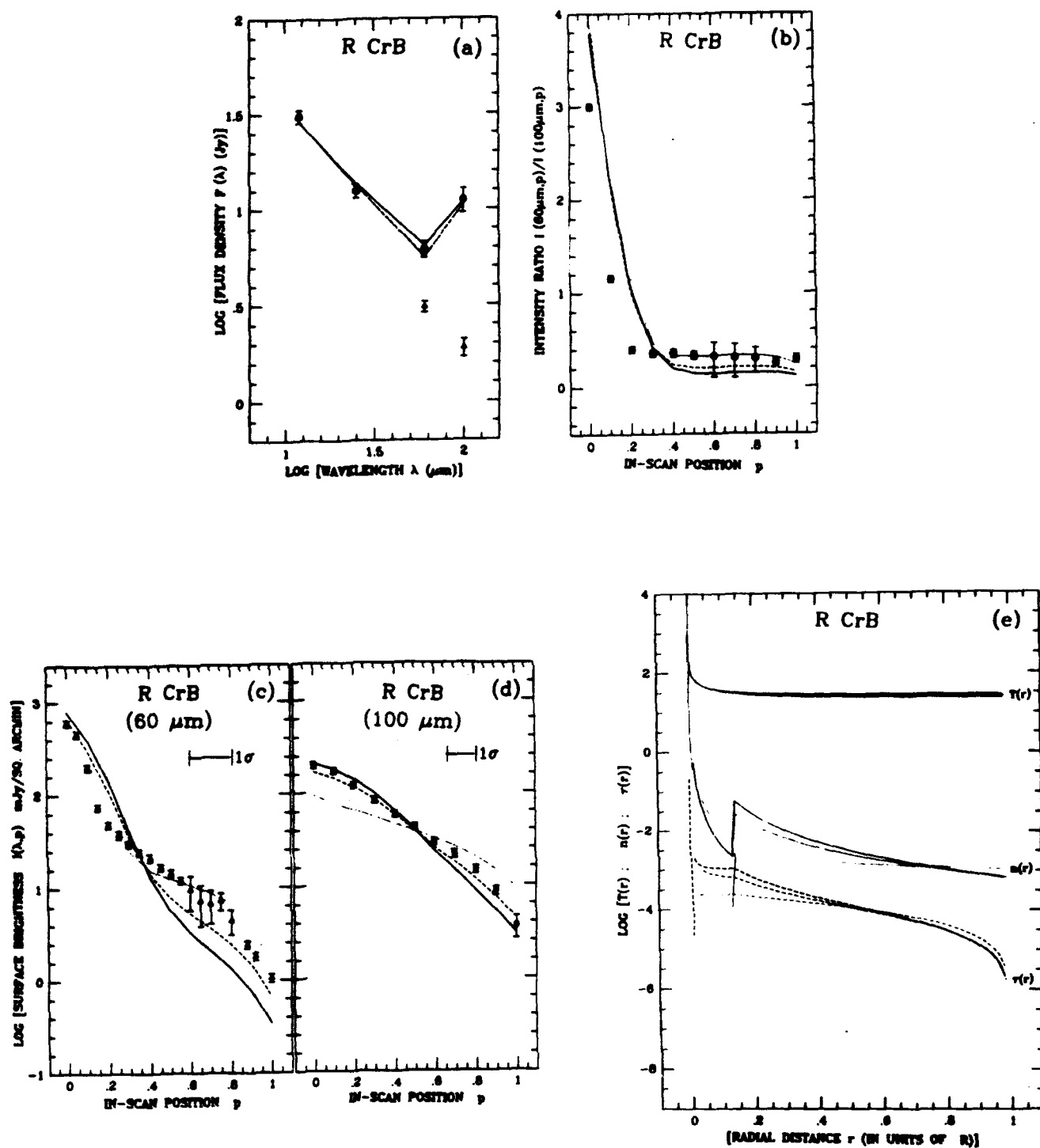


Figure 29

**A CRITICAL EVALUATION OF SEMI - ANALYTIC
METHODS IN THE STUDY OF UNRESOLVED,
CENTRALLY HEATED, INFRARED SOURCES**

STEVEN D. DOTY AND CHUN MING LEUNG

Department of Physics, Rensselaer Polytechnic Institute, Troy, NY 12180-3590

Submitted to The Astrophysical Journal

ABSTRACT

In this paper, we critically evaluate current IR data analysis techniques as applied to dusty, internally heated IR sources. This is done by constructing models of unresolved sources with a radiative transfer code. From the model results (which are treated as perfect observations) we use current IR analysis methods to attempt to derive the source parameters. The discrepancies between the actual and derived results can then be attributed to the analysis methods themselves. In general, we find that the dust temperature distribution is the most important source parameter for the emergent spectrum and hence in determining other source parameters. For internally heated sources, the temperature distribution is well described by a power law, however the power law index is strongly dependent on the source opacity. Fortunately, the temperature index can be accurately determined from the flux spectrum for sources with $\tau_0 \equiv \tau(0.55 \mu\text{m}) \leq 50$ or so. In using the slope of the IR excess to determine the continuum opacity function, we find that the derived values are consistently too low by 5-100%. The continuum opacity function may also be found by fitting the flux spectrum. In this case, the temperature distribution greatly influences the shape of the spectrum and hence the derived form of the opacity function. We also investigate the role of radiative transfer in the determination of the dust mass and optical depth among other source parameters. Where possible, we suggest alternative methods of IR data analysis short of complete radiative transfer calculations. In general, we find that although the range of applicability of current techniques is smaller than may be expected, the range can be extended with little effort.

Subject headings: infrared: spectra — interstellar: grains — nebulae: general —
radiative transfer

1. INTRODUCTION

Infrared (IR) observations have opened new areas of study of astrophysical sources. The reprocessing of radiation by dust into the infrared provides an opportunity to probe both a source and its surroundings. Through the effect that the dust has on the radiation, one may attempt to find the chemical composition and state of the grains, and something of the age and history of the associated source. This is especially true in the study of dust grains around centrally heated sources such as galaxies, planetary nebulae (PN), and their possible progenitors the circumstellar shells (CS) that are known to form around many late-type stars.

Although there has been a history of infrared observations of these objects, it has only been in the past decade that dramatic advances in both spatial and spectral resolution and signal quality have been achieved. With the successful IRAS mission in 1983, the KAO, SOFIA, and the planned deployment of SIRTf, ISO, and the IRTS, there is now and will be a large body of high quality infrared data available. During this time however, the tools used in the analysis of infrared spectra have remained relatively unchanged. In this paper we will critically evaluate the current methods of analysis of centrally heated infrared sources and, where appropriate, suggest other techniques as more reliable or robust.

The outline of this paper will be as follows: in §2 we summarize the current methods of data analysis and their underlying assumptions; in §3 we describe the procedure for solving the equation of transport and how we evaluate these methods of data analysis, in §4-9 we evaluate these methods and apply them in finding the dust mass, temperature, opacity function in the far-infrared (FIR) and for features, optical depth for features, and density distribution. In §10 we describe other miscellaneous effects, and the application of the above techniques to other IR sources. Finally, in §11, we conclude the analysis by summarizing our results.

2. CURRENT METHODS OF ANALYSIS

2.1 *Specific Luminosity*

The specific luminosity (L_ν = energy / unity frequency) observed from a thermally

emitting, spherical dust shell is often written (incorrectly) as:

$$L_V = \int \langle Q_a \pi a^2 \rangle_V B_V [T(r)] e^{-\tau(V,r)} n(r) 4\pi r^2 dr. \quad (1)$$

In the expression above, the dust density is usually chosen to be a power law

$$n(r) = n_0 (r_0/r)^m, \quad (2)$$

and the grain opacity function is taken to be a power law in the continuum,

$$Q \equiv \langle Q_a \pi a^2 \rangle_V = Q_0 (\lambda_0/\lambda)^p. \quad (3)$$

Notice that spherical emission ($dV \equiv 4\pi r^2 dr$) is combined with plane-parallel attenuation [$\exp(-\tau)$]. This expression is correct only in the optically thin limit that the curvature vanishes. Using equation (1) and applying a variety of approximations, we can find the dust and source parameters. The derivation of these techniques is given in Appendix A. Below we summarize the results for reference in later sections.

2.2 Dust Mass

The dust mass is an important macroscopic property which provides insight into the dynamics and evolution of the system. Assuming an optically thin and isothermal source, the dust mass can be written as

$$M = [F_V D^2 / \kappa_V B_V(T)], \quad (4)$$

where D is the distance to the source, and κ_V is the dust grain's absorption coefficient per unit mass (Hildebrand 1983, Beichman et al 1990). The dust mass may also be determined as a parameter when fitting the source's flux spectrum with a dust emission model. In this case, the dust mass is directly proportional to the number of emitters, and thus the constant of proportionality in equation (1), if one generalizes equation (1).

Similarly, the IR luminosity is also expected to be a measure of the dust mass. For a centrally heated source, the surrounding dust will reprocess the UV and visible light from the central object into the infrared. The greater the reprocessing, the greater the infrared luminosity. For optically thin sources, the amount of reprocessing should be directly proportional to the optical depth and hence the number of dust grains and the dust mass. Therefore, the dust mass is expected to be directly proportional to the infrared luminosity.

2.3 Dust Temperature

The dust temperature partially determines the shape of the emergent spectrum. In centrally heated sources, where the dust temperature will vary appreciably (up to 1000K between r_0 and r_{out}), a temperature distribution (TD) is used. This may be determined in the optically thin limit by assuming thermal equilibrium, giving

$$T(r) = T_0(r_0/r)^\beta = T_0(r_0/r)^{2/(4+p)}, \quad (5)$$

where β is the dust temperature index (TI), p is the power law index of the opacity function, and T_0 and r_0 are the temperature and radius at the inner edge of the dust shell respectively (Leung 1976; Kwok 1980; Sopka et al. 1985; Waters et al. 1988). Unfortunately, this still leaves an integral expression for the flux. As a result, the dust temperature is sometimes approximated as isothermal assuming that this "average temperature" will preserve the macroscopic source properties (Beichman et al. 1990)

2.4 Grain Opacity Function (Continuum)

The continuum grain opacity function (similar to the emissivity law) has been shown to vary approximately as a power law [equation (3)]. Although one may assume the opacity index (OI), p , when doing the data analysis, there are two common methods for deriving p . The index may be a parameter in fitting the output spectrum [i.e., $F_\nu = f(T, r) \times \nu^{3+p}$]. Alternately, for sources with long-wavelength emission, one may find the power law index from (Helou 1989)

$$p = [\log(F_{\nu_1}/F_{\nu_2}) / \log(\nu_1/\nu_2)]^{-2}, \quad (6)$$

by applying the Rayleigh-Jeans approximation to the Planck function and assuming an optically thin source.

2.5 Grain Opacity Function (Features)

Dust features, on the other hand, are often used as a diagnostic tool in the study of CS (Mitchell and Robinson 1978; Papoular and Pegourie 1983; Pegourie and Papoular 1984; Charnley 1989; Schutte and Tielens 1989). Attempts to derive information about the features,

and hence the source or the dust itself, rely upon the optically thin assumption again. Simpson and Rubin (1989) suggest that the opacity function of the feature may be derived by "inverting" the spectrum with (assuming $m = 2$)

$$\kappa_v = L_v / \left[\int B_v(T) \rho_0 (r_0/r)^2 4\pi r^2 dr \right], \quad (7)$$

where the values of the temperature, radius, etc are chosen from other fitting.

2.6 Optical Depth

Many of the sources under consideration are expected to be optically thin in the infrared. For CS this is often true as $0.0013 \leq \tau(10 \mu\text{m}) \leq 0.13$ when $0.1 \leq \tau_0 \equiv \tau(0.55 \mu\text{m}) \leq 10.0$ (using $p = 1.5$). In general, one must apply the optically thin approximation as this is the only way to analytically solve the equation of transfer due to the effects of reprocessing by dust.

In this case, it is possible to determine the optical depth by assuming that a dust absorption features arise from wholly absorbing cool dust in the exterior of these objects. Using this assumption, the optical depth may be found because the dust will simply attenuate the central source intensity. If we again assume a vanishing curvature, the optical depth becomes [assuming an $\exp(-\tau)$ attenuation]

$$\tau_v = \ln [F_v(\text{back})/F_v], \quad (8)$$

where F_v is the observed flux and $F_v(\text{back})$ is the background or continuum emission.

2.7 Dust Density Distribution

The dust density distribution is usually assumed to be known both for ease of use, and on physical grounds. For CS, the density profile is taken to be a power law as in equation (2), where $m = 2$ is expected for constant mass outflow. Not only is this expected from elementary theory, but many observations can be well described with this assumption (Kuiper 1967; Kwok 1980; Sopka et al. 1985). On the other hand, it has been shown by Leung (1976) that the emission can be sensitive to the density index. As a result, a determination of the index is preferable. Based on observations of 51 Ophiucus (a supposedly β Pic type object where $m = 2$ gives poor results), Waters et al. (1988) suggest a method for deriving the density power law index for CS. If the dust is optically thin in the infrared, then the index can be given by

$$m = [6 + p + 2\alpha] / [4 + p], \quad (9)$$

where p is the power law of the FIR opacity function (assumed to be known), and α is the slope of the excess flux spectrum for the source in the mid-infrared.

2.8 Fitting Spectra

Although equation (1) is a simplified solution of the transfer equation, it still involves the temperature gradient and optical depth. Consequently, we are left with two integrals in evaluating it. Only in the very optically thin, isothermal case does the specific luminosity become non-integral, namely

$$L_v = \langle Q_a \pi a^2 \rangle_v B_v(T) n_0 r_0^m (r_{out}^k - r_0^k) / [k r_{out}^2] \quad (10)$$

where $k \equiv 3-m$ for $m \neq 3$.

When fitting the flux spectrum, equation (1) may be used under the assumptions given. In this case, the equation used to fit the specific luminosity (or the flux) may be written as

$$L_v = a_1 f(a_2, \dots, a_m, \lambda) \int B_v[g(a_{m+1}, \dots, a_n, r)] n(r) 4\pi^2 dr, \quad (11)$$

where the function $f(a_2, \dots, a_m, \lambda)$ describes the opacity function, $g(a_{m+1}, \dots, a_n, r)$ gives the temperature distribution, and the a_i 's are the parameters to be fit. Due to the difficulties in fitting an integral expression, we can simplify this by assuming an isothermal temperature. In this case, equation (11) reduces to

$$L_v = a_1 f(a_2, \dots, a_{n-1}, \lambda) B_v(a_n), \quad (12)$$

where the parameter a_1 now incorporates the dust density parameter n_0 , and the length factors from the integral in equation (11).

Best fits are achieved by minimizing the chi-squared parameter defined by

$$\chi^2 \equiv \sum_i [y_{act}(i) - y_{fit}(i)]^2 / \sigma^2(i). \quad (13)$$

The parameter $\sigma(i)$ defines the uncertainty in the measurement of the point $y(i)$. In one set of fits, we have taken $\sigma(i)$ to be a very small fraction of the actual value (on the order of 10^{-9}) to simulate equally weighted, but nearly perfect observations. In a second set, we assume that $\sigma(i)$ is a constant to describe constant observational (over wavelength) uncertainty so that the

largest value in the spectrum are those most certain and thus best fit. Although these are not fully complete cases, they treat both limits in the uncertainty of observed data.

3. THE TESTING PROCEDURE

To test the derivation of dust parameters from current analysis techniques, one must be able to compare the derived dust parameters to their true values. Since this is not possible when reducing data from observations as the true values are not known, we use computer modeling of the radiative transfer to produce simulated observations. We then apply the analysis techniques described in §2 (and others developed in this paper) to derive the dust properties. Since there are no observational uncertainties, any discrepancies between the parameters used in making the models and those derived from the analysis can be ascribed to the analysis procedures themselves. The modeling is done by solving the spherically symmetric equation of transport as a two-point boundary value problem with the CSDUST3 code as detailed by Egan, Leung, and Spagna (1988).

3.1 Model Parameters

Characteristic model parameters are given in Table 1. In general, we assume a 2500K (Willems 1988) central source to characterize an evolved star. We chose to model the circumstellar shells of evolved stars as they most clearly and most often meet the requirements of unresolved, centrally heated, IR objects. Of possible centrally heated IR sources, molecular clouds, galaxies, novae and planetary nebulae are generally resolved leaving stars as the only common, unresolved sources. Furthermore, the shells around young stars are expected to be disks, and thus violate our requirement of spherical symmetry.

The dust density was taken to be a power law as in equation (2) with $m = 0, 1.5$, or 2 depending upon the model. The grain opacity function was also taken to be a power law as in equation (3) and was normalized to Draine's (1987) values at $2.2 \mu\text{m}$ for the scattering component and $190 \mu\text{m}$ for the absorption component for $p = 1.5$. The wavelength integrated opacity for other power laws was then normalized to the value for $p = 1.5$. It is expected that

the index p can well describe the opacity function in the IR/FIR with $1 \leq p \leq 2$ (Cox and Mezger 1989). As either limit may or may not be correct depending upon the source, we have taken the index as $p = 1.5$ for most models to best simulate an "average" case. In certain cases, we have run models varying p to probe the effect of the opacity function. The shell size was usually chosen with the inner radius at about the dust condensation radius ($1000\text{K} \leq T \leq 1500\text{K}$). As there is little observational constraint on the full shell size, we arbitrarily chose an inner to outer shell ratio of $r_0/r_{\text{out}} = 0.01$ which gave dust temperatures at the outer edge of the shell on the order of 150K . We have also examined a detached shell [$T(r_0) \leq 350\text{K}$] to describe an episodic mass-loss scenario and to test the dynamic range of the procedures in question.

A normal model with 67 radial grid points and 51 wavelength grid points took approximately 5 minutes to run on an IRIS 4-D workstation, and 7 seconds on a CRAY X-MP/24.

4. DUST MASS

4.1 Dust Mass via Fitting Spectrum

The dust mass can provide information about the dynamics and history of a source. However, mass determination is an uncertain process as many factors play competing roles. For example, the dust mass may be determined by a fit to the observed spectrum, using

$$L_v = 4\pi^2 n_0 Q_0 (\lambda_0/\lambda)^p \int B_v(T) dr, \quad (14)$$

in the case that $m = 2$. The constant of proportionality is directly proportional to the dust mass, thus fitting the source spectrum will indirectly give a measure of the dust mass through n_0 . Beichman et al. (1990) have used this formulation as given in equation (4) to find the dust mass.

To test this result to first order, we have determined the ratio of the dust masses between two similar sources. This removes the uncertainty in the leading coefficients, but retains the physics of the isothermal, optically thin assumptions. If two sources have similar physical

parameters, but different dust masses due to different density scaling factors, then their dust masses will be related by

$$M/M' = [L_\nu/L'_\nu] \times [B'_\nu/B_\nu], \quad (15)$$

where the primed and unprimed variables correspond to the two sources. Beichman et al. use the 12 μm IRAS band in their determination of the dust mass. In this region, the ratio of the dust emission to the stellar emission will be a maximum, making this the optimal choice. We treat the 12 μm band response as flat over the range $8 \mu\text{m} \leq \lambda \leq 15 \mu\text{m}$, the approximate half-max width of the IRAS band (IRAS Explanatory Supplement). The Planck function in equation (15) is found by fitting the emergent spectrum with a dilute, isothermal blackbody, which should be reasonable due to the narrowness of the 12 μm band. We have also assumed that the continuum opacity function exponent is known to solely test the isothermal and optically thin assumptions.

The derived dust masses are shown in figure 1 normalized to the values at $\tau_0 = 0.05$. The solid line indicates the actual dust masses. Notice that the derived dust masses are quite good. In fact, the deviation is less than a factor of 2 for large optical depths ($\tau_0 = 10.0$). The deviation cannot be due to the isothermal assumption because the relationship is seen to hold quite well at small optical depths although a definite temperature gradient is known to be present. Consequently, the effect must be due to the opacity of the shell. For $\tau_0 \leq 1.0$, $\tau(11 \mu\text{m}) \leq 0.011$ (assuming $p = 1.5$). However, $\tau(11 \mu\text{m})$ becomes non-trivial once the source becomes visibly opaque, with $\tau(11 \mu\text{m}) = 0.11$ once $\tau_0 = 10.0$. By this time, the optically thin assumption begins to break down, and the derived dust masses deviate from their true values.

Although the relative masses appear to be reasonable, it would be extremely difficult to determine the absolute dust mass with similar accuracy. This is due to the inherent uncertainties in the normalization constant in equations (4) and (14). To see this, we can take equation (14) in the optically thin, isothermal, Rayleigh-Jeans (RJ) limit. The specific luminosity in this case will be given by

$$L_\nu = (\text{constant}) r_0^2 n_0 T Q_0 d, \quad (16)$$

where, r_0 is the inner dust radius, n_0 the inner dust density, T the (isothermal) dust temperature, Q_0 the absorption efficiency constant in equation (3), and d is a length factor from the evaluation of the integral in equation (14).

The uncertainty in the dust mass will be directly proportional to the uncertainties in the normalization constant, and thus the uncertainties in the quantities in equation (16) above. Although the dust temperature is unknown, it can be approximated to within a factor of 2 under the isothermal assumption because the grains must be in the range $0 < T_d \leq 1500\text{K}$ from physical arguments. The grain types are unknown, and although it may be possible to determine the *form* of the opacity function in the IR/FIR, the absorption efficiency is dependent upon the grain size, geometry, and composition -- all factors unknown by at least an order of magnitude. The source size, given by the factor d , cannot be determined from observation because most sources are unresolved. Any attempt to estimate the source size requires information about the mass loss rate (or accretion rate), and the time of outflow (inflow), both of which will be uncertain by at least factors of 2-5. Finally, the dust density is unknown. It would be possible to determine the dust density once the density distribution, optical depth, and source size are known. In general, it is not possible to accurately determine either the density distribution or the optical depth for an unresolved source.

It is clear that any determination of the dust mass through this method will be overly sensitive to so many parameters so as to make an accurate absolute mass determination impossible. If one can eliminate some of these errors, then the dust mass determination will of course be much more accurate. *Although it is quite difficult to get an accurate absolute mass determination, if one can compare sources of similar geometry, age, dust composition, etc., then one can determine an accurate ratio of dust masses between the two sources.*

4.2 Dust Mass via Luminosity

Another similar method is to find the dust mass directly from the integrated luminosity,

$$L = \int L_\nu d\nu. \quad (17)$$

In this case, it is assumed that the dust intercepts some of the radiation from the central source,

and reprocesses it into the infrared. The IR luminosity should then be directly proportional to the number of emitters and hence the dust mass. To check this, we have calculated the integrated luminosity over various wavelength ranges ($\lambda_{\min} \leq \lambda \leq 100 \mu\text{m}$), and have plotted their values versus optical depth in figure 2. As there are source-dependant constants of proportionality, we have normalized the dust mass to that at $\tau_0 = 0.05$.

As can be seen, the masses determined from the IR dust luminosity are reasonable in the optically thin limit. Beyond $\tau_0 = 1.0$, the results become worse, deviating by about 20-25% at $\tau_0 = 1.0$, and by a factor of 2 when $\tau_0 = 5.0$. This is due to the fact that when the shell becomes optically thick in the visible, essentially all of the stellar radiation will be reprocessed into the infrared, and the addition of more dust will have smaller effects on the IR luminosity.

Although there is little difference between the fits for $\lambda_{\min} = 2.2 \mu\text{m}$, and $8 \mu\text{m}$. The marginally better values for larger wavelengths are easily explained. At $2.2 \mu\text{m}$, the stellar contamination plays a role making the derived dust masses less reliable (due to the constant luminosity from the central source itself). As the minimum wavelength increases, we observe cooler dust. The emission in this region can increase as more and more grains are added even though the dust is absorbing all of the stellar radiation. This is due to the fact that the radiation is from secondary emission, and a small change in the number of grains will make a small increase in the far infrared emission. For larger optical depths the luminosities must be integrated further into the IR.

In the bottom panel, we give a sample of the dust mass derived from the total luminosity. It is clear that the derived masses do not follow the expected relationship. This is because we are observing the constant stellar luminosity along with the dust emission. Hence, a change in the number of grains will not cause a related increase in the IR luminosity.

We conclude that the only reliable method of determining the dust mass is through the infrared luminosity. This method works well only in the optically thin regime. Furthermore care must be taken to reduce the amount of stellar contamination in the derived luminosity. As a result, determinations using the dust emission should still be integrated only longward of

8 μm or so. Finally, we conclude that the total luminosity is not a good method for determining the dust mass.

5. DUST TEMPERATURES

The dust temperature is one of the most important parameters of any system. It can describe the dynamics of dust grains (and therefore their interaction with the gas), and can drive the radiation field through thermal emission. The thermal energy emitted varies as T^{4+p} (assuming eq. (3) and thermal equilibrium), so that small changes in temperature have a large effect on the mean intensity and therefore the observed spectrum.

5.1 The Isothermal Approximation

To remove the integral expression in fitting the spectrum (eqn. (11)), it is tempting to use the isothermal approximation. Frogel and Persson (1974), Gillet et al. (1975), Scoville and Kwan (1976) and Beichman et al. (1990) have used this procedure for modeling HII regions and CS. Although this is exact in the limit of both optically and geometrically thin shells, it breaks down once reprocessing or geometric dilution play a substantial role. Still, it may be argued that such a simplification will not only make the fitting much easier, but will also represent the mean values of the dust emitting from approximately one optical depth.

In figure 3 we have plotted the derived isothermal dust temperature (found by fitting the dust emission peak, and the entire dust spectrum respectively) and the dust temperature at $\tau_0 = 1$ versus the total visible optical depth. For errors of constant magnitude, the best fit will preferentially fit the peak emission region due to the higher fluxes and hence lower fractional error. *In optically thin cases, this means that the derived isothermal temperature will be a good measure of the inner dust temperature.* As the optical depth grows there is no such correlation. This is due either to the poor removal of the stellar flux for large optical depths, and/or the large proportion of hot dust grains due to the $m = 2$ density profile. On the other hand, fits using a constant fractional error will equally weight all data points. As a result, the derived temperatures will have less physical significance. Instead, they are more

likely to be a mathematical aberration to produce a "best fit" to the data. This is the case in figure 3.

5.2 Validity of Power Law

Since the isothermal assumption is not realistic, and will not *a priori* give meaningful results, we next employ a TD. In the optically thin case, the temperature will follow equation (5). Accordingly, we have compared the actual TDs to best fit power law distributions. Sample fits are given in figure 4, where it can be seen that power laws fit the temperatures well. However, the power law index is given by the optically thin TD only in the most transparent cases, as is shown in figure 5. As the optical depth grows, the best fit TD grows steeper due to radiation trapping. By $\tau_0 = 10.0$, we find the best fit yields $\beta = .42$ (with a correlation coefficient $r^2 \geq 0.99$, and a mean fractional deviation about 4 times smaller than found when assuming $\beta = .36$). Notice that the best fit values of β correspond well to the optically thin value for $\tau_0 \leq 0.5$. As is seen by inspecting figures 4 and 5, similar results are obtained for other density profiles. Therefore, *independent of dust density profile, the actual temperature distribution in centrally heated sources can be well modeled by a power law distribution. However, the TI deviates from the optically thin limit for visibly opaque sources.* Consequently, temperature profiles and opacity function power indices (OI's) derived by fitting the source flux spectra by the single parameter, p , must be done with great care and knowledge of the opacity of the source.

5.3 Fitting β as a Parameter

Although the TD has an analytical solution, it holds only for the most transparent sources. To correct for this, one may treat β as a parameter when fitting the observed flux spectrum. This method has the advantage that it is straightforward in principle. However, the expression being fit (and hence its derivatives) are integrals and are thus computationally expensive to calculate accurately, typically taking over 20 CPU minutes on our IRIS 4-D. This is not an efficient technique for determining the TD, and we will not explore it further.

5.4 Determination of TI

The dust TD can be determined without treating β as a fitting parameter. The radiation from each position within the shell peaks at a specific wavelength. In the IR ($\lambda \geq 1 \mu\text{m}$) observations should sample the entire dust shell, and the flux at specific wavelength is dominated by the emission from a specific radial position. Hence, color temperatures derived from shell fluxes will sample different parts of the dust shell and can be used to assign a temperature profile to the dust shell.

Let us assume that the color temperature, T_c , derived by fitting the spectrum at the two wavelengths λ_1 and λ_R will follow a power law of the form

$$T_c(\lambda_1, \lambda_R) = A (\lambda_1/\lambda_R)^{-k}, \quad (18)$$

where A is a constant of proportionality, λ_1 is an arbitrary wavelength, and λ_R is called the reference wavelength. We have seen that the TD is well fit by a power law, so we take it to have the form

$$T(r) = T(r_0) (r_0/r)^{[2/(4+\alpha p)]}, \quad (19)$$

with α describing the deviation of the TD from the optically thin limit. Further assuming that the color temperature corresponds to the thermal dust temperature, we have

$$r(\lambda_1)/r(\lambda_2) = (\lambda_1/\lambda_2)^{k[(4+\alpha p)/2]} = (\lambda_1/\lambda_2)^\gamma, \quad (20)$$

where $r(\lambda)$ is the radius at which the color temperature originates.

As the functional form of α is uncertain, and the color temperature is expected to follow the actual TD (for sufficiently transparent sources), we use equation (20) in the optically thin limit that $\alpha = 1$. In this way, those sources that are transparent in the IR can still be modeled (i.e. for sources that are optically thin at the wavelengths of interest, we can take $\alpha = 1$).

Although we have no analytical method for determining k at this time, figure 6 shows this relation to be approximately correct, where we have chosen $m = 2$ and $p = 1.5$ as a representative model. In the range $4 \mu\text{m} \leq \lambda_R \leq 20 \mu\text{m}$, k is approximately constant. It is not surprising that this does not hold shortward of $4 \mu\text{m}$ and longward of $20 \mu\text{m}$: for $\lambda \leq 4 \mu\text{m}$ the stellar component dominates the total flux and contaminates the derived dust emission, while

for $\lambda \geq 20 \mu\text{m}$ there is little thermal dust emission ($T(r_{\text{out}}) \geq 150\text{K}$).

It is clear from the arguments above and figure 6 that this method is insensitive to the wavelengths chosen. However, as the method uses color temperatures, one should use only wavelengths longward of the emission peak. Experience has shown that this is best accomplished by setting the shortest wavelength used as

$$\lambda_{\text{short}} \geq 3000 T_{\text{c,max}}^{-1} \mu\text{m}, \quad (21)$$

where $T_{\text{c,max}}$ is the largest color temperature in the range $4 \mu\text{m}$ and $100 \mu\text{m}$. In this way, one is guaranteed to be on the long wavelength side of the peak, but still in the region of greatest dust emission. At the least, λ_{short} should be greater than $4 \mu\text{m}$ to minimize stellar contamination.

The long wavelength limit is also important, as equation (21) requires thermal emission. Consequently these temperatures are aphysical when there is no dust emitting at the wavelengths in question (i.e. $\lambda \geq 3000 T_{\text{min}}^{-1} \mu\text{m}$). For sources with the coolest dust this is usually about $50 \mu\text{m}$ ($T = 60\text{K}$), while for hotter sources this may be as low as $15\text{-}20 \mu\text{m}$ ($T = 150\text{-}200\text{K}$).

Naturally, it is better to use more than one reference wavelength, λ_{R} , in determining the dust TD. In order to "connect" different λ_{R} groups, we interpolate between the groups using equation (5). Experience has shown that the errors are small if one uses at least 3 color temperatures per reference wavelength.

As examples, we have derived TIs using color temperatures from the reference wavelengths $\lambda_{\text{R}} = 4, 8, \text{ and } 12 \mu\text{m}$ for different opacity functions and density distributions. These results are plotted as functions of τ in figures 7 and 8. Figure 7 shows the derived values of β for $m = 2$ and $p = 1.0, 1.2, 1.5, \text{ and } 2.0$ respectively.

In general, the TIs derived from the dust emission are quite good, and are consistently better than those derived from the optically thin limit. Although the results are poorest for $p = 1.0$, once the OI becomes about 1.2 the derived TI's are much better than the optically thin limit. It is interesting to note that the β 's also become much better for larger optical depths as

p increases. This is due to the fact that the sources become increasingly transparent in the IR/FIR relative to the visible as p increases (as we assumed in taking the limit of $\alpha = 1$ in equation (20)).

It is interesting to note from these plots that the parameter γ is fairly independent of the p ; ranging from $\gamma = .50$ for $p = 1.0$ to $\gamma = .48$ for $p = 1.5$ to $\gamma = .41$ for $p = 2.0$. These results are included in Table 2, where we have given the appropriate γ 's for opacity functions in the range $1.0 \leq p \leq 2.0$. One should note that $\gamma = 0.49 \pm 0.01$ for $1.0 \leq p < 1.6$, and then decreases as $d\gamma/dp = -0.015$ for $1.6 \leq p \leq 2.0$. This is probably also due to the increasing transparency in the FIR relative to the visible as p increases.

The value of γ is not simply fortuitous, but does relate to the color temperature/wavelength relation in equation (18). When the weighted average of k between $4 \mu\text{m}$ and $20 \mu\text{m}$ is multiplied by $(4+p)/2$, the value derived for γ is usually correct to within 3%. For example, for $p = 2$ and $m = 2$, we find $k(4 \mu\text{m})$, $k(8 \mu\text{m})$, $k(12 \mu\text{m}) = 0.4918$, 0.4254 , and 0.1233 respectively. When these are weighted by the number of color temperatures for each reference wavelength and multiplied by $(4+p)/2 = 3$, we find that $\gamma = 0.40$ -- almost exactly the best value of $\gamma = 0.41$ found for $p = 2$. The difference can be attributed to the fact that we are averaging "best fit" values. We find similar results for all values of p investigated in figure 7.

Finally, even for visibly opaque sources, TDs derived from the total flux are deficient. This is probably due to the large amount of hot dust in the models given in figure 7 caused by radiation trapping. For these models, the temperature at the inner edge of the shell (where the density is the highest) is about the condensation temperature, meaning that the dust emission will peak near $\lambda = 2-3 \mu\text{m}$. As stated before, the stellar emission is very strong in comparison to the dust emission for wavelengths less than $4 \mu\text{m}$, hence the total flux does not accurately sample the dust emission for these sources.

5.5 Dust Density and Shell Position

Figure 8 is similar to figure 7, but shows the effects of density gradient and shell position.

In the two models where $m = 0$ and 1.5 respectively, more long wavelength emission is expected due to the slow density fall off. Similarly, cooler dust temperatures and hence more long wavelength emission is also expected in 8(c) where we have modeled a *detached* shell ($r_{\text{out}} = 0.05$ pc) with $p = 1.5$ and $m = 2$. In the two $m \neq 0$ cases, the derived TIs are in good agreement with the correct values.

The TIs depend weakly on the density gradient as can be seen in figure 8. For $m = 2$, $\gamma = .48$, and similarly for $m = 1.5$. However, in the constant density case ($m = 0$), we find that it is impossible to find a good fit to the derived indices for any single value of γ . Although the constant density assumption is assumed in many calculations for ease, one does not expect the density to fall off slower than $m = 1.5$. For particles in free-fall, we find $m = 1.5$. In outflows due to radiation pressure, one would expect $m = 2$ under constant velocity, and $m \geq 2$ when the grains are accelerating away from the star. Therefore, requiring that $m \geq 1.5$ in determining the TD is not as restrictive as one may expect (see §8 for further discussion on density distributions).

Thus far we have determined the TD from the dust emission itself. However, if we use the total flux rather than the dust emission we find different results. Specifically, we find good agreement only for the more opaque sources. This is because the IR dust emission will dominate the stellar emission for these sources, meaning that a measure of the total flux accurately maps the dust emission. Notice that this effect is larger for those sources that normally have a great deal of cool dust, e.g. $m \leq 1.5$ and/or detached shells.

For optically thick sources, it is difficult to know much about the internal source, making it difficult differentiate the dust emission from the total flux. When the dust is emitting at short wavelengths, the confusion between the dust and internal source will lead to poor temperature determinations. In practice, this applies to sources which have large proportions of hot to cold dust -- very thin or transparent dust shells ($\tau_0 \leq 1.0$). However, when the dust is emitting primarily at long wavelengths (i.e. sources with $m \leq 1.5$ or detached dust shells), the total flux in the IR is a good probe of the dust.

For sources where the dust and central source emission can be deconvolved, the derived TDs give good results for physically plausible cases (i.e. $1.2 \leq p \leq 2$, and $m \geq 1.5$) when fitting the dust emission from a centrally heated source. In general, these indices are much better than those derived from the optically thin approximation for optical depths $\tau_0 \leq 1.0$. These results can be extended to the optically thick regime, $\tau_0 \geq 1.0$, when the source is optically thin in the mid- to far- infrared ($p \geq 1.5$).

6. DETERMINATION OF THE OPACITY FUNCTION IN THE FIR

6.1 Fitting *OI* as Parameter

One method employed to find p (McCarthy et al. 1978, Sopka et al. 1985) is to treat it as a parameter when fitting the dust emission spectrum. The derived *OI*'s are somewhat ambiguous due to the similar effects of temperature and opacity function index on the shape of the dust emission spectrum. The emission spectrum will be consistently wider for sources that have TDs than those which are isothermal, and this widening will increase as the TD increases. This is due to the increased emission from dust over a wider range of temperatures which leads to increased infrared emission and hence a somewhat flatter spectrum. The opacity function produces a similar effect. As the opacity function flattens, the emission coefficients at long wavelengths increase (relative to those in the visible), allowing for more IR emission. Therefore, as p decreases the dust emission spectrum will widen dramatically.

These effects are evident in figure 9 where we have plotted the values of the opacity index derived by treating the dust as isothermal. In the top panel, we show fits using the assumption of errors of constant magnitude. The results are poor, with errors of greater than 87% for $\lambda \geq 1.8 \mu\text{m}$, and 33% for $\lambda \geq 10 \mu\text{m}$ (corresponding to derived p 's of 0.2 and 1.0). The greater error in the short wavelength determination is due to the contamination of the flux spectrum by the stellar component. This accounts for the downward tail in the figure. As the optical depth grows, the stellar component will be further masked (even at short wavelengths) allowing for a better determination of the opacity index. Furthermore, fits around $1.8 \mu\text{m}$ will sample the

peak dust emission, and hence the hottest, most prevalent dust. This will fix the isothermal temperature assigned to the spectrum. However, an isothermal Planck function will not be as wide as the actual emission spectrum due to the TD in the source. To fit this over all wavelengths, the opacity function will be artificially flattened to widen the isothermal spectrum and match the actual spectrum.

For longer wavelengths, the case is a bit different. Beyond $10\ \mu\text{m}$, the emission will come from the outer parts of the shell where the temperature gradient is smaller and hence the isothermal assumption is better. As the optical depth increases, so does the temperature gradient, making the spectrum wider. Hence, as τ_0 grows, the opacity function is further flattened to account for the widening the spectrum, leading to an upward tail in the top panel. For fits beyond $100\ \mu\text{m}$, this effect is even greater because the longest wavelength emission comes from the tails of the Planck functions of the cooler grains. In this case the isothermal approximation is nearly exact, and the derived opacity functions are nearly perfect. However, because we are on the Planck tails, there is very little dust emission, making this susceptible to observational uncertainties.

In the middle panel, we show similar fits under the assumption of constant fractional errors. The results are qualitatively similar to those in the top panel, however the derived values of p are much better. We see that the errors are less than 20% when fitting wavelengths longer than $1.8\ \mu\text{m}$, and 5% when fitting wavelengths longer than $10\ \mu\text{m}$. The constant fractional errors now equally fit all wavelengths rather than just the peak, meaning that the width of the spectrum is accurately taken into account. Consequently, less artificial widening of the opacity function is necessary to widen the spectrum, leading to better values of p .

To determine the effects of the density gradient, we have modeled a constant density source. The results are shown in the bottom panel of figure 9. The determination of the OI is qualitatively the same here as with $m = 2$. However, the upward tail on the derived indices is more pronounced for $m = 0$ than for $m = 2$ (top panel). This is due to the fact that for large

optical depths, $m = 0$ produces a wider range of temperatures than $m = 2$. Consequently, the opacity function is flattened even more, producing the upward turn as the optical depth increases.

We conclude that an isothermal fit to the dust emission can give adequate determinations of the OI. The derived values of p improve as one fits longer and longer wavelengths, due to the increasingly isothermal nature of the regions responsible for this emission. Unfortunately, it is difficult to achieve an accurate measure of the dust emission due to the large amount of stellar contamination at these wavelengths. In any case, an accurate determination of the dust opacity function requires information on the shape of the dust emission spectrum, and not just the peak. *In all cases, an isothermal assumption will underestimate p by anywhere from 5-100%.*

To correct for these difficulties, we have replaced the isothermal assumption with a TD. We have chosen to keep the TI a constant during the fit. As a first approximation we use the optically thin limit for the temperature index. As the cooler dust temperatures are about $T = 150\text{K}$, we fit the dust emission up to $\lambda_{\text{max}} = 20 \mu\text{m}$. We have plotted the derived values of the OI in figure 10 as a function of optical depth for a model using $p = 1.5$. The results are dramatically better than in the isothermal assumption, with errors less than 20-25%, even for large optical depths. Fits assuming constant fractional error (not shown) yield similar results. Hence, as the optical depth increases and more long wavelength emission is present, the opacity function is flattened due to poor modeling of the TD.

In the third panel of figure 10 we show derived opacity function indices using temperature indices found via equations (18)-(20). The OIs are much better than either of the previous fits, with errors less than 4% for $4 \mu\text{m} \leq \lambda \leq 20 \mu\text{m}$, and 13% for $1.8 \mu\text{m} \leq \lambda \leq 20 \mu\text{m}$. For fits in the range $4 \mu\text{m} \leq \lambda \leq 20 \mu\text{m}$, we don't sample the very dominant hot dust or the central star. Consequently, we are more sensitive to the entire TD rather than just the very central region. On the other hand, fits below $4 \mu\text{m}$ are very sensitive to the dominant hot dust and stellar contamination, making their results somewhat worse.

For comparison, we present the OIs derived by using the "actual" TDs in the bottom panel of figure 10. It is interesting to note that the results are almost the same as those in the previous case. Specifically, notice that the downturn for fits $1.8 \mu\text{m} \leq \lambda \leq 20 \mu\text{m}$ is present in figure 10 confirming that the effect is not due to an incorrect TD. By comparing figures 10 (a),(b),(c), and (d) it is clear that *although a temperature distribution is significantly better than the isothermal approximation, the optically thin temperature distribution is also deficient beyond $\tau_0 = 1.0$. However, the use of a more correct temperature distribution resolves this problem as long as care is used in fitting the dust spectrum.*

6.2 Slope of Spectrum in Far-Infrared

The more commonly used method of determining the index to the opacity function is by examining the slope of the flux spectrum in the FIR ($\lambda \geq 50 \mu\text{m}$) as in equation (6). Figure 11 shows the derived OI, for a model constructed with $p = 1.5$ and $m = 2$. Notice that the derived values are somewhat too low, but limit to within 0.1 (6.7%) of the correct value as the optical depth and wavelengths of observation increase. As can be seen by this figure, the optimal value of p is derived when $\lambda_1, \lambda_2 \geq 300 \mu\text{m}$. This is due to the fact that, at these wavelengths, both the isothermal and Rayleigh-Jeans approximations are valid. *It is clear that a reasonable choice of the longest wavelengths possible can lead to a determination of p to within 10%.*

In the top panels of figure 11 we have also plotted the derived opacity function indices for $m = 0$. Although the spread of points is larger than for $m = 2$, the derived indices are still fairly good (errors less than 13% using $\lambda_1, \lambda_2 \geq 300 \mu\text{m}$). This error is due to the assumption of $m = 2$ in deriving the shell emission, and the inherent effect of m on the slope of the flux spectrum. By comparing the top and bottom panels it is clear that the convergence in the limit of long wavelengths is due to the quality of the Rayleigh-Jeans approximation and not the amount of cool dust. This is because although the $m = 0$ and $m = 2$ models have different amounts of cool dust (and the $m = 0$ model has cooler dust), both models achieve their limiting values of p at about the same wavelength.

In neither case ($m = 2$, or $m = 0$) is it possible to accurately determine the OI based on the

total flux. This is clear in figure 12 where we see that the OI derived from the total flux is underestimated by over 100% for $m = 2$. In these cases, the stellar flux is much greater at these wavelengths than that from the dust, and therefore the method does not probe the dust at all. Furthermore, moving to shorter wavelengths would effectively invalidate both the isothermal and RJ approximations. *Hence, determinations of the FIR opacity index from the total flux are poor and cannot be corrected.*

7. DETERMINATION OF THE OPACITY FUNCTION FOR DUST FEATURES

Many materials show features in their emission/absorption spectra (e.g. silicates at about 10 and 18 μm). It is tempting to try to use these features as a diagnostic for the type and state of the grain material, and other source parameters. We have modeled the silicon carbide feature (SiC), as a gaussian feature peaking at 11 μm added to a $p = 1.5$ continuum. Although the match in the features or the continuum is not exact, the gaussian + continuum is a good representation of the actual opacity function, so that our results should be applicable to features in general and the SiC feature specifically.

7.1 Fitting the Feature as a Parameter

Due to the complexity of the opacity function, any attempt to model it with a generic function (e.g. multiple power laws) leads to an unacceptable number of parameters to be fit. Consequently, we have assumed that the functional form of the opacity function is known, i.e.

$$Q \equiv \langle Q_a \pi a^2 \rangle = a_1 \lambda^{-p} + a_2 \exp(-\phi^2 x^2), \quad (22)$$

where $\phi^2 \equiv \ln(Q(\text{peak})/Q(\text{continuum}))$, and $x \equiv (\lambda - \lambda_{\text{peak}})/\lambda_{\text{width}}$, with λ_{width} being the half width of the feature. Although Leung and Egan (1992) have shown that the shape, size, and position of a feature are somewhat dependent upon the source parameters, we will restrict ourselves to only optical depth and radiative transfer effects in keeping with the spirit of the previous analyses. Consequently, we assume that the values of λ_{peak} and λ_{width} can be obtained for all sources from observational data, theory, or laboratory measurements. In this way, we must fit only a_1 , a_2 , and ϕ^2 , making the problem tractable.

In figure 13 we show sample emission spectra at $\tau_0 = 0.05, 1.0, 5.0$, and 15.0 to represent the optically thin, self-absorption, and optically thick cases. As the optical depth increases, notice that the height of the feature decreases, and its width increases. This is due to the absorption and subsequent re-emission of the feature radiation by dust grains in the outer part of the dust shell.

We have fit the spectra using the opacity function in equation (22) and have assumed that the index p is known. The subsequent opacity functions are given in figure 14. In the optically thin case [$\tau(11 \mu\text{m}) = 0.02$], the derived opacity function is nearly correct. However, as the opacity and effects of self absorption increase, notice that the derived opacity functions become too small and too wide in agreement with the flux spectra.

In figure 15 we plot the fractional change in the peak of the opacity function,

$$\Delta Q/Q \equiv [Q_{\text{fit}}(11 \mu\text{m}) - Q_{\text{act}}(11 \mu\text{m})]/Q_{\text{act}}(11 \mu\text{m}), \quad (23)$$

as a function of the visible optical depth. Notice that the figure appears to follow a power law relationship for small optical depths. This can be understood by assuming that the emission region is approximately isothermal. If this is true, then

$$Q_{\text{act}} B_{\nu}(T_{\text{act}})[1 - \tau + \tau^2/2] = Q_{\text{fit}} B_{\nu}(T_{\text{fit}}), \quad (24)$$

where we have set the optically thin emission expression equal to the expression used to fit it.

After some algebra, and defining $\theta \equiv B_{\nu}(T_{\text{act}})/B_{\nu}(T_{\text{fit}})$, we see that

$$\Delta Q/Q = (1 - \theta) + \theta(\tau - \tau^2/2). \quad (25)$$

In the optically thin limit, $\theta \equiv 1$, and equation (25) becomes

$$\Delta Q/Q = \tau - \tau^2/2, \quad (26)$$

which can be approximated by

$$\Delta Q/Q = a\tau^b, \quad (27)$$

where we expect that $0 \leq a, b \leq 1$ due to the subtraction of the τ^2 term. A fit of a and b yields $a = 0.29$ and $b = 0.82$ for $0.05 \leq \tau_0 \leq 1.0$, and $a = 0.29$, $b = 0.52$ for $1.0 \leq \tau_0 \leq 10.0$. These two fits are shown in figure 15, where it can be seen that they work well in the optically thin limit, but poorly for optically thick sources.

This is a direct result of the effects of radiation transfer and the reprocessing of IR radiation by dust grains. No semi-analytical model can accurately account for these effects in the optically thick limit. For transparent sources, where radiation transfer effects are not as large [as evidenced by the small value of $\exp(-\tau)$], we can account for the decreasing feature height easily by simple absorption while neglecting re-emission. This is not the case once reprocessing becomes important. This can be seen by realizing that θ is an unknown function of several variables and is unity only in the optically thin limit.

7.2 Determination Opacity Function via Inversion

A more common method for determining the opacity function for spectral features stems from modeling the dust emission as optically thin, and "inverting" the flux spectrum according to equation (7) to find the opacity function. This method obviously suffers from the fact that the shape of the opacity function is directly tied to that of the flux spectrum. Consequently, this method is inapplicable in optically thick cases where self absorption plays a role.

Again, in figure 13 we have plotted the flux spectra for sources with optical depths of $\tau_0 = 0.05, 1.0, 5.0, \text{ and } 15.0$ [corresponding to $\tau(11 \mu\text{m}) = 0.02, 0.40, 2.01, \text{ and } 6.02$]. It is clear that the cooler dust grains plays a role in decreasing the height and widening the feature, and finally producing the classic self absorption "double peak" when the dust is optically thick. In figure 16 we have plotted the opacity functions derived from fitting these flux spectra according to equation (7), and assuming that the continuum opacity function was known. Notice the strong correlation between the shape, width, and height of the opacity functions with their corresponding fluxes. This is an outgrowth of the inversion process. *Although the inversion method does not work for optically thick cases, the derived opacity functions are good in the optically thin ($\tau_{\text{feature}} \leq .40$) limit.*

7.3 Comparison of the two methods

From figures 14 and 16 it is clear the the two methods give complementary results. The assumption of a gaussian feature (or of any feature shape) is somewhat restrictive. However, this reduces the effects of self absorption on the derived features. In accord with this, the

gaussian assumption gives consistently better fits in the peak region of the spectrum, but poorer fits in the wings. On the other hand, the inversion process better maps the wings since these wavelengths are left relatively unchanged as the optical depth increases. Hence, a simple inversion of the flux spectrum will yield a reasonable opacity function, whereas assuming the functional form will lead to a widening of the wings in accord with the widening of the peak.

8. OPTICAL DEPTH FROM FEATURES

As many of the effects mentioned above can be functions of the number of dust grains and hence the optical depth, we would like to be able to determine the optical depth from observations. If one assumes a plane-parallel geometry and neglects re-emission, the central source emission will be attenuated by a factor of $\exp(-\tau)$ as shown in equation (1). The plane-parallel assumption is necessary as it is the only geometry which yields the simple exponential factor.

Persson et al. (1976), Lacy et al. (1984), and Pegourie & Papoular (1985) (among others) have applied this method with some success. Their reported data show a definite tendency toward small optical depths. This is to be expected because all of the dust will both emit and absorb. Hence, the assumption of pure absorption is not correct. This is especially true in the IR where absorption efficiencies are fairly small in comparison to the visible. Consequently, the absorption "troughs" will not be as deep as they would be under pure attenuation due to the effect of emission, meaning that the derived optical depths will be smaller than the true optical depth at that frequency.

Sarazin (1978) analytically examined a similar problem when he investigated the effect of multiple grain types on source spectra. In the optically thin limit, the intensity summed over different grain types, i , can be written as,

$$I_V = \sum_i \tau_V(i) B_V(T_i), \quad (28)$$

where T_i is the temperature of the i^{th} grain type. Equivalently, if we consider a temperature

gradient and divide the dust shell into isothermal subshells we derive the same expression. The summation would now be carried over all subshells rather than grain types. It is clear, then, that the effects of multiple grain types and temperature gradients are qualitatively similar.

In the case of multiple grain types, Sarazin found that the absorption feature "saturates." In his examples, even as the physical optical grows to infinity, the derived optical depth did not go beyond about 2. We have examined this effect for temperature distributions by *self-consistently solving the equation of transfer and then solving for the optical depth using equation (8)*. We have used a gaussian feature at $3\ \mu\text{m}$ (similar to the $11\ \mu\text{m}$ feature discussed in §7) in investigating this effect. The feature was placed at $3\ \mu\text{m}$ rather than at $11\ \mu\text{m}$ due to the greater contrast in dust temperatures, and hence more absorption. In this way, we can probe the effect over a larger range of reasonable optical depths than for the silicate feature.

We have investigated this effect for $3.0 \leq \tau_0 \leq 1000$ (corresponding to $12 \leq \pi(3\ \mu\text{m}) \leq 4000$). Although there is absorption for $\tau_0 \leq 10$, the features in this range show the characteristic reversal of self absorption (absorption and emission). Once the optical depth becomes large enough, the absorption can overcome the emission leading to a "pure absorption" spectrum. We find the optical depth by fitting the continuum with two blackbodies, and applying equation (8) at the lowest point in the flux spectrum of the feature. This point is usually shortward of the $3\ \mu\text{m}$ peak in the opacity function, and is in the range $2.2\ \mu\text{m} \leq \lambda \leq 2.5\ \mu\text{m}$ due to the fact that the feature falls shortward of the continuum peak wavelength.

In figure 17 we plot this derived optical depth as a function of the visible optical depth. Notice that there is some inconsistency in the data below $\tau_0 \leq 10$ compared to that above $\tau_0 = 30$. This is due the change over from a self-absorption spectrum to a pure absorption type spectrum. Aside from this, there are two major trends in figure 17. First, the derived optical depth is consistently much lower than the actual optical depth. This is due to the re-emission by dust grains, making the absorption feature less deep, which in turn suggests a smaller

optical depth in an absorption- only model. Secondly, as the optical depth grows very large, the calculated optical depth of the feature tends to a constant. This is just the effect noted by Sarazin for silicate features. Although the limiting optical depths are different, this is understandable as we have treated a different feature, for a dissimilar source, outside the optically thin limit. As suggested above, however, the effect of a temperature distribution is qualitatively similar to the effect of multiple grain types.

Obviously, the differences between the actual and derived optical depths are due to temperature and density distributions, along with radiative transfer effects. *We conclude that the optical depths derived from spectral features will always be too small by a factor depending upon unknown source parameters and radiative transfer effects.* The factor is not constant as a function of optical depth; the derived optical depth tends to a limiting value as the actual optical depth tends to infinity. Radiative transfer effects due to combined emission/absorption cannot be accounted for by a simple analytical model. Therefore, in sources where the dust responsible for the absorption can also emit in large amounts, one must be very careful in determining the optical depth.

9. DUST DENSITY DISTRIBUTION

The dust density is an important source parameter. Leung (1976) has shown that the emergent spectra can be very sensitive to the dust density profile. This is due to the fact that the density gradient will lead to different amounts dust near $r = r_0$ in proportion to dust near the outer parts of the shell. Consequently, the density gradient will determine the proportion of cool to hot dust, and hence the emergent spectrum.

Unfortunately, the effect of the density gradient on the emergent spectrum of an unresolved source can also be mimicked by effects of source geometry. Consider a central source surrounded by a spherical shell of dust. For each amount of short wavelength radiation intercepted by the dust (and taken from the flux spectrum), an equal amount will be added to the long wavelength region of the spectrum. This leads to a rounded emission spectrum

because for each subtraction at one point, there is an addition at another point, with a peak somewhere in the middle of the spectrum.

On the other hand, consider a star surrounded by an axially-symmetric dust shell. In this case, the column density of dust along any line of sight will depend upon the orientation of that line of sight with respect to the disk. To be specific, consider a flattened disk so that the poles (top and bottom) of the disk are optically thin, but so that the disk is optically thick when viewed edge-on. The viewing angle will determine the proportion of short to long wavelength emission from the dust. If viewed from the pole (top), where the disk is the most optically thin, there will be much more short wavelength emission than long wavelength emission. However, the situation will be reversed when viewing the disk from edge on due to the large optical depth and effects of reprocessing. As a result, when viewing from an arbitrary angle, both effects will be evident. Consequently, an observation of a source with disk geometry will tend to show a *flatter* spectrum than an equivalent spherical source. This effect has been noted by and Evans et al. (1990) in their examination of L1551, and Dent (1988) in a theoretical discussion of disk sources.

A similar effect is seen in spherical symmetry with an $m < 2$ density distribution. For example, in studying 51 Oph, Waters et al (1988) attributed the flattening of the excess flux spectrum to a spherical density distribution with $m = 1.3$. Similar to §6, they use the slope of the FIR flux spectrum to determine the continuum opacity function. From this, they use the slope in the mid-infrared to derive the density distribution as given in equation (9). However, given the geometrical arguments above and the fact that 51 Oph may be a Be star (stars which should have flattened disks surrounding them), it is unclear whether the effect mentioned is due to geometrical effects or the density gradient.

Many sources show spectra that are fairly rounded, and have no "flat" top. Furthermore, many of those sources that show spherical symmetry can be well modeled by an $m = 2$ dust density distribution, and an $m \geq 2$ electron density distribution. There are also other compelling physical reasons to believe that the density distribution should be $m \geq 1.5$, where

there is little or no flattening of the mid-infrared spectrum for use in equation (16).

Specifically, we would expect $m = 1.5$ for free-fall, $m = 2$ for constant mass outflow, and $m \geq 2$ for accelerating outflow. Beyond this, it is expected that a source with disk geometry will show such a spectrum due to the flattening of the disk and hence optical depth effects.

Consequently, it is difficult to accurately find the dust density distribution because for realistic values of m the spectra do not show the necessary flattening, while flat spectra are easily generated in a geometry in which equation (9) does not hold.

10. MISCELLANEOUS CONCERNS

In this section we will address effects other than those discussed in the preceeding sections for evolved stars. We will use these discussions in order to generalize our results to other IR sources.

10.1 Effects of Other Source Parameters

Parameters which could effect the temperature distribution and hence radiation field include the density gradient, shell position, grain composition, stellar luminosity, stellar effective temperature, and shell extent. We have shown in previous sections that, within limits, the first three parameters have minimal effect. Specifically, we showed that for $m \geq 1.5$, and $1.0 \leq p \leq 2.0$ that the TD and hence other derived parameters are fairly accurate. The inner shell position was varied between the condensation radius and a detached shell. The only effect was to improve the derived temperature distribution. Consequently, shell position also plays little if any role.

The stellar luminosity plays a role analogous to shell position. A source with an inner shell position r_0 would have an energy density equivalent to a much more luminous source with an inner shell position $r'_0 = r_0 [L'/L]^{1/2}$ where the primed and unprimed variables correspond to the two sources. Consequently, we expect the stellar luminosity to have little effect in analogy with shell position.

The stellar effective temperature also plays a role akin to shell position. In the optically

thin case, T_* comes into the temperature distribution equation in the same way as L_* . For optically thick sources, the effective temperature does not play a role due to the fact that the dust will have reprocessed all of the stellar radiation. Consequently, in neither limit is T_* an important parameter. This, coupled with the fact that the methods shown above for deriving dust parameters work well in one of the two limits, suggests that we do not need to worry about the role of T_* for most sources.

The final parameter is shell extent. This will obviously have an effect in the FIR by producing more cool dust. However, for most of the sources considered here ($m \geq 1.5$), shell extent will have almost no effect on the mid-IR radiation field ($5 \mu\text{m} \leq \lambda \leq 20 \mu\text{m}$), which we used in deriving the temperature distribution. This can be seen by considering the maximum fractional change in optical depth by extending the shell from $(r_{\text{out}}/r_0) = 100$ to ∞ :

$$(\Delta\tau/\tau)_{\text{max}} = 1 / [(r_{\text{out}}/r_0)^{m-1} - 1] \quad (29)$$

which, for $m = 2$, becomes $(\Delta\tau/\tau)_{\text{max}} \approx 0.01$. Consequently, the only effect of an extended shell would be to provide a stronger FIR emission. In practice, this means that one could probe cooler, more isothermal parts of the source with better accuracy, making the determination of the FIR opacity function better than in the current analysis (see discussions in §6).

10.2 Effects of Remnant Shell

Stellar evolution theory (Willems 1987; Olofsson et al. 1990) suggests that IR stars may have remnant dust shells around them. This seems to be borne out by the modeling of Egan and Leung (1991), where the IRAS color of these sources can only be explained by cooler remnant shells. Even though they may be common, they will have little effect on the previous analyses. A remnant shell should behave (qualitatively) like an extended shell. We would expect cool, nearly isothermal dust in the remnant shell emitting in the FIR ($\lambda \geq 50 \mu\text{m}$). As such, the emission will have no consequence for those parameters derived using the mid-IR fluxes.

However, this extended emission could be easily fit by a dilute blackbody due to its

isothermal nature. Furthermore, as noted before, the greater FIR emission will only enhance the determination of the FIR opacity function by giving better long-wavelength data, and in better satisfying the isothermal approximation. Beyond this, it would also be expected that the dust mass determinations would be somewhat better -- again due to the isothermal assumption. Obviously, the magnitude of these effects will be complex combination of source strength, shell position, shell temperature, and dust density. However, if the mass of the remnant shell is of the order of that for the regular shell, one would expect a fairly small effect due to the low temperatures expected in the remnant shell.

10.3 Application to Other IR Sources

In applying the previous results to other IR sources, the two most important effects will be the luminosity/optical depth ratio, and the amount of central source obscuration. Let us first examine the luminosity/optical depth ratio for completely obscured sources. If it is similar to what we've examined in the previous sections, our results should be similar. For higher temperatures, we expect a situation with a shell near the star. On the other hand, low temperature situations should be similar to a detached or extended shell. Both cases have yielded good results.

For sources with much increased luminosity, the situation is somewhat different. The higher luminosity will simulate a lower optical depth for the shell. For optically thin sources, we expect no change as most of the radiation will be able to "make it through" anyway. For very optically thick sources, we again expect no change other than the total FIR luminosity emitted because most of the radiation will be reprocessed anyway. The transition between these two regimes will depend upon the luminosity of the central source. The larger the luminosity, the further the internal radiation will be able to "burn into" the surrounding dust shell before it is totally absorbed. Consequently, for reasonable luminosity/optical depth combinations, one would expect little change in our results.

On the other hand, for sources where the optical depth is very high or the central source luminosity is very low, the case is much different. This situation is similar to an object

without an internal heat source, and the discussions developed in this paper are not applicable.

The second effect would be due to the amount of central source obscuration. If the central source is completely enshrouded by the dust shell, then the radiation received will be that reprocessed by the dust. If, as in the case for thin disks, the source is not completely obscured, then the radiation received will be a combination of the direct source radiation and the dust emission. Consequently, attempts to derive dust source parameters will be hampered by the contamination of the emission spectrum by the underlying source. In this case, there should be a great deal of mid-IR contamination, making the determination of the dust temperature invalid. To fully understand this problem, one should run a complete set of radiation transfer models for disks with varying scale heights and optical depths. This, however, is beyond the scope of this paper.

11. CONCLUSIONS

We have studied the current methods of analysis of centrally heated, infrared sources. Specifically, we have examined the validity of current assumptions employed in semi-analytic methods and the parameter space regions in which they are reasonably applicable. Where possible, we have indicated other or better methods in the study of these sources. Below is a summary of the major points we would like to emphasize:

11.1 Dust Mass

1. It is not easily possible to determine the absolute dust mass for a source due to the gross uncertainties in the constant of proportionality (equations (28) & (29)). On the other hand, one can well determine the *ratio* of dust masses between similar sources. (with differences of only a factor of 2 for $\tau_0 = 10.0$ and assuming an isothermal source).
2. The dust mass can be determined with similar accuracy from the excess, frequency-integrated luminosity. Better results are achieved for integrations further into the infrared (i.e. $8 \mu\text{m} \leq \lambda \leq 100 \mu\text{m}$ gives $\Delta M/M \leq 0.4$ while $2.2 \mu\text{m} \leq \lambda \leq 100 \mu\text{m}$ yields $\Delta M/M \leq 0.6$). However, reasonable dust mass determinations are not possible from the total frequency

integrated luminosity due to stellar contamination of the flux spectrum (where $\Delta M/M = 0.99$).

11.2 Dust Temperature

3. For optically thin ($\tau_0 \leq 1.0$) sources, an isothermal best fit to the peak of the excess flux spectrum is a good measure of the inner dust temperature. However, fits to the entire spectrum, or fits of optically thick sources show no such correlation.
4. For expected density distributions ($m \geq 1.5$), the TD can be well modeled by $T(r) = T(r_0) (r/r_0)^\beta$. For $\tau_0 \leq 0.5$, $\beta = 2/(4+p)$ as is expected. For larger optical depths, this approximation is poor ($\Delta\beta/\beta \geq 0.1$).

A more correct value of β can be derived (as outlined in §5) assuming that the FIR opacity function is known to within $\Delta p = \pm 0.2$. The results are best when $1.5 \leq p \leq 2.0$, but can be used down to $p = 1.0$. This procedure works well even for optically thick sources ($\Delta\beta/\beta \leq 0.05$).

5. Due to stellar contamination, the TD must be derived from the excess flux spectrum. Only in the case of extremely cool dust emission ($m \leq 1.5$, or detached shell) is the total flux a good probe, and even then only for opaque sources.

11.3 FIR Opacity Function

6. Attempts to find the FIR opacity index, p , by fitting the excess flux spectrum by an isothermal blackbody results in a wide range of error ($0.03 \leq \Delta p/p \leq 1.00$). The inherent TD allows an isothermal fit only for very long wavelengths (where dT/dr is small). The deviations are quite sensitive to source opacity, giving results which are worse for $\tau_0 \geq 1.0$ by more than a factor of 3. The sensitivity is greater for smaller m due to the effect of cool grains widening the spectrum.

As p strongly effects the shape of the spectrum, isothermal fits are much better when all wavelengths are equally weighted in comparison to fitting the peak preferentially (This yields $\Delta p/p$ better by more than a factor of 2).

7. To better account for the effects of temperature on the shape of the spectrum, a TD is necessary. The optically thin approximation to β gives errors ≤ 20 -25% even for large optical

depths. The errors are much smaller ($\leq 4\%$) when using β as derived in §5. Furthermore, this value of β is much less sensitive to optical depth effects.

8. The index p can be fairly well determined (to within 10-20%) by the slope of the FIR excess flux spectrum (the total flux spectrum yields $\Delta p/p \geq 0.5$). When using this method, it is best to use two wavelengths in the FIR (i.e. $\lambda_1, \lambda_2 \geq 300 \mu\text{m}$) to ensure the Rayleigh-Jeans and isothermal approximations.

11.4 Feature Opacity Function

9. When determining the opacity function assuming its functional form, one derives a feature that is too wide and too small (although reasonable heights are achieved for $\tau_0 \leq 1.0$ where $\Delta Q/Q = 0.29$). On the other hand, opacity functions determined from inversion of the spectra give better widths. Unfortunately, since the derived opacity function retains the shape of the flux spectrum, this method is only applicable for optically thin sources.

11.5 Optical Depth and Dust Density

10. Measures of optical depth from absorption features are suspect. The derived optical depth will limit to a constant value even as the physical optical depth tends to ∞ . Furthermore, the (variable) factor between the derived and physical optical depths is dependent upon complex radiative transfer effects and observationally undetermined source parameters.

11. Although the dust density plays a large role in the shape of the IR/FIR spectrum, it is expected that source geometry will play a similar role for unresolved sources. Consequently, it is not clear that one can accurately determine the density distribution of such a source.

In general, there are some observations that can be made about the trends shown above. First of all, the optically thin approximation generally works well only for truly optically thin sources -- i.e. $\tau_0 \leq 0.5$ or so. Beyond this, optical depth and radiative transfer effects become large. In general, the treatment of the dust temperature is quite important. When one must fit a spectrum over only a small wavelength range (peak of emission spectrum or feature, etc.) an isothermal assumption will work well even if the source is not isothermal. In all cases, the choice of TD is quite important as it not only effects the magnitude but also the shape of the

emergent spectrum.

The effects mentioned above can (sometimes) be decreased by considering only certain physical regimes or invoking more complicated physics. However, no matter how restricted the cases or complicated the physics, semi-analytical modeling can only approximate the true situation. Consequently, although there is no substitute for complete and accurate modeling of infrared sources, semi-analytical methods work well in many instances.

Acknowledgments:

We would like to thank Dr. Sun Kwok of the University of Calgary and Dr. Scott Tremaine of the Canadian Institute for Theoretical Astrophysics for their hospitality and financial support while one of us (CML) was on sabbatical leave from Rensselaer in 1988 when this work was initiated. This work was partially supported by NASA under grant NAGW-1103 and by the Air Force under grant AFOSR 89-0104.

APPENDIX A

DERIVATION OF SOME SEMI-ANALYTIC EXPRESSIONS

As was given in equation (1) of the text, the specific luminosity is often written as

$$L_v = \int Q B_v [T(r)] e^{-\tau(v,r)} n(r) 4\pi r^2 dr. \quad (A1)$$

In the limit that Q and $n(r)$ can be written as power laws as given in equations (2) and (3), this expression becomes

$$L_v = Q_v n_0 \int e^{-\tau} B_v (r_0/r)^m 4\pi r^2 dr \quad (A2)$$

Using these expressions, we can easily derive the most common analysis techniques for the interpretation of IR data.

A.1 Dust Mass

The total dust mass can be written as

$$M = m_g n_0 \int (r_0/r)^m 4\pi r^2 dr. \quad (A3)$$

In the optically thin ($e^{-\tau} = 0$) and isothermal ($T = \text{constant}$) limits, we can re-write the dust mass in terms of (A2)

$$M = [m_g L_v] / [B_v Q_v]. \quad (A4)$$

Now, defining the mass opacity

$$\kappa_v \equiv Q_v / m_g, \quad (A5)$$

we have the dust mass,

$$M = [F_v D^2] / [\kappa_v B_v(T)]. \quad (A6)$$

As this depends upon the distance and the mass opacity, we can find the ratio of dust masses for similar sources by taking the ratio of equation (A6) between two sources, which gives

$$M/M' = [L_v/L'_v] [B'_v/B_v]. \quad (A7)$$

From this, one can also see that the dust mass should be proportional to the integrated luminosity. It should be recalled here that the above expressions were carried out for $e^{-\tau} = 0$ and $T = \text{constant}$.

A.2 Dust Temperature

The dust temperature distribution can be determined from equation (A1) by assuming the

dust shell to be optically thin, and in thermal equilibrium. If we take the absorptivity to be $\langle Q_a \pi a^2 \rangle = Q_a v^a$, and the emissivity to be $\langle Q_e \pi a^2 \rangle = Q_e v^e$, then from energy balance we can write:

$$\int Q_a v^a J_\nu(r) dv = \int Q_e v^e B_\nu(T(r)) dv, \quad (A8)$$

where $J_\nu(r)$ is the mean intensity. If we take the mean intensity to be the diluted stellar radiation field, and integrate equation (A8), we have

$$C Q_a L_* T_*^a r^{-2} = Q_e [T(r)]^{4+e} \quad (A9)$$

where C is a normalization constant. Therefore, the TD is given by

$$T(r) = [C L_* T_*^a r^{-2} (Q_a/Q_e)]^{1/(4+e)} \quad (A10)$$

which, in the limit that $a, e = p$ reduces to

$$T(r) = T(r_0) [r_0/r]^{2/(4+p)}. \quad (A11)$$

A.3 Opacity Function (Continuum)

The FIR continuum opacity function can also be determined by taking the limit of equation (A1). In this case, we assume the dust to be isothermal, and optically thin. We also assume that the Rayleigh-Jeans limit will hold (i.e. $h\nu \ll kT$). In this limit, the specific luminosity becomes:

$$L_\nu = C v^{3+p} \int [kT/h\nu] 4\pi^2 n(r) dr. \quad (A11)$$

Taking the ratio of the specific luminosities at two different frequencies, and taking the log of that expression we have:

$$\log(L_{\nu,1}/L_{\nu,2}) = (2 + p) \log(\nu_1/\nu_2) \quad (A12)$$

which becomes

$$p = [\log(L_{\nu,1}/L_{\nu,2}) / \log(\nu_1/\nu_2)] - 2.0. \quad (A13)$$

APPENDIX B

NOTES ON THE APPLICATION OF THE COLOR TEMPERATURE DISTRIBUTION

The dust temperature distribution may be derived by computing the color temperatures of the source using equation (23) from the text, which again is:

$$r(\lambda_1)/r(\lambda_2) = (\lambda_1/\lambda_2)^\gamma. \quad (B1)$$

By computing the color temperature $T_c(\lambda_i/\lambda_R)$ from the fluxes at the two wavelengths λ_i and λ_R , one can use equation (B1) to derive the TD referenced on a *single* reference wavelength λ_R . To improve the statistics, one should use more than one reference wavelength in deriving the TD.

Equation (B1) gives only normalized radii (i.e. not the absolute positions), hence, for each reference wavelength, the TD is normalized to itself but not to the others. In order to connect two reference wavelength temperature distributions, we relate the first position in the for the j^{th} reference wavelength to the last position in the $(j-1)^{\text{th}}$ reference wavelength according to the optically thin approximation,

$$r_1(\lambda_R(j)) = r_n(\lambda_R(j-1)) [T_c(r_n)/T_c(r_1)]^{[2/(4+p)]}. \quad (B2)$$

Although this is not strictly correct, its effect should be minimized as long as more than 2 or 3 color temperatures are used for each reference wavelength, and the span of temperatures over which one interpolates is small. In general, this is fairly easy to ensure. To illustrate the above, we offer an example:

Let us assume that we have fluxes at 4, 8, 9, 12, 18, and 20 μm , giving us color temperatures $T_c(\lambda_i, \lambda_R)$ for the arbitrarily chosen reference wavelengths 4, 8, and 12 μm . We set $r_1 = 1.0$ to correspond to $T_c(8 \mu\text{m}, 4 \mu\text{m})$. From this, $r_2 = r_1 \times (9 \mu\text{m}/8 \mu\text{m})^\gamma$ with $T(r_2) = T_c(9 \mu\text{m}, 4 \mu\text{m})$ where γ has been specified as in the text. This procedure is followed until we reach $r_5 = r_4 \times (20 \mu\text{m}/18 \mu\text{m})^\gamma$ with $T(r_5) = T_c(20 \mu\text{m}, 4 \mu\text{m})$. We join $\lambda_R = 4 \mu\text{m}$ to $\lambda_R = 8 \mu\text{m}$ using the optically thin approximation as in equation (B2). In doing this, we let $r_6 = r_5 \times [T(r_5)/T_c(9 \mu\text{m}, 8 \mu\text{m})]^{[2/(4+p)]}$ because $T_c(9 \mu\text{m}, 8 \mu\text{m})$ is the first color temperature for $\lambda_R = 8 \mu\text{m}$. As before, $r_7 = r_6 \times (12 \mu\text{m}/9 \mu\text{m})^\gamma$ with $T(r_7) = T_c(12 \mu\text{m}, 9 \mu\text{m})$, etc. This procedure

(along with the interpolation between reference wavelength groups) is continued until all desired color temperatures have been used.

As this TD is supposed to map out the dust emission, we must limit ourselves to wavelengths greater than $4\text{ }\mu\text{m}$ and less than $20\text{-}50\text{ }\mu\text{m}$ depending upon the dust temperatures. In our models, we have used wavelengths at $4, 8, 9, 12, 18,$ and $20\text{ }\mu\text{m}$ in order to accomplish this without requiring a prohibitively small bandwidth. This also has the added benefit of not interfering with the $11\text{ }\mu\text{m}$ SiC feature.

When determining the lowest wavelength to use, one must attempt to subtract the stellar component from the total flux, and find the color temperatures from this "shell flux." The wavelength (from the Wein law) corresponding to the highest temperature found should then be the smallest wavelength used to ensure that only the long-wavelength side of the shell flux is used as discussed in the text. This formula should be followed even when one wants to find the index directly from the total flux. In this way, one is guaranteed to be in the region of highest dust emission and thus greatest dust to stellar emission ratio.

TABLE 1

MODEL PARAMETERS FOR CENTRALLY HEATED SOURCES

Parameter	Value
Dust Shell Size [R_{out}]	0.005 pc
Shell Thickness [$r_{\text{in}}/R_{\text{out}}$]	0.01
Dust Optical Depth [τ_0]	0.1 - 10.0
Grain Opacity Function [Q_{ν}]	$Q = Q_0(\lambda_0/\lambda)^p$ (continuum) $Q = Q_0(\lambda_0/\lambda)^p + \text{Gauss (feature)}$
Dust Density Profile [$n(r)$]	$n(r) = n_0(r_0/r)^m$
Central Heat Source [T_* , L_*]	$T_* = 2500\text{K}$, $L_* = 10^4 L_{\odot}$

TABLE 2**DEPENDENCE OF RADIUS-WAVELENGTH POWER LAW ON OPACITY FUNCTION**

$\gamma(\pm 01)$	p
0.50	1.0
0.49	1.2
0.48	1.5
0.47	1.6
0.45	1.7
0.44	1.8
0.43	1.9
0.41	2.0

REFERENCES

- Beichman, C. *et al.* 1990, *AJ*, 99, 1569
- Butner, H. M., Evans, N. J., Lester, D. F., Levreault, R. M., and Strom, S. E. 1991, *ApJ*, 376, 636
- Charnley, S. B. 1989, private communication.
- Cox, P., Mezger, P. G. 1989, *ARA&A*, 1, 49
- Dent, W. R. F. 1988, *ApJ*, 325, 252
- Draine, B. T. 1985, *ApJS*, 57, 587
- Egan, M. P., Leung, C. M., Spagna, G. F. 1988, *Comput. Phys. Comm.*, 48, 271
- Fogel, J. A., Persson, S. E. 1974, *ApJ*, 192, 351
- Gillet, F. C. *et al.* 1975, *ApJ*, 200, 609
- Helou, G. 1989, in *IAU Symposium No. 135 on Interstellar Dust*, eds. Allamandola, L. J., Tielens, A. G. G. M.
- Hildebrand, R. H. 1983, *QJRAS*, 24, 267
- IRAS Catalogs and Atlases: Explanatory Supplement 1985*, ed. C. A. Beichman, G. Neugebauer, H. J. Habing, P. E. Clegg, & T. J. Chester (Washington: GPO)
- Kuiper, T. B. H. *et al.* 1976, *ApJ*, 204, 408
- Kwan, J., Scoville, N. 1976, *ApJ*, 209, 102
- Kwok, S. 1980, *ApJ*, 206, 592
- Lacy, J. H., Bass, F., Allamandola, L. J., Persson, S. E., McGregor, P. J., Lonsdale, C. J., Geballe, T. R., and van de Bult, C. E. P. 1984, *ApJ*, 276, 533
- Leung, C. M. 1976, *ApJ*, 209, 75
- Leung, C. M., Egan, M. P. 1992, in preparation
- McCarthy, J. F. *et al.* 1978, *ApJ*, 224, 109
- Mitchell, R. M., Robinson, G. 1978, *ApJ*, 220, 841
- Olofsson, H., Carstrom, U., Eriksson, K., Gustafsson, B., and Willson, L. A. 1990, *A&A*, 230, L13
- Papoular, R., Pegourie, B. 1983, *A&A*, 128, 335
- Pegourie, B., Papoular, R. 1985, *A&A*, 142, 451
- Persson, S. E. *et al.* 1976, *ApJ*, 208, 753
- Sarazin, C. L. 1978, *ApJ*, 220, 165
- Schutte, W., Tielens, A. G. G. M. 1989, *ApJ*, 343, 369
- Simpson, J. P., Rubin, R. H. 1988, in *Interstellar Dust: Contributed Papers*, eds. Tielens A. G. G. M., Allamandola, L., NASA CP-3036
- Sopka, R. J., Hildebrand, R., Jaffe, D. T., Gatley, I., Roellig, T., Werner, M., Jura, M., and

- Zuckerman, B. 1985, ApJ, 294, 242
Waters, L. B. F. M. et al. 1988, A&A, 203, 348
Willems, F. J. 1987, Ph. D. thesis, Universiteit van Amsterdam
Willems, F. J. 1988, A&A, 203, 51

FIGURE CAPTIONS

- FIG. 1. - Dust mass derived from Equation (15) by fitting the $12\ \mu\text{m}$ band of simulated observations. The solid line is the actual dust mass-optical depth relationship. The filled circles are the derived masses normalized to the solid line at $\tau_0 = 0.05$.
- FIG. 2. - Dust mass derived from IR luminosity. In the top two panels, (a) and (b), we integrate only the dust luminosity for $2.2\ \mu\text{m} \leq \lambda \leq 100\ \mu\text{m}$ (dot-dash line), and $8\ \mu\text{m} \leq \lambda \leq 100\ \mu\text{m}$ (long dash line) for both $m = 2$ and constant density ($m = 0$) sources. Even though we find good results for fairly transparent sources, the derived masses are consistently too low with errors increasing as the optical depth increases. In the bottom panel, (c), we integrate the *total* (shell plus star) IR luminosity. In this case, the errors are due to the dominant effect of the direct stellar contribution. In all cases, we have normalized the derived dust masses to the actual dust mass - optical depth relationship (solid line) at $\tau_0 = 0.05$.
- FIG. 3. - Derived isothermal dust temperature vs. optical depth of the source. The dust temperatures were derived by fitting a dilute, isothermal blackbody to the flux spectrum. The triangles correspond to the assumption that the errors are of constant magnitude; the squares represent fits assuming constant fractional errors. The circles give the actual dust temperature at a visible optical depth of 1. Notice that in the optically thin limit, the inner dust temperature is well represented by isothermal fits to the peak of the spectrum (triangles).
- FIG. 4. - Sample fits of temperature distribution (TD). The solid line is the actual TD, while the short - dashed line is the optically thin TD using relevant source parameters. The long - dashed line gives the best fit power law to the actual TD (correlation coefficient, $r^2 \geq 0.99$; mean fractional deviation 4 times smaller than optically thin power law for $\tau_0 = 10.0$). As expected, the two results merge for optically thin sources. However, as τ_0 increases, the actual TD is well modeled by a power law different from the optically thin value. This is true over a wide range of optical depths and density distributions.
- FIG. 5. - Exponents of the power law TD vs. source opacity. Notice the deviation of the best fit values (short - and long - dashed lines) from the optically thin value once $\tau_0 \geq 0.50$.

- FIG. 6. - Color temperatures, $T_c(\lambda, \lambda_R)$, vs. one of the two wavelengths used (λ_R). The range in reference wavelength, λ_R , is given in the range of symbols. Notice that the derived color temperature is a power law in the wavelength chosen in the range of greatest dust emission ($4 \mu\text{m} \leq \lambda \leq 20 \mu\text{m}$; $1000 \text{ K} \leq T \leq 150 \text{ K}$). Outside this range, stellar contamination plays a large role.
- FIG. 7. - Temperature indices (TI) derived from color temperatures as detailed in text. The long-dashed line gives the optically thin index, and the solid line the best fit index. The circles and triangles denote indices derived from the shell and total flux respectively. Notice that the derived TI is consistently better than the optically thin index, and is dramatically better for $p \geq 1.2$ when using the shell flux (circles). However, the total flux (triangles) yields poor results due to stellar contamination.
- FIG. 8. - Similar to Fig. 7, but for different source characteristics. Notice the poor results for the constant density case ($m = 0$). However, once $m \geq 1.5$, the results improve. We find similarly good results for the detached shell model due to the greater IR excess above the stellar component. Interestingly, the total flux give good results once the sources become very opaque ($\tau_0 \geq 5.0$).
- FIG. 9. - Derived continuum opacity function using an isothermal fit to the flux spectrum. The solid line gives the actual opacity index, while the long-dash-dot, long-dash, and short-dash-dot lines give results for fits $\lambda \geq \lambda_{\min} = 1.8 \mu\text{m}$, $10 \mu\text{m}$ and $100 \mu\text{m}$ respectively. The results are better for longer wavelengths due to the increasingly isothermal nature of the dust. However, this result is offset in practice by the small dust fluxes beyond $\lambda = 10\text{-}20 \mu\text{m}$. Notice that for $\lambda \leq 10 \mu\text{m}$, the derived indices are consistently too high by between 5-100%.
- FIG. 10. - A comparison of derived opacity functions, similar to Fig. 9, but for different TD's. Again the solid line gives the actual opacity index, but in this case the long-dash-dot, and long-dashed lines correspond to $1.8 \mu\text{m} \leq \lambda \leq 20 \mu\text{m}$ and $4.0 \mu\text{m} \leq \lambda \leq 20 \mu\text{m}$ respectively. Notice that a non-isothermal TD gives good results in general. Specifically, the TD derived in the text (third panel - (c)) gives results which are better than the optically thin values (b), but almost equal to those derived when using the *actual* TD (d).
- FIG. 11. - Continuum opacity index as derived by slope of FIR shell spectrum using Equation (6) from the text. Notice the good results ($\Delta p/p \leq 0.2$) when both

wavelengths are beyond $300\text{ }\mu\text{m}$ for all combinations of optical depth and density distribution. The large scatter for $\tau_0 = 0.1$ is due to the small amount of shell flux at these wavelengths.

- FIG. 12. - Similar to Fig. 11, but for the total flux. The results are poor, independent of optical depth, density distribution, or wavelengths chosen.
- FIG. 13. - Sample fluxes for simulated SiC ($11\text{ }\mu\text{m}$) feature as a function of optical depth. The fluxes follow the form of the feature opacity function for small optical depths, but the peak flux decreases and finally goes into self-absorption as the optical depth increases.
- FIG. 14. - Derived opacity function for different optical depths assuming the functional form of the feature is known. Notice that good results are achieved for transparent sources. However, the derived features (dashed lines) are always too wide and too small compared to the actual features (solid lines).
- FIG. 15. - Fractional deviation in feature height (as defined in text) vs. source optical depth. The circles give the derived fractional deviations. The solid and long-dashed lines give the best fits through these points for $0.05 \leq \tau_0 \leq 1.0$ and $1.0 \leq \tau_0 \leq 10.0$ respectively. Notice that the deviation is well fit by a power law for optically thin sources, as is discussed in the text.
- FIG. 16. - Opacity function derived by "inverting" the flux spectrum for different optical depths as labeled in the figure (see text). The actual opacity function is given by the solid line. We find reasonable results for optically thin sources, but the shape of the derived features reflects the shape of the flux spectrum (e.g., $\tau_0 = 15.0$). The opacity functions derived by this method tend to be too small, but of approximately correct width.
- FIG. 17. - Optical depth derived from features. The circles and long-dash line give the optical depth derived from a simulated $3\text{ }\mu\text{m}$ feature. The solid lines gives the actual optical depth of the feature. Notice that the derived values are always too small, and that the derived values *saturate* as the source becomes more opaque.

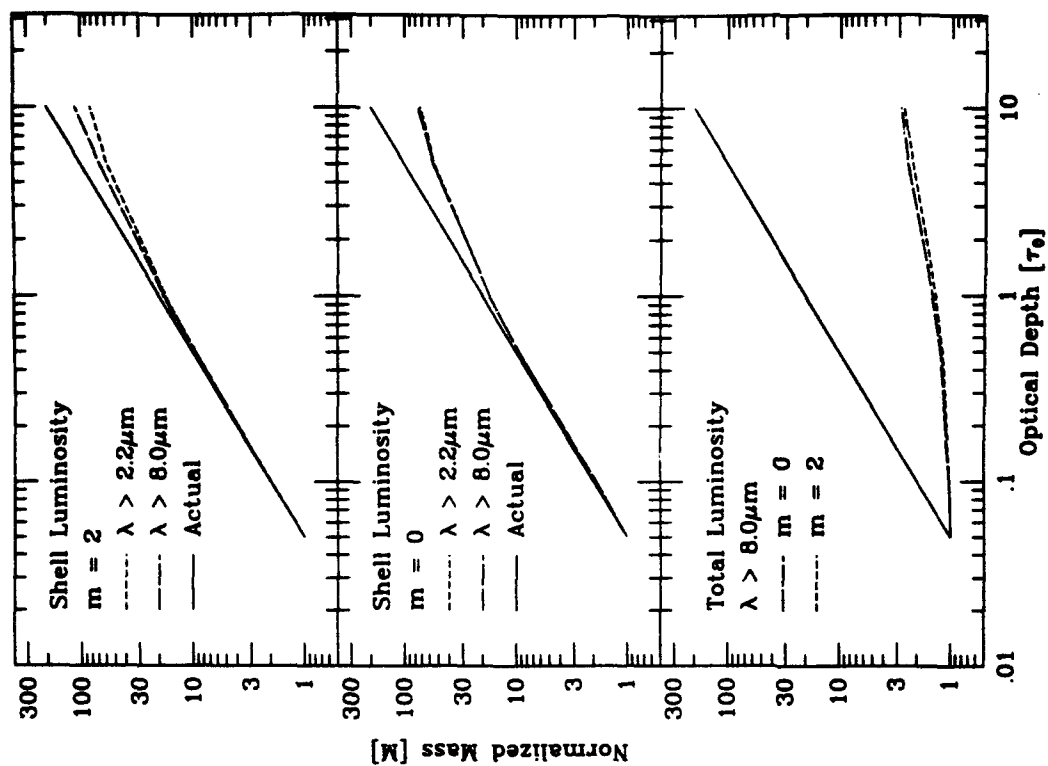


Figure 1

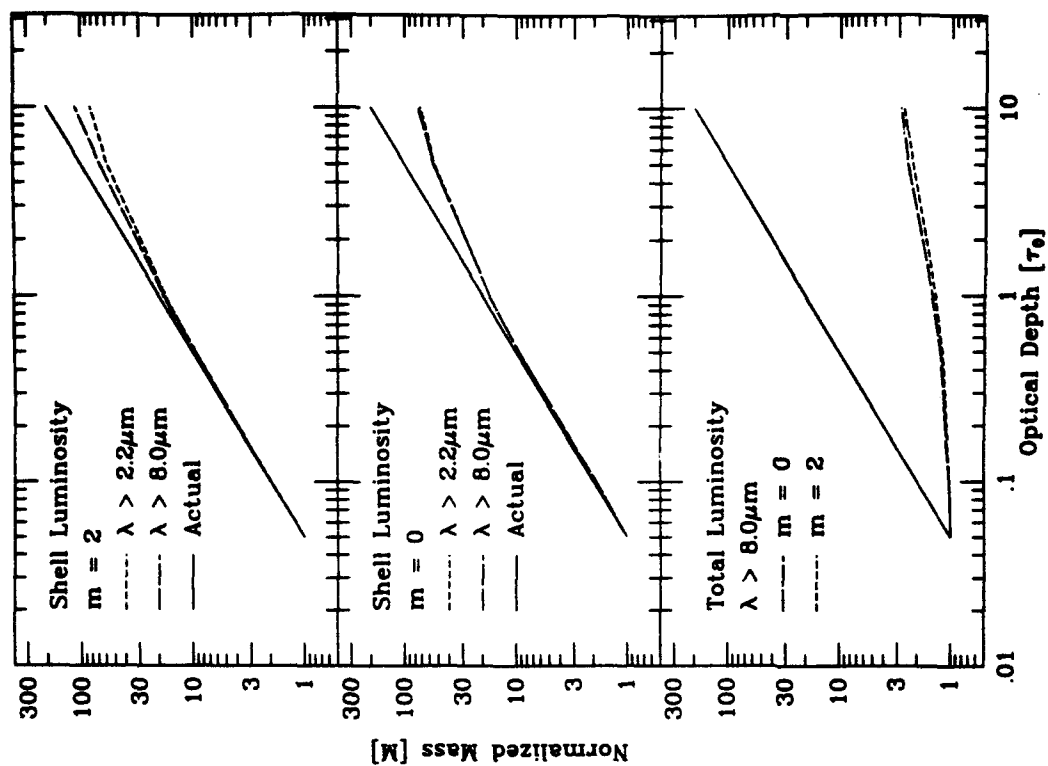


Figure 2

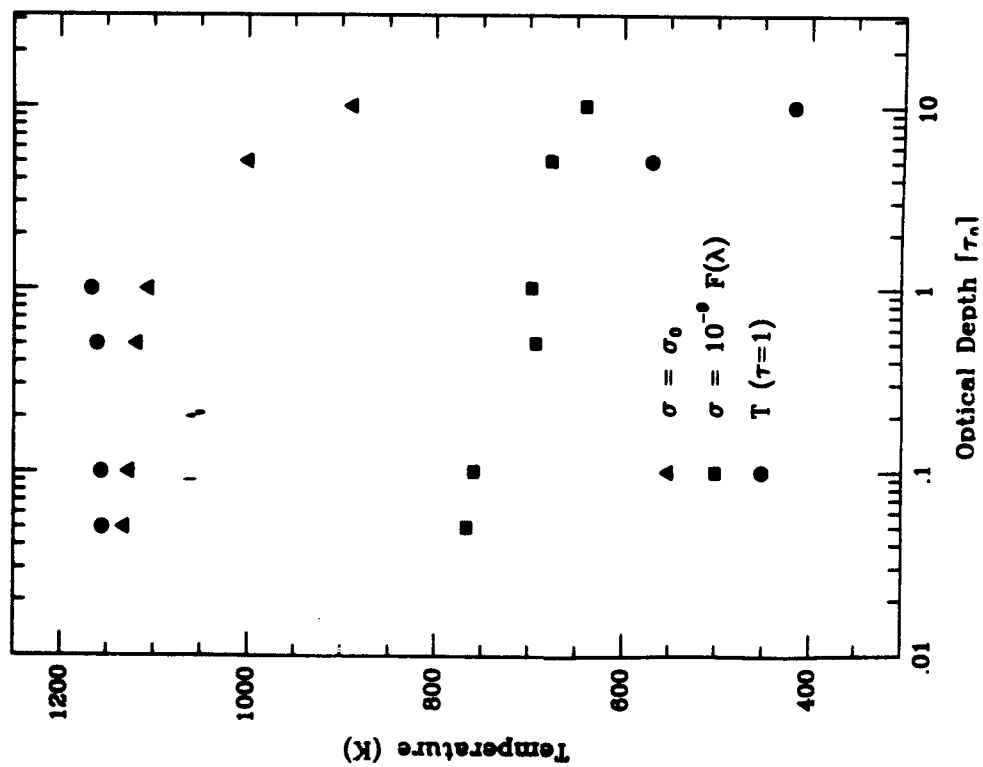


Figure 3

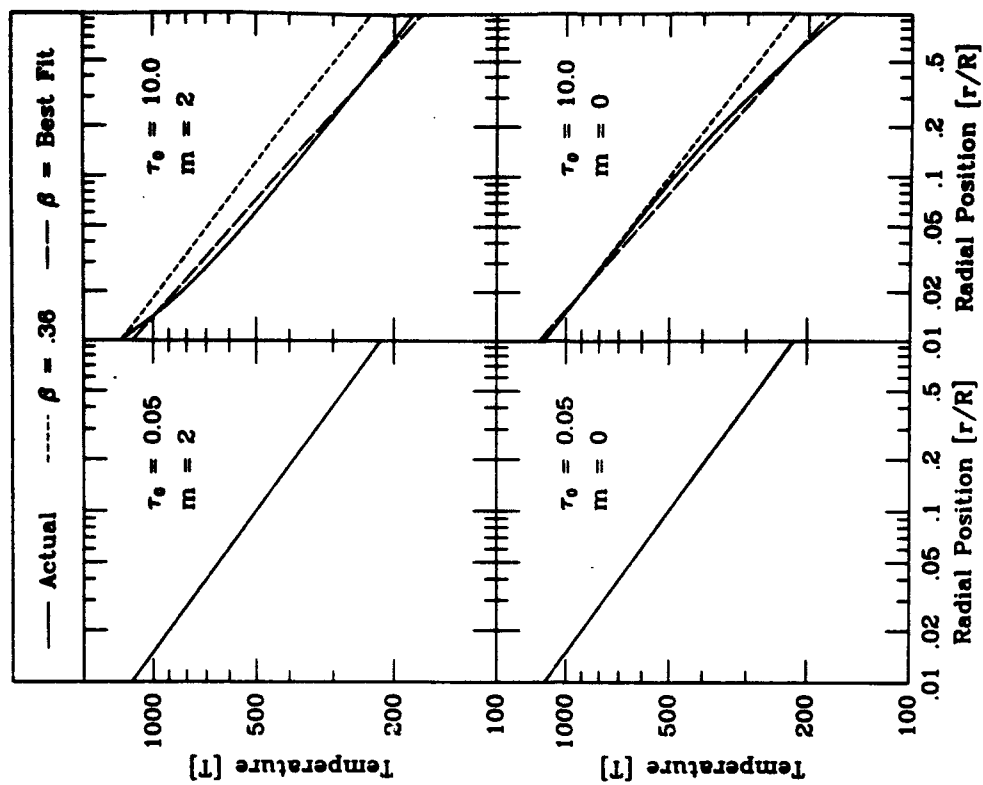


Figure 4

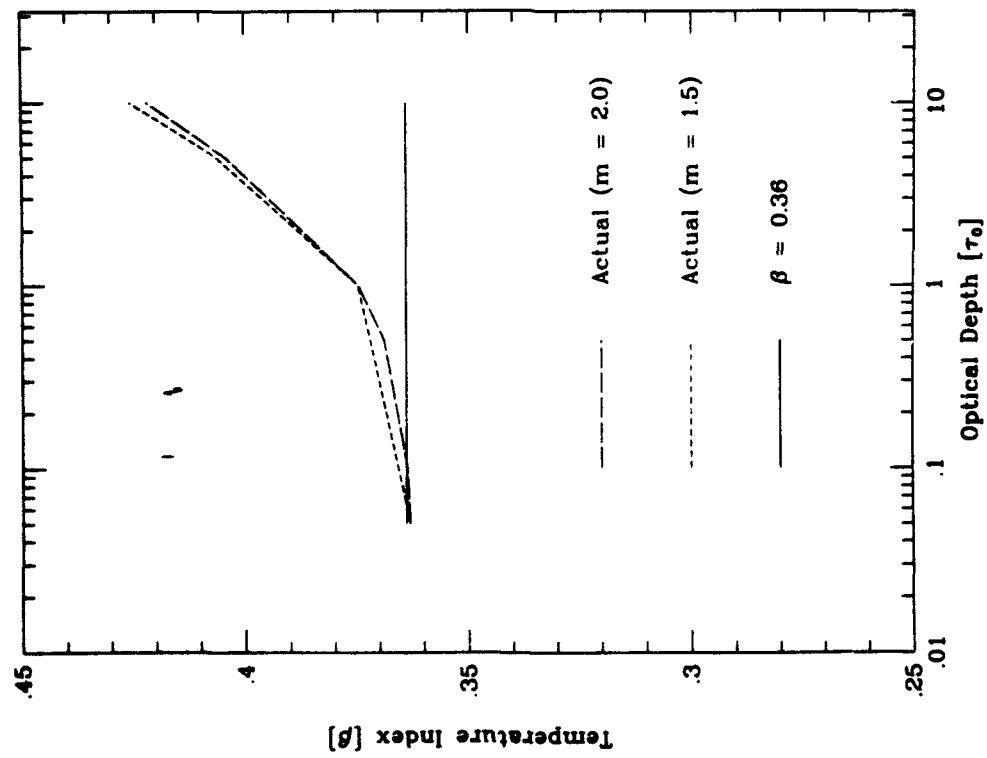


Figure 5

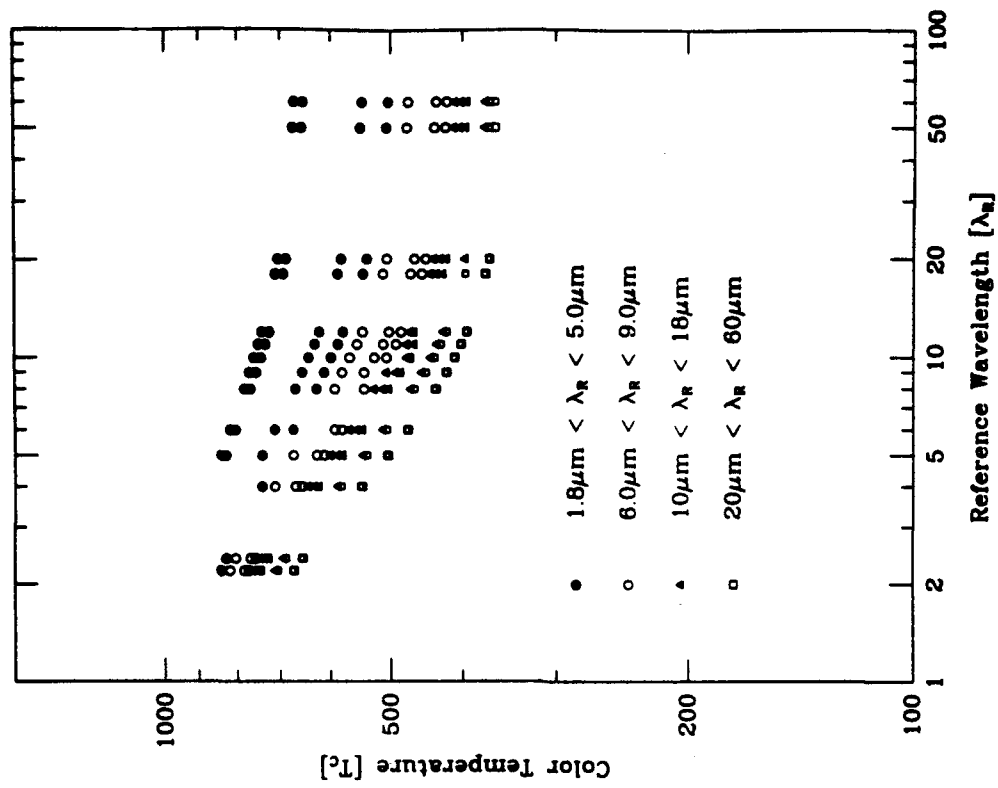


Figure 6

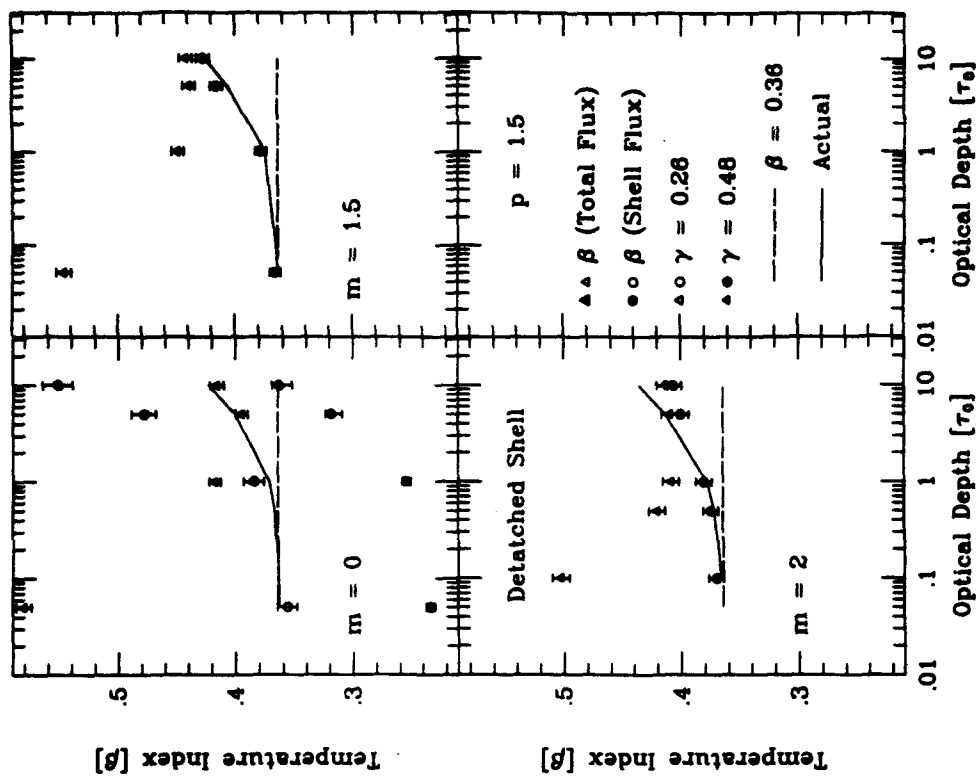


Figure 7

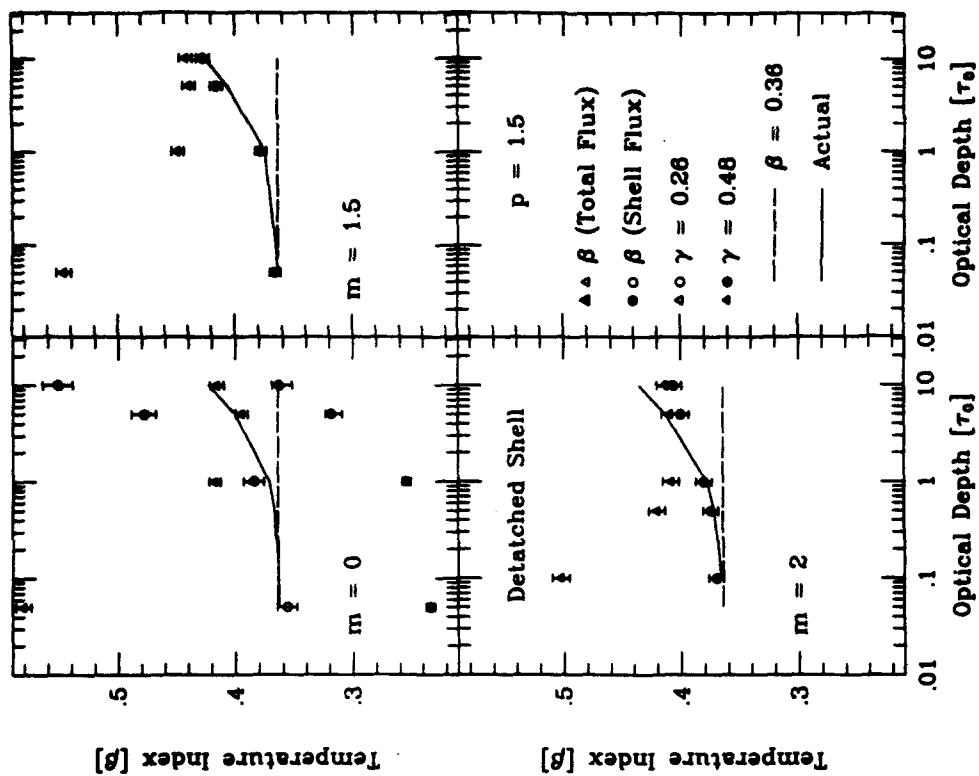


Figure 8

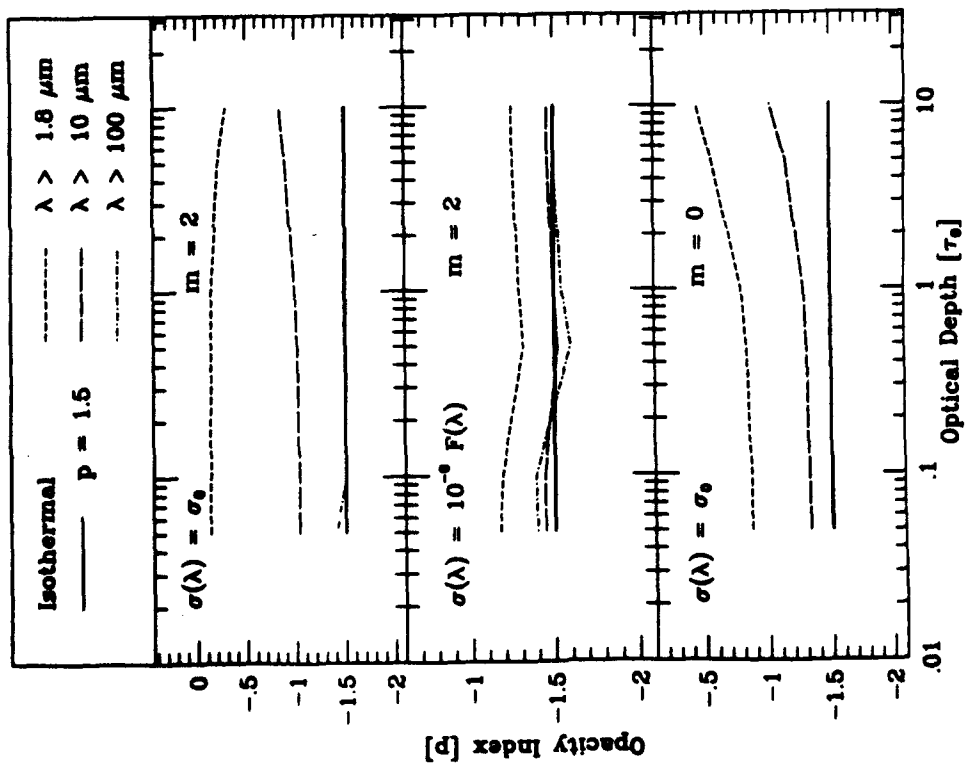


Figure 9

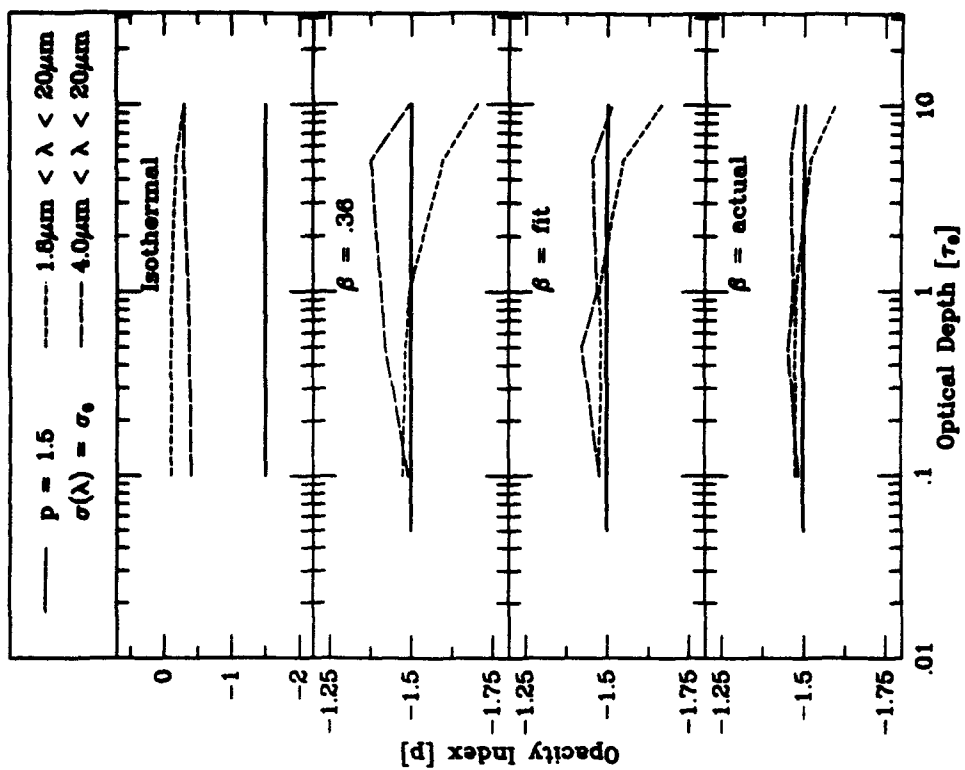


Figure 10

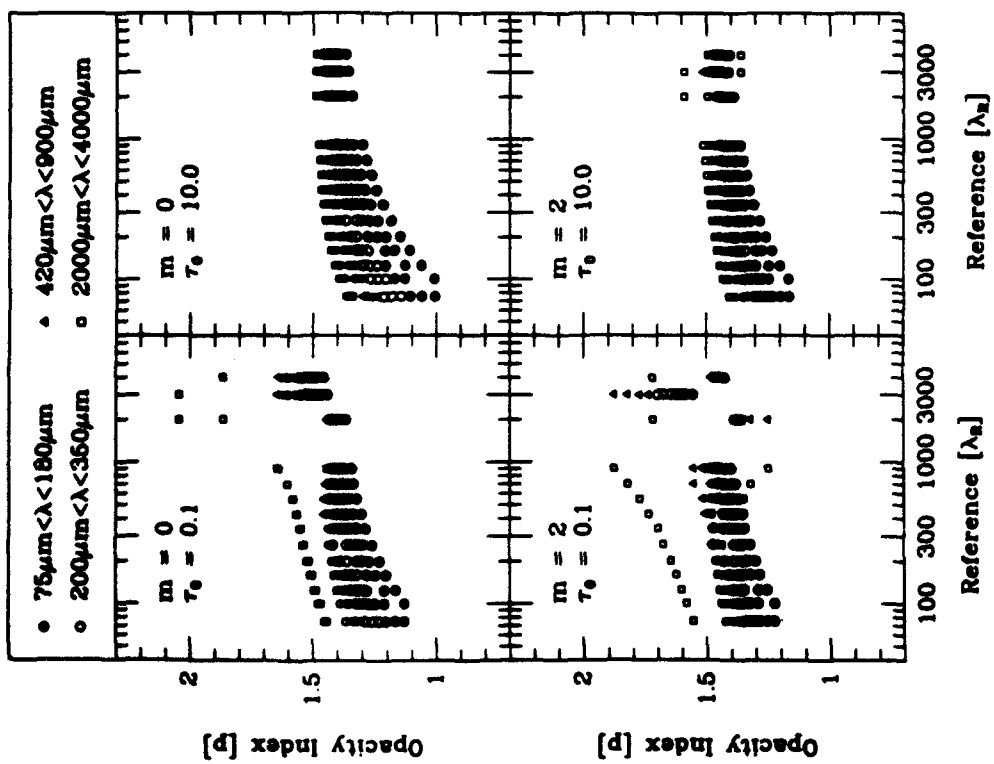


Figure 11

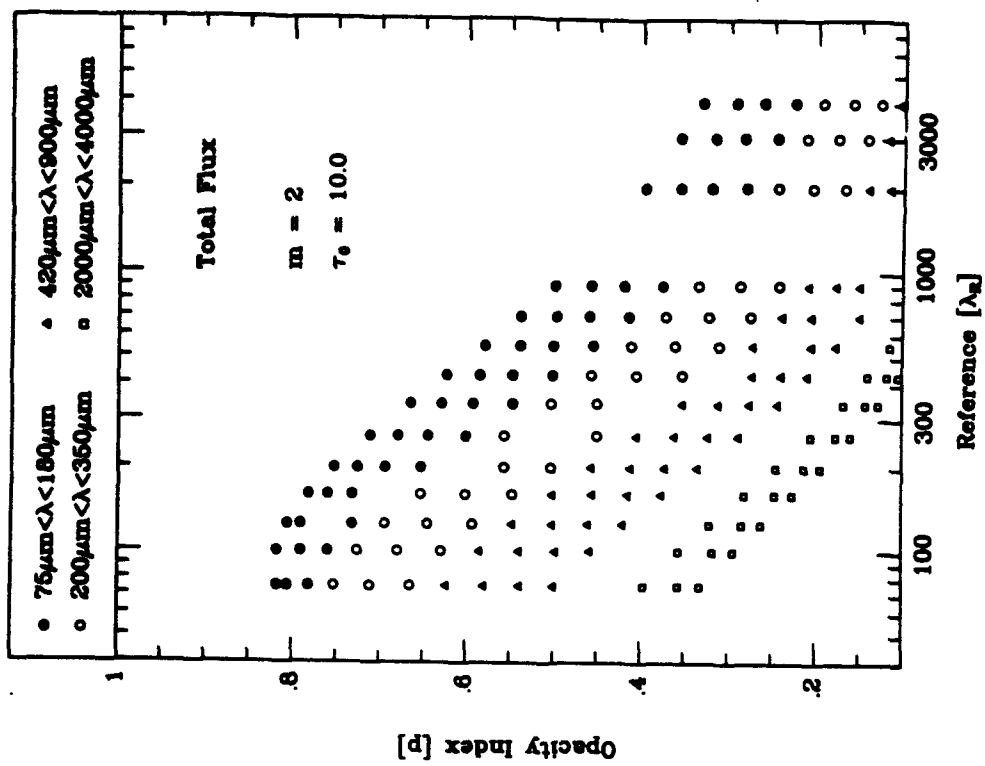


Figure 12

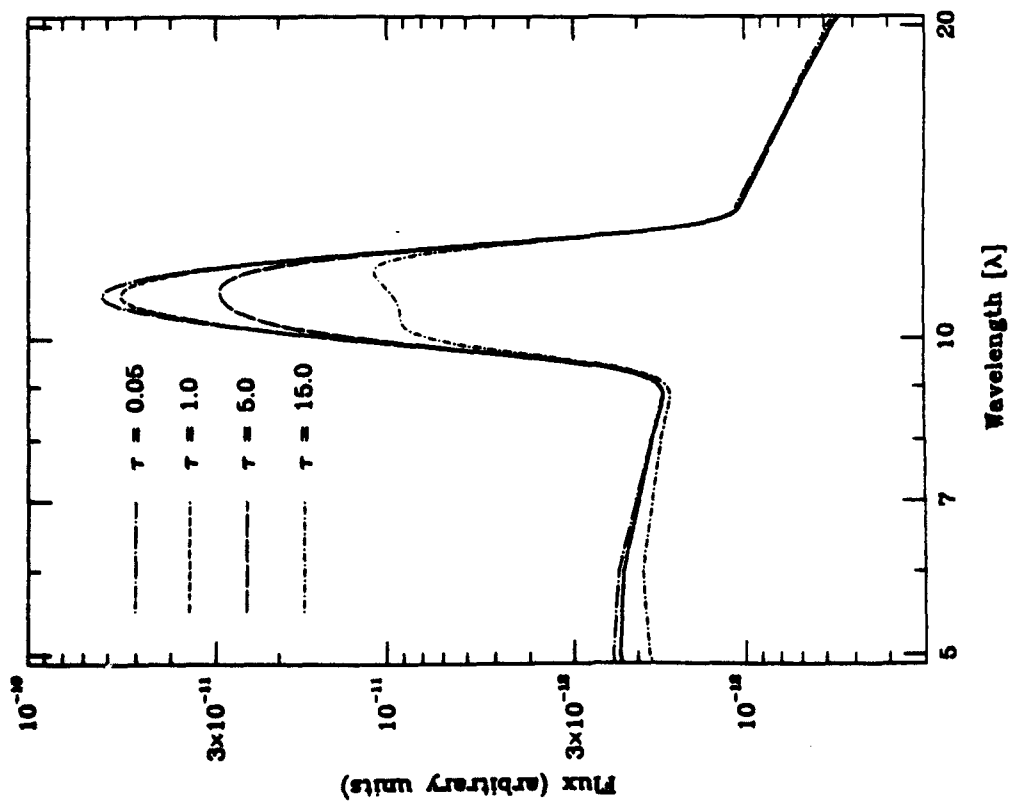


Figure 13

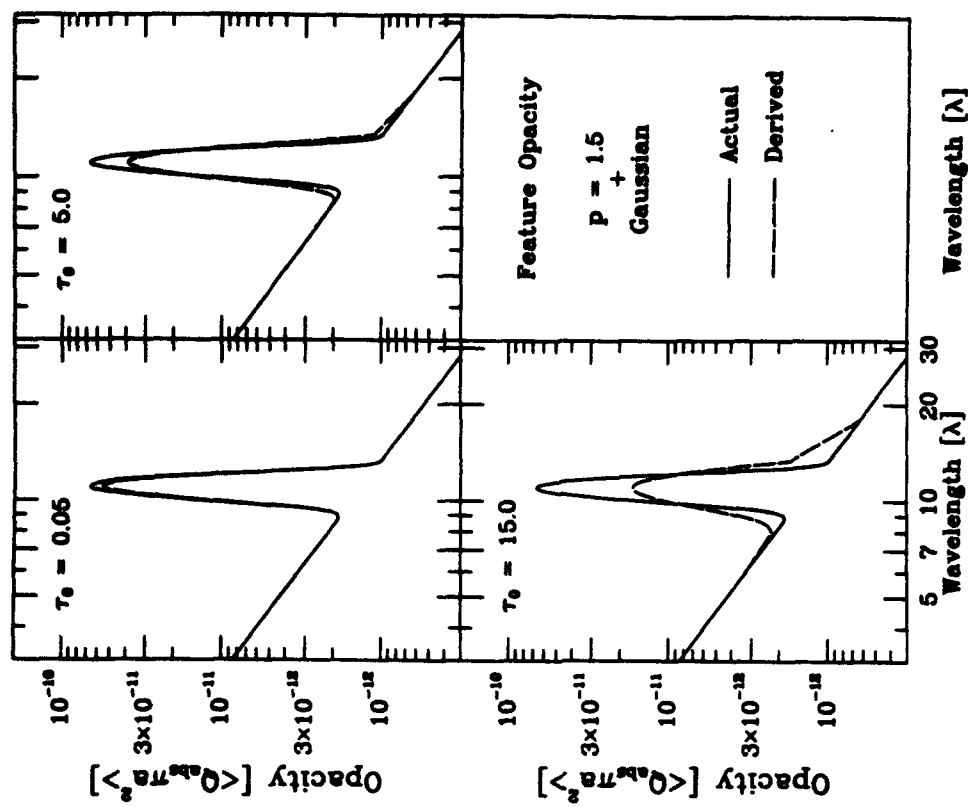


Figure 14

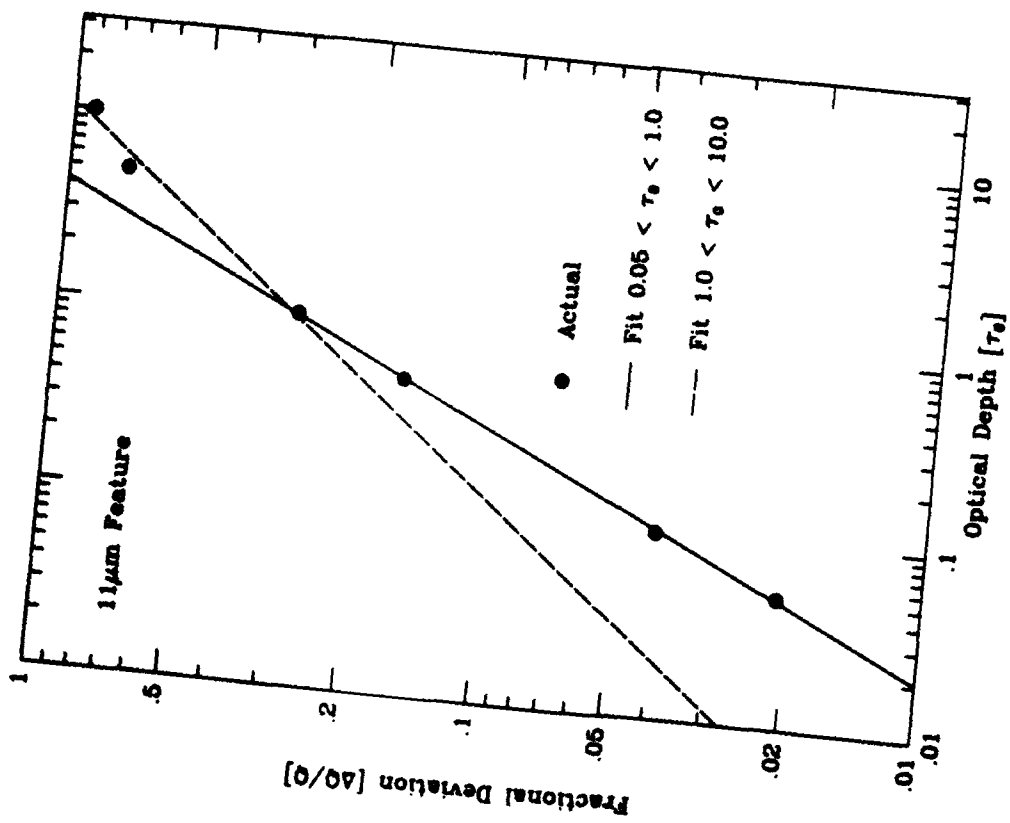


Figure 15

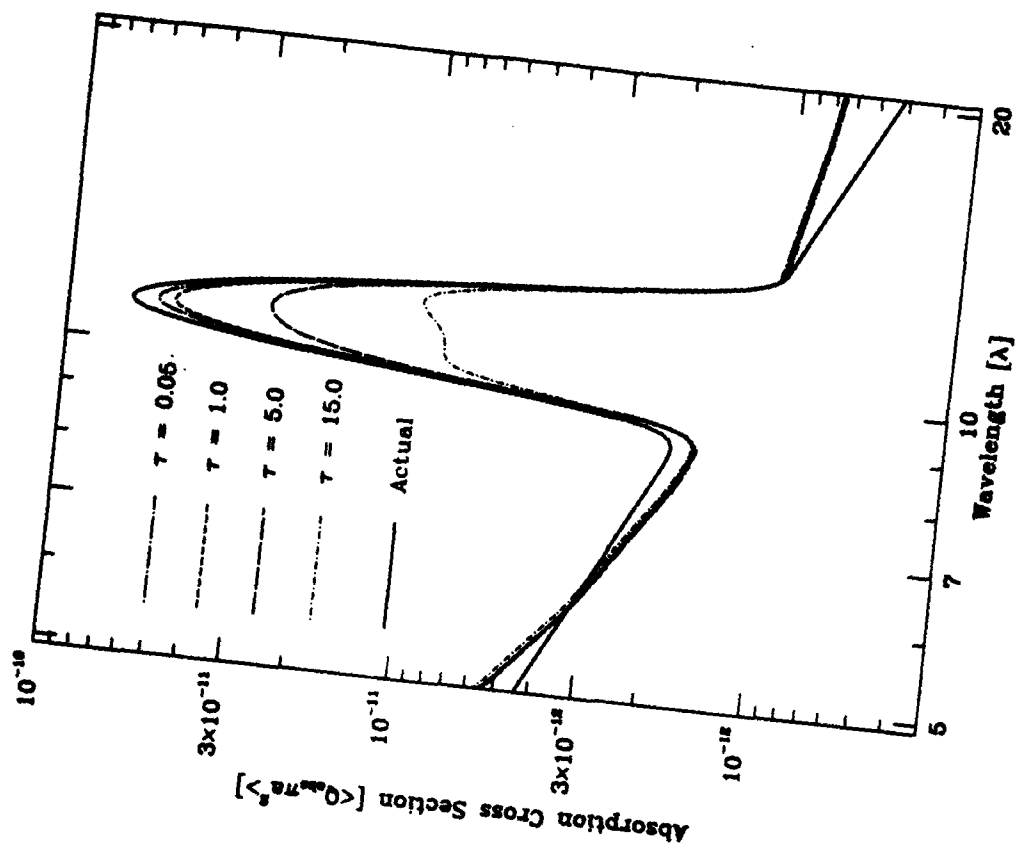


Figure 16

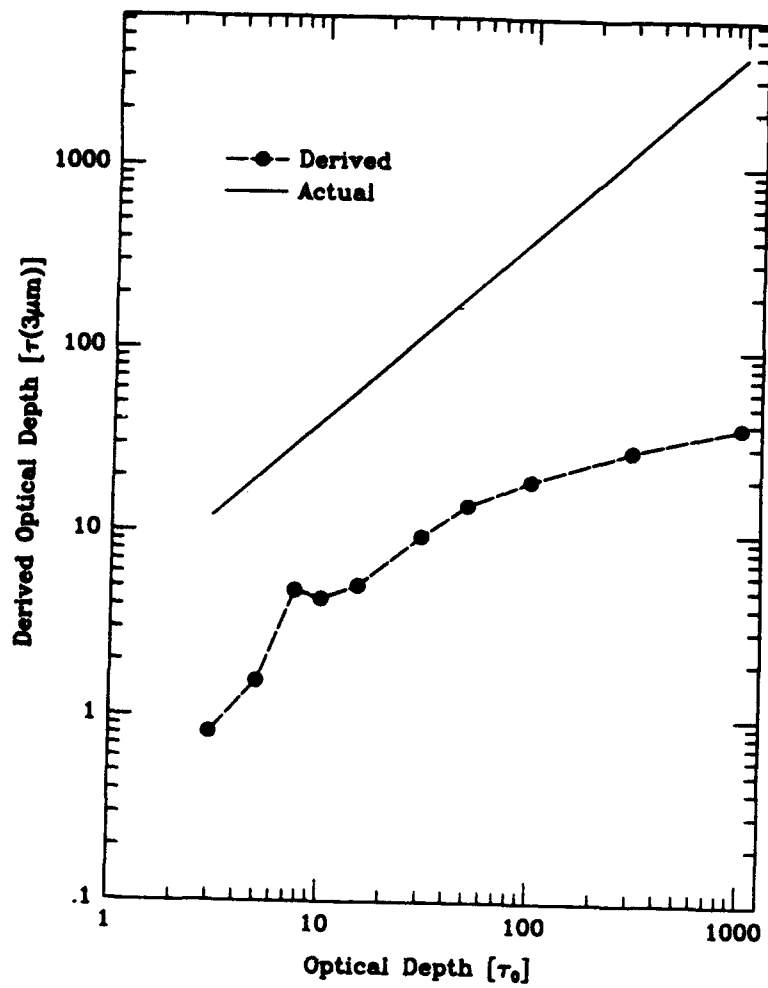


Figure 17

**MODELING GRAIN FORMATION
IN STELLAR OUTFLOWS:
A MASTER EQUATION APPROACH**

MICHAEL P. EGAN AND CHUN MING LEUNG

Department of Physics, Rensselaer Polytechnic Institute, Troy, NY 12180-3590

Submitted to *The Astrophysical Journal*

ABSTRACT

Previous studies of grain formation in astrophysical environments have relied on classical nucleation theory to find the rate of grain nucleation. We have coupled a truncated set of master equations to the equations of grain growth described by Gail and Sedlmayr in order to treat grain formation in a self-consistent manner. In addition, we have considered the effects of grain drift velocities on the coagulation of PAH-sized clusters, which are expected to be important in the formation of grains around carbon stars. We find that using classical nucleation theory underestimates the supersaturation ratio at which grain formation occurs by a factor of 2 - 3, with corresponding discrepancies in the grain size and number density. In addition, we have used the master equation method to model the effect of streaming velocities of grains due to radiation pressure on the coagulation of grains. Inclusion of these velocities results in a large degree of cluster coagulation, resulting in a much lower grain number density than is computed if radiation pressure effects are ignored. Correspondingly, the grains are much larger.

1. INTRODUCTION

With the increasing importance of the field of infrared astronomy, questions concerning the origin, composition, and size of both circumstellar and interstellar grains have come to be of major concern to the community. The discovery of infrared excesses around late-type stars provided evidence of ongoing dust formation. Applying knowledge from terrestrial nucleation problems (e.g. fog) to astrophysical situations constituted the early work on grain formation (Fix 1969; Salpeter 1974; Draine and Salpeter 1977). A paper by Gail, Keller, & Sedlmayr (1984 hereafter GKS84) demonstrates a method to rapidly and accurately compute grain growth via moments of the grain size distribution function. A subsequent paper (Gail & Sedlmayr, 1988 henceforth GS88) details the relationship between the kinetic master equations for grain formation and these moment equations, but proceeds to replace the nucleation rate calculated by the master equations with an approximation due to classical nucleation theory.

In most astrophysical situations, including mass loss from evolved stars, the physical conditions are far from the equilibrium conditions under which classical nucleation theory is valid. In addition, the condensation processes described by classical nucleation theory are based on classical thermodynamic arguments and are not good approximations to the chemical reaction networks thought to be occurring in stellar atmospheres (Donn & Nuth, 1985). The proper way to model grain nucleation would be to consider the chemical kinetics of the reaction network involved (Keller 1987). To this end, we have followed the suggestion of Rossi and Benevides-Soares (1988) and coupled a truncated set of the kinetic (master) equations to the moment equations used in GS88. If the rate constants for the reactions considered were known, we could then construct a proper solution of the grain nucleation problem.

In this paper we solve the kinetic equations, but use thermodynamic arguments to compute the rate coefficients between cluster sizes. We have used thermodynamic constants for graphite as they are relatively complete and allow direct comparison of this method to other

work in the field. While not realistic in terms of the expected grain composition (amorphous carbon, which forms at lower temperatures than graphite) or nucleating species (hydrogenated carbon compounds rather than simple carbon clusters) this should serve as an adequate illustrative example of the differences between the master equation approach and classical nucleation theory.

2. BASIC EQUATIONS

2.1 The Kinetic Equations

Let us consider the rate of change in number density of clusters consisting of i atoms. We define our initial conditions such that at $t=0$ the grain number density is $n_0(i)$. We have constructed the master equations following the method of Yamamoto and Nishida (1977) by defining the quantity $f(i,t) = E(t)n(i,t)/n_0(i)$ where $E(t) = \Delta V(t)/\Delta V(t=0)$ is the ratio of the volume element at the current time to the initial volume element. If we consider that clusters of up to M atoms are involved in the reactions and that $i > M$. In this case,

$$\begin{aligned} df(i)/dt = \\ \sum_{j=1}^M f(j)[P_{i+j,i}f(i+j) + P_{i-j,i}f(i-j) - f(i)\{P_{i,i+j} + P_{i,i-j}\}] \end{aligned} \quad (2.1.1)$$

where $P_{m,n}$ is the rate at which m -clusters become n -clusters. If cases where $i \leq M$ are considered, the equation becomes more complex because these species are involved in all reactions. Furthermore, it is possible to, for example, break a dimer into two monomers. The rate equation then becomes

$$df(i)/dt = \sum_{j=1+i}^N f(i) [-P_{j-i,j}f(j-i) + P_{j,j-i}f(j)]$$

$$\sum_{m=1}^{i-1} f(m)[P_{i-m,i}f(i-m) + P_{i+m,i}f(i+m) - f(i)\{P_{i,i+m} + P_{i,i-m}\}] \quad (2.1.2)$$

where $\ell = \begin{cases} 2 & \text{if } j/i = 2 \\ 1 & \text{otherwise} \end{cases}$ and N is the maximum cluster size considered under the master equations.

2.2 Calculation of Rates

Ideally, the rate coefficients $P_{i,j}$ would be determined by the chemical reaction rate of the reaction involved. Since these data are not known in most cases, we will proceed with standard kinetic theory and thermodynamic arguments to find the rate coefficients. We will consider two cases, one which considers particles with no systematic velocity with respect to each other, and the other with a systematic velocity difference due to radiation pressure on grains.

Case 1: If no systematic motion is considered, the rate collision rate between clusters consisting of i and j atoms can be shown to be (Hammes 1978)

$$Z_{i,j} = \kappa 4\pi d_{i,j}^2 [\langle v \rangle / 4] n(i) n(j) \quad (2.2.1)$$

where $\kappa = \begin{cases} 1/2 & \text{if } j = i \\ 1 & \text{otherwise} \end{cases}$ to avoid double counting, $\langle v \rangle = [8kT(m_i + m_j)/\pi m_i m_j]^{1/2}$. It will be important to note that the quantity $4\pi d_{i,j}^2$ is essentially an effective surface area of a particle of radius $d_{i,j} = r_i + r_j$. This will be important in the derivation of the moment equations.

Case 2: Let us consider the effect of radiation pressure on grains in a stellar envelope. It is well known that (up to a certain point), larger grains will feel a greater acceleration due to radiation pressure, and will be driven out faster than the smaller grains. Therefore, the particle flux a given particle sees will be modified. In this case, the rate $Z_{i,j}$ becomes

$$Z_{i,j} =$$

$$\pi d_{i,j}^2 [m_i m_j / (4\pi^2 k^2 T^2)]^{3/2} \exp[-(m_i V_i^2 + m_j V_j^2) / 2kT] I_1 I_2 n(i) n(j) \quad (2.2.2)$$

where V_i and V_j are the radial velocities (away from the star) of particles i and j . Defining the center of mass velocity, V_{CM} , and relative velocity V_R of the particles as

$$V_{CM} = \frac{m_i V_i + m_j V_j}{m_i + m_j}; \quad V_R = V_i - V_j \quad (2.2.3)$$

we determine the integrals I_1 and I_2 to be:

$$I_1 = \int_0^{2\pi} \int_0^\pi \int_0^\infty V_{CM}^2 \exp[-AV_{CM}^2 + BV_{CM} \cos\theta] dV_{CM} \sin\theta d\theta d\phi \quad (2.2.4)$$

$$I_2 = \int_0^{2\pi} \int_0^\pi \int_0^\infty V_R^3 \exp[-CV_R^2 - DV_R \cos\theta] dV_R \sin\theta d\theta d\phi. \quad (2.2.5)$$

The constants A, B, C, and D are defined as

$$A = (m_i + m_j) / 2kT \quad (2.2.6a)$$

$$B = (m_i V_i + m_j V_j) / kT \quad (2.2.6b)$$

$$C = m_i m_j / [(m_i + m_j) 2kT] \quad (2.2.6c)$$

$$D = m_i m_j (V_j - V_i) / [(m_i + m_j) kT]. \quad (2.2.6d)$$

Solving the integrals for I_1 and I_2 yield

$$I_1 = (\pi/A)^{3/2} \exp[B^2/4A] \quad (2.2.7)$$

$$I_2 =$$

$$\pi/C^2 + (4\pi/D)(2C)^{-3/2}(\pi/2)^{1/2}(1 + D^2/2C)\exp[D^2/4C]\operatorname{erf}[D/2\sqrt{C}]. \quad (2.2.8)$$

In order to solve the moment equations we are interested in the rates at which clusters enter and leave the state in which they consist of j atoms. For example, if $i < j$, a cluster consisting of i atoms must gain a cluster with $j-i$ atoms to move to the j atom state. Assuming a sticking coefficient of α , we define the upward rate $P_{i,j}$ as

$$P_{i,j} = \alpha Z_{i,j-i}/(n(i)n(j-i)). \quad (2.2.9)$$

To determine the rate at which a cluster consisting of j atoms spontaneously breaks up into clusters of i and $j-i$ atoms, we use the detailed balancing argument put forth by Abraham (1974). Defining the supersaturation ratio, S , as the pressure of the monomers over the vapor pressure of the solid ($S = p_1/p_v$), we find that our rate of destruction is

$$P_{j,i} = P_{i,j} \exp\left[-\frac{4\pi r_0^2 \sigma_s}{kT} \{j^{2/3} - i^{2/3}\} - \ln(S^{j-i})\right] \quad (2.2.10)$$

where σ_s is the surface tension of the grain material and r_0 is the radius of the monomer atom.

2.3 Derivation of the Moment Equations

In GS88, moments (over the grain size distribution) of the master equations are taken in order to create moment equations describing the growth of dust grains. The moments of the grain size distribution are defined as:

$$K_j(t) = \sum_{i=N_0}^{\infty} i^{j/3} f(i,t). \quad (2.3.1)$$

Thus one can use the ratios of certain moments to determine average grain properties (see

GKS84). After taking moments over the master equations (and making certain simplifying assumptions), Gail and Sedlmayr developed the following equations for grain growth:

$$dK_0/dt = J_* \quad (2.3.2a)$$

$$dK_j/dt = N_0^{j/3} J_* + 4\pi a_0^2 \langle v \rangle / 4\alpha [1 - 1/S] \sum_{i=1}^j f(i,t) K_{j-i} \quad (j > 0). \quad (2.3.2b)$$

While GS88 did develop a proper expression for J_* using based on the values of $f(i,t)$, this was deemed unsolvable and abandoned in favor of a J_* computed on the basis of classical nucleation theory.

Since we are solving the nucleation rate via the master equations, we will use the derivation of the moment equation to determine the truncation point for the master equations. Considering the zeroeth moment, we find that the master equation becomes

$$\begin{aligned} dK_0/dt &= \frac{d}{dt} \sum_{i=N_0}^{\infty} f(i) = \sum_{i=N_0}^{\infty} \frac{d}{dt} f(i) \\ &= \sum_{i=N_0}^{\infty} \sum_{m=1}^M f(m) \times \\ &\quad [P_{i-m,i} f(i-m) - P_{i,i-m} f(i) + P_{i+m,i} f(i+m) - P_{i,i+m} f(i)]. \end{aligned} \quad (2.3.3)$$

Considering that $f(\infty) \rightarrow 0$, we see that the summations collapse to

$$dK_0/dt = \sum_{m=1}^M \sum_{i=N_0}^{N_0+m-1} f(m) [P_{i-m,i} f(i-m) - P_{i,i-m} f(i)]. \quad (2.3.4)$$

Thus we see that the master equations must be solved to at least the $N_0 + M - 1$ level.

For higher moments, the moment equations are

$$\begin{aligned}
 dK_j/dt &= \frac{d}{dt} \sum_{i=N_0}^{\infty} i^{j/3} f(i) = \sum_{i=N_0}^{\infty} i^{j/3} \frac{d}{dt} f(i) \\
 &= \sum_{i=N_0}^{\infty} \sum_{m=1}^M i^{j/3} f(m) [P_{i-m,i} f(i-m) - P_{i,i-m} f(i) + P_{i+m,i} f(i+m) - P_{i,i+m} f(i)]. \\
 &= \sum_{m=1}^M \sum_{i=N_0}^{N_0+m-1} i^{j/3} f(m) [P_{i-m,i} f(i-m) - P_{i,i-m} f(i)] \\
 &\quad + \sum_{i=N_0}^{\infty} \sum_{m=1}^M f(m) [P_{i,i+m} f(i+m) - P_{i+m,i} f(i)] \left\{ (i+m)^{j/3} - i^{j/3} \right\}. \quad (2.3.5)
 \end{aligned}$$

From this expression we would like to construct a set of coupled equations such as those produced by Gail and Sedlmayr. Under a binomial expansion, we may write $\left\{ (i+m)^{j/3} - i^{j/3} \right\}$ as $\frac{j}{3} m i^{(j-3)/3}$. As was the case in GS88, we make the assumption that $f(i) \approx f(i+m)$. This should be valid as long as $i \gg M$. Our introduction of an effective radius for the interaction of two species makes life somewhat more difficult. Since $i \gg m$, the relative velocity between species will be approximately equal to the thermal velocity of the smaller particle. Thus, the difference between upward and downward rates becomes

$$\begin{aligned}
 [P_{i,i+m} - P_{i+m,i}] &= \\
 \kappa \alpha 4 \pi a_0^2 \left[i^{1/3} + m^{1/3} \right]^2 \frac{\langle v \rangle}{4} m \left\{ 1 - \exp \left[\frac{4 \pi a_0^2 \sigma_s}{kT} \left[(i+m)^{2/3} - i^{2/3} \right] - (m) \ln S \right] \right\} \\
 &\approx \kappa \alpha 4 \pi a_0^2 \frac{\langle v \rangle}{4} m \left\{ 1 - S^m \right\} \left[i^{2/3} + 2 i^{1/3} m^{1/3} + m^{2/3} \right]. \quad (2.3.6)
 \end{aligned}$$

Under this approximation, the moment equations become

$$\begin{aligned}
 \frac{dK_j}{dt} &= \sum_{m=1}^M \sum_{i=N_0}^{N_0+m-1} i^{j/3} f(m) [P_{i-m,i} f(i-m) - P_{i,i-m} f(i)] \\
 &+ \sum_{m=1}^M mf(m) \kappa \alpha 4 \pi a_0^2 \frac{2 \leq v}{4} m \left\{ 1 - S^m \right\} - \frac{j}{3} \sum_{i=N_0}^{\infty} i^{(j-3)/3} \left[i^{2/3} + 2i^{1/3} m^{1/3} + m^{2/3} \right] f(i) \\
 &= \sum_{m=1}^M \sum_{i=N_0}^{N_0+m-1} i^{j/3} f(m) [P_{i-m,i} f(i-m) - P_{i,i-m} f(i)] \\
 &+ \sum_{m=1}^M mf(m) \kappa \alpha 4 \pi a_0^2 \frac{2 \leq v}{4} m \left\{ 1 - S^m \right\} - \frac{j}{3} \times \\
 &\quad \left[K_{j-1} + 2m^{1/3} K_{j-2} + m^{2/3} K_{j-3} \right]. \tag{2.3.7}
 \end{aligned}$$

We note that the dependence of K_j on only K_{j-1} as shown by GS88 is lost under the more accurate treatment of cluster cross-sections. Since the first and second moments will depend on K_{-1} and K_{-2} we run into a slight problem. However, since these terms are of order $N_0^{-1} K_0$ and $N_0^{-2} K_0$ respectively, these terms are insignificant if N_0 is large enough.

2.4 Numerical Method

We would like to simultaneously solve the truncated master equations and the moment equations. First we must make corrections to the master equations for $i \leq M$ in order to account for material used up in grain growth. Because the moment K_j is equal to the number of monomers contained in grains of size N_0 and larger, we see that dK_j/dt yields the time rate of change of reaction products. Furthermore, equation 2.3.7 demonstrates that this rate of change is broken down by m -mer reactions such that for $i \leq M$

$$\begin{aligned}
\frac{df_i}{dt} = & \sum_{j=1+i}^{N_0-1} f(i) \ell [-P_{j-i,j} f(j-i) + P_{j,j-i} f(j)] \\
& + \sum_{m=1}^{i-1} f(m) [P_{i-m,i} f(i-m) + P_{i+m,i} f(i+m) - f(i) (P_{i,i+m} + P_{i,i-m})] \\
& - \sum_{j=N_0}^{N_0+m-1} j f(i) [P_{j-i,j} f(j-i) - P_{j,j-i} f(j)] \\
& + i f(i) \kappa \alpha 4 \pi a_0^2 \frac{2 \leq v_i}{4i} \left\{ 1 - S^i \right\} \frac{1}{3} \left[K_2 + 2i^{1/3} K_1 + i^{2/3} K_0 \right]. \quad (2.4.1)
\end{aligned}$$

The master equations for $i > M$ are unaffected by the moment equations.

To facilitate in the numerical solution of the problem, we first define a vector \vec{x} such that

$$\vec{x} = \{f(1), f(2), \dots, f(N), K_0, K_1, \dots, K_L\}. \quad (2.4.2)$$

We are then able to write our system of differential equations as

$$d\vec{x}/dt = \underline{A}\vec{x}. \quad (2.4.3)$$

The equations turn out to be quite stiff, thus we use an implicit Euler difference scheme

$$\vec{x}^{n+1} - \vec{x}^n = \underline{A}\vec{x}^{n+1} \Delta t \quad (2.4.4)$$

or

$$(1 - \underline{A}\Delta t)\vec{x}^{n+1} = \vec{x}^n \quad (2.4.5)$$

to obtain our solution.

3. MODELS

In order to test the importance of a more exact treatment of grain nucleation, we have run a series of models using varying degrees of sophistication in their nucleation schemes. First, we have constructed a model based on the treatment of grain nucleation used by GS88, which we will refer to as CNT (for classical nucleation theory). This model considers only monomer reactions.

Our next three models use the master equation approach outlined above under the condition that the grains have no systematic velocity due to radiation pressure. Thus the rate equations correspond to those shown under case 1 in section 2.2. We consider cases in which

- a) only monomers contribute to grain growth ($M = 1$, denoted as ME1)
- b) monomers and dimers contribute to grain growth ($M = 2$, ME2)
- c) clusters consisting of up to 20 atoms contribute to grain growth ($M = 20$, ME20)

Finally, we have constructed a model equivalent to ME20 except that systematic particle velocities due to radiation pressure on grains is included in the determination of the reaction rates. This model is noted in the discussion as SV20. Since we are not solving the complete hydrodynamics, we are adding these velocities in an *ad hoc* manner, computing the velocity of the particles according to the method discussed in Dominik *et al.* (1989).

For the model, we have assumed mass loss of 10^{-5} solar masses per year from a star with an effective temperature of 3000 K and a radius of 10^{13} cm. This results in a luminosity of about 1400 solar luminosities. We use a constant velocity outflow with a velocity of 10 km/s. The nucleating species we take to be carbon, with a [C]/[O] ratio of 8. The grain composition is taken to be graphite, with thermochemical constants taken from GKS84.

4. RESULTS AND DISCUSSION

4.1 Classical Nucleation Theory vs. Master Equations

The initial question we would like to answer in this study is: How valid is classical nucleation theory? Since it is computationally much less expensive to solve grain formation problem using the classical theory than it is to solve even a truncated set of master equations

we are interested in how well the two approaches agree. Examination of Figure 1 demonstrates the difference in the supersaturation ratio required to form grains under the different methods of nucleation. Using the classical theory one notes that rapid grain nucleation and growth takes place when the supersaturation ratio is slightly greater than 4. The equivalent master equation model, ME1, does undergo substantial grain formation until $S \approx 10$. This indicates that the use of the classical theory predicts grain formation at a much earlier stage than one would see in nature.

The effect of the premature nucleation can be seen in the plots of the number density of grains and their average sizes (Figures 2 and 3). While not huge effects, the classical theory does predict grain number densities higher than expected under the ME1 model. A more pronounced effect is seen in the number of atoms per grain produced. The average grain size computed under CNT is over a factor of 5 smaller than that predicted using the master equations. This is equivalent to a 30% difference in grain radius. In addition, we have computed the grain size distribution according to the prescription given in Gauger *et al.* (1990). Figure 4 demonstrates quite clearly how the CNT model overestimates grain numbers while underestimate the grain size.

4.2 The Importance of Cluster Coagulation

In addition to master equations with only monomeric reactions, we constructed the ME2 and ME20 models to determine the importance of cluster coagulation. While increasing cluster size does increase the collision cross section of the grain, it turns out that the number density for even dimers is too low, *in the absence of drift motion* to affect the grain nucleation and growth. As can be seen in Figures 1 through 4, there is only a slight difference between the results of the ME1 model and the ME2 model. The ME2 and ME20 models are virtually identical. Thus we may conclude that if systematic velocities due to radiation pressure are unimportant, only monomers will contribute significantly to grain nucleation and growth.

4.3 The Effect of Streaming Motions

As noted in section 2.2, the inclusion of grain drift velocities will have a major effect on

collisional rates of grain forming particles. In our SV20 model, we have included grain drift velocities as determined by radiation pressure and the drag force of the ambient gas on the grains. Since this model does not treat the hydrodynamics, it is not completely accurate, since those grains with the highest velocities will tend to be swept out of the grain forming region faster. This effect is ignored in this model, but we should be able to gain an understanding of the importance of the effect of this streaming motion from the SV20 model.

Figure 1 shows that the increased collisional rates due to the systematic velocity allow grain formation at a supersaturation ratio near 8. While less than that predicted by ME20, it is still much larger than the supersaturation ratio at which nucleation takes place under classical nucleation theory. The most drastic effects, however, are seen in Figures 2 through 4. Here we see that the coagulation of grains is greatly enhanced when radiation pressure on grains is considered. This coagulation of grains decreases the predicted number density by nearly three orders of magnitude while increasing the average number of atoms per grain by three orders of magnitude. Calculating the grain radius, we find that the ME20 model yields an average grain radius of about $0.1 \mu\text{m}$. The SV20 model on the other hand predicts an average grain radius of nearly $1 \mu\text{m}$. While this is rather large, we expect that a more realistic treatment of the hydrodynamics will result in slightly less extensive grain growth. Furthermore, inspection of Figure 4 shows that the SV20 model produces a much broader spectrum of grain sizes as compared to any of the other models. Thus, a proportionally large number of smaller grains are still produced under these conditions.

5. CONCLUSIONS

From this work we are able to draw a number of conclusions about modeling the formation of dust in circumstellar environments.

1. We find that a master equation solution of the nucleation problem is justified over the use of classical nucleation theory. Our models demonstrate that the classical approach does not allow for enough large cluster decomposition and allows complete grain formation to occur at

much too low a supersaturation ratio. This results in an incorrect grain number density and size distribution, as well as causing grain formation to occur too close to the stellar photosphere.

2. If the effect of radiation pressure on grain velocities is unimportant or ignored, only the most abundant particles (in this case monomers) are important in the nucleation and growth of grains. If systematic velocities due to radiation pressure are included, the coagulation of larger particles does become important, yielding rather few large grains.

3. Calculation of the grain size distribution shows that the master equation method results in a broader grain size distribution than allowed by the classical theory. Inclusion of velocity effects due to radiation pressure broadens the distribution even more.

While useful as a test of the accuracy of the classical theory used by previous authors, we cannot say we have solved the grain formation problem. Modeling the more complex effects due to the hydrodynamics of the gas-grain fluid together with this more accurate treatment of grain nucleation will be the subject of future work.

Acknowledgement:

This work has been partially supported by the U. S. Air Force under grant AFOSR 89-104 and by NASA under grant NAGW-2817.

REFERENCES

- Abraham, F. F. 1974, *Homogeneous Nucleation Theory*, Academic Press, New York
- Dominik, C., Gail, H.-P., and Sedlmayr, E. 1989, *A&A*, 223, 227
- Donn, B., and Nuth, J. A. 1985, *Ap. J.*, 288, 187
- Draine, B. T., and Salpeter, E. E. 1977, *J. Chem. Phys.*, 67, 2230
- Fix, J. D. 1969, *MNRAS*, 146, 37
- Gail, H. P., Keller, R., and Sedlmayr, E. 1984, *A&A*, 133, 320
- Gail, H. P., and Sedlmayr, E. 1988, *A&A*, 206, 153
- Gauger, A., Gail, H.-P., and Sedlmayr, E. 1990, *A&A*, 235, 345
- Hammes, G. G. 1978, *Principles of Chemical Kinetics*, Academic Press, New York
- Keller, R. 1987, in *Polycyclic Aromatic Hydrocarbons and Astrophysics*, A. Leger, L. B. d'Hendecourt, and N. Boccarda, eds., Reidel, Dordrecht, p. 387
- Rossi, S. C. F., and Benevides-Soares, P. 1988, *A&A*, 192, 379
- Salpeter, E. E. 1974, *Ap. J.*, 193, 579
- Yamamoto, T., and Nishida, S. 1977, *Prog. Theor. Phys.*, 57, 1939

FIGURE CAPTIONS

- FIG. 1 - Supersaturation ratio vs. radial position (in stellar radii).
- FIG. 2 - Dust density normalized to hydrogen atom density vs. radial position. The dust-to-gas density ratios (n_d/n_H) for the models CNT, ME1, ME2, ME20, and SV20 are respectively 1.59×10^{-11} , 1.18×10^{-11} , 7.71×10^{-12} , 7.71×10^{-12} , and 1.04×10^{-14} .
- FIG. 3 - Average number of atoms per grain ($\langle N \rangle$) vs. radial position. The peak values of $\langle N \rangle$ for the models CNT, ME1, ME2, ME20, and SV20 are respectively 1.04×10^8 , 5.41×10^8 , 5.84×10^8 , 5.85×10^8 , and 4.24×10^{11} .
- FIG. 4 - Grain size distribution vs. dimensionless grain size. The values for y-axis is scaled by $\times 10^{13}$ for the models CNT, ME1, ME2, and ME20, while for the model SV20, the scaling factor is $\times 10^{16}$.

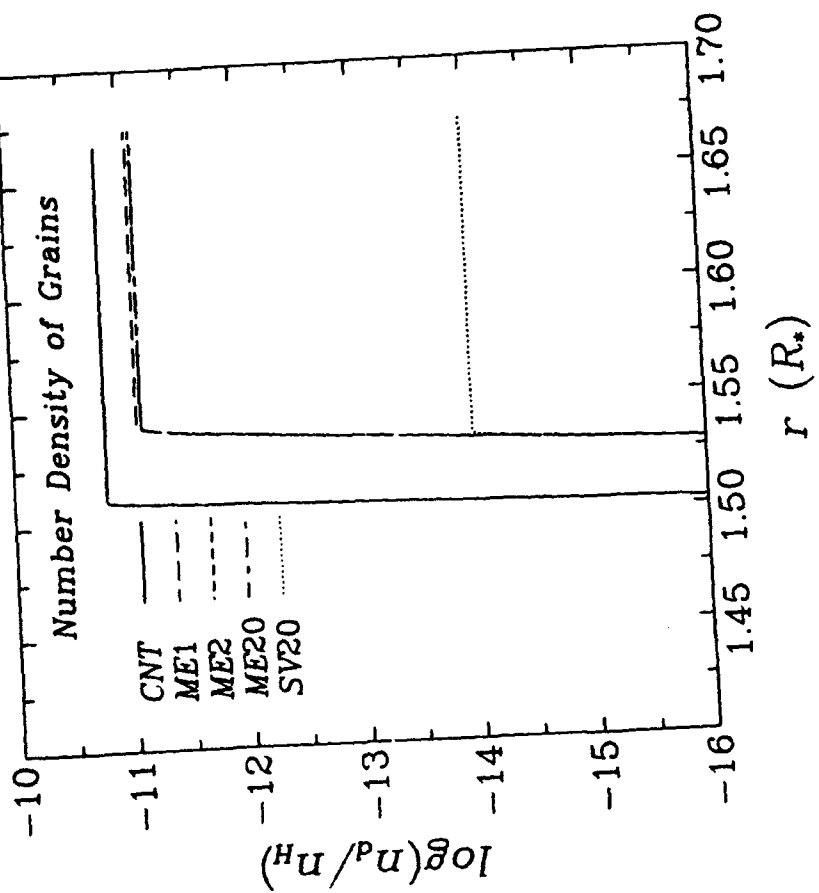


Figure 1

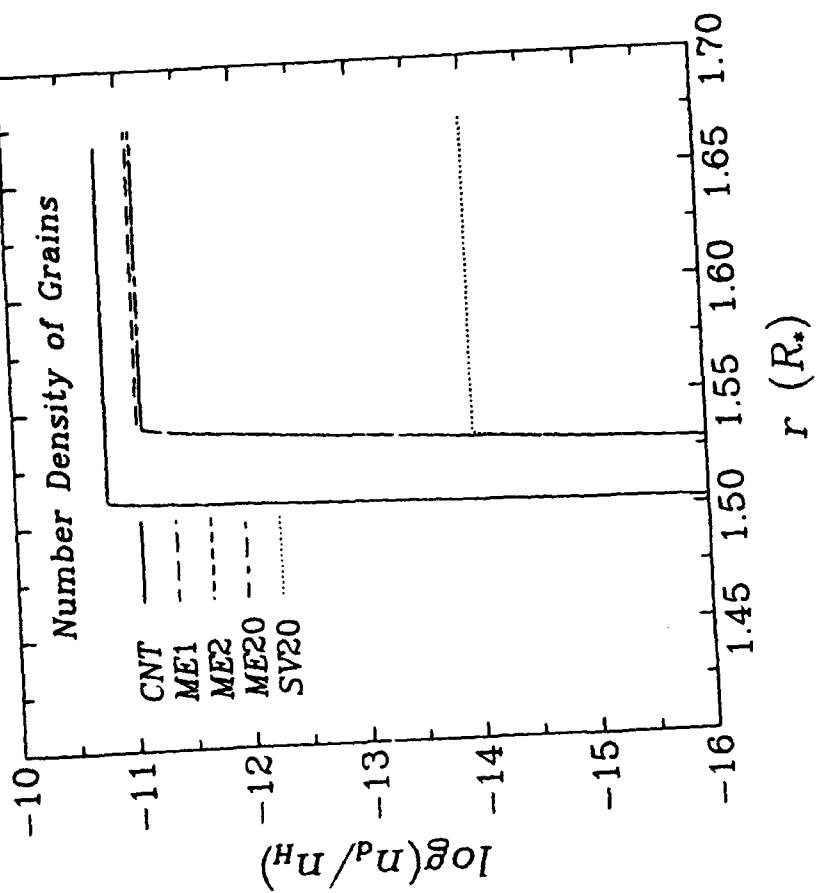


Figure 2

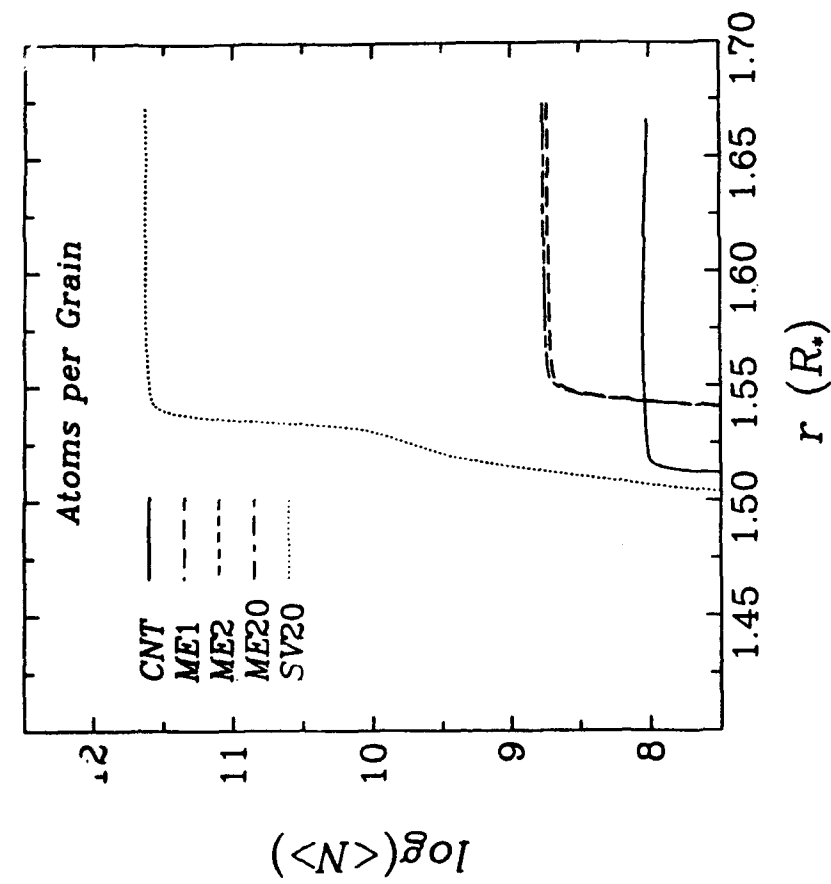


Figure 3

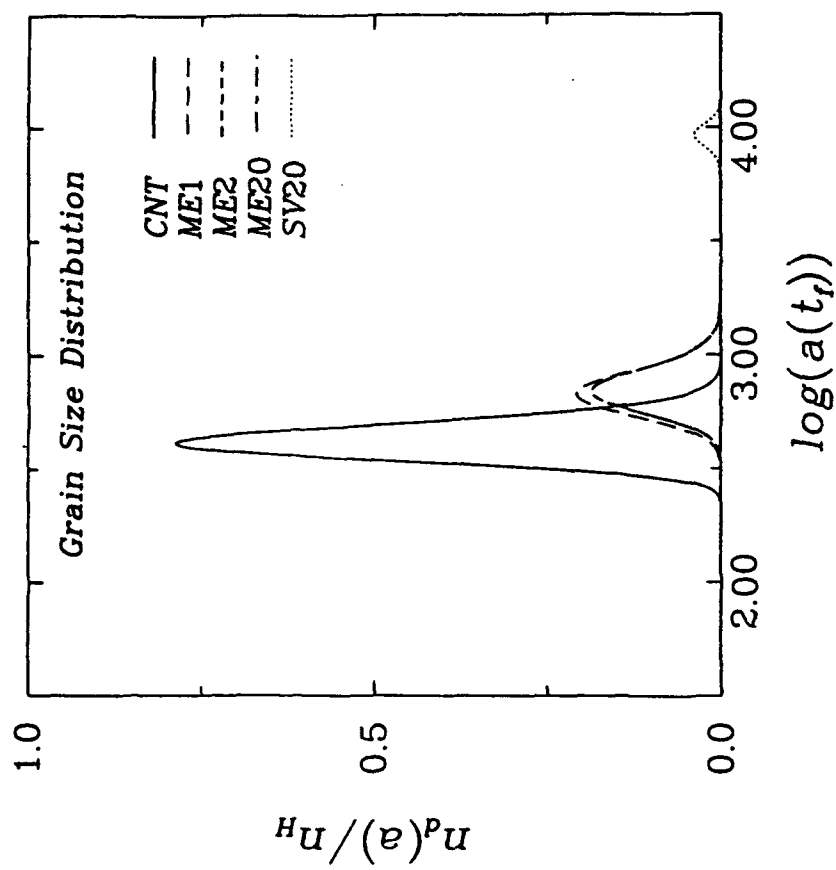


Figure 4

APPENDIX 5: SELECTED POSTER PAPERS PRESENTED

- A5.1 Charnley S. B. and Leung, C. M., "Modeling the 3 μm Feature in the Infrared Spectra of Circumstellar Envelopes.", poster paper presented at the 176th AAS Meeting (Albuquerque, NM) in June 1990.**
- A5.2 Potterveld, C. and Leung, C. M., "Modeling the 3 μm Water Ice Band of Evolved Stars: Temperature Effects?", poster paper presented at the 25th Anniversary Meeting of the Astronomical Society of New York (Ithaca, NY) in April 1992.**
- A5.3 Charnley S. B., Kress, M. E., and Leung, C. M., "A Chemical Kinetic Model of Radical Reactions in Molecular Mantles.", poster paper presented at the 177th AAS Meeting (Philadelphia, PA) in January 1991.**
- A5.4 Fogel, M. E. and Leung, C. M., "Modeling the Infrared Spectra of Fractal Dust Grains.", poster paper presented at the 179th AAS Meeting (Atlanta, GA) in January 1992.**
- A5.5 Doty, S. D. and Leung, C. M., "Modeling the Effect of Radiative Transfer on the Photochemistry of Evolved Circumstellar Envelopes.", poster paper presented at the 25th Anniversary Meeting of the Astronomical Society of New York (Ithaca, NY) in April 1992.**
- A5.6 Kress, M. E., Leung, C. M., and Irvine, W. M., "Probing the Carbon-to-Oxygen Ratio in Dense Interstellar Clouds.", poster paper presented at the 179th AAS Meeting (Atlanta, GA) in January 1992.**

Modeling the 3 μm Ice Feature in the Infrared Spectra of Circumstellar Envelopes

Steven B. CHARNLEY & Chun Ming LEUNG

Rensselaer Polytechnic Institute

In the cool, thick circumstellar envelopes of O-rich red giants, abundant water molecules will condense onto previously-formed silicate grains and form ice mantles which exhibit an infrared absorption feature at 3.1 μm (see Figure 1). Circumstellar ice mantles thus form in a different manner to those observed in the dense interstellar medium where the accretion of O and H atoms, followed by hydrogenation reactions on the grain surface, leads to water ice formation. Due to the low gas and dust temperatures in molecular clouds, the ices formed there are expected to be amorphous and to contain other molecules besides H_2O . Observations of the 3 μm region in a wide variety of molecular sources do indeed show a broad H_2O absorption feature, indicative of amorphous ice, and also additional structure at longer wavelengths due to absorption by other (hydrocarbon) molecules present in the ice mantle. Observational studies of the 3 μm region in the circumstellar shells of several late-type stars (e.g. OH231.8+4.2 and IRAS 09371+1212) show that it is narrower than the interstellar one and, furthermore, that the absence of any significant additional absorption is consistent with the ices being very pure (Geballe *et al.* 1988, *Ap.J.*, 326, L65; Hodapp *et al.* 1988, *Ap.J.*, 326, L61). The narrowness of the feature is interpreted as being due to crystalline ice mantles which are formed in the hotter regions of the circumstellar envelope ($\leq 135\text{K}$), although an amorphous ice component may also be present (Rouan *et al.* 1988, *Astron. Ap.*, 189, L3; Smith *et al.* 1988, *Ap.J.*, 334, 209). Recent observations of the 40-70 μm ice bands in some shells clearly confirm the presence of crystalline ice (Onont *et al.* 1990, *Ap.J.*, 355, L27). Information concerning the physical conditions in the shell and on the state of the ice mantles is normally obtained by fitting models to the observed feature. Conclusions from such studies depend upon two factors in the analysis of the observational data: 1) the accuracy of the continuum fitted to the observed spectrum to estimate the optical depth in the ice feature, and 2) the validity of a simple Mie theory analysis which assumes that the total extinction is due entirely to absorption, and which ignores such effects as dust emission and self-absorption when calculating a flux spectrum for comparison with observation.

It is not clear that such a simple treatment of the radiative transfer problem in these dust shells is justified. We have thus computed theoretical fluxes from a full solution of the problem using a transfer code (Egan *et al.* 1988, *Comp. Phys. Comm.*, 48, 271), and have compared these with those fluxes obtained using the simple Mie theory treatment.

We have modeled the shell as comprising of two dust components. At radii where the dust temperature is greater than the condensation temperature of crystalline ice the grains are amorphous silicates of radius $0.5\mu\text{m}$, whereas in the cooler outer regions of the shell they also possess crystalline ice mantles of thickness 0.1 or $0.6\mu\text{m}$. We have studied a spherically asymmetric dust shell with model parameters characteristic of late-type stars. The stellar radius, luminosity, and effective temperature were taken to be $3.7 \times 10^{12}\text{cm}$, $10^4 L_\odot$ and 2500K , respectively. The inner and outer radii of the dust shell were $9.4 \times 10^{13}\text{cm}$ and $3.0 \times 10^{16}\text{cm}$.

Our method of analysis proceeds as follows: we compute a theoretical flux spectrum using the radiative transfer code, and essentially regard this as an 'observation'; we then fit a continuum from three Planck functions to the $3\mu\text{m}$ feature and estimate the optical depth in ice, τ_{31}^{ice} , and finally attempt to reproduce the theoretical flux using a simple Mie theory analysis. We have examined the applicability of this approach in the light of radiative transfer effects.

Some exemplary calculations are shown in Figures 2, 3 and 4. In each we have chosen to fit the Planck functions to the $3.6\text{--}4.0\mu\text{m}$ region of the long wavelength side of the feature, as done in practice. We find that the ice optical depths obtained from this fitting, τ_{31}^{ice} , are typically underestimated by about 10-25 percent.

Figures 2 and 3 show that the $3\mu\text{m}$ feature is much broader than that due solely to crystalline ice, additional absorption at both shorter and longer wavelengths is present. The simple Mie theory treatment cannot reproduce the shape of the 'observed' flux profile obtained from the transfer code. Also, the fit at longer wavelengths from the Mie treatment worsens as the ice optical depth increases.

Figure 4 shows a model calculation with a different value of ice mantle thickness and total optical depth, but with the same theoretical value of $\tau_{31} (=1)$ as the model of Figure 2. Here it can be seen that the fit obtained from Mie theory is much better in the longer wavelength region, but that additional absorption still persists at shorter wavelengths and the shape of the feature still cannot be fitted well there.

The variation of the shape of the theoretical $3\mu\text{m}$ feature with total optical depth, illustrated by comparing Figures 2 and 4, can be understood as being due to radiative transfer effects arising from the presence of differing amounts of hot dust in the shell. At the higher optical depth, photon trapping occurs deep in the shell and this leads to saturation of the short wavelength wing of the $3\mu\text{m}$ feature (Figure 4), and to an increase in the dust temperature there. In the model with lower optical depth (Figure 2), short wavelength absorption is still evident but the presence of cooler dust tends to shift the absorption to longer wavelengths. Figure 5 shows the radial distribution of dust temperature in each of these models. For the model with the lower value of τ_0 , the silicate dust temperature in the innermost regions is lower, by as much as $\sim 250\text{K}$.

CONCLUSIONS

- Accurate Planck fitting of the theoretical flux spectra through $3.6\text{--}4.0\mu\text{m}$ is difficult. The continua we have obtained tend to underestimate the optical depth in ice.
- A simple analysis based on Mie theory, which assumes that the total extinction through the dust shell is due solely to absorption, and which ignores dust emission and self absorption, fails to reproduce the shape of the theoretical ('observed') $3\mu\text{m}$ feature.
- Our preliminary calculations emphasise that radiative transfer effects must be considered when attempting to model the observed ice spectra of circumstellar shells, and that caution should be exercised in drawing conclusions from analyses which neglect to do so.

This research is supported in part by the US Air Force under Grant AFOSR-89-0104.

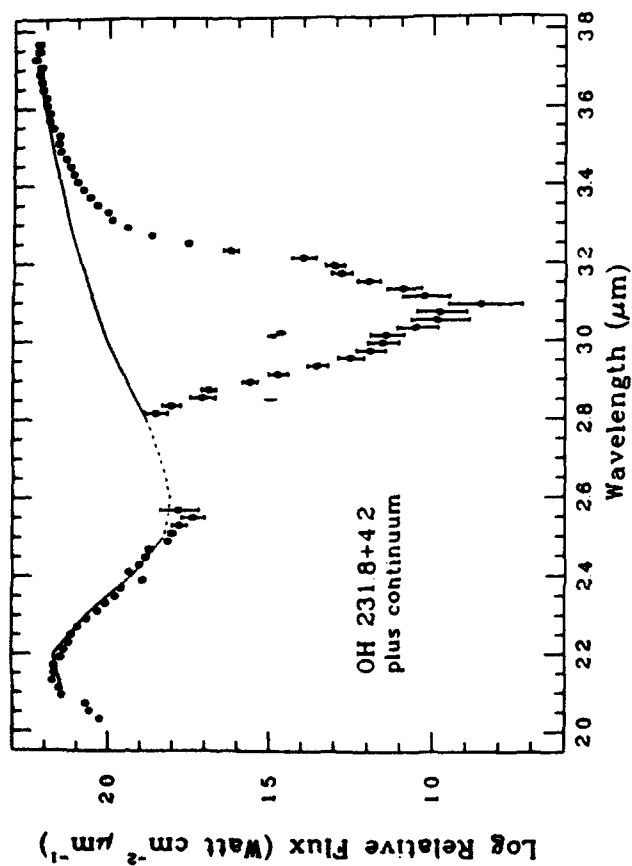


FIGURE 1
The 2.0-3.8 μm spectrum of OH231.8+4.2 and fitted continuum (From Smith et al. 1988, *ApJ*, 334, 299)

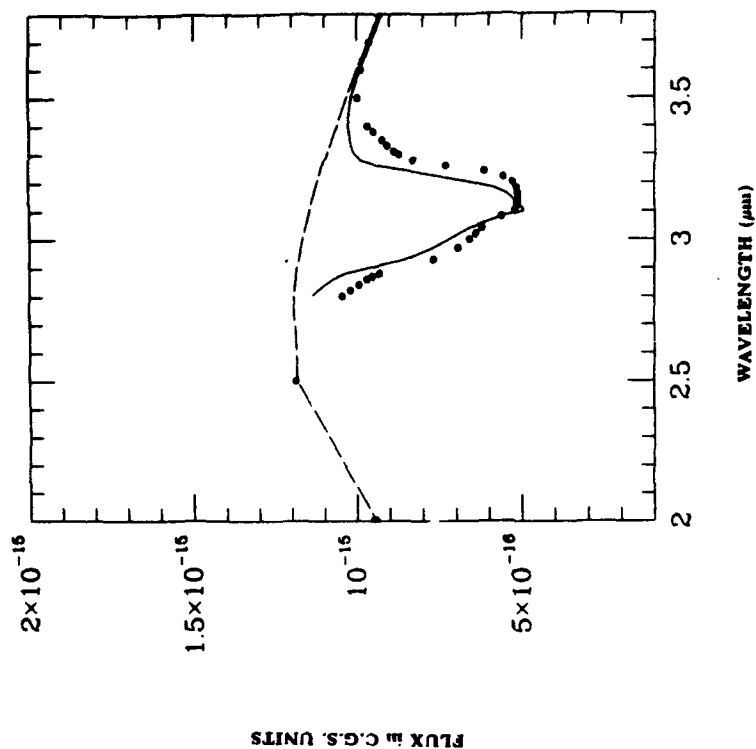


FIGURE 2 The flux spectrum (solid circles) obtained from the transfer code for an ice model thickness, τ_{ice} , of 0.6 μm and a total optical depth (at 3.1 μm), τ_{ice} , of 2.3. The broken line shows the fitted continuum and the solid line is the observed flux as reconstructed from the Mie theory treatment. The optical depth in ice from the model is, $\tau_{\text{ice}}=1.0$, and the fitted value is $\tau_{\text{ice}}=0.71$.

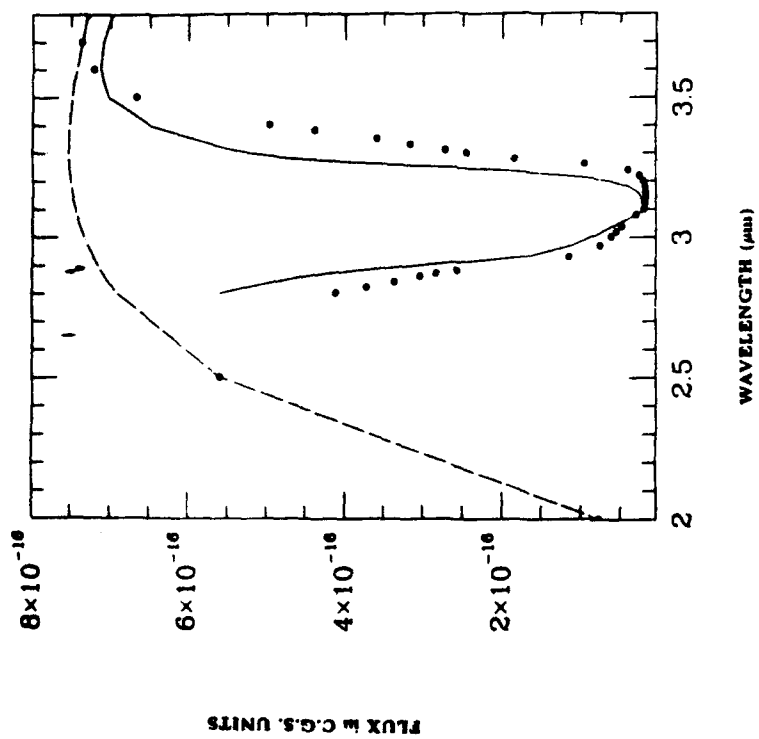


FIGURE 3 As Figure 2 with $\alpha_{\text{m}} = 0.6 \mu\text{m}$, but for $\tau_0 = 10$, $\tau_{2.1} = 4.35$ and $\tau_{3.1}^{\text{m}} = 3.21$.

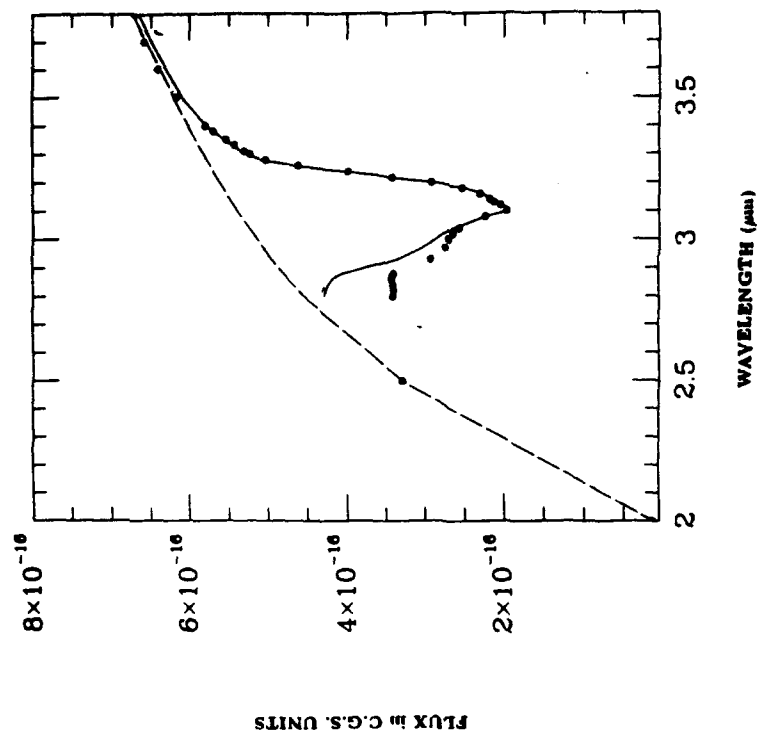


FIGURE 4 As Figure 2 but for $\alpha_{\text{m}} = 0.1 \mu\text{m}$, $\tau_0 = 10$, $\tau_{2.1} = 1.0$ and $\tau_{3.1}^{\text{m}} = 0.87$.

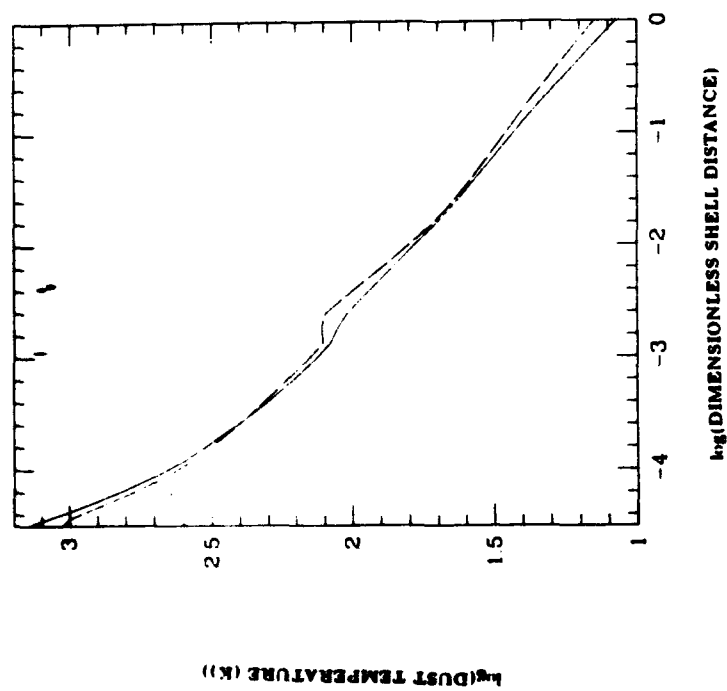


FIGURE 5 The dust temperature distributions in the model circumstellar shells corresponding to Figure 2 (solid line) and to Figure 4 (dashed line)

**Modeling the 3 μ m Water Ice Band
of Evolved Stars:
Temperature Effects?**

by

**C. Potterveld
S. B. Charnely
C. M. Leung
Rensselaer**

Introduction

The absorption coefficients for some molecular ices change with temperature. Of these ices, water ice is seen in the spectra of molecular clouds and circumstellar dust shells. The change in the coefficients for water ice consist of two effects. The first effect is brought about by an irreversible phase change in the ice from an amorphous state to a crystalline state, at around 100 K. This effect narrows the feature and increases the peak strength.

The second effect is that upon recooling the ice feature undergoes another, smaller shift. The changes in the feature are qualitatively similar, but much smaller than the first effect. However, the feature still retains its structure from the initial warm up.

We have run radiative transfer models to determine what changes the first effect would have on the 3 μ m feature observed in circumstellar dust shells. Quantitative data is available only for the first effect. Our models do not take into account the recooling of the ice grains.

Model Parameters

Our models assume a source with :

$L = 1000 L_{\odot}$ $R_{\text{star}} = .97 \text{ Parsecs}$

$T = 2500 \text{ K}$ $\tau_{3.1\mu\text{m}} = 1$

$R_{\odot} = 536 R_{\oplus}$ $\tau_{1.1\mu\text{m}} = 1$

The dust grains consist of bare silicate cores, with radius $a = .5\mu\text{m}$, from R_{\odot} to where the temperature fell below 150K. Beyond that point the silicate grains have an ice mantle, with a thickness of $.1\mu\text{m}$. The absorption and scattering coefficients were computed from Mie theory using laboratory-measured optical constants.

Three models were run with these parameters.

Model A. Optical constants taken at 140 K

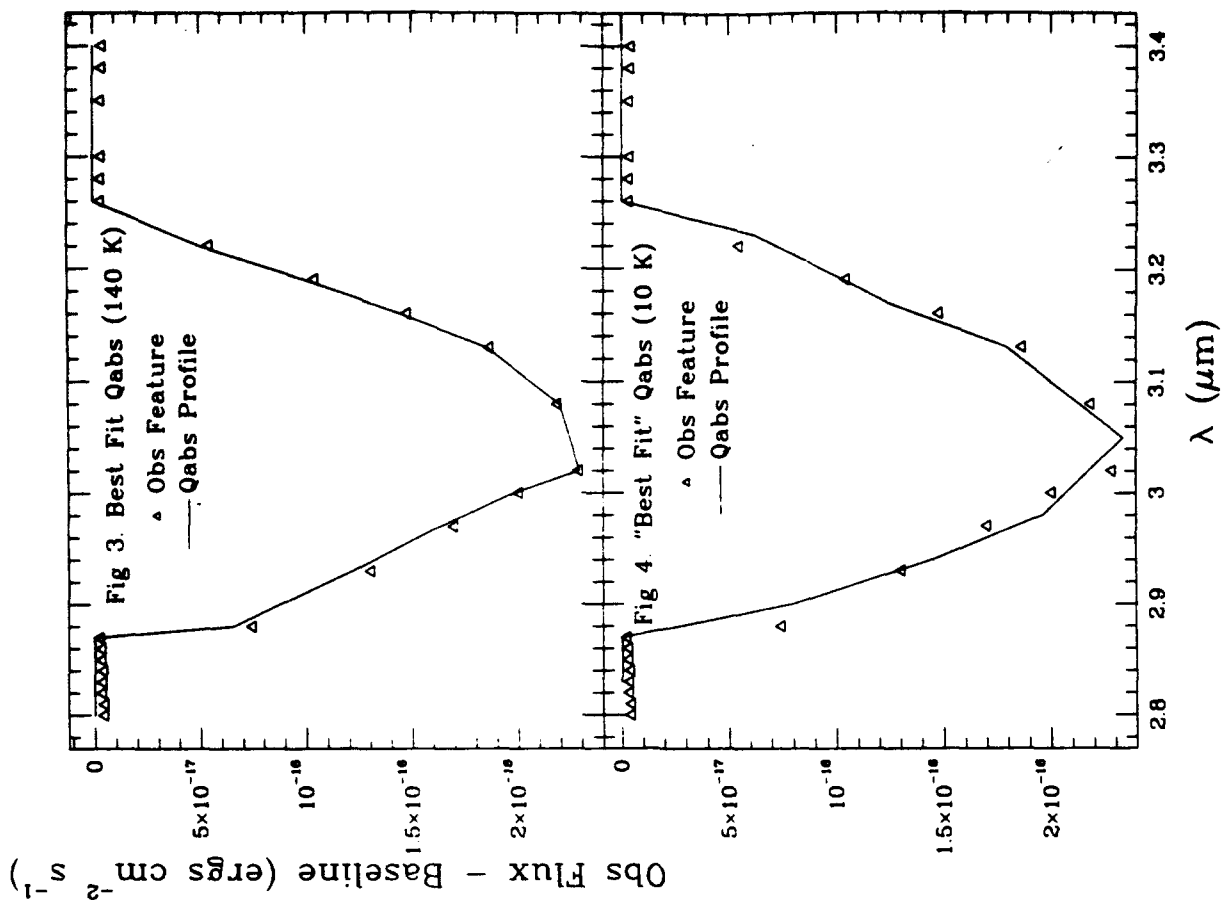
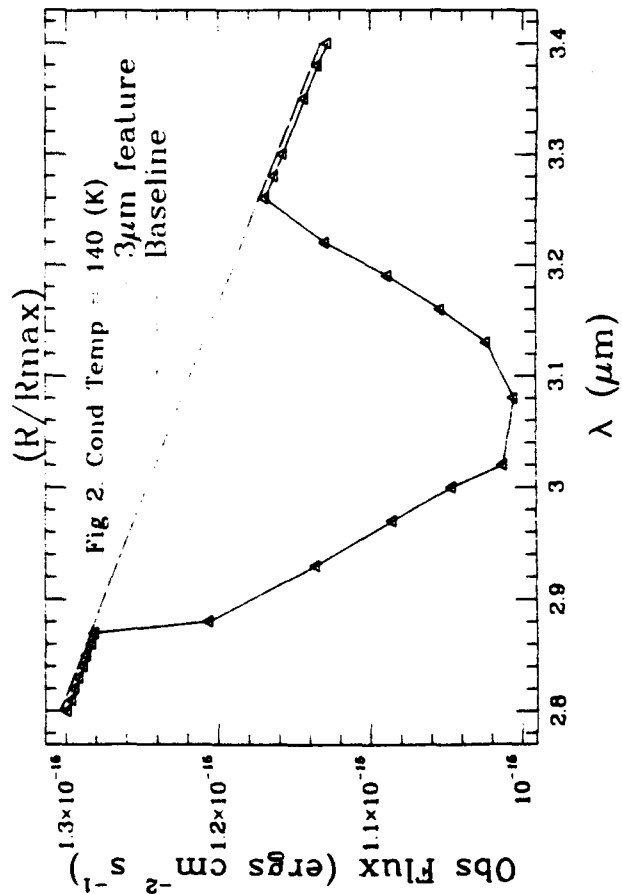
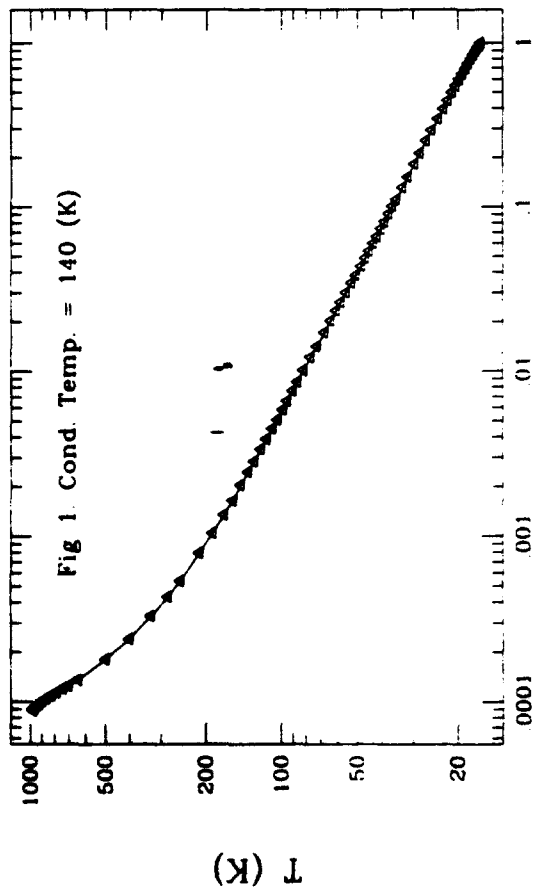
Model B. Optical constants taken at 10 K

Model C. Optical constants were approximated with a temperature dependent function. Optical constants were computed at each point for the current temperature.

Radiative Transfer Effects

All three models show significant weakening of the $3.1\mu\text{m}$ ice feature due to emission from hot silicate grains close to the star (See Figure 1). This radiation 'fills' in the $3.1\mu\text{m}$ feature leading to an underestimation of the dust opacity at $3.1\mu\text{m}$. Although $\tau_{1.1} = 1$ in all the models, the optical depths calculated from the feature ($\tau = -\ln(F/F_{\odot})$) was .204 for model A, .18 for model B, and .176 for model C (See Figures 2, 5, 8).

A second effect from the radiative transport is a broadening of the feature, leading to a possible mis-identification of the type of ice producing the feature. The feature produced by the crystalline ice is broadened to the extent that the absorption coefficients of this ice are too narrow to fit the feature well (See Figure 3). However, coefficients of amorphous ice can fit the feature reasonable well (See Figure 4).



Comparison of Crystalline and Amorphous Ice Features

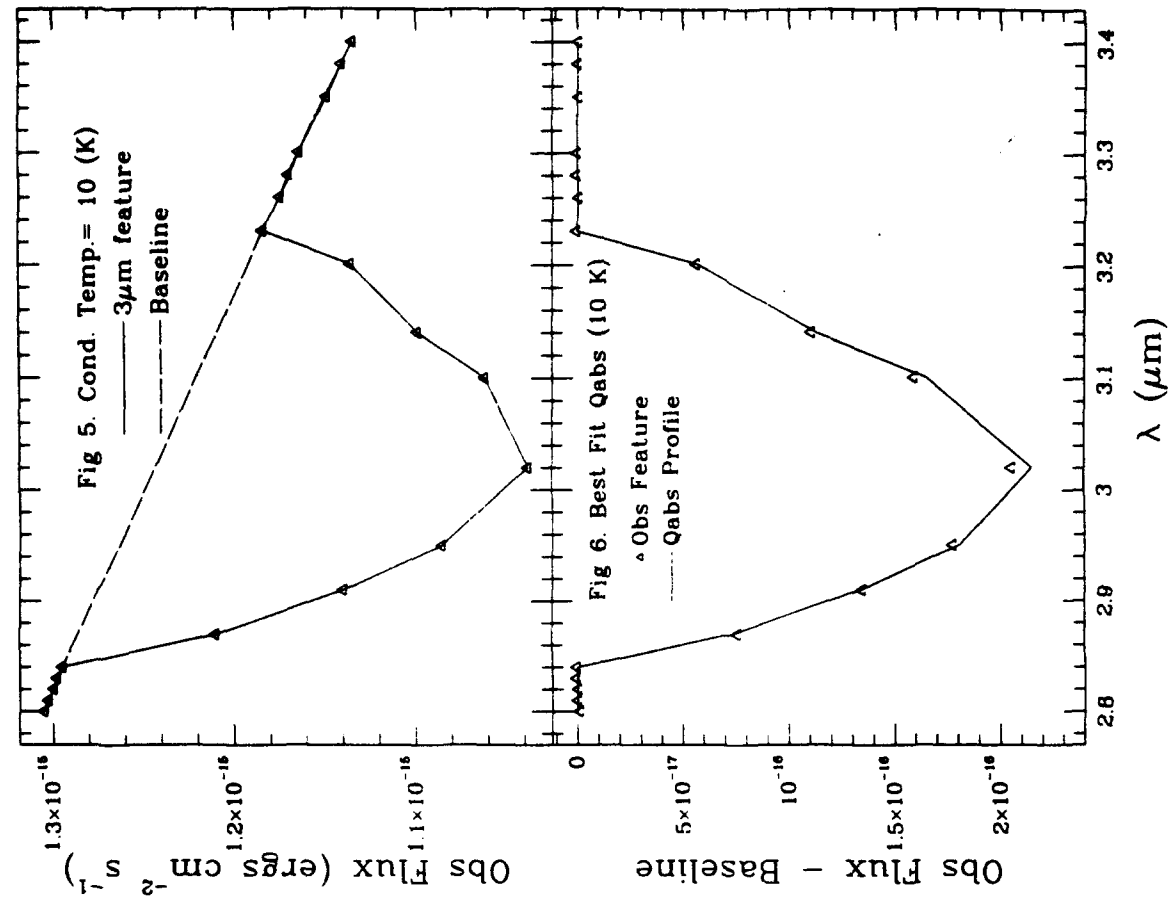
The differences in the absorption coefficients between these two phases can be seen in the features each produces at $3.1\mu\text{m}$. First, the feature arising from the amorphous ice is weaker than the crystalline feature. They peak at the same wavelength, however. Second, the amorphous ice feature is more symmetric than the crystalline ice. Its centroid wavelength is close to the peak while the crystalline centroid is red shifted (see Fig 9).

140 K

$\tau_{\text{fit}} = .204$
Peak $\lambda = 3.02\mu\text{m}$
Centroid $= 3.05\mu\text{m}$

10 K

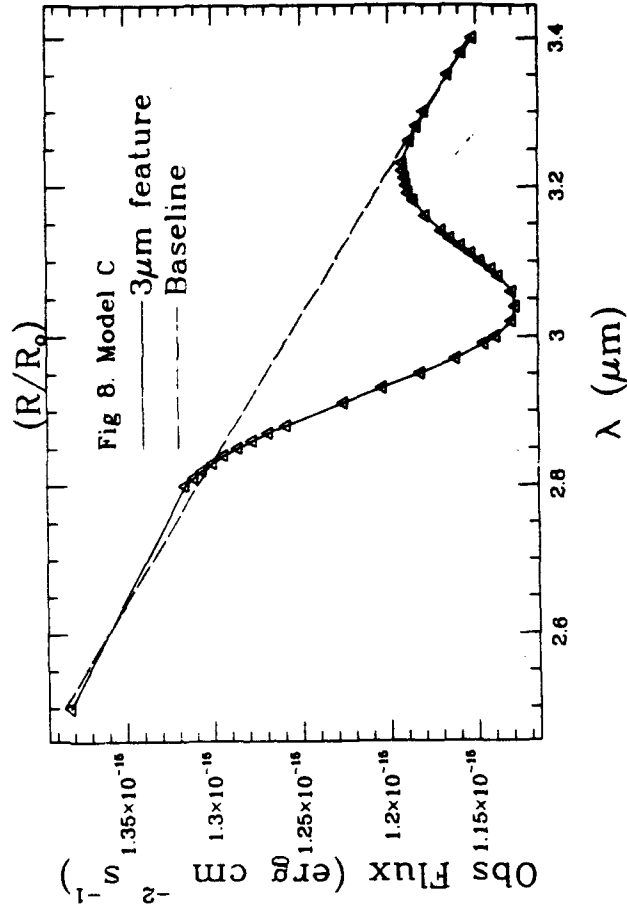
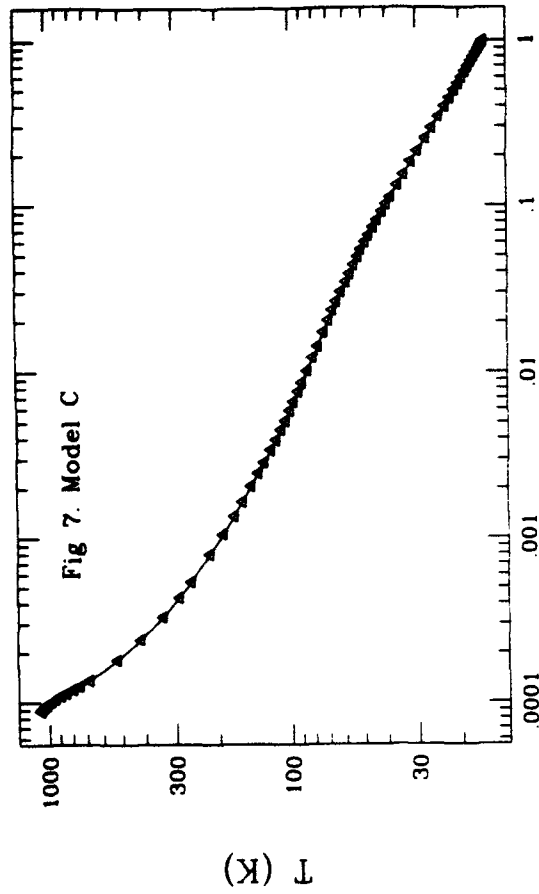
$\tau_{\text{fit}} = .180$
Peak $\lambda = 3.02\mu\text{m}$
Centroid $= 3.02\mu\text{m}$



Model C

To model the effects of ice condensed onto the grains over a range of temperatures, we take $Q_{\text{abs}} = a\lambda + b + \text{Gaussian}$, for the $3\mu\text{m}$ feature. For this first model the height and peak wavelength of the Gaussian were given a linear dependence on the grain temperature.

The feature from this model is quite a bit weaker than any of the previous models, $\tau_{0.1} = .102$. The peak wavelength remained at $3.02\mu\text{m}$. The feature, like model A, is also very symmetric, Centroid = 3.02μ . This symmetry arises from the form chosen for the ice and not from the radiative effects discussed earlier (see Figures 8,9).



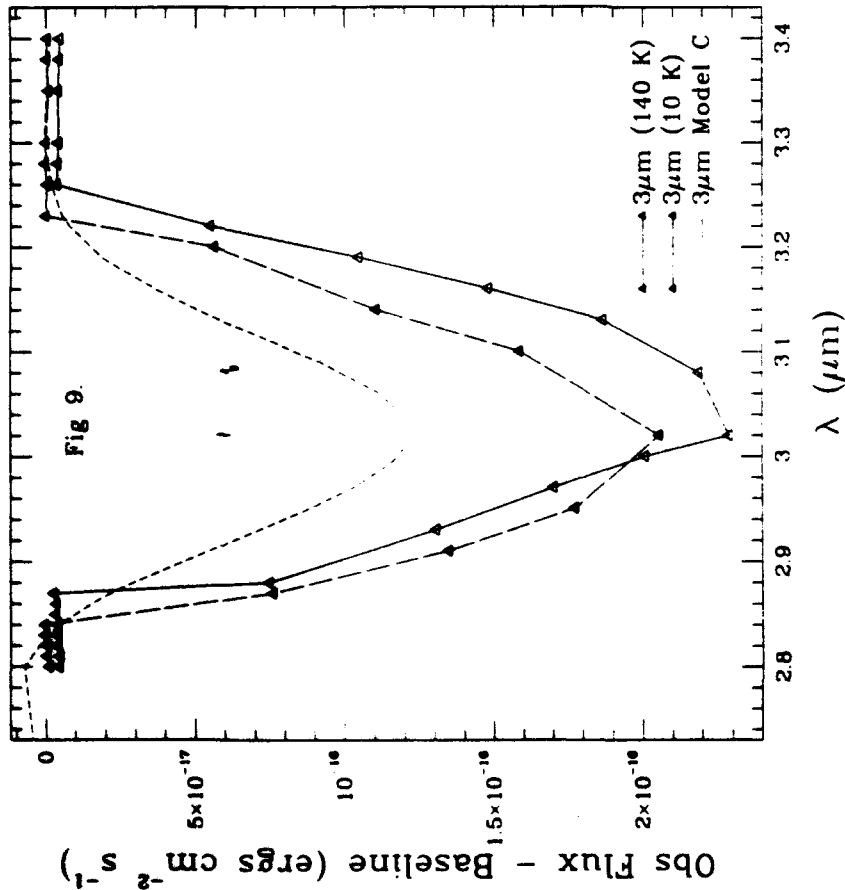


Fig 9.

140 K	10 K	Model C
$\tau_{1.0} = .204$	$\tau_{1.0} = .180$	$\tau_{1.0} = .102$
Peak $\lambda = 3.02\mu\text{m}$	Peak $\lambda = 3.02\mu\text{m}$	Peak $\lambda = 3.02\mu\text{m}$
Centroid = $3.05\mu\text{m}$	Centroid = $3.02\mu\text{m}$	Centroid = $3.02\mu\text{m}$

Conclusions

1. Radiative transfer effects produce large changes to the characteristics of the ice features and must be taken into account when trying to deduce from observation properties of dust in a circumstellar shell. Ignoring this effect underestimates dust opacity by at least a factor of 5 and also lead to a mis-identification of the form of ice.
2. Both the shape and strength of the feature increase with temperature. In particular, the centroid wavelength shifts toward the red as the grain temperature increases.

A better physical understanding of the causes of these changes and more laboratory measurements are needed to produce a better model. Qualitative data on the reversible cooling and heating of the ices should also be pursued.

A CHEMICAL KINETIC MODEL OF RADICAL REACTIONS IN MOLECULAR MANTLES.

S.B. Charnley^{1,2,*}, M.E. Kress² and C.M. Leung²

1. Space Science Division, NASA Ames Research Center, Moffett Field, CA 94035.
2. Physics Department, Rensselaer Polytechnic Institute, Troy, NY 12180.

* NRC Research Associate

INTRODUCTION

TWO IMPORTANT PROBLEMS IN ASTROCHEMISTRY ARE TO EXPLAIN HOW MOLECULES ARE RETURNED TO THE GAS PHASE FOLLOWING ACCRETION ON TO DUST GRAINS, AND TO DETERMINE WHICH COMPLEX MOLECULES CAN BE FORMED BY GRAIN SURFACE REACTIONS

THE PRESENCE OF SUCH MOLECULES AS NH_3CN , CH_3NH_2 , $\text{C}_2\text{H}_5\text{CN}$ AND NH_2CHO IN SOME STAR-FORMING REGIONS, WHERE DUST MANTLES ARE BELIEVED TO HAVE BEEN EVAPORATED (ORION A & SGR B2), SUGGESTS THAT REACTIONS INVOLVING AMIDE, METHYL, AND FORMYL RADICALS CAN TAKE PLACE.

IN MOLECULAR CLOUDS, GRAINS ARE SUBJECT TO A VARIETY OF PHYSICAL PROCESSES: COSMIC RAY AND UV PHOTON IMPACTS, AS WELL AS HEATING IN STAR-FORMING REGIONS. IN DARK CLOUDS IT HAS BEEN PROPOSED THAT STORED RADICALS WHICH ARE PRODUCED BY UV PHOTOLYSIS OF ICE MANTLES CAN, FOLLOWING HEATING TO ABOUT 24-28K, DIFFUSE AND REACT TO RELEASE ENERGY WHICH LEADS TO AN EXPLOSION AND MANTLE REMOVAL (GREENBERG AND YENCHU 1973). THIS HAS BEEN FOUND TO OCCUR IN LABORATORY ANALOGUES OF INTERSTELLAR ICES.

WE HAVE DEVELOPED A TIME-DEPENDENT CHEMICAL MODEL TO STUDY THE FORMATION OF COMPLEX MOLECULES IN THE MOLECULAR MANTLES OF DUST GRAINS IN DARK CLOUDS. WE FOLLOW THE CHEMISTRY IN A MANTLE CONSISTING PRIMARILY OF WATER, AMMONIA, METHANE AND CARBON MONOXIDE WHICH IS LOCATED IN A REGION OF HIGH EXTINCTION BUT SUBJECT TO A WEAK AMBIENT UV FIELD. AT SOME POINT IN THE EVOLUTION A COSMIC RAY STRIKES THE GRAIN AND RAISES THE TEMPERATURE ABOVE A CRITICAL VALUE ($\sim 25\text{K}$). WE CALCULATE THE THERMAL AND CHEMICAL EVOLUTION OF THE MANTLE AFTER THIS EVENT AS THE MANTLE HEATS UP AND A THERMAL RUNAWAY (=EXPLOSION) OCCURS.

THE CRITICAL TEMPERATURE IS THAT AT WHICH THE RATE OF RECOMBINATION HEATING BY A GIVEN CONCENTRATION OF RADICALS EQUALS THE RADIATIVE COOLING RATE.

FIGURE 1 SHOWS THE CRITICAL TEMPERATURES FOR SEVERAL RADICAL CONCENTRATIONS IN THE MANTLE.

MANTLE PHOTOLYSIS

IN THE MODEL WE CONSIDER:

- A GRAIN IN A DARK CLOUD ($A_V=10$ MAG.) OF CORE RADIUS $0.06\mu\text{m}$ AND MANTLE THICKNESS $0.02\mu\text{m}$. THE ICE MANTLES INITIALLY HAVE A 'PRISTINE' COMPOSITION OF $\text{H}_2\text{O}/\text{NH}_3/\text{CH}_4/\text{CO}/\text{O}_2 = 0.50/0.15/0.15/0.15/0.05$ CONSISTENT WITH SIMPLE ACCRETION AND ACTIVATIONLESS HYDROGENATION OF GAS PHASE ATOMS AND MOLECULES ON THE GRAIN SURFACE (BROWN & CHARNLEY 1990).

- THE MANTLED GRAINS ARE SUBJECT TO A WEAK UV FLUX OF 1.4×10^8 PHOTONS $\text{cm}^{-2}\text{s}^{-1}$ FROM THE COSMIC RAY IONIZATION OF MOLECULAR HYDROGEN (PRASAD & TARAFDAR 1983)

- WE ARE INTERESTED IN THE MOLECULAR CHEMISTRY DEEP IN THE BULK OF THE MANTLE AND ASSUME THAT ACCRETED H ATOMS WILL NOT PENETRATE EFFICIENTLY INTO THE ICE MATRIX.

- THE UV PHOTONS PRODUCE RADICALS BY PHOTODISSOCIATION OF THE ABUNDANT SATURATED MOLECULES IN THE MANTLE. FOLLOWING EXPERIMENTS ON UV-PHOTOLYSED ICES AT 10K, WE HAVE USED ENHANCED PHOTOABSORPTION CROSS SECTIONS OF 4, 160 AND 100 TIMES THE GAS PHASE VALUES OF WATER, AMMONIA AND METHANE. THE HYDROGEN ATOMS PRODUCED CAN REACT WITH RADICALS, FORM H_2 , OR REACT WITH OTHER MANTLE MOLECULES SUCH AS CO AND O_2 . FORMATION OF THE FORMYL RADICAL BY REACTION WITH H HAS A BARRIER BUT IS OBSERVED TO TAKE PLACE READILY IN 10K ICES (HAGEN 1982).

- CO AND MOLECULAR OXYGEN ARE CRITICAL TO THE MAINTENANCE OF A SMALL RADICAL POPULATION. THESE MOLECULES TAKE UP HYDROGEN ATOMS PRODUCED BY THE PHOTOLYSIS AND SO PREVENT RECOMBINATION OF SOME RADICALS. AT 10K THE DIFFUSION TIME IN THE ICE MATRIX IS LONG AND THE RADICALS ARE EFFECTIVELY STORED. THIS IS CONSISTENT WITH EXPERIMENT (SCHUTTE & GREENBERG 1991).

- FOR A $0.1\mu\text{m}$ GRAIN THE TIME BETWEEN HEATING EVENTS CAPABLE OF INDUCING EXPLOSIONS IS ABOUT 8×10^3 YEARS (LEGER, JURA & OMONT 1985; SCHUTTE & GREENBERG 1991)

FIGURE 2 SHOWS THE CHEMICAL EVOLUTION IN THE MANTLE. THE TOTAL RADICAL CONCENTRATION IS 1.5% AFTER 8×10^3 YEARS

EXPLOSION PHYSICS

IF THE CRITICAL TEMPERATURE HAS BEEN ATTAINED, MANTLE HEATING BY RADICAL ANNEALING IS RAPID. COOLING BY EVAPORATION OF VOLATILE CO MOLECULES CANNOT PREVENT A THERMAL RUNAWAY TO MAXIMUM TEMPERATURES IN THE RANGE 110-180K. FIGURE 3 SHOWS THE EVOLUTION DURING SUCH AN EXPLOSION

THE THERMAL EVOLUTION OF THE MANTLE IS SENSITIVE TO THE INITIAL RADICAL CONCENTRATION AND IMPACT TEMPERATURE, AS WELL AS TO THE RELATIVE AMOUNTS OF CO EVAPORATING FROM CO ICE, AND FROM WATER ICE.

ONCE ALMOST ALL THE RADICALS HAVE ANNEALED THE MANTLE BEGINS TO COOL. ALTHOUGH THIS OCCURS FOR THE MODEL OF FIGURE 2 (AND IS INVISIBLE AT THE GIVEN RESOLUTION), WE HAVE SO FAR BEEN UNABLE TO FOLLOW THE TEMPERATURE BACK DOWN TO THE PRE-IMPACT VALUE AS THE SYSTEM OF DIFFERENTIAL EQUATIONS BECOMES EXCEEDINGLY STIFF AT THIS POINT

MOLECULE FORMATION

PRELIMINARY MODELS USING A REACTION NETWORK BASED ON ACTIVATIONLESS RADICAL-RADICAL REACTIONS (ALLEN AND ROBINSON 1971) HAVE BEEN CALCULATED FOR THE SIMPLE SET OF REACTIONS CHOSEN THUS FAR. THE MAIN NEUTRAL SPECIES FORMED ARE CH_3NH_2 , N_2H_4 , CH_3OH AND NH_2CHO .

SUMMARY

THE WEAK UV FLUX IN DARK MOLECULAR CLOUDS MAY PRODUCE A SMALL POPULATION ~ 1-2% OF STORED RADICALS WITHIN 10,000 YEARS.

A COSMIC RAY IMPACT WITH GRAIN WHICH RAISES ITS TEMPERATURE ABOVE A CRITICAL VALUE INDUCES A THERMAL RUNAWAY. THE PHYSICS OF THE EXPLOSION IS SENSITIVE TO THE FRACTIONS OF CO AND OF RADICALS PRESENT, AND ALSO TO THE RELATIVE AMOUNTS OF CO CONTAINED IN CO ICE AND IN WATER ICE.

MAXIMUM MANTLE TEMPERATURES IN THE RANGE 110-180K ARE THEORETICALLY POSSIBLE AND IT IS LIKELY THAT OTHER MOLECULES WHICH ARE MORE REFRACTORY THAN CO WILL ALSO EVAPORATE.

COMPLEX MOLECULE FORMATION TAKES PLACE AND IS PROBABLY A FUNCTION OF THE INITIAL RADICAL COMPOSITION.

AS WELL AS THE POSSIBILITY OF MODELLING MOLECULE FORMATION IN ACTUAL ICE ANALOGUE EXPERIMENTS, THESE THEORETICAL MODELS MAY ULTIMATELY HAVE APPLICATION TO SOLID PHASE CHEMISTRY STUDIES OF OTHER REGIONS IN WHICH ICY GRAINS ARE SUBJECT TO UV IRRADIATION AND PERIODIC WARMING, SUCH AS THE 'HOT CORES' OF STAR-FORMING REGIONS OR IN COMETS.

This research is supported in part by the US Air Force under Grant AFOSR-89-0104.

REFERENCES

- Allen, M. and Robinson, G. 1977. *Astrophys. J.* 212, 396.
- Brown, P.D. and Charalzy, S.B. 1990. *Mon. Not. R. astr. Soc.* 244, 432.
- Greenberg, J.M. and Yench, A. 1973. in *Interstellar Dust and Related Topics*, eds. J.M. Greenberg and H.C. van de Hulst, Reidel, p. 369.
- Hagen, W. 1982. *Ph.D. Thesis, University of Leiden.*
- Leger, A., Jura, M. and Omon, A. 1985. *Astron. Astrophys.* 144, 147.
- Prasad, S.S. and Tarafdar, S.P. 1983. *Astrophys. J.* 267, 603.
- Schutte, W.A. and Greenberg, J.M. 1991. *preprint*

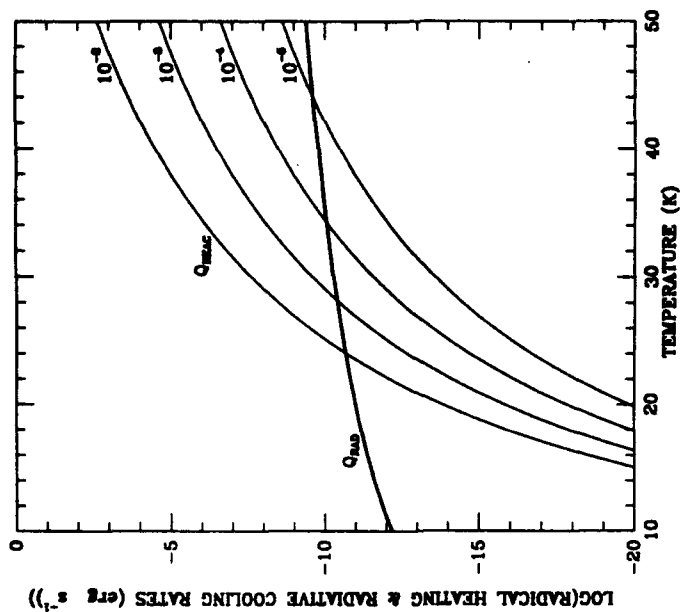


FIGURE 1. RADIATIVE COOLING RATE (Q_{rad}) AND THE HEATING RATE DUE TO RADICAL REACTIONS (Q_{acc}) FOR SEVERAL VALUES OF THE RADICAL CONCENTRATION. THE AVERAGE ENERGY RELEASED PER REACTION IS 3eV. THE INTERSECTIONS OF THE CURVES DEFINE A CRITICAL MANTLE TEMPERATURE ABOVE WHICH A THERMAL RUNAWAY WILL OCCUR.

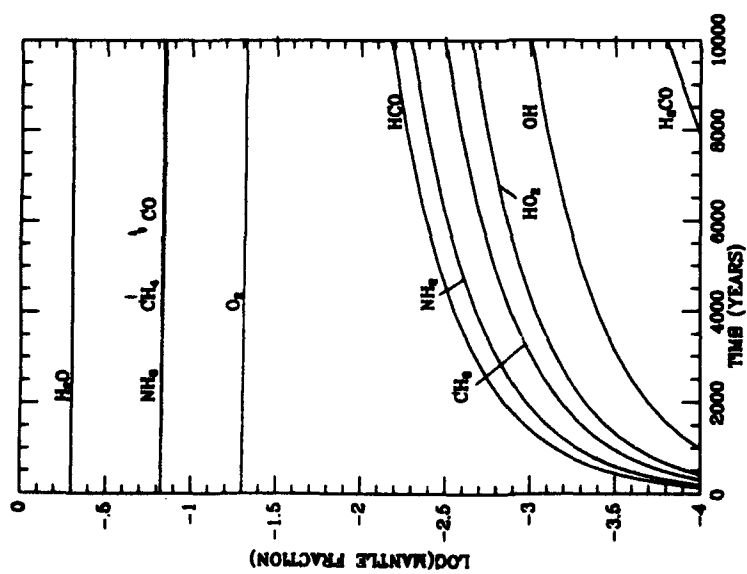
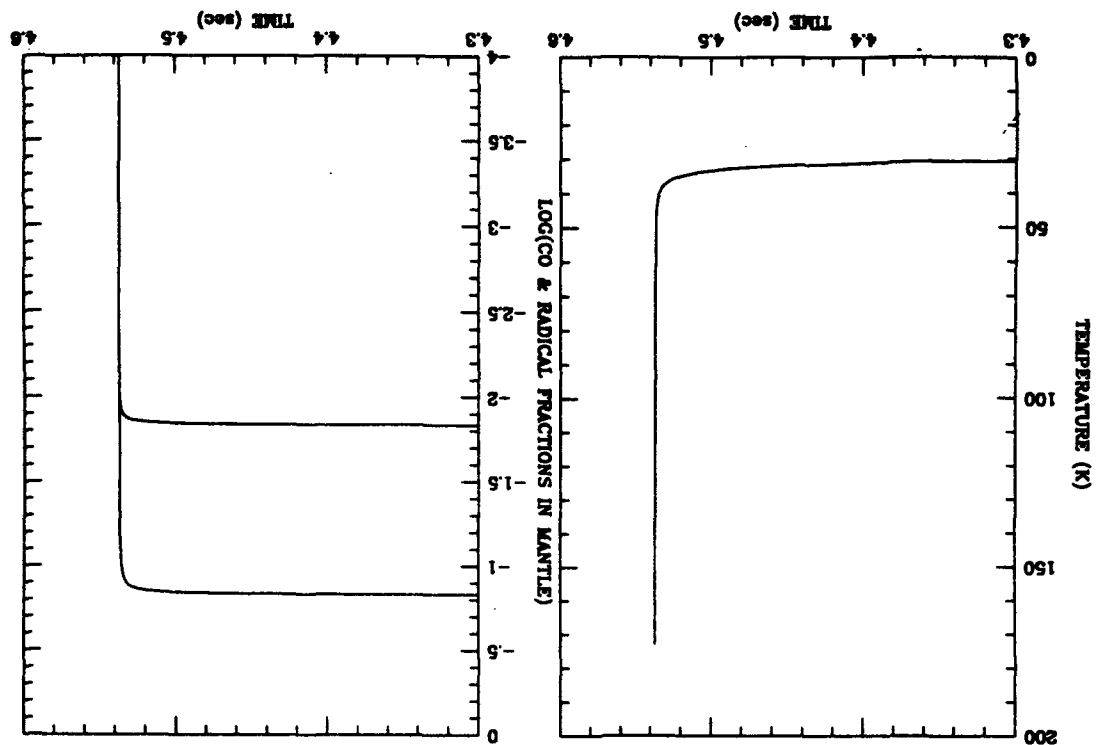


FIGURE 2. CHEMICAL EVOLUTION IN THE ICE MANTLE OF A $0.1 \mu\text{m}$ GRAIN IN THE PEASAD-TARAFDAR UV RADIATION FIELD. THE FINAL RADICAL CONCENTRATION IS 1.3%.

MODELING THE INFRARED SPECTRA OF FRACTAL DUST GRAINS

M. E. Fogel and C. M. Leung
Rensselaer

ASNY Meeting
April 25, 1992

MOTIVATION AND METHOD

In modeling the IR spectrum of dust emission from infrared sources, spherical dust grains are often assumed and dust opacity is calculated using Mie theory with the optical constants of bulk materials. Polarization measurements in the infrared readily suggest a non-spherical dust shape. In astrophysical environments, dust grains are more likely to have irregular shapes whose formation can be modeled by fractal growth processes (Whitten and Cates 1986, *Science*, **232**, 1607), e.g., particle-by-particle aggregation or cluster-by-cluster aggregation. For fractal dust grains, the use of bulk optical constants may not be appropriate.

We have studied the effects of fractal dust grains on the IR spectrum of different sources by considering non-spherical dust grains formed by the two fractal processes. To calculate the grain opacity, we use the Discrete Dipole Approximation or DDA (Draine 1988, *ApJ*, **333**, 848) which approximates a fractal as a collection of point dipoles. Optical constants for both bulk materials (Mathis and Whiffen 1989, *ApJ*, **341**, 808) and amorphous clusters (Roubeau and Martin 1991, *ApJ*, **337**, 326) are utilized. Using these fractal opacities, radiation transport models of infrared sources (e.g., interstellar dust clouds and circumstellar dust shells) are constructed (Egan, Leung, and Spagna 1988, *Computer Phys. Comm.*, **48**, 271) to study the effect of grain size, shape, and composition on the IR spectrum.

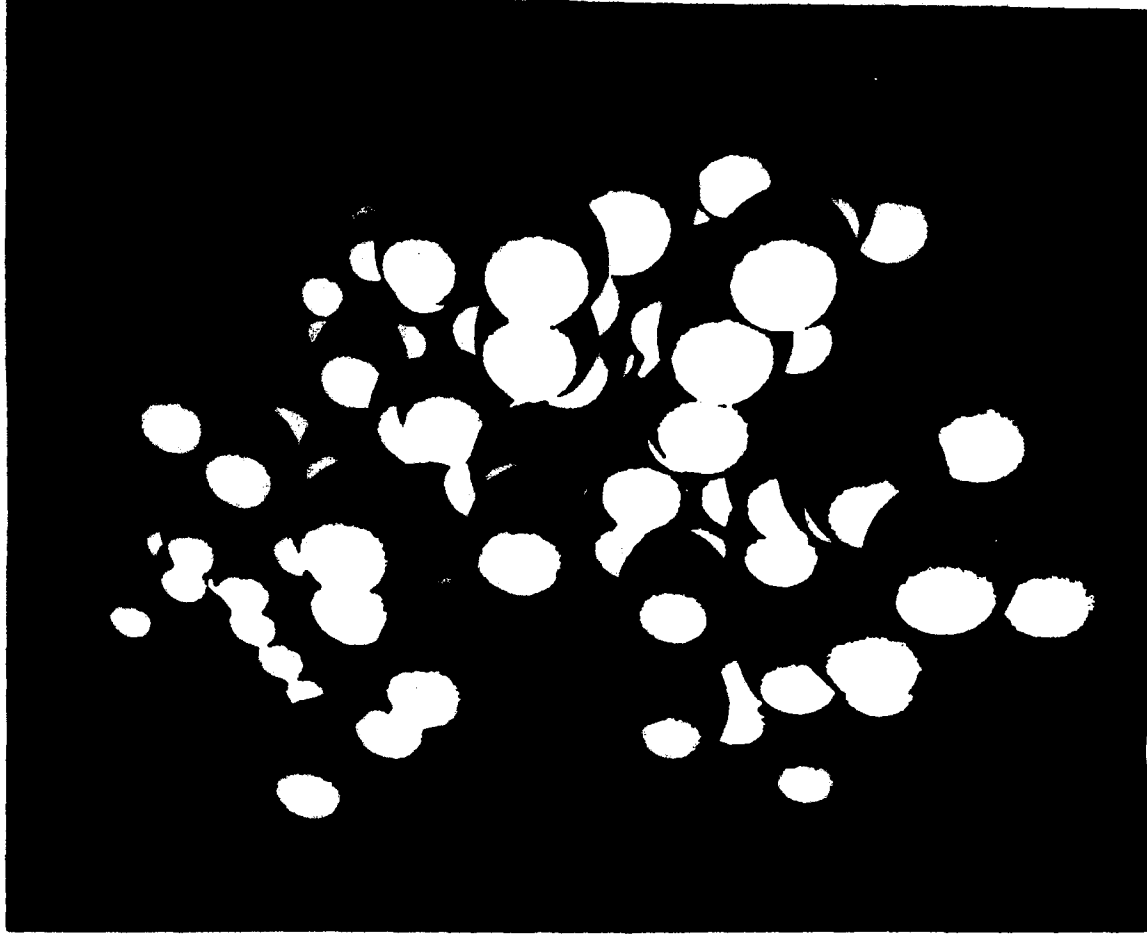
MODEL PARAMETERS

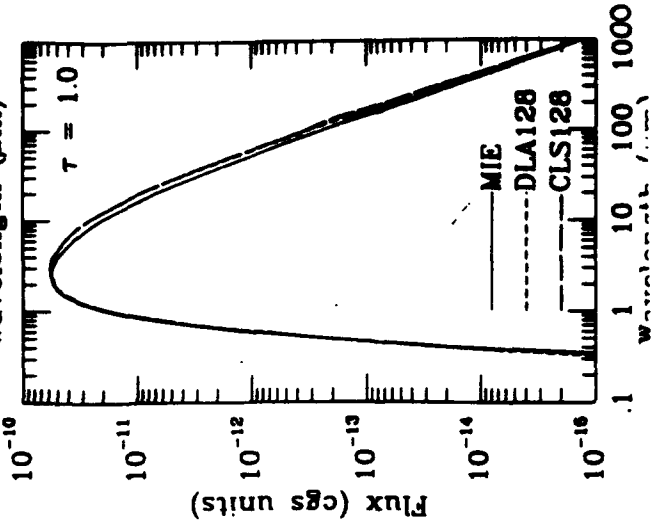
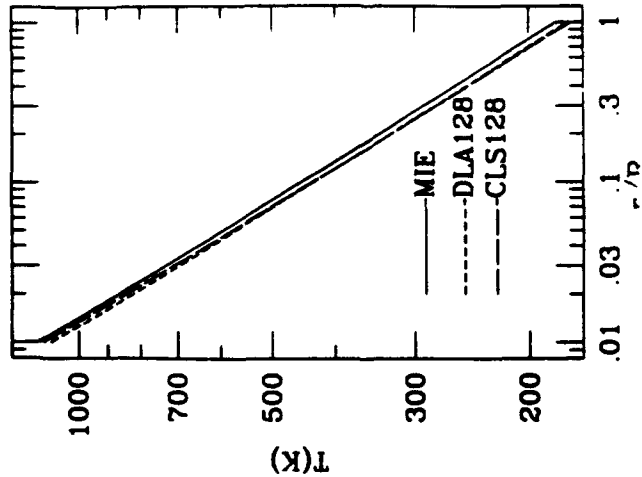
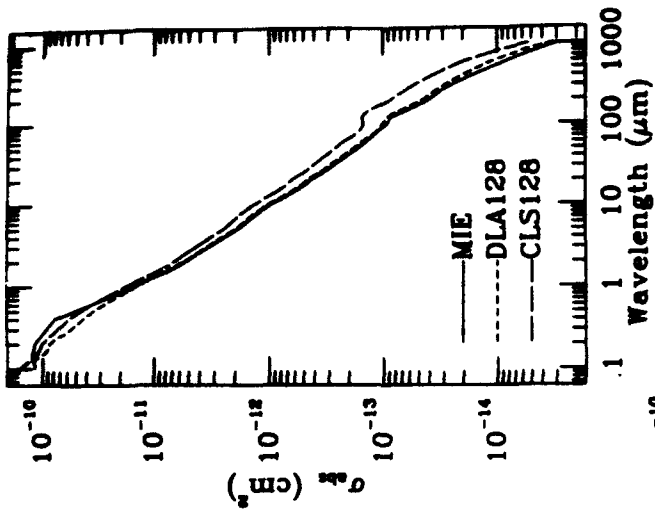
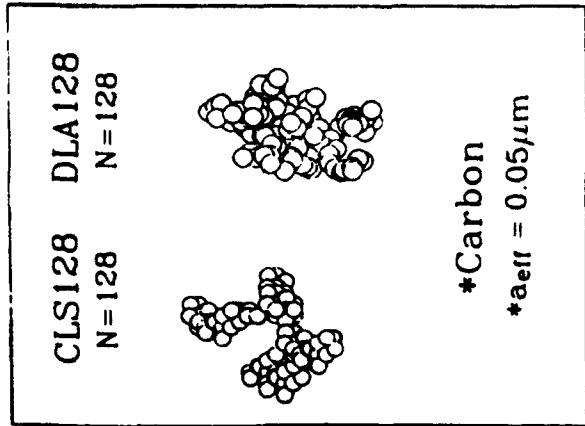
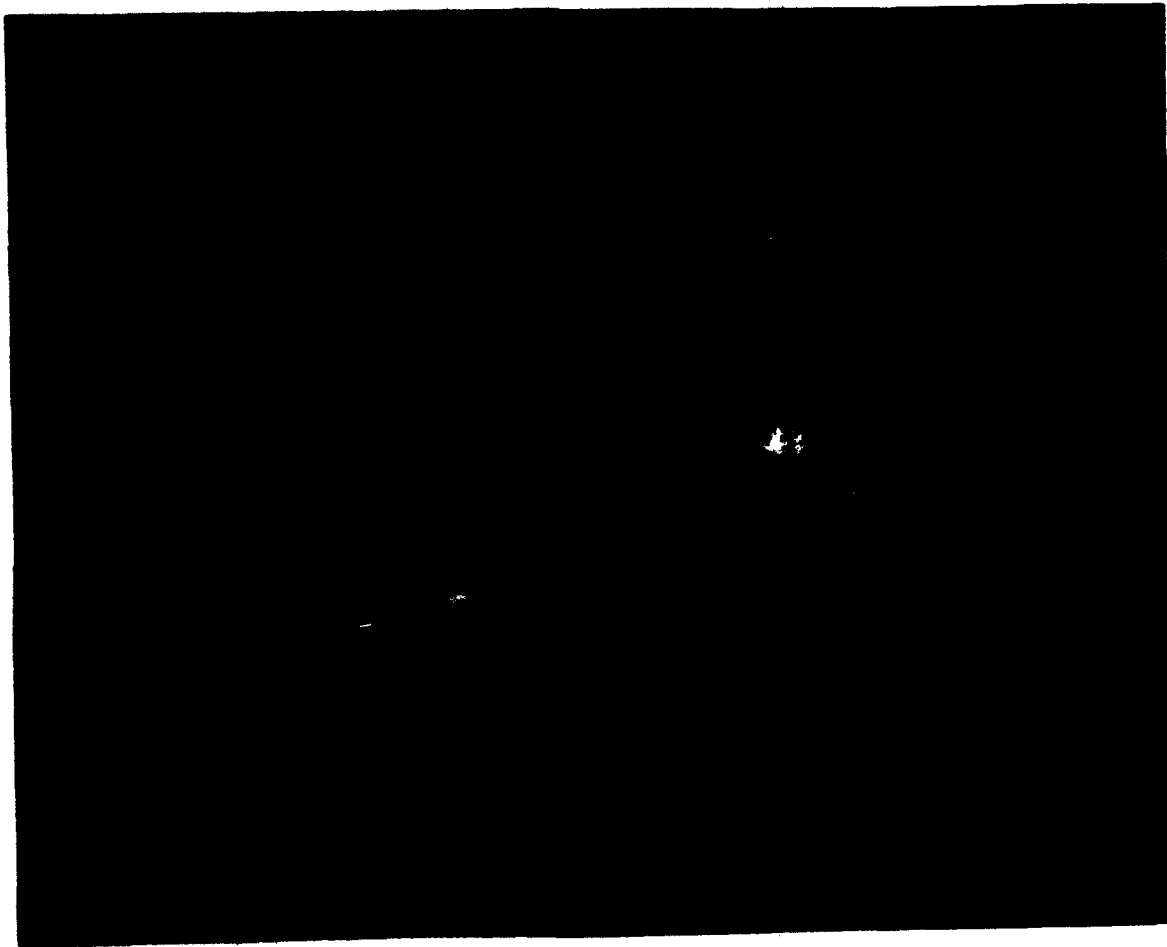
Dust Grains

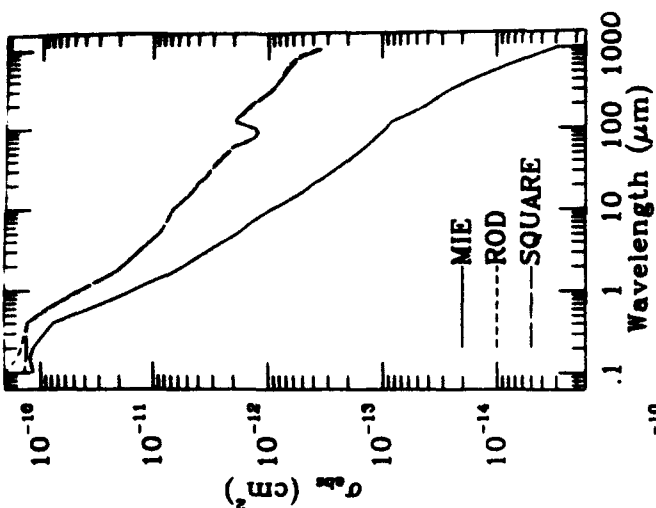
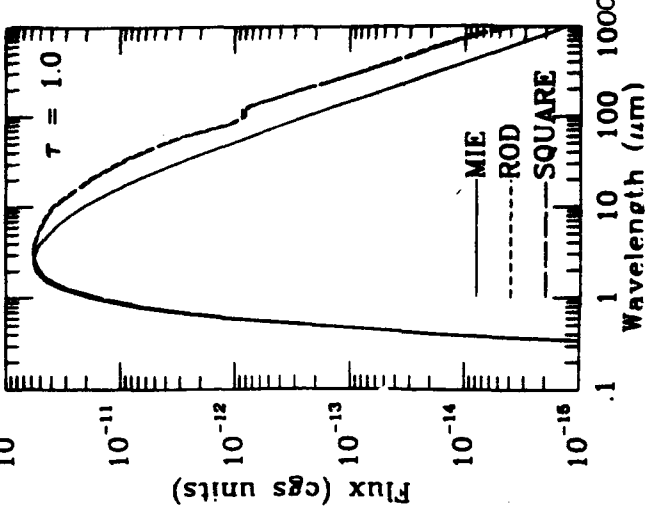
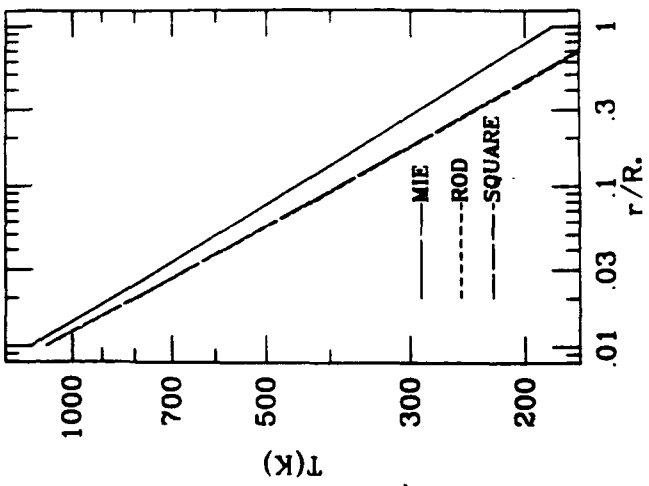
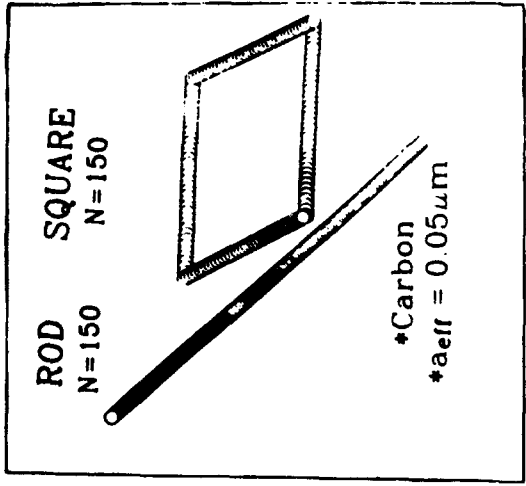
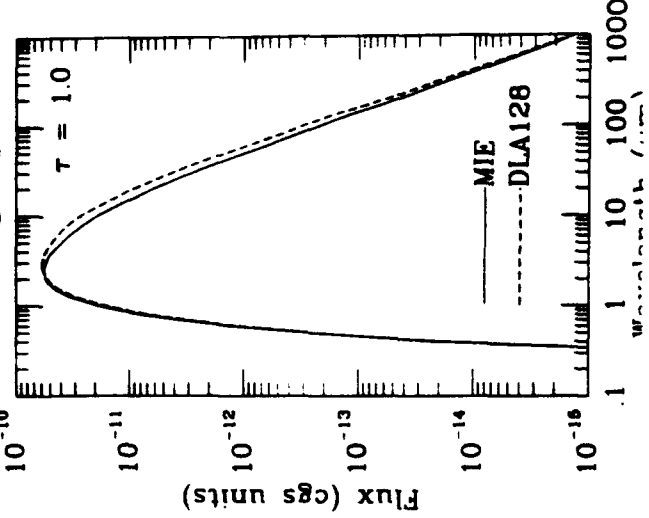
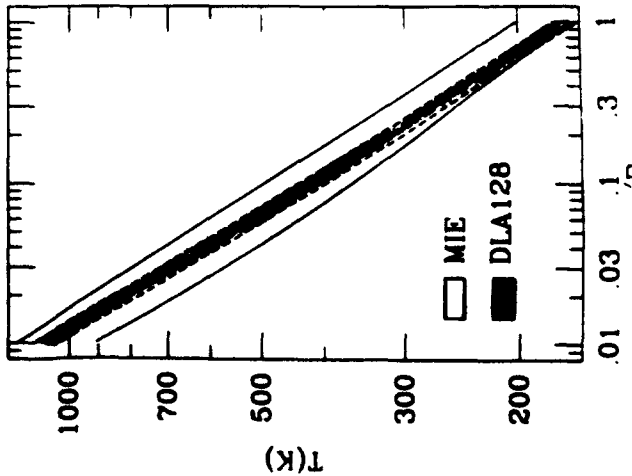
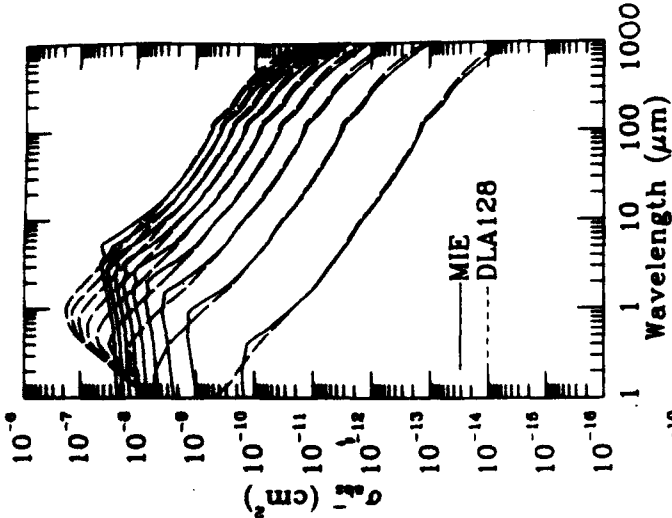
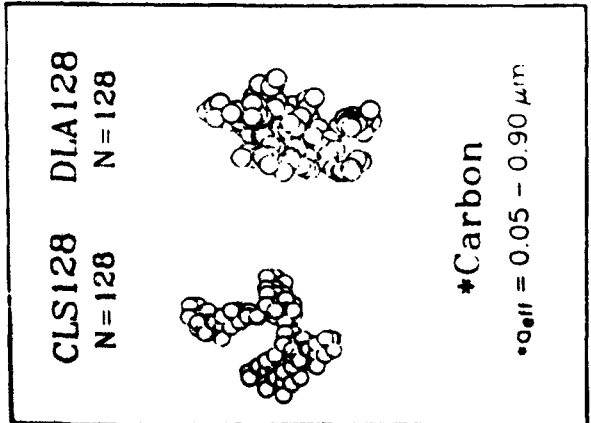
Effective Radius	0.05 μ m
Composition	amorphous carbon fractal carbon silicate
Grain Size Distribution	$n(a) \sim a^{-3.5}$

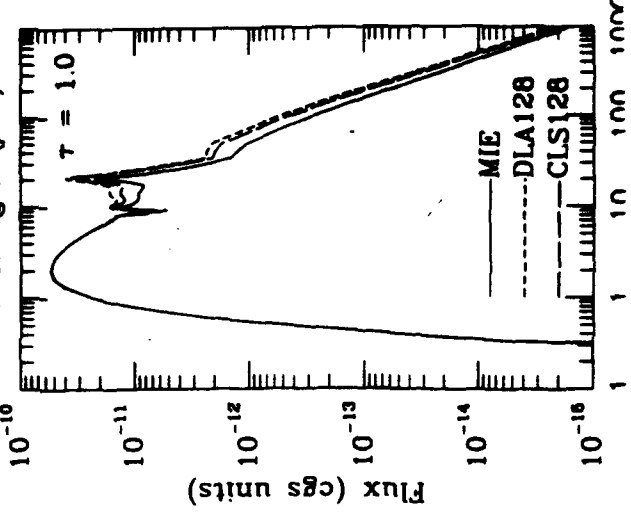
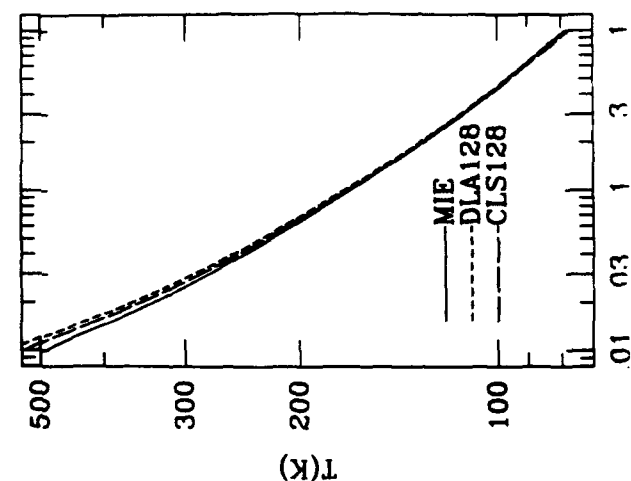
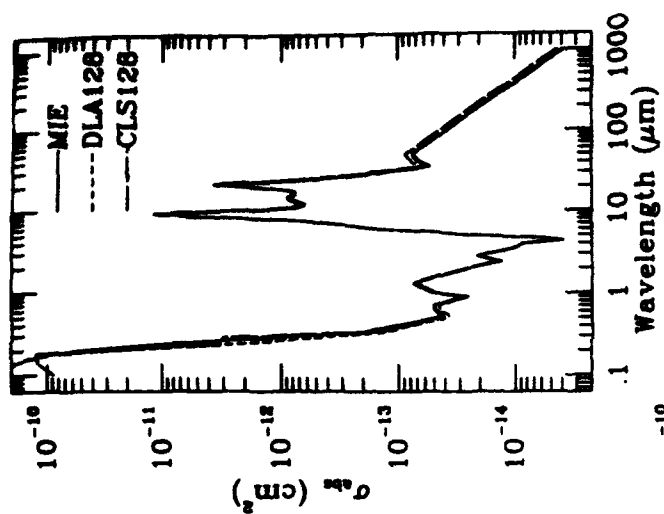
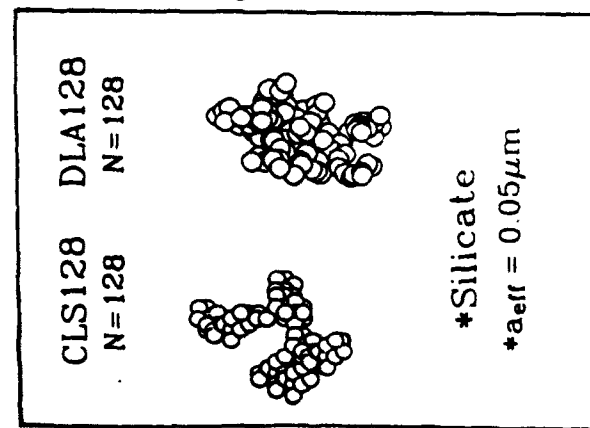
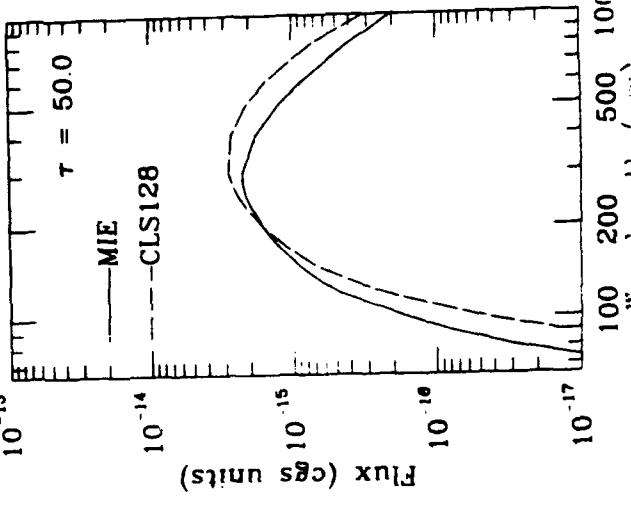
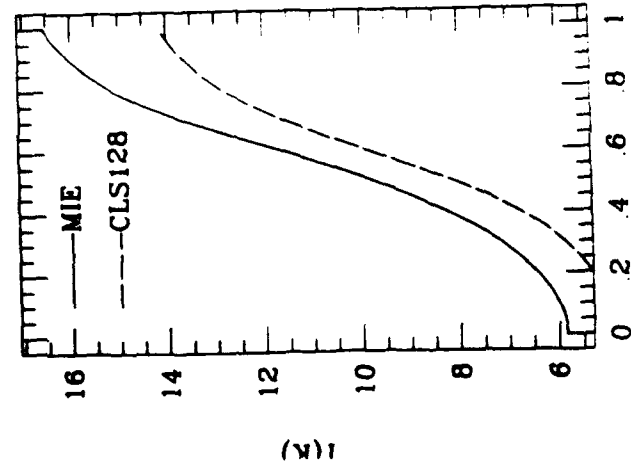
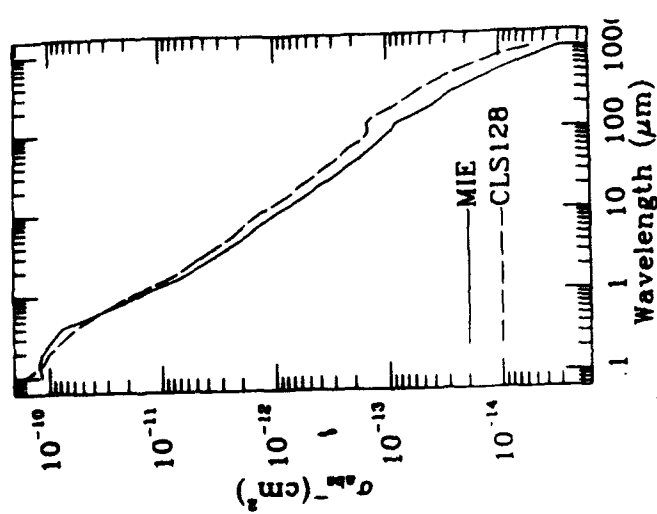
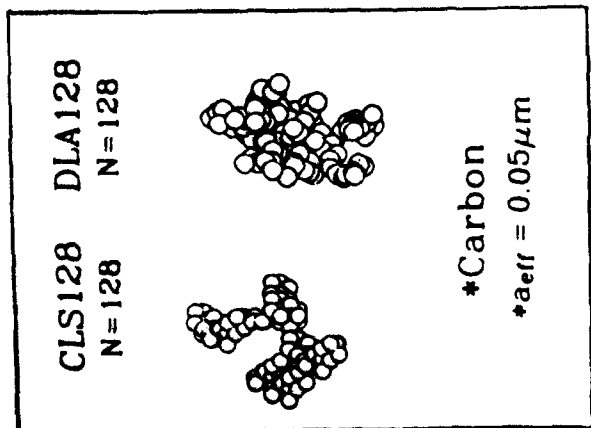
Circumstellar Dust Shell

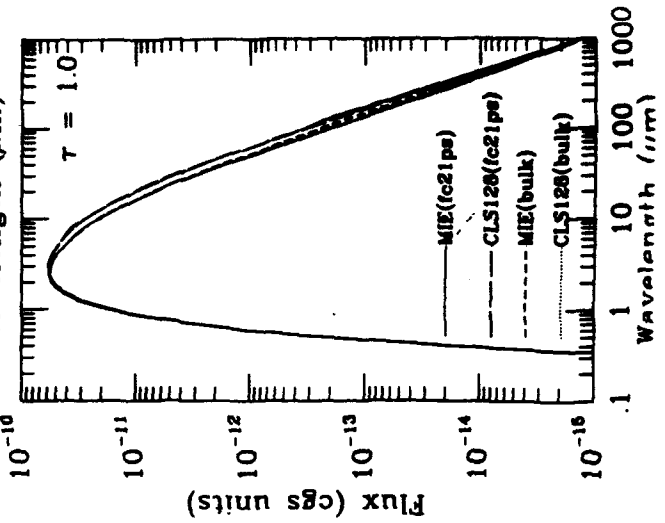
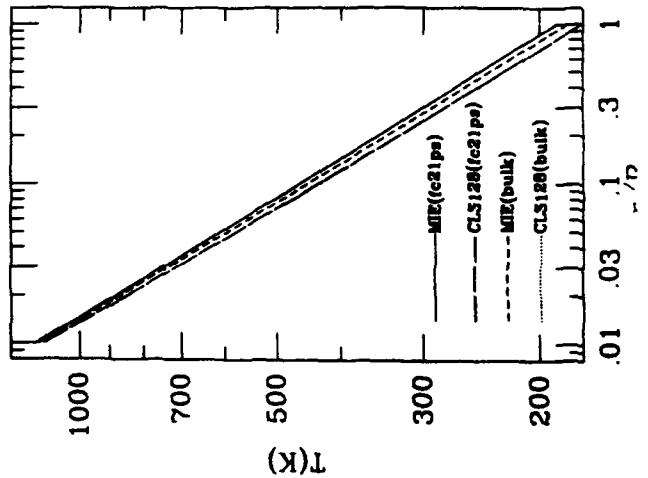
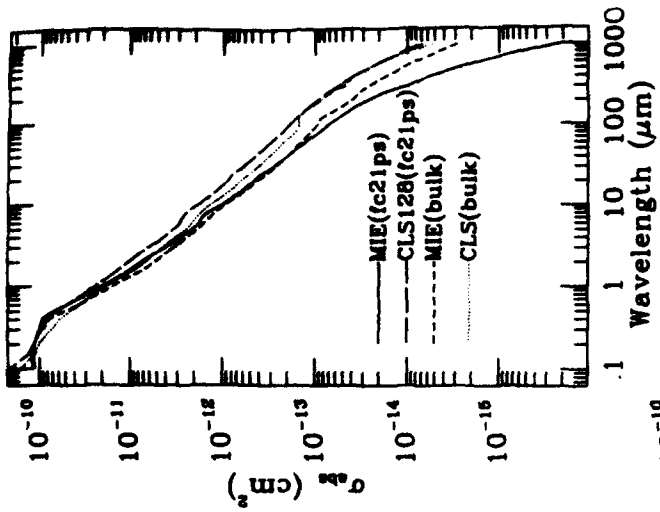
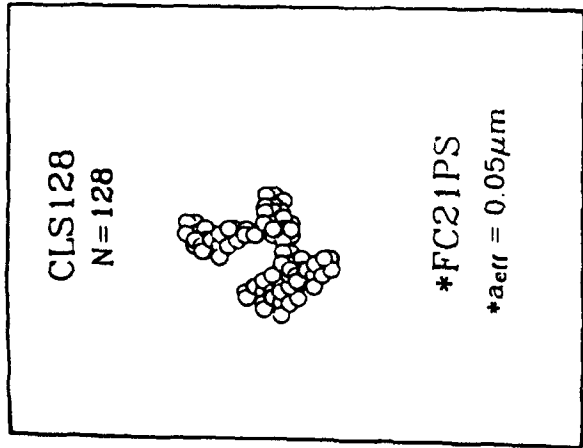
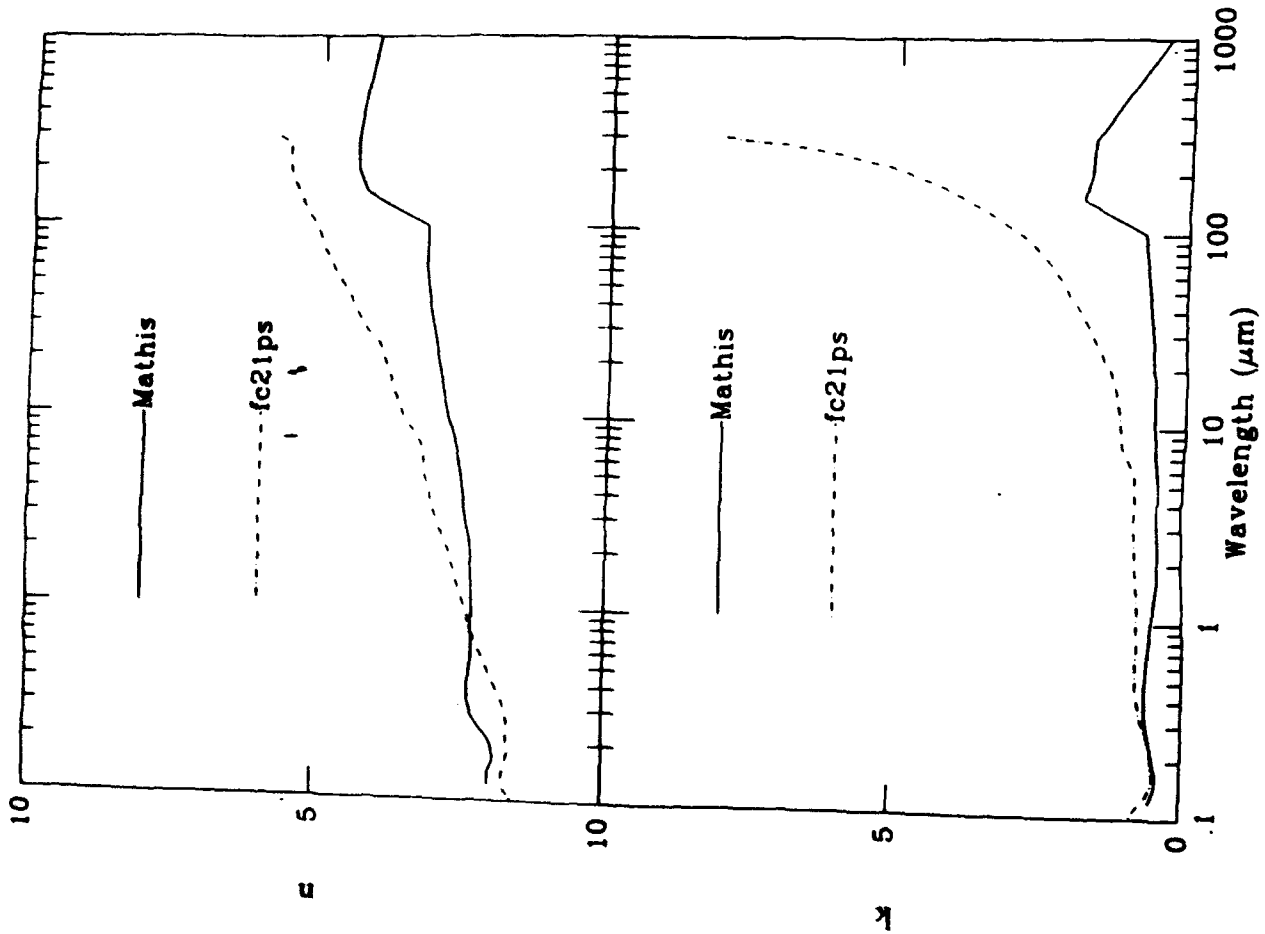
Shell Thickness	$5.0 \times 10^{-5} - 5.0 \times 10^{-3}$ pc
Star Temperature	2500 K
Star Luminosity	$10^4 L_{\odot}$
Grain Density Distribution	$n(r) \sim r^{-2}$
Optical Depth	$\tau(0.5\mu\text{m}) = 1.0$











CONCLUSIONS

Figure 3 - Effect of grain shape on the infrared spectrum of circumstellar dust shell.

Figure 4 - Effect of grain shape on the infrared spectrum of circumstellar dust with a MRN size distribution.

Figure 5 - Effect of grain shape for grains with the same ratio of cross section to volume.

Figure 6 - Effect of grain shape on spectral features of circumstellar dust shell.

Figure 7 - Optical constants of amorphous carbon (bulk vs. amorphous clusters).

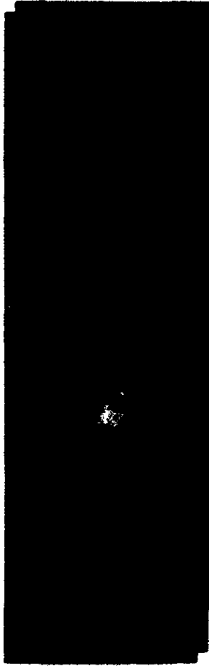
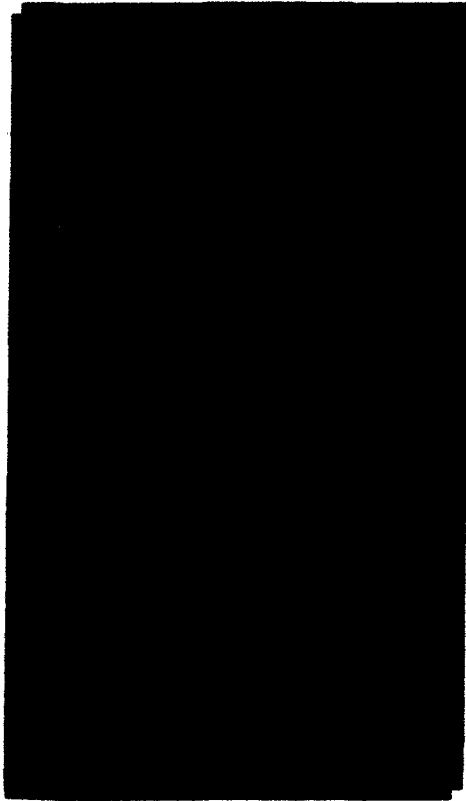
Figure 8 - Effect of fractal vs. bulk optical constants on the infrared spectrum of a circumstellar dust shell.

Figure 1 - Model interstellar dust grain formed through particle by particle aggregation.

Figure 2 - Model interstellar dust grain formed through cluster by cluster aggregation.

1. Compared to spherical grains with the same composition and volume, fractal grains are better absorbers/emitters, and will have a lower temperature. This results from a larger ratio (P) of geometric cross section to volume in fractal grains. Hence model spectra of infrared sources with fractal grains tend to peak toward longer wavelengths (see Figures 3 and 4).
2. Fractal grains of different shapes but with the same value of P have similar temperatures and spectral peaks. The overall grain shape plays only a minor role. (see Figure 5).
3. For spectral features, models of infrared sources with fractal silicate grains show both a deeper absorption at 10 microns and a stronger emission at 20 microns because, compared to spherical grains, fractal grains are more efficient both as absorbers and emitters (see Figure 6).
4. For dust grains of the same composition, the effects on the temperature and infrared spectra of using different optical constants (bulk materials vs. amorphous clusters as seen in Figure 7) are less drastic compared to those of assuming different grain shapes (see Figure 8).

This work has been partially supported by the US Air Force under grant AFOSR-89-0104.



Circumstellar Envelopes (CSEs) are rich chemical environments. However, current models cannot reproduce some of the over 35 observed species or their abundances.

Recently (Millar, Mamon, Glassgold), it has become clear that photoprocessing of certain species can dramatically alter the observed chemistry.

S.D. Doty & C.M. Leung

Rensselaer



In particular, the following may occur:

- Species may photodissociate, creating an extra source of basis species
 $(\text{CO} + \gamma \rightarrow \text{C} + \text{O})$
- Species may photoionize, giving rise to many fast ion-molecule reactions
 $(\text{C} + \gamma \rightarrow \text{C}^+; \text{C}^+ + \text{C}_2\text{H} \rightarrow \text{C}_3^+ + \text{H})$





● **Chemical Reaction Networks**

- Millar (26 species, 34 reactions)
- Millar (85 species, 270 reactions)

● **Continuum Transfer: (dust & H₂)**

- Analytic Approximation
- $I = I_0 \exp(-1.644\tau^{0.88})$

● **Line Transfer: Ignored -or-**

- Sobolev Approximation
for CO only
No H₂ dissociation

■ **This work:**

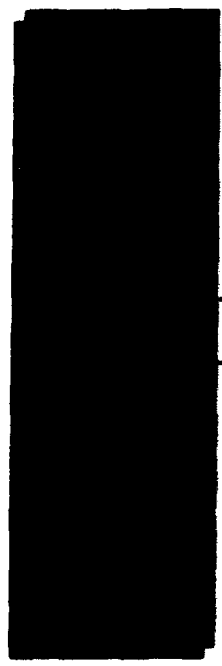
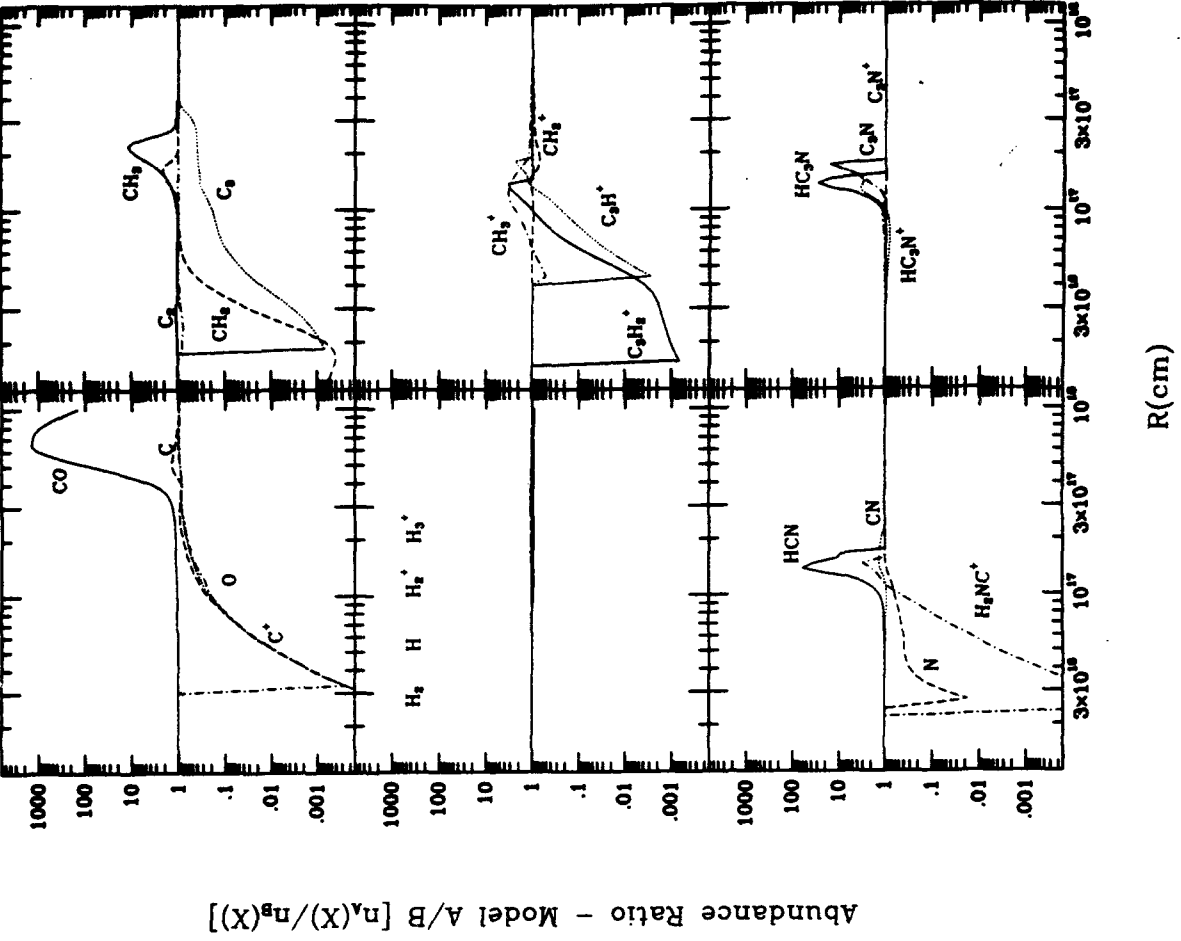
- Chemistry (67 species, 462 reactions)
- Sobolev Approximation for CO
- Dust and H₂ continuum self-consistently
- H₂ dissociation analytically

To explore the effects of different treatments of radiative transfer on CSEs, we have constructed 4 models of increasing complexity. These models are labeled A, B, C, and D, and are detailed in *Table 1*.

In *Figures 1, 2, and 3*, we plot the ratio between models of selected species. Note that the CO difference increases due to the increasingly better treatment of the radiative transfer. Also note the large number of species with differences of over 10x, suggesting that the radiation field affects the chemistry as well as direct photo-processing.

In the next two pages, we detail how (through photoprocessing and ion-molecule chemistry) the radiation field can affect specific species. Usually, this occurs via fast ion-molecule rxns.

Finally in *Figure 4*, we compare a "Normal" CSE chemical model, and our most sophisticated treatment of the transfer. Notice the large differences, especially in the Hydrocarbons.

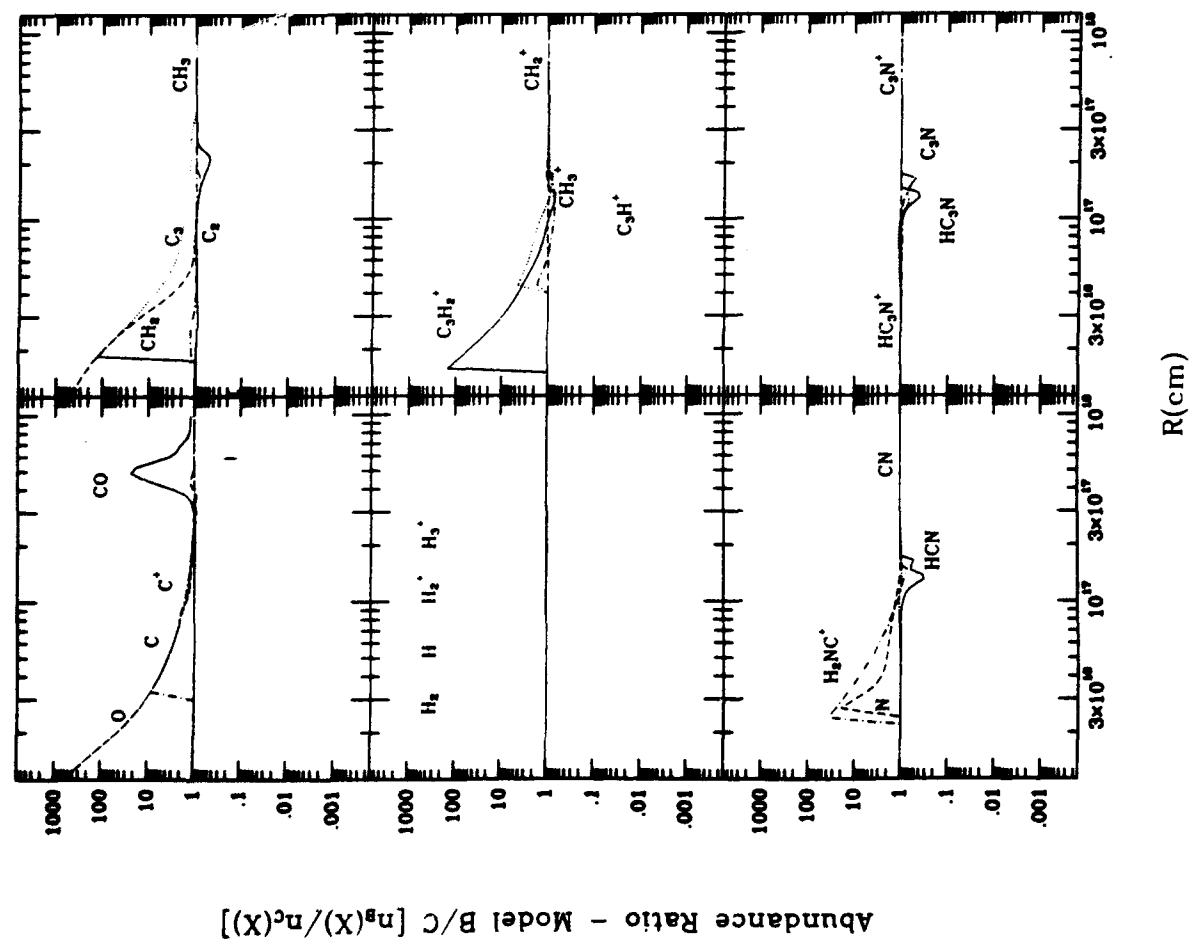
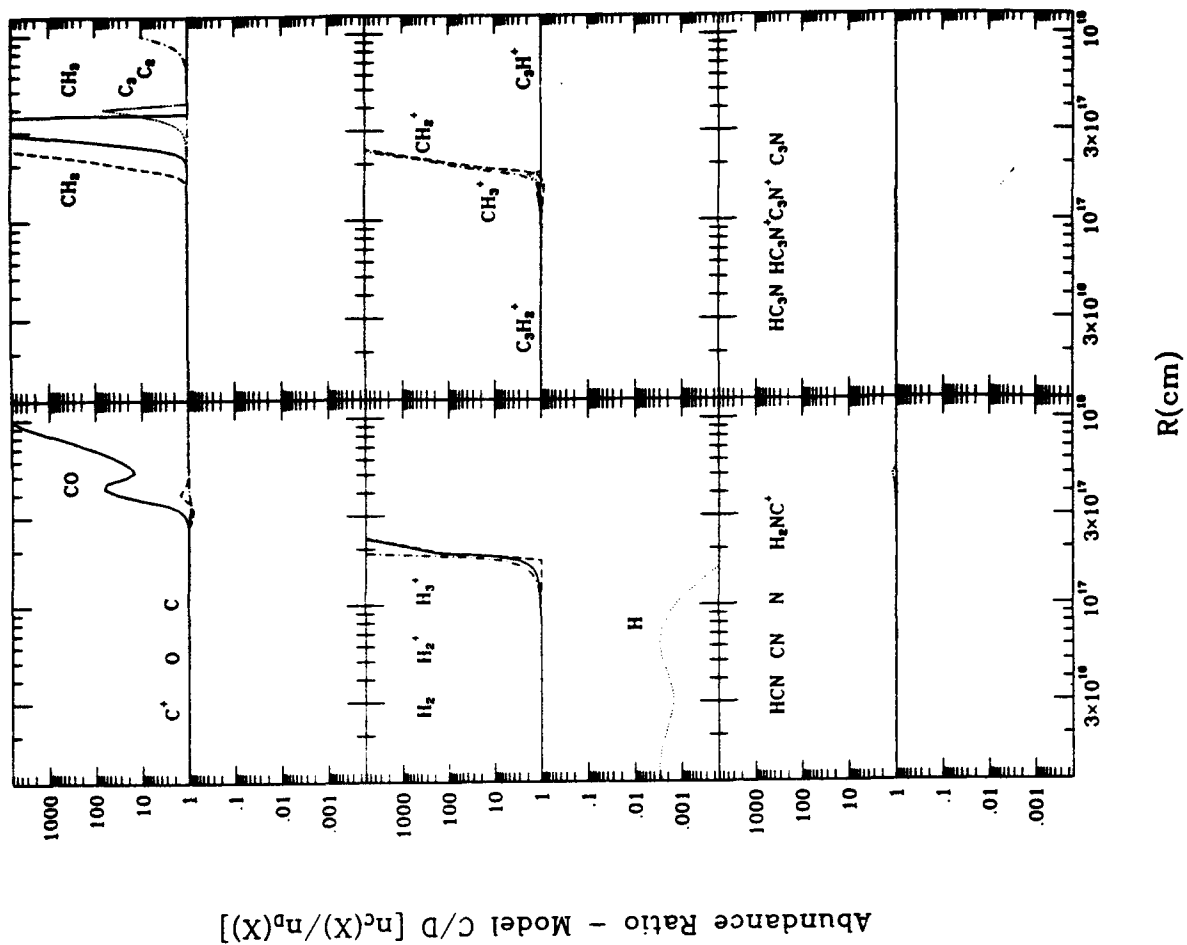


	A	B	C	D
exp(- τ^{ab})	✓	✓		
Self Con.			✓	✓
Sobolev:				
Self-Shielding H ₂ blocking		✓	✓	✓
H ₂ Dissociation				✓

D U S T

C O

H₂



To explain the differences in abundances, we must explore creation/destruction pathways:

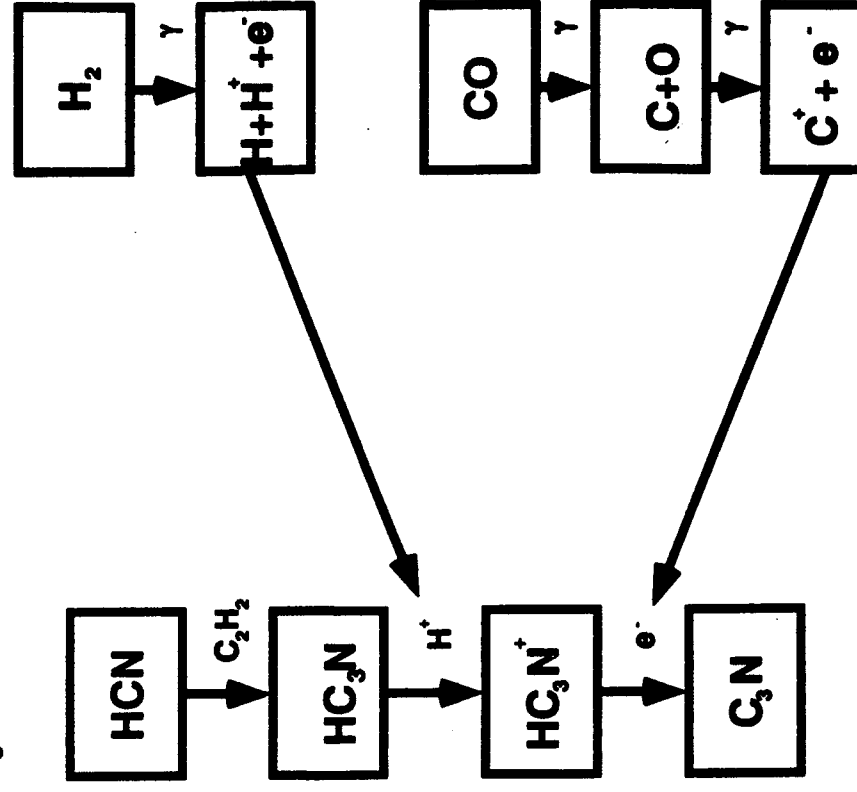
- *CO: Shielding from Dust, H₂, & CO.*
Also affects other species through C, C⁺, O.

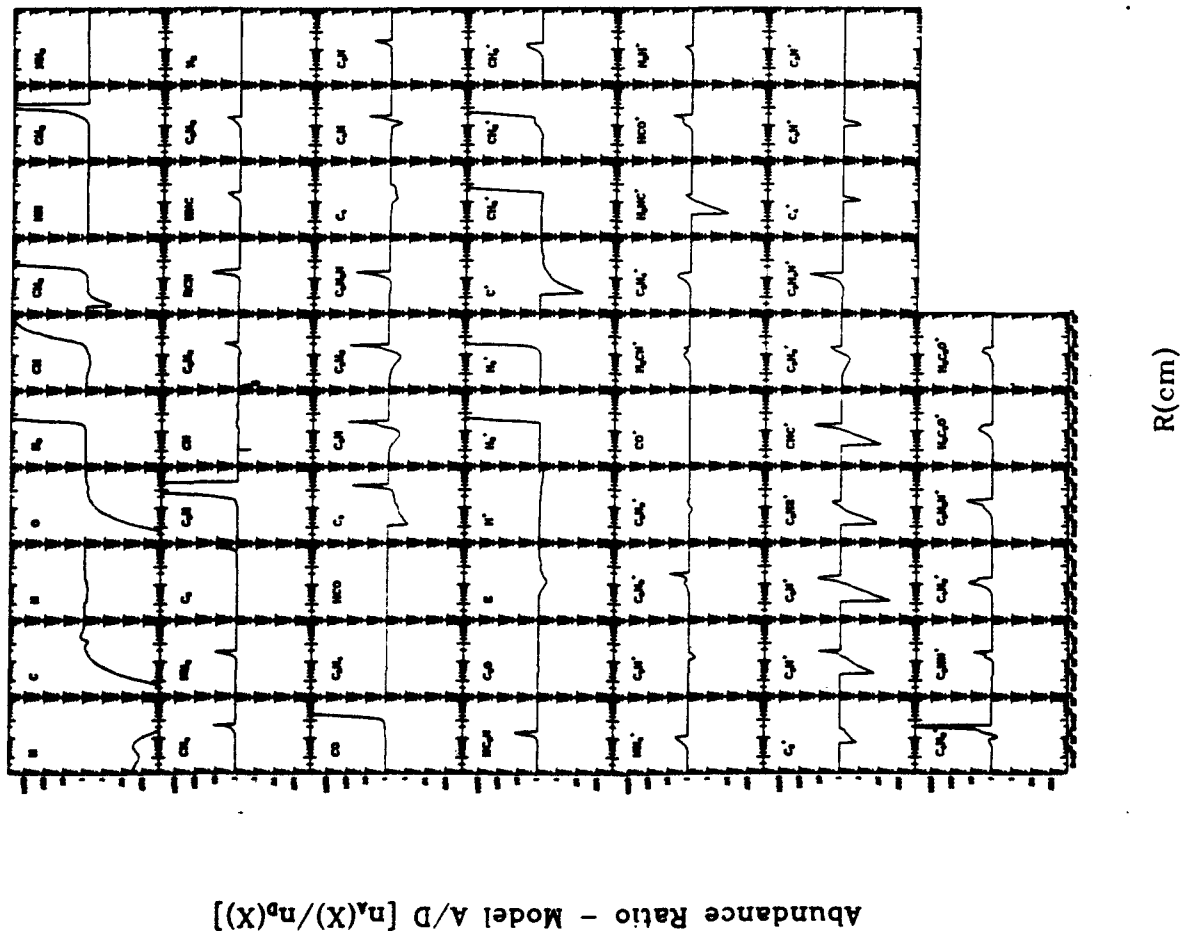
- *C₃: Example of photoprocessing*



- *C₃N: Production Enhancement*
Production of C₃N, is by Ion-Molecule reactions, with key species enhanced by photoprocessing. (See next page)

C₃N differences: Production





As shown, the self-consistent application of radiative transfer can have pronounced effects on the abundance of not only the photo-processed species, but also other chemically active species.

We conclude that:

- 1) Analytic approximations to the continuum radiative transfer underestimate the destruction rate for photodissociating molecules.
- 2) CO self-shielding dominates dust shielding
- 3) H_2 is an effective shield
- 4) H_2 dissociation is an important process in

Circumstellar Envelopes.

- 5) Detailed chemistry is needed as the fast ion-molecule reactions propagate chemical differences deep into the reaction network.

Probing the Carbon-to-Oxygen Ratio in Dense Interstellar Clouds

Monika E. Kress
Chun Ming Leung
William M. Irvine (UMass)

Rensselaer

INTRODUCTION

The two dense interstellar clouds, L134N and TMC-1, have similar physical conditions (e.g., gas temperature and density) but display remarkable differences in chemical abundances. In particular, whereas TMC-1 exhibits relatively large abundances of many complex, unsaturated, carbon-rich species (e.g., cyanopolyyynes and complex hydrocarbons), L134N has larger abundances of some oxygen-rich species as well as simple saturated molecules (e.g., NH_3 , H_2S , and SO_2).

The focus of our research is to determine if this discrepancy may be due to a difference in the initial gas phase carbon-to-oxygen ratio. To delineate the effects of different initial composition versus cloud evolutionary status, the pseudo-time-dependent chemical models of Herbst and Leung are used to study the chemical evolution of these clouds. The original reaction network of Herbst and Leung has been expanded to include 3517 reactions involving 385 chemical species. The model results are then compared with observations of 45 species.

Several molecules have shown sensitivity to the initial C-to-O ratio. Among these are NO and SO_2 ; both of which are observed in TMC-1 and L134N.

ASSUMPTIONS & MODEL PARAMETERS

- Constant physical conditions

- constant gas and grain densities ($n = 2 \times 10^4 \text{ cm}^{-3}$)
- constant gas temperature ($T = 10 \text{ K}$)

The interplay between dynamical and chemical time scales is ignored.

- Gas-grain interactions are ignored except for grain surface reactions involving

- formation of H_2
- selected charge neutralization

- Cloud is opaque and photodissociation by interstellar radiation field is ignored. This is justified since molecular evolution occurs mostly after a cloud becomes dense and therefore opaque to UV radiation.

- Cosmic ray ionization rate: $1.3 \times 10^{-17} \text{ s}^{-1}$

- Number of species: 385
- Number of reactions: 3517

- Initial chemical composition

- pertains to a diffuse cloud with significant amount of H_2
- non-zero initial abundance for H_2 , He, N, O, Cl, e^- , C^+ , S^+ , Si^+ , Fe^+ , Na^+ , Mg^+ , P^+ , and neutral grains
- normal depleted gas-phase abundance
- "low-metal" abundance with [S], [Si], [Na], [Fe], [Mg], and [P] depleted by a factor of 100

- Cloud evolution - chemistry evolves for 10^8 years

FIGURE LEGEND

- Model 1: (standard model, $[\text{C}]/[\text{O}] = 0.4$)
- Model 2: (oxygen depleted, $[\text{C}]/[\text{O}] = 0.8$)
- Model 3: (carbon enriched, $[\text{C}]/[\text{O}] = 0.8$)
- observed value in TMC-1
- observed value in L134N

DISCUSSION OF RESULTS

We show results from three cloud models with different $[C]/[O]$ ratios. Models 2 and 3 have the same ratio but one is oxygen depleted while the other is carbon enriched. In Figures 1 - 3, we show the time evolution of the calculated abundance (relative to H_2) of all the species observed in TMC-1 and L134N. The observed values are also shown. Note that for most species the observed and calculated abundances agree only for time beyond 10^4 years. One can estimate the cloud age from the points at which the observed and calculated abundances intersect. Our results indicate that on average TMC-1 is at a slightly earlier stage of evolution.

The effect of $[C]/[O]$ ratio can be summarized as follows: (a) all the carbon and oxygen are channeled into CO and the equilibrium CO abundance (attained after 10^6 years) reflects the initial abundance of C or O, whichever is lower, (b) after the CO formation, an excess of carbon (in an O-depleted medium) will lead to an overpopulation of hydrocarbons while an excess of oxygen (in an O-enriched medium) will result in an over-abundance of oxygen-bearing molecules. For complex molecules, significant production occurs only when the abundance of atomic carbon is high and when the $[C]/[CO]$ ratio is of order unity. Finally, as shown in Figure 4, one can use the abundance ratio of certain molecules to distinguish between the effects of C-enrichment and O-depletion.

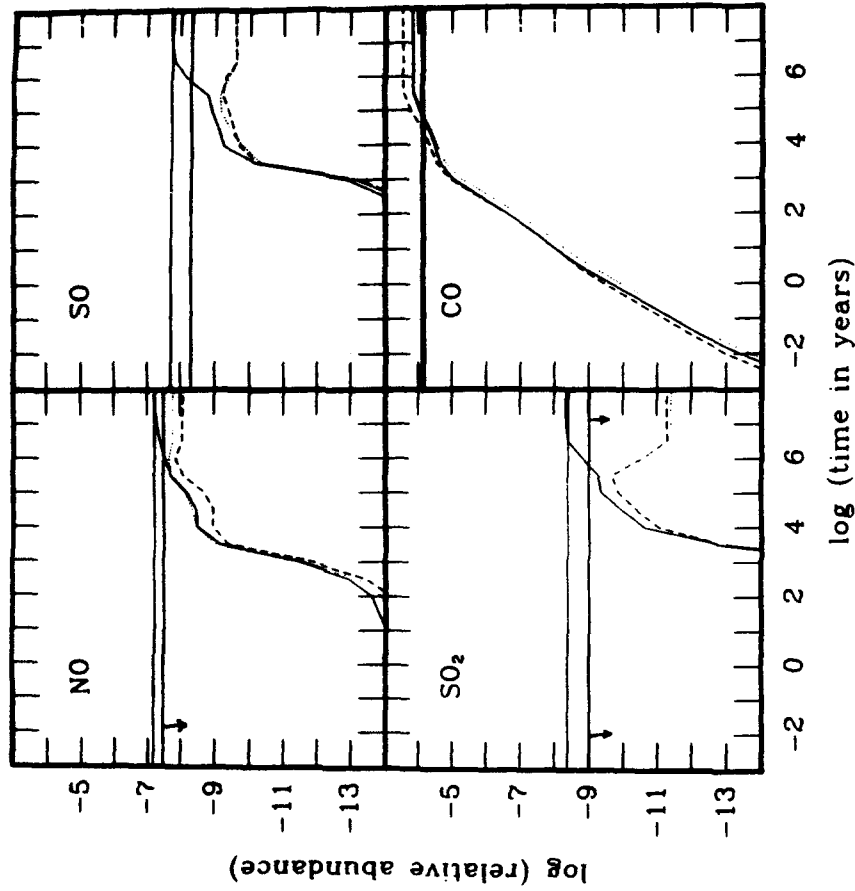
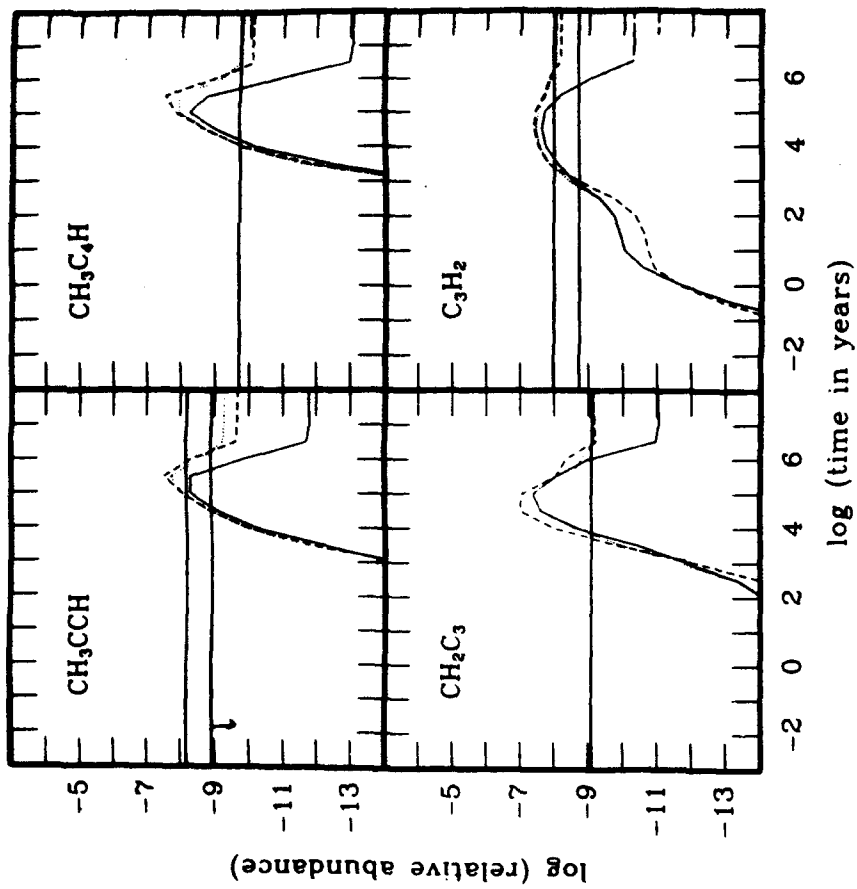
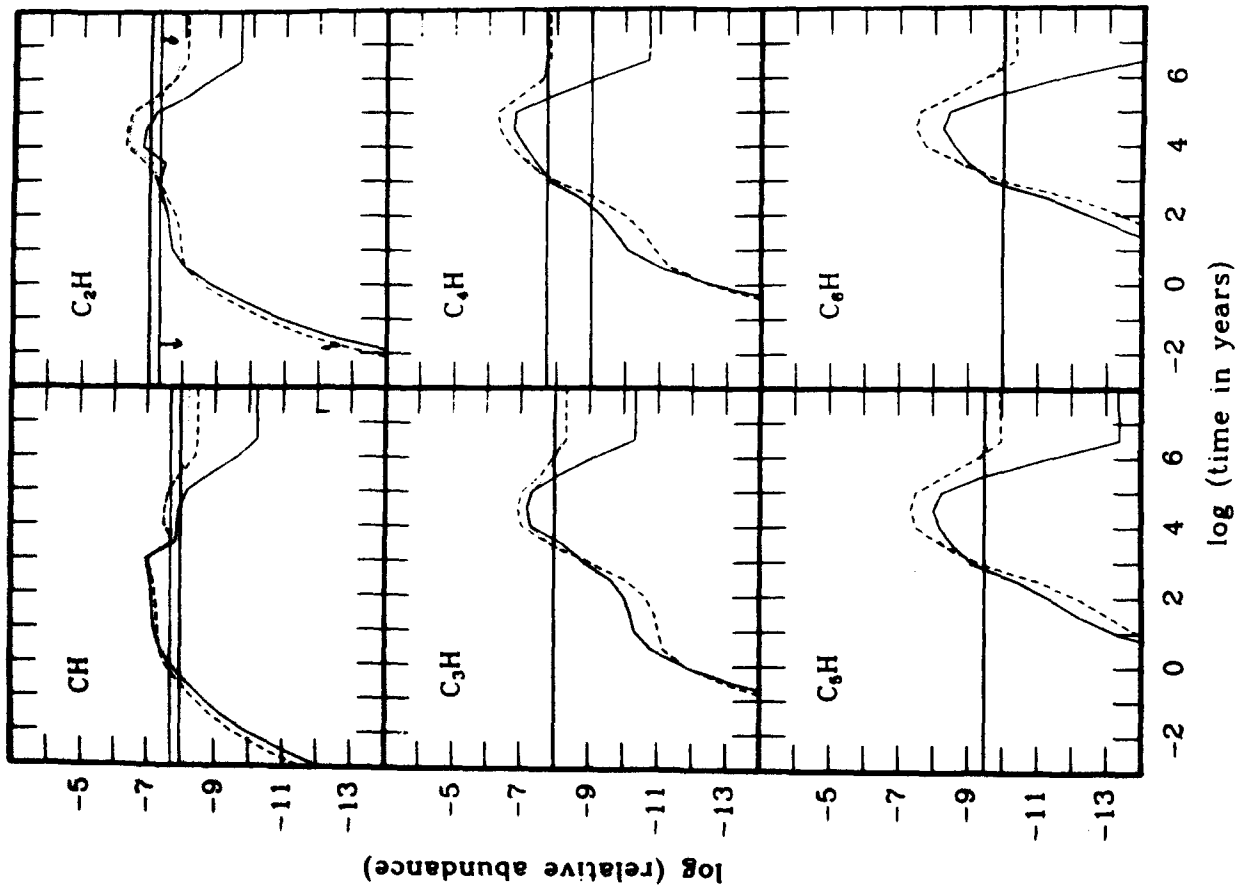


Figure 1 - The molecule NO shows a significant difference in abundance between models 2 and 3, and is a sensitive probe of the actual abundance of carbon or oxygen. On the other hand, SO and SO_2 are extremely dependent on the actual $[C]/[O]$ ratio, but not on the actual abundance of oxygen or carbon. The abundance of CO depends only on the amount of carbon available, i.e., the amount of carbon dictates the abundance of CO, particularly after 10^5 years. The C_nH family of molecules demonstrates its preference for a high value of the $[C]/[O]$ ratio as do other hydrocarbons.



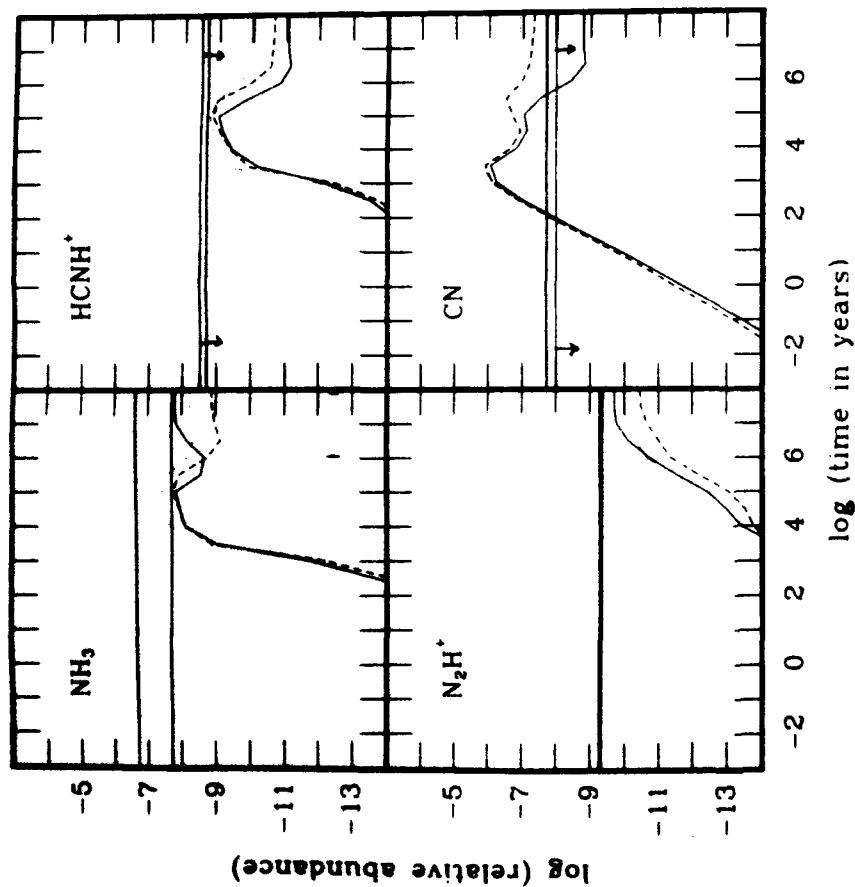
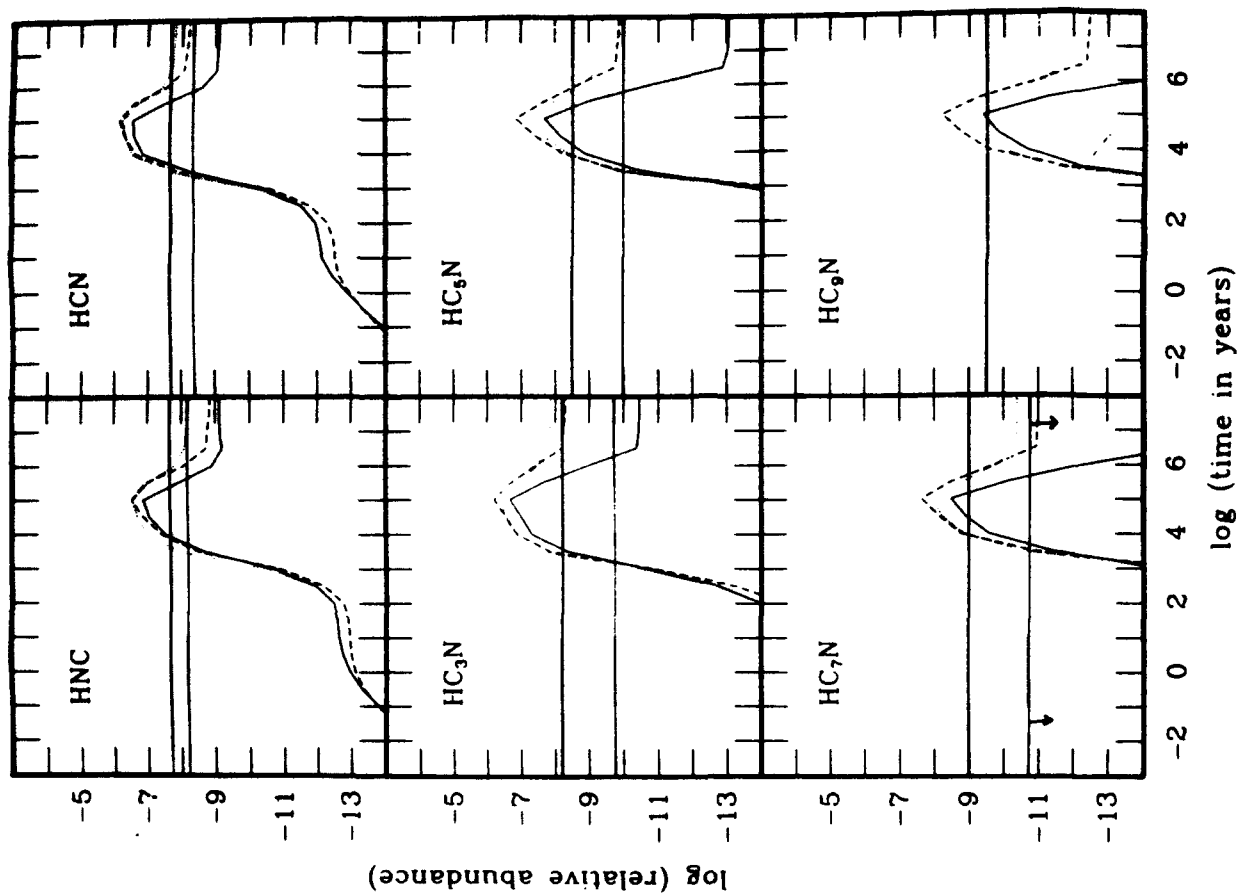


Figure 2 - The observed abundance for NH_3 in L134N is higher than predicted by any of our models. This may be due to grain-surface chemistry which is not considered in our models. On the other hand, TMC's observed abundance is not higher than predicted, perhaps implying that grain-surface chemistry for this molecule in this cloud is not as important. TMC-1 shows very high abundances of the cyanopolynes (HC_nN) relative to L134N, perhaps implying that L134N is in a later stage of evolution than TMC-1, since all of these molecules undergo a steep drop in abundance after 10^5 years.



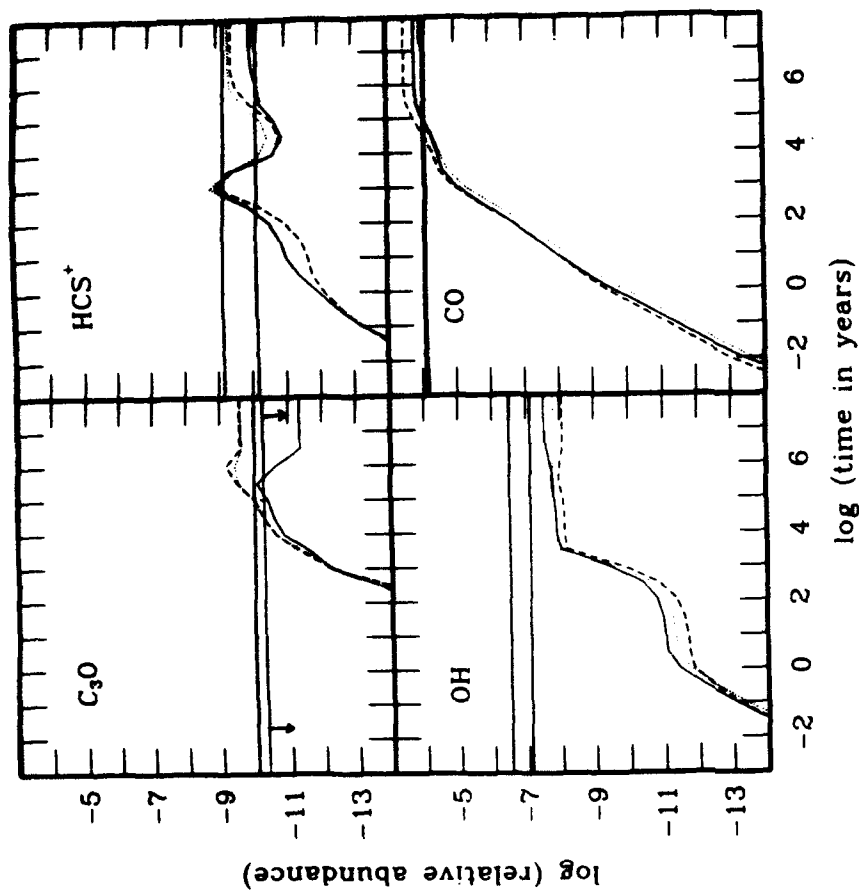
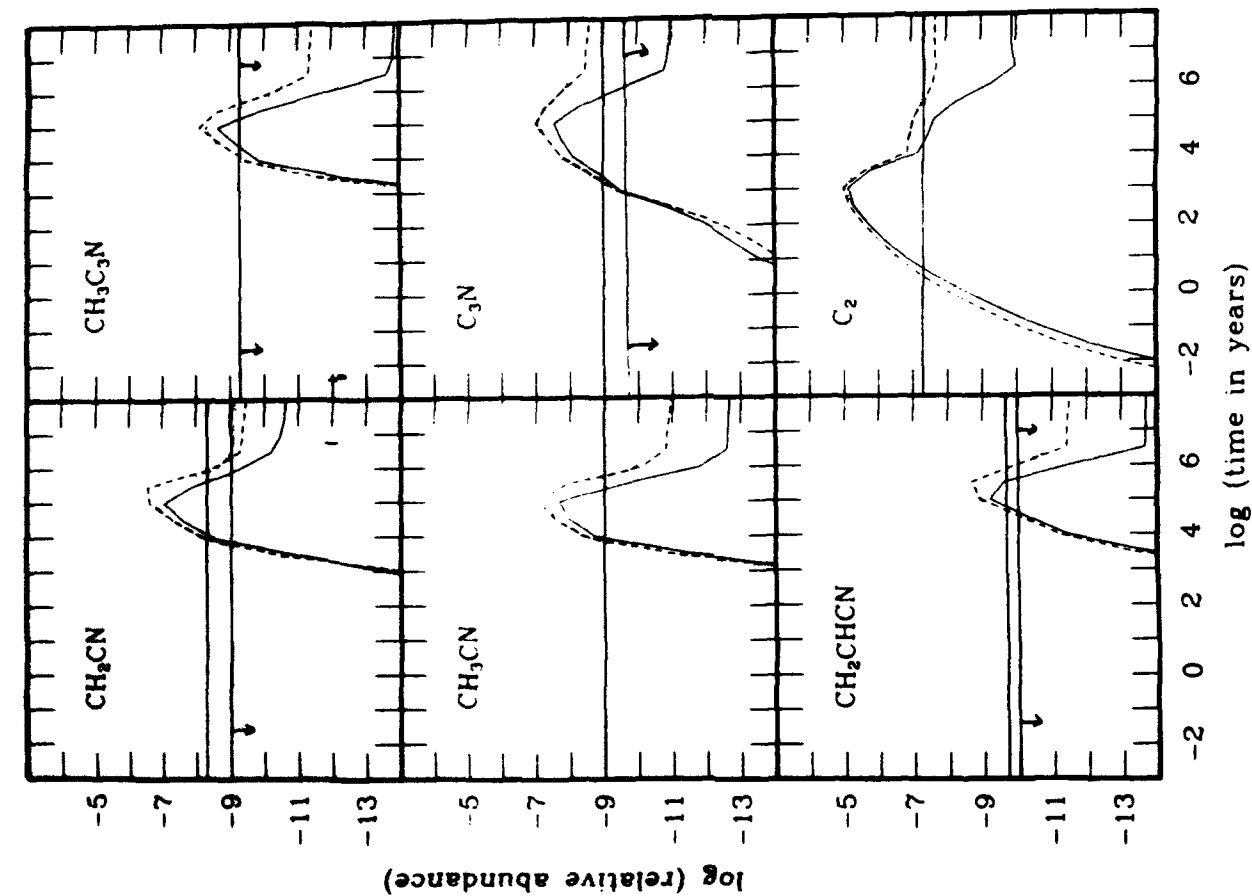
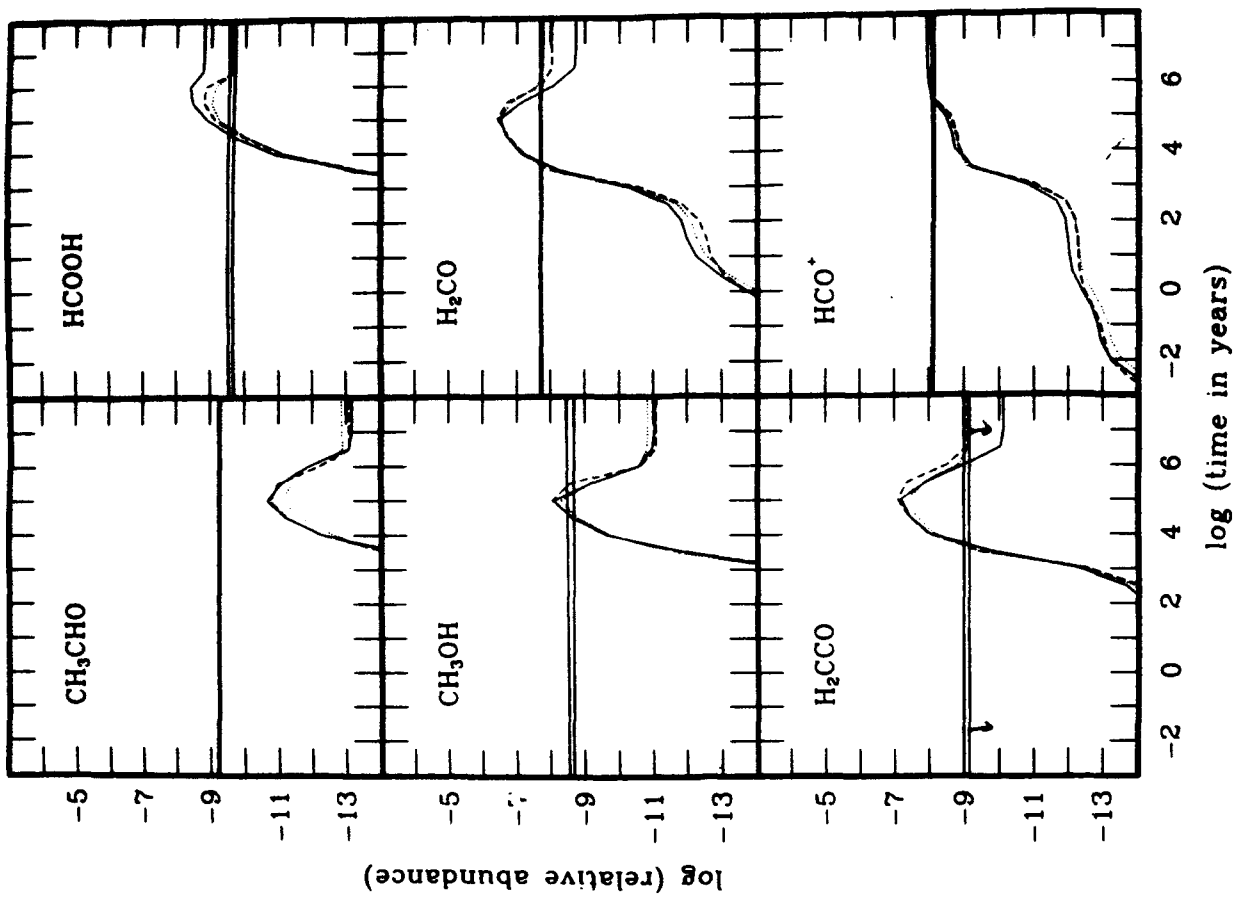
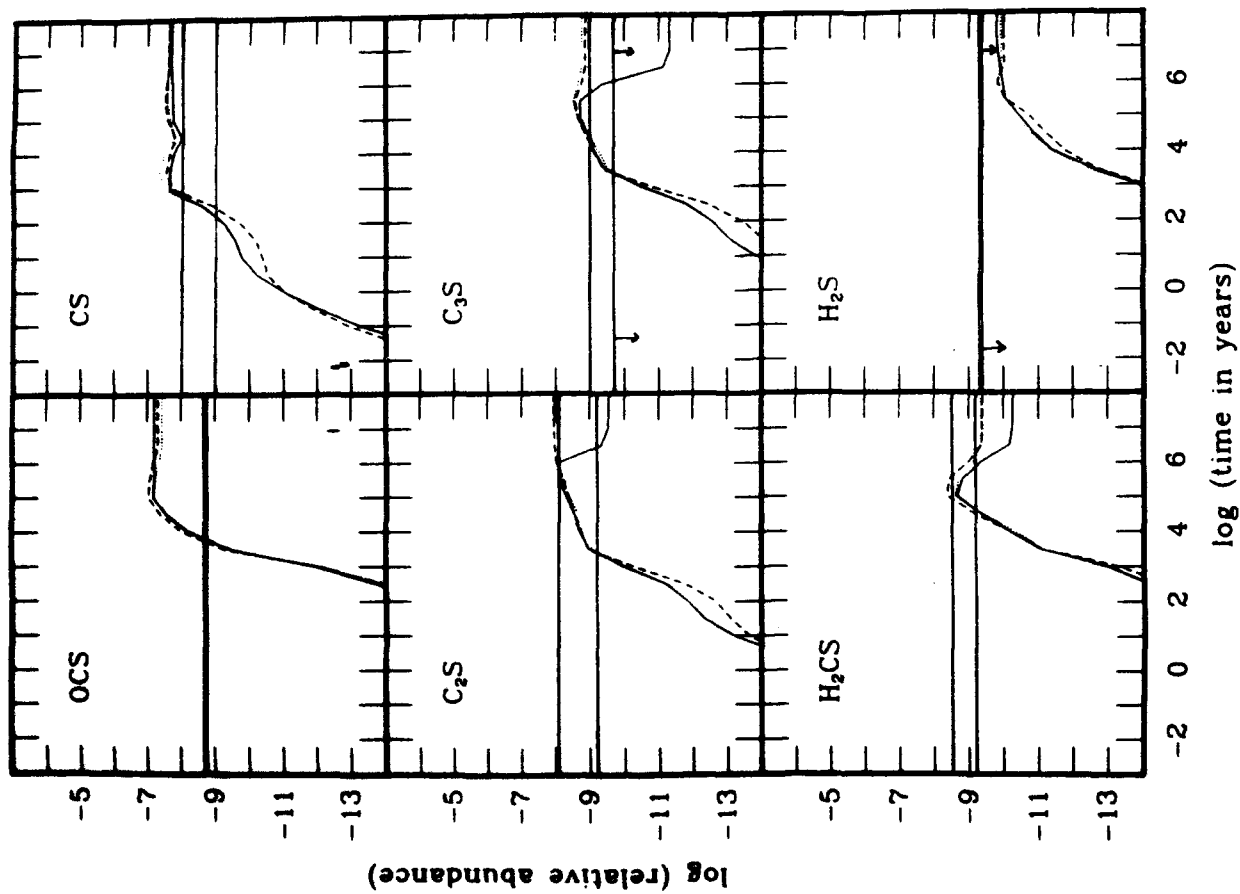


Figure 3 - Like NH_3 , the observed abundance of OH and H_2S in both clouds exceed any abundances predicted by our models. This is consistent with the fact that OH and H_2S are thought to play an active role in grain-surface chemistry. The sulfur-bearing molecules (e.g., OCS, CS, and H_2S) do not appear to be much affected by the $[\text{C}]/[\text{O}]$ ratio. Oxygen-bearing hydrocarbons show relatively little dependence on the value of the $[\text{C}]/[\text{O}]$ ratio compared to other species. Some of these molecules are also associated with grain-surface chemistry.



CONCLUSIONS

1. Considering the uncertainties in the chemical reactions and their rate coefficients, the overall agreement between the calculated abundances and those observed in TMC-1 and L134N is good.
2. The observations of L134N and TMC-1 are consistent with the interpretation that either TMC-1 has a somewhat higher $[C]/[O]$ ratio or that TMC-1 is at a slightly earlier stage of evolution.
3. For a given value of the $[C]/[O]$ ratio, abundance ratios of certain molecules, such as $[NO]/[CO]$ and $[N_2H^+]/[CO]$, may be used to distinguish between the case of oxygen depletion and carbon enrichment. On the other hand, abundance ratios of other molecules, such as $[SO]/[CH]$ and $[HCOOH]/[H_2CCO]$, can be used to probe the $[C]/[O]$ ratio and they are insensitive to the actual abundance of oxygen or carbon.